Apparatus and Methods for a New Measurement of the Electron and Positron Magnetic Moments

A dissertation presented

by

Elise M. Novitski

to

The Department of Physics

in partial fulfillment of the requirements

for the degree of

Doctor of Philosophy

in the subject of

Physics

Harvard University

Cambridge, Massachusetts

December 2017

Thesis advisor

Professor Gerald Gabrielse

Author

Elise M. Novitski

Apparatus and Methods for a New Measurement of the Electron and Positron Magnetic Moments

Abstract

This thesis presents contributions to two precision measurement experiments: electron and positron $g/2$, and ATRAP antihydrogen spectroscopy.

The magnetic moment of the electron in Bohr magnetons, $g/2$, is the most precisely measured fundamental property of an elementary particle, with an uncertainty of 0.28 parts per trillion. Positron $g/2$ is known a factor of 15 less precisely. Improvements in positron $g/2$ will improve on the best test of charge-parity-time (CPT) symmetry in leptons. Electron $g/2$ provides the most precise determination of α, the fine structure constant. The comparison of this value with an independent measurement of α is the most precise test of the Standard Model of particle physics.

A new apparatus has been built for making improved positron and electron $g/2$ measurements by performing quantum jump spectroscopy between the lowest quantum states of either particle trapped in a 100 mK cylindrical Penning trap. In this new apparatus, single cyclotron transitions of a single electron have been driven and detected in the precision measurement trap, and positrons have been trapped in a dedicated positron accumulation trap. This thesis describes progress toward improved $g/2$ measurements in this new apparatus. A new pulsed positron transfer system addresses significant challenges in transferring positrons into the precision measure-

ment trap without compromising the single-particle detection system and control of the resonant microwave cavity mode structure. Helium is recovered, pressure tightly controlled, and vibrations mitigated in cryogen spaces critical for magnetic field stability. A parametric cavity mode detection technique for systematic $g/2$ corrections is demonstrated for the first time in the new apparatus.

ATRAP is an experiment that aims to test CPT symmetry through precision spectroscopy of trapped antihydrogen. This thesis describes analytical quench propagation predictions and a new quick-turnoff system for ATRAP's Ioffe trap. These systems are important both for antihydrogen detection and for the protection of magnets in case of quenches.

Contents

List of Figures

List of Tables

Publications

Published

1. *High efficiency positron accumulation for high-precision magnetic moment experiments*
   S. Fogwell Hoogerheide, J. C. Dorr, E. Novitski, and G. Gabrielse. Rev. Sci. Inst. **86** 053301 (2015).

2. *Precise matter and antimatter tests of the Standard Model with electrons, positrons, protons, antiprotons, and antihydrogen*
   G. Gabrielse, S. Fogwell Hoogerheide, J. Dorr and E. Novitski, in Fundamental Physics in Particle Traps, edited by W. Quint and M. Vogel, Springer, Darmstadt, pp. 1 - 37 (2014).

3. *Adiabatic cooling of antiprotons*
   G. Gabrielse, W.S. Kolthammer, R. McConnell, P. Richerme, R. Kalra, E. Novitski, D. Grzonka, W. Oelert, T. Sefzick, M. Zielinski, D. Fitzakerley, M.C. George, E.A. Hessels, C.H. Storry, M. Weel, A. Müllers, and J. Walz, Physical Review Letters **106**, 073002 (2010).

4. *Centrifugal separation of antiprotons and electrons*
   G. Gabrielse, W.S. Kolthammer, R. McConnell, P. Richerme, J. Wrubel, R. Kalra, E. Novitski, D. Grzonka, W. Oelert, T. Sefzick, J.S. Borbely, D. Fitzakerley, M.C. George, E.A. Hessels, C.H. Storry, M. Weel, A. Müllers, J. Walz, and A. Speck, Physical Review Letters **105**, 213002 (2010).

In Preparation [1]

1. *Two-Symmetry Penning-Ioffe Trap for Antihydrogen Cooling and Spectroscopy*
   E. Tardiff and the ATRAP collaboration (incl. E. Novitski). Manuscript in preparation.

[1] Other manuscripts concerning the ^{3}He NMR probe, the planar Penning trap, the helium recovery and pressure control system, and pulsed positron transfer are in earlier stages of preparation but will include content from this thesis.

Dedicated to my parents, Peggy and Charles Novitski.

Acknowledgments

I thank Jerry Gabrielse, my advisor, for his vision and tireless effort in creating and sustaining the Harvard electron/positron $g/2$ and ATRAP experiments. I deeply appreciate his support for me as a scientist and a person. I thank my committee members, Masahiro Morii and Markus Greiner, for their support throughout my time in the graduate program.

I thank my predecessors on the Gabrielse electron $g/2$ experiment: Joseph Tan, Ching-hua Tseng, Daphna Enzer, Steve Peil, Kamal Abdullah, Brian D'Urso, Brian Odom, and David Hanneke. From my time on the electron/positron $g/2$ experiment, I thank Josh Dorr and Shannon Fogwell Hoogerheide for building most of the current-generation apparatus and for patiently helping and teaching me. Josh Goldman on the planar trap experiment has been a kind mentor to me. I thank Maryrose Barrios, Ronald Alexander, and Melissa Wessels for their steadfast companionship through hard times. I particularly want to thank Ron for his contributions to (among many other things) amps, moderator heat-treating, and gold-plating of electrodes. I thank Melissa for her gold-plating and second-stage amplifier development. The experiment is in good hands now with Tom Myers, Sam Fayer, and Xing Fan. I thank Tom and Sam for their help taking data for and giving comments on this thesis. I've been lucky to work with many others on the experiment: Samantha Whitmore, David Gonzalez-Dysinger, Olivier Simon (vibration studies), Roman Berens, Makinde Ogunnaike, David von Lindenfels (helium level control), Rubain Sateu, Marco Wiesel, Edouard Nottet, Marco Dembecki (2nd generation ^{3}He probe), and Scott Bustabad.

I thank Phil Richerme and Steve Kolthammer for their guidance on the ATRAP experiment when I first began in the group, Robert McConnell for his friendship, and

Dan Fitzakerley, Andi Müllers, and Rita Kalra for their camaraderie. Nate Jones (building on Phil Richerme's work) contributed to the quench dynamics analysis and helped me launch my contribution.

It's been a pleasure to brainstorm with the deeply insightful Jack DiSciacca, Kathryn Marable and Mason Marshall of the proton and antiproton $g/2$ experiments. I also thank all the other members of the Gabrielse group, who have always been eager to lend a hand or help think through an idea: Yulia Gurevich, Ben Spaun, Paul Hess, Vitaly Andreev, Geev Nahal, Andra Ionescu, Daniel Zambrano, Ghanshayam Khatri, Chris Hamley, Daniel Ang, Cole Meisenhelder, Tharon Morrison, Cris Panda, Eric Tardiff, and Stephan Ettenauer.

Jim MacArthur of the Harvard Electronic Instrument Design Lab built many instruments used in this work. He dealt with any problem I brought to him with tremendous expertise, patience, generosity and humor. Stan Cotreau taught me to machine, weld, torch braze, and have a great time doing it. Thank you to the machinists of the SEAS Scientific Instrument shop for their excellent work. RIP, Rich Anderson, who expertly machined the trap electrodes. I thank Bruce Gold at Joining Technologies for doing the tricky e-beam welds on the pinbase.

I thank Rachelle Gaudet and Jenny Hoffman for mentoring me. I thank Tom Hayes for making it such fun to TF Physics 123. I also thank the many other teachers and mentors who have helped me along the way, too many to list in full but including Claudia Douglass, Al Jackson, Bill Segraves, Rick Casten, Volker Werner, Matthias Liepe, Eric Dufresne, Meg Urry, Bonnie Fleming, Adam Cohen, Jacob Barandes, Chris Stubbs, and Melissa Franklin.

Jan Ragusa, Pattee McGarry, Carol Davis, Silke Exner-Su, Lisa Cacciabaudo, Samantha Dakoulas, and the rest of the physics department staff have tirelessly solved problems and made the department a welcoming place for me. I thank Eleanor Millman, Sofia Magkiriadou, my G-cohort, my co-mentees in the HGWISE mentoring program, and my mentees in the physics department mentoring program for their companionship and moral support. I thank the organizing committees, volunteers, and attendees of the Conferences for Undergraduate Women in Physics and Supporting Inclusion of Underrepresented Peoples Workshop for challenging me to help build a more just future. I thank Suparna Damany for keeping me healthy. I thank Mara and Daniel Coelho, Taylor King, Natalia Hernandez, Emily Steenberg, Kaitie Hensal, and Rachel Novak for taking loving care of my children.

I thank my family, including Mum for reading to me, Dad for infusing my childhood with the fun of science, and Nancy and Linda for always being there for me. I thank Grandpa Eddie for mailing me a strong ferromagnet and suggesting I observe its effect on my parents' TV, and later for giving me that fatefully compelling comic book about quantum mechanics. I thank Octavia and Cordelia for their love and for giving me perspective. I thank Alex for enduring terrible commutes to support my career, for reading almost all of this thesis, and most of all for his unwavering love.

I have been supported by a National Science Foundation (NSF) Graduate Research Fellowship, a Merit/Term-Time Fellowship and the An Wang Fellowship from the Harvard Graduate School of Arts and Sciences. The electron/positron $g/2$ and ATRAP experiments are both supported by the NSF. ATRAP is also supported by the Air Force Office of Scientific Research (AFOSR).

Chapter 1

Introduction

1.1 Magnetic Moments of the Electron and Positron

The g-factor of a particle is a dimensionless measure of the magnitude of its intrinsic magnetic moment $\vec{\mu}$ due to spin $\vec{S}$. For the electron (e^-),

$$\vec{\mu} = -g\frac{e\hbar}{2m}\frac{\vec{S}}{\hbar} = -\frac{g}{2}\mu_B\frac{\vec{S}}{\hbar/2}, \tag{1.1}$$

and for the positron (e^+),

$$\vec{\mu} = g\frac{e\hbar}{2m}\frac{\vec{S}}{\hbar} = \frac{g}{2}\mu_B\frac{\vec{S}}{\hbar/2}, \tag{1.2}$$

where $\hbar$ is the reduced Planck constant, e is the elementary charge, m is mass, and the scaling factor is the Bohr magneton $\mu_B = e\hbar/(2m)$. For a spin-1/2 particle, where $\vec{S} = \frac{1}{2}\hbar\vec{\sigma}$ and $\vec{\sigma}$ is the dimensionless Pauli operator, the value of $g/2$ gives the magnitude of the intrinsic magnetic moment in Bohr magnetons,

$$\frac{g}{2} = \frac{\|\vec{\mu}\|}{\mu_B}. \tag{1.3}$$

For the electron and positron, $g/2$ differs from the Dirac equation's prediction of 1 by about one part per thousand due to interactions with the fluctuating quantum vacuum [1, 2]. Electron $g/2$ is the most precisely measured property of an elementary particle, with a value measured at Harvard in 2008 to be

$$\frac{g_{e^-}}{2} = 1.001\ 159\ 652\ 180\ 73\ (28)\ [.28\ ppt^{1}] \qquad [3,\ 4]. \tag{1.4}$$

The positron $g/2$ was measured 15 times less precisely at the University of Washington in 1987 to be

$$\frac{g_{e^+}}{2} = 1.001\ 159\ 652\ 1879\ (43)\ [4.3\ ppt] \qquad [5]. \tag{1.5}$$

This thesis describes progress toward measurements of electron and positron $g/2$ exceeding the precision level of the most recent Harvard electron $g/2$ measurement. In this chapter, the role of $g/2$ measurements in testing fundamental symmetries and the Standard Model is reviewed.

1.2 $g/2$ and Charge-Parity-Time Symmetry

Symmetry tests have played a key role in the history of physics. If a Hamiltonian H describing a physical system is invariant under transformation by an operator Θ such that $\Theta H \Theta^{-1} = H$, the system is said to exhibit a symmetry. Three examples of discrete transformations with associated symmetries are parity (P), which reverses all spatial directions ($\vec{r} \to -\vec{r}$), charge conjugation (C), which exchanges matter particles for their antimatter counterparts, and time reversal (T), which takes $t \to -t$.

[1] ppt = part per trillion

The laws of nature were once thought to be invariant under P transformation. However, P violation was discovered in 1957 by Wu in the beta decay of Co^{60} after a proposal by Lee and Yang [6, 7]. Combined charge and parity symmetry (CP) was then proposed as a good symmetry, but was found to be violated in the decay of neutral kaons by Cronin and Fitch in 1964 [8].

It is now believed that combined CPT symmetry is upheld in nature. All locally Lorentz-invariant quantum field theories, including the Standard Model of particle physics, are CPT-symmetric [9, 10, 11]. The Standard Model has been extraordinarily successful, so far withstanding all experimental tests. Why, then, is it worth searching for violations of CPT symmetry? One answer is that the Standard Model has shortcomings and omissions, including:

- The interactions of the Standard Model do not include enough CP-violation to explain how our universe made of matter survived annihilation of nearly-equal numbers of particles and antiparticles produced in the Big Bang [12]. This is called the baryon asymmetry problem.

- The Standard Model does not include the dark matter and dark energy that comprise the vast majority of the universe's mass-energy [13, 14, 15, 16].

- General relativity is not renormalizable; it becomes non-perturbative and non-predictive at the Planck scale ($\sim 10^{19}$ GeV) [17, 18].

Probing the boundaries of applicability of the Standard Model's symmetries is one possible way to make progress toward a more complete theory of physics. It has been noted that Lorentz symmetry and CPT symmetry might be broken in theories

that UV-complete the Standard Model, such as string theory [19, 20, 21]. Without strong reason to favor a specific Beyond-the-Standard-Model (BSM) theory, it is not known at what energy scale or in what sector this symmetry-breaking might manifest. Experiments at high-energy particle colliders and extremely precise measurements of low-energy phenomena are two complementary ways to probe for symmetry violations at new scales.

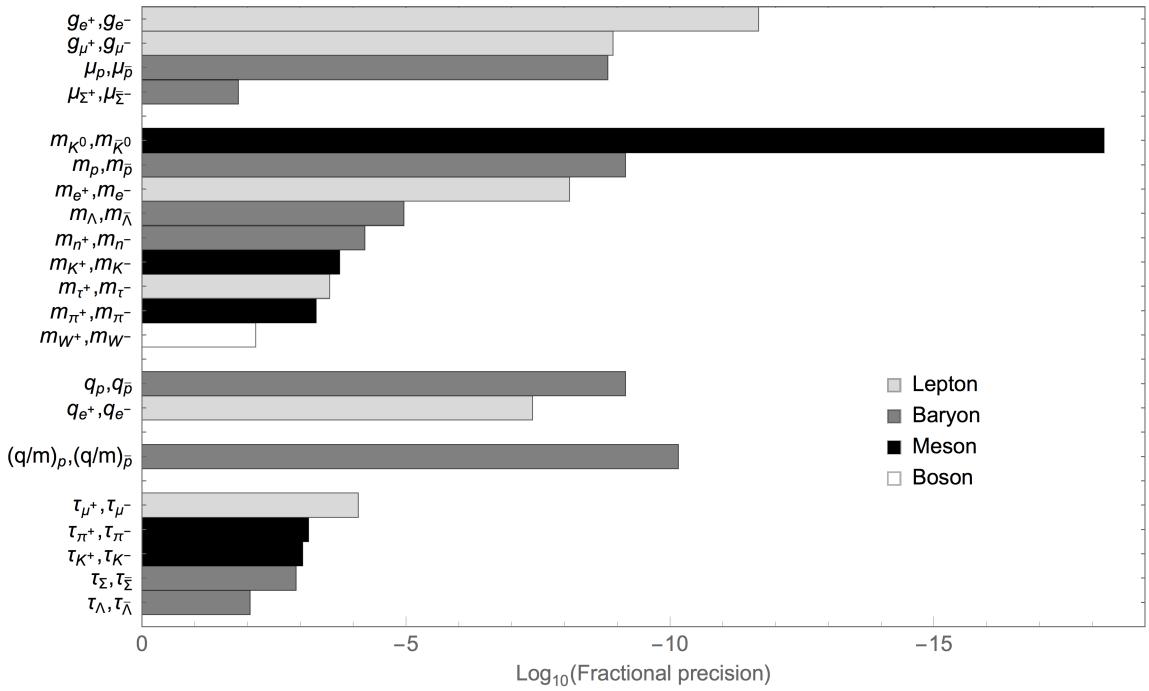

Figure 1.1: CPT symmetry tests. Fractional precision (e.g., $\Delta g/g$) is shown for particle/antiparticle comparisons of g-factors, magnetic moments μ, masses m, charges q, a charge-to-mass ratio q/m, and lifetimes τ. Data were tabulated from [22, 23, 24]. Not pictured are hydrogen/antihydrogen spectroscopy comparisons, which could eventually be the most precise CPT tests in a lepton-baryon system.

The Standard Model predicts that the mass and lifetime of particles and their antiparticle analogs shoud be identical, while charge and magnetic moment should be

equal in magnitude and opposite in sign. Precise comparisons of these properties are the most stringent tests of CPT symmetry. In all tests so far in many sectors (Fig. 1.1), no violation of CPT symmetry has yet been found. Comparison of electron $g/2$ to positron $g/2$ is the most precise test of charge-parity-time symmetry in a lepton system, with a ratio of

$$\frac{g_{e^-}}{g_{e^+}} = 1 + (0.5 \pm 2.1) \times 10^{-12} \qquad [5]. \tag{1.6}$$

This comparison is limited by the precision of the 1987 UW positron $g/2$ measurement. An improvement in positron $g/2$ precision to the level of the most recent Harvard electron $g/2$ measurement would improve this CPT test by at least a factor of 15.

1.2.1 $g/2$ and a Standard Model Extension

The quantities displayed in Fig. 1.1 are the most fundamental figures of merit for these CPT tests because they are model-agnostic; they have meaning regardless of the form of an underlying BSM theory. However, some have suggested that not all these figures of merit are directly comparable because some entries in Fig. 1.1 are comparisons of dimensionless quantities (e.g., $r_e \equiv |(g_{e^-} - g_{e^+})/g_{av}|$ for electron/positron $g/2$) and some are comparisons of dimensionful quantities (e.g., $r_K \equiv |(m_K - m_{\bar{K}})/m_K|$ for the neutral kaon mass comparison, the only experiment in Fig. 1.1 exceeding the precision of the electron/positron $g/2$ comparison). To propose a figure of merit for the electron/positron $g/2$ comparison that is directly comparable to r_K, reference [25] presents a simple model of Lorentz violation and defines an r'_e that, like r_K's mass-energy comparison, is a ratio of energies. In this model, the modified Dirac equation

for the electron and positron is

$$(i\gamma^\mu\partial_\mu - eA_\mu\gamma^\mu - a_\mu\gamma^\mu - b_\mu\gamma_5\gamma^\mu - m_e)\psi = 0 \tag{1.7}$$

where γ^μ and γ_5 are defined as is conventional in quantum field theory, A_μ is the photon field, ψ is the electron-positron field, and a_μ and b_μ are coefficients of the proposed new Lorentz-violating terms. These terms lead to a shift to the electron and positron Hamiltonians of

$$\Delta H_{e^\mp} = \pm a_\mu\gamma^0\gamma^\mu - b_\mu\gamma_5\gamma^0\gamma^\mu. \tag{1.8}$$

In Penning trap $g/2$ experiments, the electron or positron is in a magnetic field $\vec{B} = B\hat{z}$, and the quantities measured are its cyclotron frequency ω_c and anomaly frequency $\omega_a \equiv \omega_s - \omega_c$, where ω_s is its spin frequency. (For more details, see Ch. 2.) In this context, a figure of merit for CPT violation for Penning trap $g/2$ experiments of

$$r'_e \equiv |(E^-_{n,s} - E^+_{n,-s})/E^-_{n,s}| \tag{1.9}$$

can be defined, where n is the cyclotron quantum number, s is the spin quantum number, and the $E^\pm_{n,s}$ are the energies associated with these states. This r'_e is found to be $|\Delta\omega_a/2m| = |2b_3/m|$, where the 3 comes from the magnetic field orientation in direction $\hat{x}^3 \equiv \hat{z}$. The cyclotron frequency ω_c is found to be unchanged by the perturbations to the Hamiltonian, but serves as a magnetometer to eliminate error due to drifts in B. For the present precision of the electron and positron $g/2$ measurements,

$$r'_e \leq 10^{-20}, \tag{1.10}$$

which compares favorably to the kaon mass CPT test's $r_K < 2 \times 10^{-18}$.

It is valuable to be able to understand the overlap between many different experiments testing CPT in various sectors. Kostelecký and colleagues therefore created a framework within the confines of quantum field theory in which many possible Lorentz violations, including those described above, are parameterized separately. This Standard Model Extension (SME) is based on a Lagrangian that includes all Standard Model terms, plus all Lorentz-violating terms that preserve power-counting renormalizability and obey SU(3)×SU(2)×U(1) gauge invariance. Though these constraints make limits in this theory less general than Eq. 1.6, the SME is a widely-used framework for comparing CPT tests. The SME Lagrangian contains many terms. Here is a small selection of terms involving the same b coefficient as in Sec. 1.2.1 [26]:

$$\Delta L_{b,CPT-odd} = -b^{\mu}\bar{\psi}\gamma_5\gamma_\mu\psi - \frac{1}{2}b^{(5)\mu\alpha\beta}\bar{\psi}\gamma_5\gamma_\mu iD_{(\alpha}iD_{\beta)}\psi - \frac{1}{2}b_F^{5\mu\alpha\beta}F_{\alpha\beta}\bar{\psi}\gamma_5\gamma_\mu\psi. \quad (1.11)$$

Electron $g/2$ measurements set limits on linear combinations of these b coefficients with coefficients of other terms (not shown here). These terms are given by

$$\begin{aligned}\tilde{b}_e^3 = b_e^3 + H_e^{12} - m_e d_e^{30} - m_e g_e^{120} + m_e^2 b_e^{(5)300} \\ + m_e^2 H_e^{(5)1200} + m_e^3 d_e^{(6)3000} - m_e^3 g_e^{(6)12000},\end{aligned} \quad (1.12a)$$

$$\tilde{b}_{F,e}^{33} = b_{F,e}^{(5)312} + H_{F,e}^{(5)1212} - m_e d_{F,e}^{(6)3012} - m_e g_{F,e}^{(6)12012}. \quad (1.12b)$$

All non-b terms are defined in [26]. Analogous quantities for positrons are represented by $\tilde{b}_e^{*3}$ and $\Delta\tilde{b}_{F,e}^{*33}$. The 1987 electron/positron $g/2$ comparison [5] sets the best limits on comparisons $\Delta\tilde{b}_e^3$ and $\Delta\tilde{b}_{F,e}^{33}$ of electron- and positron-associated constants in this framework. Because Lorentz-violating terms can define a preferred direction in space, SME coupling constant limits can also be derived from an electron measurement alone (or a positron measurement alone) by observing variations over sidereal time.

Limits on $\tilde{b}_e^3$, $\Delta\tilde{b}_{F,e}^{33}$, $\tilde{b}_e^{*3}$, and $\Delta\tilde{b}_{F,e}^{*33}$ are currently set by [5], but those on $\tilde{b}_e^3$ and $\Delta\tilde{b}_{F,e}^{33}$ could currently be limited by data at the precision level of the most recent Harvard electron $g/2$ measurement [26]. Improved electron and positron $g/2$ measurements with careful timestamping would improve all of these limits. References [26, 27] have detailed descriptions of limits set by electron and positron $g/2$ measurements, and a comprehensive list of experimental limits on SME parameters appears in [28].

1.3 $g/2$ and the Fine-Structure Constant

In addition to the powerful generality of the CPT test, electron and positron $g/2$ measurements also enable the most precise test of extremely detailed predictions of the Standard Model. In the Standard Model, electron $g/2$ can be expressed in terms of the fine structure constant α as

$$\begin{aligned}\frac{g}{2} &= 1 + A_2\left(\frac{\alpha}{\pi}\right) + A_4\left(\frac{\alpha}{\pi}\right)^2 + A_6\left(\frac{\alpha}{\pi}\right)^3 + A_8\left(\frac{\alpha}{\pi}\right)^4 + A_{10}\left(\frac{\alpha}{\pi}\right)^5 + ... \\ &\quad + a_{\mu,\tau}\left(\frac{m_e}{m_\mu}, \frac{m_e}{m_\tau}, \alpha\right) + a_{hadronic} + a_{weak}.\end{aligned} \tag{1.13}$$

The A_n coefficients in Eq. 1.13 are calculated by evaluating Feynman diagrams of QED interactions (Fig. 1.2).

The A_2, A_4, and A_6 coefficients are known exactly and involve contributions from

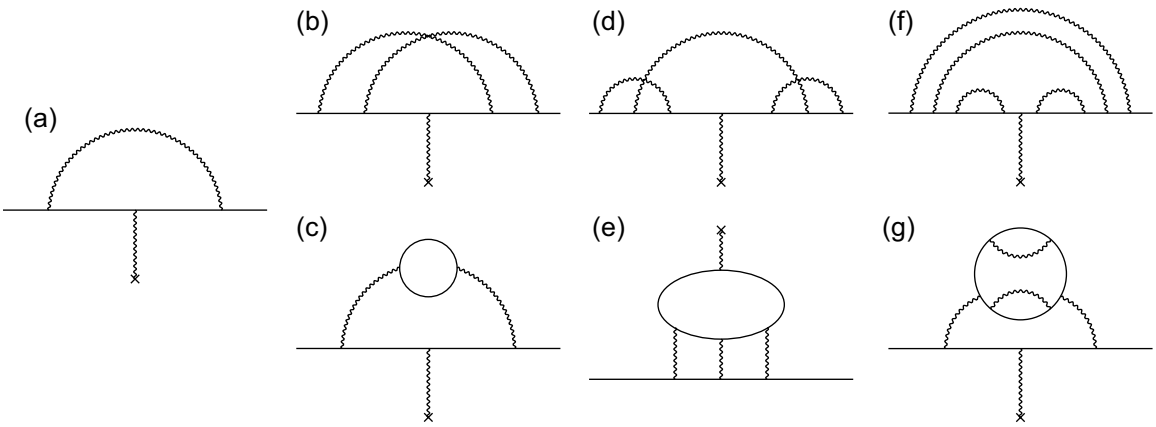

Figure 1.2: A small sample of the many Feynman diagrams contributing to $g/2$. (a) is the sole diagram for A_2, (b) and (c) contribute to A_4, (d) and (e) to A_6, and (f) and (g) to A_8. From [27].

1, 7, and 72 diagrams respectively. They are given by

$$A_2 = \frac{1}{2} = 0.5 \qquad [2], \tag{1.14a}$$

$$\begin{aligned} A_4 &= \frac{197}{144} + \frac{\pi^2}{12} + \frac{3}{4}\zeta(3) - \frac{1}{2}\pi^2 \ln 2 \\ &= -0.328\,478\,965\,579\ldots \qquad [29,\ 30,\ 31], \end{aligned} \tag{1.14b}$$

$$\begin{aligned} A_6 = {} & \frac{83}{72}\pi^2\zeta(3) - \frac{215}{24}\zeta(5) \\ & + \frac{100}{3}\left[\left(\sum_{n=1}^{\infty}\frac{1}{2^n n^4} + \frac{1}{24}\ln 2^4\right) - \frac{1}{24}\pi^2 \ln 2^2\right] \\ & - \frac{239}{2160}\pi^4 + \frac{139}{18}\zeta(3) - \frac{298}{9}\pi^2 \ln 2 + \frac{17101}{810}\pi^2 + \frac{28259}{5184} \\ = {} & 1.181\,241\,456\ldots \qquad [32]. \end{aligned} \tag{1.14c}$$

Extremely challenging A_8 and A_{10} calculations have been the culminations of multi-decade efforts. Finding agreement with an earlier independent numerical calculation [33, 34], A_8 was recently calculated by evaluating the integrals for its 891 diagrams to 1100 digits, finding

$$A_8 = 1.912\,245\,764\ldots \qquad [35]. \tag{1.15}$$

The A_{10} coefficient, with 12672 diagrams, was recently determined by numerical methods to be

$$A_{10} = 7.795\,(336) \qquad [34]. \tag{1.16}$$

The $a_{\mu,\tau}$ term in Eq. 1.13 is the sum of contributions from diagrams that include virtual μ or τ leptons in loops. This term is given by

$$a_{\mu,\tau}\left(\frac{m_e}{m_\mu}, \frac{m_e}{m_\tau}\right) = 2.747\ 57(3) \times 10^{-12} \qquad [36]. \tag{1.17}$$

where the uncertainties come primarily from uncertainties in the lepton mass ratios. The final terms, $a_{hadronic}$ and a_{weak}, are sums of diagrams that include vertices from the strong and weak forces. They are given by

$$a_{hadronic} = 1.734(15) \times 10^{-12} \qquad [37,\ 38,\ 39,\ 36], \tag{1.18}$$

$$a_{weak} = 0.029\ 73(23) \times 10^{-12} \qquad [40,\ 36]. \tag{1.19}$$

Fig. 1.3 shows the contributions of different terms in Eq. 1.13 to the determination of $g/2$ from α.

1.3.1 Test of the Standard Model

By independently measuring α, predicting $g/2$ from Eq. 1.13, and comparing to the directly measured electron or positron $g/2$, the validity of the Standard Model prediction in Eq. 1.13 can be tested. The most precise independent measurement of α relies on the relation

$$\alpha^2 = \frac{2R_\infty}{c}\frac{A_r(Rb)}{A_r(e)}\frac{h}{m_{Rb}}. \tag{1.20}$$

where c is the speed of light, R_∞ is the Rydberg constant ([36] and e.g., [41, 42, 43, 44]), $A_r(e)$ is the relative atomic mass of the electron as measured by bound electron g

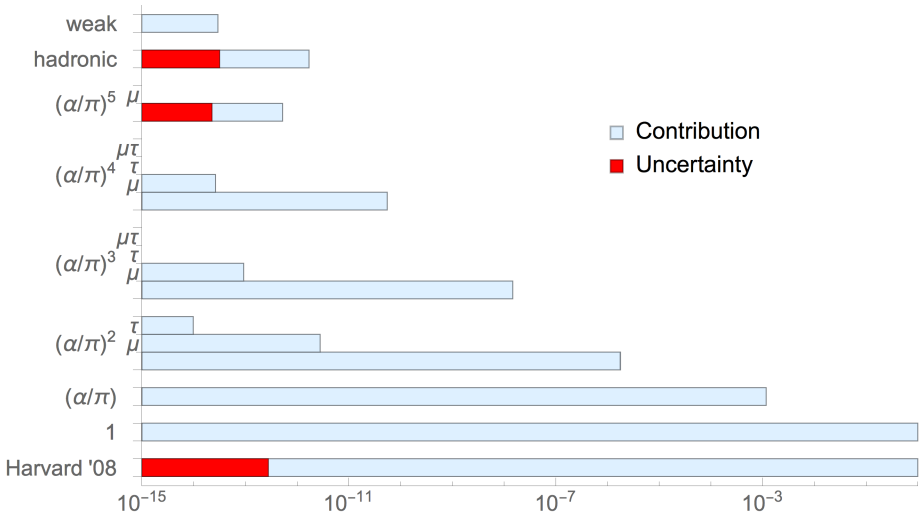

Figure 1.3: Contributions of different terms in Eq. 1.13 to the determination of $g/2$ from α are shown in light blue. Errors due to theoretical uncertainties are superimposed in red. The $g/2$ value and uncertainty from the most recent electron $g/2$ measurement at Harvard [3] are shown in the lowest bar for comparison.

measurements [45, 46], $A_r(Rb)$ is the relative atomic mass of the ^{87}Rb atom [47], and h/m_{Rb} is the ratio of the Planck constant to the ^{87}Rb mass [48]. The factor h/m_{Rb} is determined by atom-recoil experiments and is the least precisely measured of these ingredients, limiting the precision of this determination of α (here called $\alpha_{h/m}$):

$$\alpha_{h/m}^{-1} = 137.035\,998\,996\,(85)\ [.62\ ppb^2] \qquad [48,\ 36]. \tag{1.21}$$

Combining $\alpha_{h/m}$ with Eq. 1.13 gives a determination of electron and positron $g/2$

$$\begin{aligned}\left(\frac{g}{2}\right)_{\alpha,theory} &= 1.001\ 159\ 652\ 182\ 112\ (23)(16)(718) \quad [48,\ 34,\ 36,\ 35] \\ &= 1.001\ 159\ 652\ 182\ 112\ (719)\ [.718\ ppt],\end{aligned} \tag{1.22}$$

where the errors come from A_{10}, $a_{hadronic}$, and $\alpha_{h/m}$, respectively. The comparison of this $g/2$ with the Harvard measurement of electron $g/2$ is the best test of the

[2] ppb = part per billion

Standard Model's most precise prediction. The determinations agree to within 1.001 ppt (1.8σ).

The uncertainty of the $g/2$ determination from α is currently limited by the precision of the measured h/m. Ongoing research on h/m_{Cs} and h/m_{Rb} is progressing and might soon lead to a significantly more precise $g/2$ calculated from $\alpha_{h/m}$ [49, 50]. A competitive evaluation of $g/2$ from $\alpha_{h/m}$ would enable any improvement in the directly measured electron or positron $g/2$ to improve the Standard Model test, giving a strong physics motivation for further improvements in $g/2$ measurements.

1.3.2 Relationship to Muon $g/2$

The calculated muon $g/2$ is given by an expansion similar to Eq. 1.13. Contributions to $g/2$ from loops containing other particles are larger for muon $g/2$ than for electron $g/2$ by a factor of $(m_\mu/m_e)^2 \approx 43,000$. While this makes muon $g/2$ more sensitive to Beyond-the-Standard-Model (BSM) particles, it also increases the contribution to $g/2$ of loops with difficult-to-calculate strong interactions between Standard Model particles (e.g., the hadronic vacuum polarization and light-by-light terms), limiting the muon $g_{\alpha,theory}/2$ precision to 0.4 ppb [22, 51, 52, 53, 54]. Muon $g/2$ is also measured about 2500 times less precisely than electron $g/2$, with a precision of 0.54 ppb [55]. Electron and muon $g/2$ at their current precision are complementary probes for new physics, testing partially overlapping but distinct subsets of parameter space in BSM theories (see, e.g., Sec. 1.3.3). There is presently a 3.3-3.6 σ tension between muon $g/2$ theory and experiment [55, 56], which could be suggestive of new physics.

1.3.3 Searches for New Physics

In addition to validating calculations within the Standard Model to the fifth order in perturbation theory, the comparison between $g_{exp}/2$ and $g_{\alpha,theory}/2$ also puts constraints on specific BSM physics models, including dark matter candidates. BSM particles and forces would appear as virtual elements of Feynman diagrams not yet included in Eq. 1.13, creating a mismatch between $g_{exp}/2$ and $g_{\alpha,theory}/2$. Agreement can therefore exclude such BSM theories; discrepancies are evidence for new physics. The following is a non-exhaustive selection of BSM theories for which electron $g/2$ provides competitive constraints.

1.3.3.1 Dark photons

With direct-detection and LHC searches finding little evidence so far for ≥ 100 GeV Weakly Interacting Massive Particles (WIMPs), interest has been building in alternative theories of dark matter [57]. The "dark photon" is a proposed vector boson that would be the force carrier for a dark-sector analog to the electromagnetic force [58]. It is hypothesized to interact with ordinary photons via the "kinetic mixing" mechanism, whereby a dark photon can turn into an ordinary photon; interactions with Standard Model particles would therefore be proportional to their electric charges [59, 60]. A dark photon with kinetic mixing adds a perturbation ΔL to the Lagrangian of

$$\Delta L = -\frac{1}{4}B_{\mu\nu}B^{\mu\nu} + \frac{1}{2}\varepsilon B_{\mu\nu}F^{\mu\nu} + \frac{1}{2}m^2_{dark\ photon}B_\mu B^\mu, \tag{1.23}$$

where $B_{\mu\nu}$ and $F^{\mu\nu}$ are the fields of the dark and ordinary photons, respectively, ε is the coupling strength of the dark photon to the ordinary photon, and $m_{dark\ photon}$

is the mass of the dark photon. Fig. 1.4 shows the region of dark photon ε^2 vs. $m_{dark\ photon}$ space that is excluded by electron $g/2$ (along with the regions excluded by muon $g/2$ and suggested by the muon $g/2$ discrepancy.)

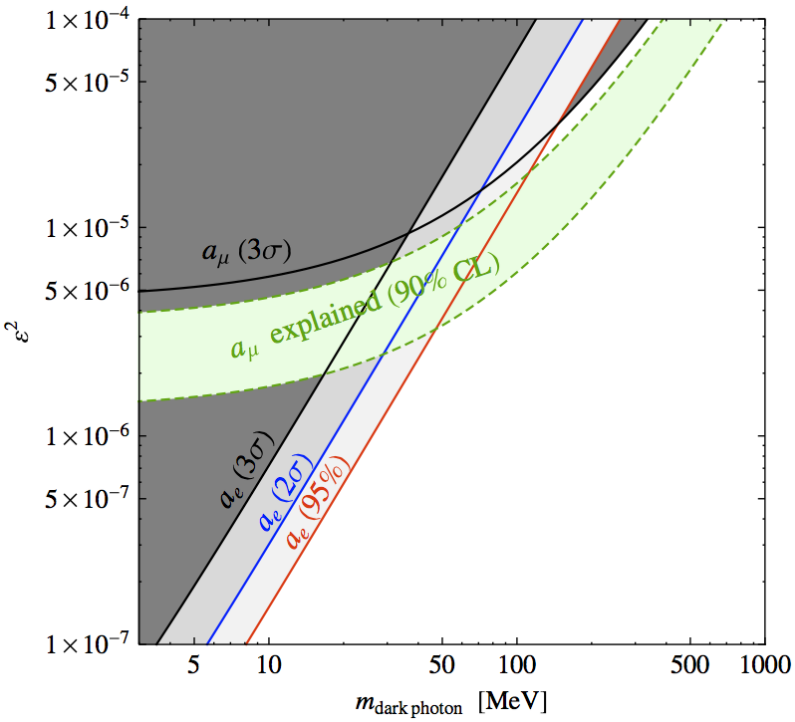

Figure 1.4: Limits on dark photon properties from predicted and measured electron $a_e = g_e/2 - 1$ and favored parameters from muon $a_\mu = g_\mu/2 - 1$ discrepancy. Exclusions from other experiments are not shown. Reprinted, with permission, from [61].

Other types of experiments also exclude parts of dark photon parameter space, with various limits compiled in [57]. However, many experiments' constraints depend on the assumption that dark photons can decay only into Standard Model particles; such limits weaken if "invisible" decays into a richer dark sector are available [57]. Limits from $g/2$ and from "missing-energy" beam-dump [62] and collider [63] experiments are among the few that are not affected by invisible decays [61]. For

a time, the electron $g/2$ set the most stringent limits in some regions of parameter space. Recently, NA64 excluded all of the parameter space with $m_{dark\ photon} > 1$ MeV that had previously been excluded only by electron $g/2$ [62]. BaBar also recently excluded the $m_{dark\ photon} > 1$ MeV portion of the region suggested by the muon $g/2$ discrepancy [63]. Limits on dark photons could be strengthened by an order-of-magnitude-improved comparison between measured and calculated electron $g/2$, making a better electron $g/2$ measurement an important component of the dark photon search landscape.

1.3.3.2 Light dark matter

Other dark matter candidates are also constrained by electron $g/2$. Reference [64] describes a model that explains both dark matter and the excess of 511 keV γ-rays from the Milky Way's galactic bulge [65]. The model includes three new particles: a light scalar ϕ forms dark matter, a new heavy fermion F_e can interact with the electron and ϕ via a Yukawa coupling, and a new gauge boson, Z', can interact both with ϕ and with the electron [66, 67]. Up to an order-one factor from astrophysical constraints, these interactions are predicted to shift $g/2$ by $10(5) \times 10^{-12}$ [64]. This is already probed by the comparison between g_{exp} and $g_{\alpha,theory}$, with little room left for this theory in the current 1.8σ, 1 ppt disagreement.

1.3.3.3 Other new bosons

Electron $g/2$ also constrains more general classes of new particles. References [68] and [69] explore experimental limits on potential bosons with spin $s = 0$, 1, or 2 that couple to electrons and nuclei, creating a potential $V(r) = -1 \times (-1)^s y_e y_N e^{m_x r}/(4\pi r)$,

where y_e is the strength of the new boson's interaction with an electron, y_N is the strength of its interaction with a nucleus N, and r is the distance from electron to nucleus. (Unlike in the case of dark photons, the proposed bosons are not constrained to interact only via kinetic mixing.) Electron $g/2$ sets the leading constraints on y_e [69]. Combined with neutron scattering or astrophysical data, electron $g/2$ also excludes some parts of the $y_e y_N$ vs. mass parameter space that are not excluded by other methods such as isotope-shift spectroscopy or fifth-force searches [68, 69].

1.3.3.4 Electron substructure

It is possible that the electron, like the proton, is a composite particle. Because the electron's radius is known to be small, any constituent particles would need to be tightly bound. To accommodate both the electron's small mass and this large binding energy, the constituent particle masses m^* would have to be large. A simple model in which contributions to $g/2$ went as $O(m_e/m^*)$ would entail $O(m^*)$ contributions to self-energy; an accidental precise cancellation between these contributions and binding energy would therefore be required to avoid a large electron mass [70]. If the self-energy contribution were suppressed with a selection rule, e.g., in a model with chiral invariance [70], contributions to $g/2$ would go like $O(m_e/m^*)^2$. In this model, the electron $g/2$ comparison gives limits on constituent mass and electron radius R_e of

$$m^* > 360 \text{ GeV}/c^2 \qquad [27,\ 71], \tag{1.24}$$

$$R_e < 5 \times 10^{-19} \text{ m} \qquad [27,\ 71]. \tag{1.25}$$

The Harvard electron $g/2$ uncertainty, if independent α were improved, would set a limit of $m^* > 1$ TeV. This can be compared to the LEP e^+ e^- collider probe for a contact interaction at the 10.3 TeV, 2×10^{-20} m scale [72, 22].

1.3.4 Determination of the Fine-Structure Constant α

If the Standard Model's validity is assumed, the series in Eq. 1.13 can be inverted to yield the most precise determination of the fine structure constant α:

$$\alpha^{-1} = 137.035\ 999\ 160\ (33)(4) \qquad [3,\ 34,\ 35] \tag{1.26}$$

$$= 137.035\ 999\ 160\ (33)\ [0.25\ ppb]. \tag{1.27}$$

This is the most precise way to determine α. As the low-energy limit of the coupling constant of electromagnetism and one of the 26 dimensionless parameters of the Standard Model, α is of fundamental physics interest. The fine structure constant is related to other fundamental constants by

$$\alpha = \frac{1}{4\pi\epsilon_0}\frac{e^2}{\hbar c}, \tag{1.28}$$

where ϵ_0 is the electric permittivity of free space. These relationships give α an important role in the International System of Units (SI). A planned 2018 redefinition of the SI units will eliminate the reliance of the kilogram on a physical artifact and improve the definition of the ampere, among other changes [73, 74]. In this new system, uncertainty in α will set the uncertainty of ϵ_0, μ_B, m_e, proton mass m_p, nuclear magneton μ_N, vacuum permeability μ_0, and vacuum impedance Z_0. As of 2012, theoretical uncertainties have been reduced enough that improvements in electron or

positron $g/2$ measurements beyond the existing Harvard electron $g/2$ precision level will enable a more precise determination of α by about a factor of ten [51, 34].

1.4 The History of Electron and Positron $g/2$

The early history of theory and experiments related to $g/2$ is reviewed in [75]. A brief summary is included here. Starting with Compton's analysis of the origins of ferromagnetism in 1921 [76] and culminating in the Dirac equation in 1927 [1], it was realized that $g/2 \approx 1$ for the electron's intrinsic angular momentum due to spin, rather than $g/2 = 1/2$ as for orbital angular momentum [75]. With the Lamb shift [77] and other observations [78] in 1947, evidence grew that $g/2$ differed slightly from 1 so that $g/2 = 1 + a_e$, where a_e is the electron's anomalous magnetic moment [75]. In the next few years, there followed a series of developments in QED theory (e.g., [79, 2, 80]) and in experiment [81, 82] that led to quantitative predictions and indirect measurements of a_e [75]. Free electron $g/2$ was first measured precisely at the University of Michigan in 1953 in an experiment that observed the spin precession of polarized electrons in a static magnetic field [83]. Over the next 20 years, this technique was further developed to make increasingly precise positron and electron $g/2$ measurements [75].

In parallel, another category of experiments developed in which oscillating electromagnetic fields were used to drive transitions between energy levels of electrons and positrons in a magnetic field [84, 85, 75]. It is experiments in this second category that have developed into the modern standard of precise measurements of electron and positron $g/2$ in Penning traps. Dehmelt's 1987 measurement of electron and positron

$g/2$ in a hyperbolic Penning trap at 4.2 K remains the most precise measurement of $g/2$ of the positron [5].

1.5 Measuring $g/2$ in a Penning Trap, in Brief

Electron $g/2$ was measured more precisely in the Gabrielse group at Harvard in 2006. Individual cyclotron transitions were resolved for the first time, improving precision and making this the first fully quantum measurement [86]. Precision was also improved by using a cylindrical Penning trap [87] to control and measure the electron's interactions with the microwave cavity formed by the trap electrodes [88]. A second electron $g/2$ measurement in the same apparatus achieved even higher precision in 2008, when the cavity-electron interaction was better understood [3, 4].

The basic measurement techniques used in previous Harvard magnetic moment experiments are outlined here and described in more detail in Ch. 2 and Ch. 3. A single electron or positron is suspended in vacuum in a cylindrical Penning trap, cooled to its ground cyclotron state by a dilution refrigerator at 100 mK. Quantum-jump spectroscopy is performed. A single cyclotron or single "anomaly" (spin+cyclotron) transition at a time is driven by microwaves or radiofrequency (RF) waves. Spontaneous emission is inhibited by the trap cavity, allowing an excited cyclotron state to persist long enough to be detected. Transitions are detected by a quantum nondemolition (QND) coupling to the electron's axial motion, which is amplified and monitored. Transition attempts at multiple frequencies are combined to make lineshapes from which the cyclotron and anomaly frequencies can be extracted with sub-ppb precision. With lower-precision measurements of the electron's axial and

magnetron frequencies, as well as corrections for coupling to the resonant microwave cavity modes of the trap, $g/2$ of the trapped particle is determined.

1.6 This Work

This thesis describes progress toward a new measurement of electron and positron $g/2$ with greater precision than the most precise existing electron $g/2$ measurement. A new cryogenic Penning trap apparatus has been constructed [89]. This apparatus (referred to from now on as the "current-generation" or "current" apparatus) shares many features and techniques with the previous Harvard apparatus, but has been comprehensively redesigned to eliminate sources of instability and uncertainty that are believed to have been the primary causes of the uncertainty in the previous measurement. The design of the current apparatus will also enable the use of new techniques, such as cavity-assisted axial-cyclotron sideband cooling. Unlike the previous apparatus, the current apparatus contains a radioactive source and an open-endcap accumulation trap to allow loading of positrons for a positron $g/2$ measurement. I contributed to the first demonstrations of control of a single electron in the precision measurement trap in this apparatus [90] and to the first loading of positrons and electrons into the positron accumulation trap [71, 89].

This thesis describes the further development of the current apparatus toward $g/2$ measurement readiness. Ch. 2 gives an overview of $g/2$ measurement methods in a Penning trap. Ch. 3 describes the current apparatus, including design features relevant for stability and work I led on an improved ^{3}He nuclear magnetic resonance (NMR) probe and a pressure control system. Ch. 4 describes the RF drive and detec-

tion systems for interacting with a particle's axial motion, including significant strides I made in solving problems caused by an unexpected interaction between the single-particle detection circuit and the positron accumulation trap. Ch. 5 examines the role of resonant microwave cavity modes in this apparatus, including measurements I made that are the first detection of cavity mode structure in this apparatus. Ch. 6 describes a system I designed and built for transferring positrons into the precision measurement trap. Ch. 7 presents my proposal for a design change that is expected to improve single-particle detection, make it easier to achieve positron transfer, and improve apparatus reliability.

Two additional chapters concern my contribution to the ATRAP antihydrogen experiment. ATRAP aims to do the most precise test of CPT symmetry in a combined lepton-baryon system by comparing precision spectroscopy of antihydrogen and hydrogen. Ch. 8 introduces ATRAP and describes a quench protection and quick turnoff system in the ATRAP Ioffe trap, the design and construction of which I led. Ch. 9 presents my calculation of the predicted evolution of a quench in this Ioffe trap.

Chapter 2

Measuring $g/2$ in a Penning Trap

This chapter introduces the basic techniques for measuring $g/2$ in a Penning trap. It describes a charged particle's motion in a Penning trap, defines the frequencies that must be measured to determine $g/2$, describes how transitions are driven and detected to measure these frequencies, and introduces the sources of uncertainty in the best measurement to date of electron $g/2$, which was done in the previous apparatus in our group at Harvard.

2.1 $g/2$ in a Magnetic Field

An electron[1] in a homogeneous magnetic field $\vec{B} = B\hat{z}$ undergoes cyclotron motion at cyclotron frequency

$$\nu_c = \frac{eB}{2\pi m}. \tag{2.1}$$

[1]Positrons and electrons have opposite-sign charge and magnetic moment but the same mass. Other than with respect to some signs (e.g., of voltages for trapping), the discussions in this chapter apply identically to electrons and positrons. The main text of the chapter refers primarily to electrons, omitting the implied "and positrons" for succinctness. Particle-specific loading methods are covered in Ch. 4.

Cyclotron energy levels are separated by $h\nu_c$, where h is the Planck constant.

The electron's intrinsic angular momentum due to spin also interacts with the magnetic field. As a spin-1/2 particle, it has two eigenstates of S_z: $|\uparrow\rangle$, with spin aligned with the magnetic field, and $|\downarrow\rangle$, with spin anti-aligned. They are separated by energy $2\vec{\mu}\cdot\vec{B} = 2\|\vec{\mu}\|B = h\nu_s$, where ν_s is defined as

$$\nu_s = \frac{2\|\vec{\mu}\|B}{h}. \tag{2.2}$$

Fig. 2.1 shows the two ladders of cyclotron energy levels that correspond to the two spin states.

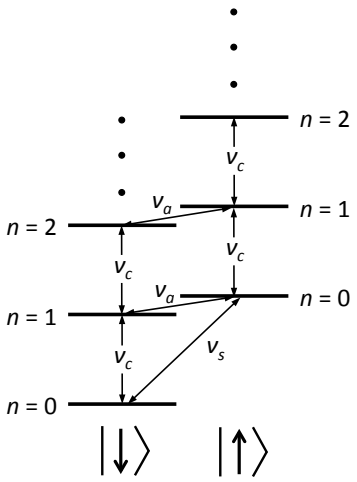

Figure 2.1: Energy level diagram for an electron in a magnetic field, showing ladders of cyclotron states for both spin states. ν_a is not to scale. The spin labels are switched for the positron because its magnetic moment has opposite sign.

The ratio ν_s/ν_c gives $g/2$:

$$\frac{\nu_s}{\nu_c} = \left(\frac{2\|\vec{\mu}\|B}{h}\right)\left(\frac{2\pi m}{eB}\right) = \|\vec{\mu}\|\frac{2m}{e\hbar} = \frac{\|\vec{\mu}\|}{\mu_B} = \frac{g}{2} \tag{2.3}$$

However, because $g/2$ differs from 1 by just one part per thousand, a factor of 10^3 higher precision $g/2$ measurement can be made by measuring the anomaly frequency

$\nu_a \equiv \nu_s - \nu_c$ instead of ν_s, with

$$\frac{g}{2} = \frac{\nu_s}{\nu_c} = 1 + \frac{\nu_s - \nu_c}{\nu_c} = 1 + \frac{\nu_a}{\nu_c}. \tag{2.4}$$

2.1.1 Special Relativistic Shift

Because of the effects of special relativity, cyclotron energy levels are not precisely equally spaced but become closer together for higher excitation energy [91]. This shift is given by

$$\Delta\nu_c = -\delta\,(n + 1 + m_s) \tag{2.5}$$

where $n = 0, 1, 2, \ldots$ is the cyclotron quantum number, $m_s = \pm 1/2$ is the spin quantum number, and δ is given by

$$\frac{\delta}{\nu_c} = \frac{h\nu_c}{mc^2}. \tag{2.6}$$

Fig. 2.2 represents the special relativistic shifts to the level diagram.

At a cyclotron frequency of 145.5 GHz (set by $B = 5.2$ T), the fractional special relativistic shift δ/ν_c is approximately 1×10^{-9}. Because ν_c must be determined on the sub-ppb level for the $g/2$ measurement, the transition frequency must be measured between known cyclotron levels. One of our research group's major advances was resolving transitions between different levels, thereby making it possible to eliminate uncertainty from the relativistic shift. To achieve this, the electron is kept in the cyclotron ground state unless a transition is intentionally driven. A superconducting solenoid[2] is used to create the large magnetic field, establishing a cyclotron level spacing of about 7 K. The electron's environment is then cooled to 100 mK by a dilution

[2] described in Sec. 3.2

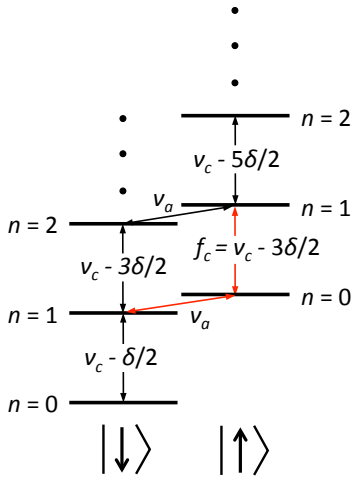

Figure 2.2: Level diagram as in 2.1 but including special relativistic shifts (not to scale). The red arrows show the cyclotron and anomaly transitions measured for the $g/2$ experiment.

refrigerator[3]. A trapped electron decays into a cyclotron ground state by cyclotron radiation, and black-body photons are insufficiently energetic to cause unintentional cyclotron transitions.

The cyclotron transition chosen for the measurement is $|\uparrow, n = 0\rangle \rightarrow |\uparrow, n = 1\rangle$, marked by a red arrow in Fig. 2.2. The frequency of this transition is $f_c \equiv \nu_c - 3\delta/2$. Electron $g/2$ is then determined by

$$\frac{g}{2} = 1 + \frac{\nu_a}{f_c + \frac{3\delta}{2}}. \tag{2.7}$$

[3]described in Sec. 3.1

2.2 Measuring $g/2$ in a Penning Trap

2.2.1 Fields and Particle Motions

To measure $g/2$, an electron is confined by a combination of magnetic and electric fields in a Penning trap [92]. Radial confinement is provided by the overall $\vec{B} = B\hat{z}$ field that causes cyclotron motion. Axial confinement is provided by a static quadrupole electric field, which causes harmonic oscillation in the $\hat{z}$ direction at axial frequency ν_z. (Fig. 2.3)

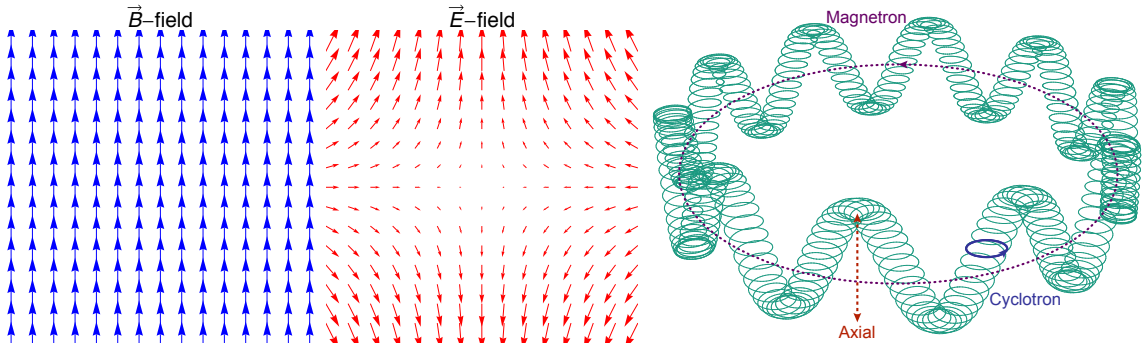

Figure 2.3: Cross sections of the magnetic field (left) and electric field (center) that comprise a Penning trap, from [90]. Motions of a trapped electron (right), from [93]. For a positron, electric field direction is reversed and cyclotron and magnetron motions are clockwise.

By Laplace's equation, the quadrupole electric field must have a radial component; the electric potential goes like $V \propto z^2 - \rho^2/2$, where ρ is the radial coordinate in standard cylindrical coordinates. The radial component of the quadrupole electric field affects the electron's radial motion in the magnetic field, causing a slow $\vec{E} \times \vec{B}$ drift called the magnetron motion at a frequency ν_m, as well as slightly shifting the cyclotron frequency to the trap-modified cyclotron frequency $\nu_c' = \nu_c - \nu_m$. The

magnetron frequency for this ideal trap is given by

$$\nu_m = \frac{\nu_z^2}{2\nu_c'}. \tag{2.8}$$

By the Brown-Gabrielse Invariance Theorem [94], observed trap eigenfrequencies (barred quantities) are related to ν_c by

$$\nu_c^2 = \bar{\nu}_c^2 + \bar{\nu}_z^2 + \bar{\nu}_m^2. \tag{2.9}$$

This holds not only for an ideal trap, but even when the trap electric and magnetic fields are not perfectly aligned and when the quadrupole electric field is slightly elliptical. These are the unavoidable leading imperfections of a more realistic Penning trap. When, in addition,

$$\bar{\nu}_c \gg \bar{\nu}_z \gg \bar{\nu}_m, \tag{2.10}$$

as is the case for electrons in the Penning traps discussed in this thesis, then

$$\nu_c \approx \bar{\nu}_c + \frac{\bar{\nu}_z^2}{2\bar{\nu}_c}. \tag{2.11}$$

The electron's spin frequency is defined by its interaction with the magnetic field and is unaffected by the electric quadrupole field. Therefore, $\bar{\nu}_a$, the trap-modified anomaly frequency, is related to ν_a by the good approximation

$$\bar{\nu}_a \equiv \nu_s - \bar{\nu}_c \approx \nu_s - (\nu_c + \frac{\bar{\nu}_z^2}{2\bar{\nu}_c}). \tag{2.12}$$

Recalling $\bar{f}_c \equiv \bar{\nu}_c - 3\delta/2$, the revised energy level diagram is shown in Fig. 2.4.

Electron $g/2$ can be determined from measured frequencies from

$$\frac{g}{2} \approx 1 + \frac{\bar{\nu_a} - \frac{\bar{\nu_z}^2}{2\bar{f_c}}}{\bar{f}_c + \frac{3\delta}{2} + \frac{\bar{\nu_z}^2}{2\bar{f_c}}}. \tag{2.13}$$

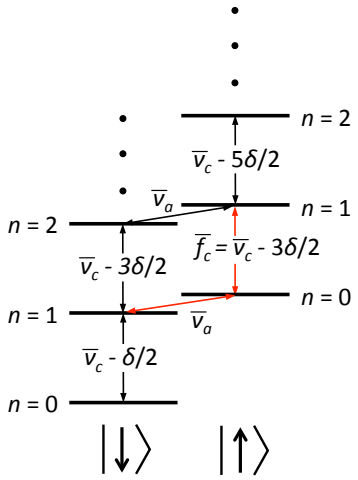

Figure 2.4: Cyclotron and spin energy level diagram with trap-modified frequencies.

Eq. 2.13 is an almost, but not quite, complete description of the experimental ingredients needed to calculate electron $g/2$ from quantities measured in a Penning trap; it omits the systematic cavity shift term that is included in Sec. 2.5 and is described in greater detail in Ch. 5.

2.3 Frequencies and Damping Rates

Charged particles radiate as they accelerate according to the Larmor formula,

$$P = \frac{q^2 a^2}{6\pi\varepsilon_0 c^3}, \tag{2.14}$$

where P is power, q is charge, and a is proper acceleration. Each of an electron's magnetron, axial, and cyclotron motions in a Penning trap therefore has a damping rate associated with its acceleration. Frequencies and damping rates are listed in Table 2.1 for the precision measurement trap currently in use.

Trap Motion	**Frequency**	**Radiative Damping**
magnetron	$\nu_m \approx 137$ kHz	$\gamma_m^{-1} \approx 4$ Gyr
axial	$\nu_z \approx 200$ MHz	$\gamma_z^{-1} \approx 1$ yr
cyclotron	$\nu_c \approx 145.5$ GHz	$\gamma_c^{-1} \approx 100$ ms
spin	$\nu_s \approx 145.7$ GHz	$\gamma_s^{-1} \approx 5$ yr

Table 2.1: Precision measurement trap frequencies and radiative damping rates.

The axial frequency is set by electrode dimensions and voltages chosen as described in Sec. 2.3.2. In practice, an electron's axial motion is damped by a tuned circuit for detection as described in Ch. 4, yielding $\gamma_z^{-1} \approx 0.2$ s. The spin decay from $|\uparrow\rangle$ to $|\downarrow\rangle$ is a magnetic dipole transition; the decay rate is therefore suppressed by a factor of $\hbar\omega_s/(mc^2)$ with respect to the electric dipole cyclotron transitions, leading to a lifetime so long that unwanted spin transitions are never a problem.

In addition to the precision measurement trap, the current-generation $g/2$ experiment has an adjacent "positron accumulation" (or "loading") trap for collecting and cooling positrons from the radioactive source before their transfer into the precision measurement trap. The frequencies and damping rates for this trap are in Table 2.2.

Trap Motion	**Frequency**	**Radiative Damping**
magnetron	$\nu_m \approx 9.75$ kHz	$\gamma_m^{-1} \approx 10 \times 10^{12}$ yr
axial	$\nu_z \approx 53.3$ MHz	$\gamma_z^{-1} \approx 62$ yr
cyclotron	$\nu_c \approx 145$ GHz	$\gamma_c^{-1} \approx 100$ ms
spin	$\nu_s \approx 145$ GHz	$\gamma_s^{-1} \approx 5$ yr

Table 2.2: Positron accumulation ("loading") trap frequencies and radiative damping rates. Cyclotron and spin transitions are not driven in this trap, but frequencies and damping rates are similar to those in the precision measurement trap.

2.3.1 Electrode Geometries

Our Penning traps' electric fields are created by a stack of metal electrodes held at different voltages. Because a quadrupole electric field has equipotentials defined by hyperbolae, early Penning traps for electron and positron $g/2$ measurements (and some modern Penning traps for precision mass spectrometry, e.g., [95]) were built with hyperbola-shaped electrodes. Fig. 2.5 shows a cross section of the electrodes of a hyperbolic trap. The frequency of the electron's axial oscillation is primarily determined by the voltage difference between the "ring" electrode and the "endcap" electrodes; "compensation" electrodes between the ring and the endcaps are adjusted to make the axial motion more harmonic [96].

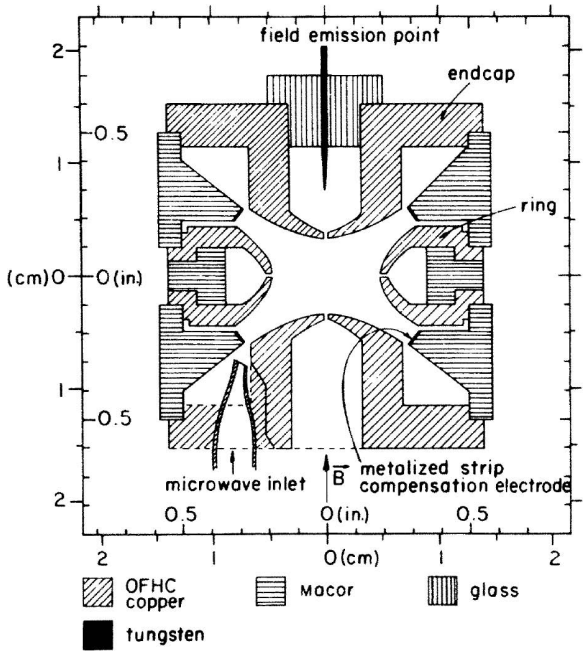

Figure 2.5: Cross section of a hyperbolic Penning trap. From [96].

The 2006 and later electron $g/2$ measurements have instead used cylindrical electrodes, which provide a very good approximation of a quadrupole field near trap

center [87]. Cylindrical electrodes can be fabricated much more easily than hyperbolic electrodes and can be made with a closer-to-ideal shape. Crucially for the sub-ppt precision of electron $g/2$ measurements, cylindrical traps' simpler geometry also permits a fuller understanding of a systematic error due to resonant microwave cavity modes, covered in Ch. 5. The closed-endcap cylindrical Penning trap for the electron and positron $g/2$ measurements in the current apparatus is shown in Fig. 2.6.

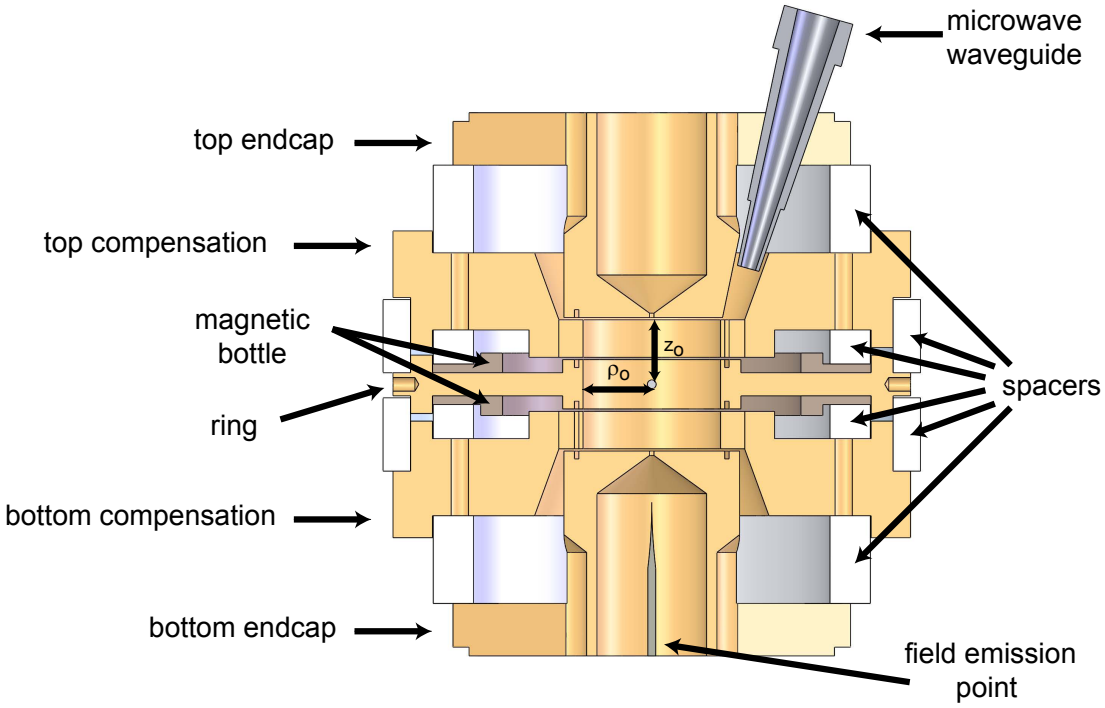

Figure 2.6: Cross section of the precision measurement trap in the current-generation apparatus. Radius ρ_0 and half-height z_0 of the trap cavity are given in Sec. 2.3.2. From [90].

Open-endcap Penning traps can also be designed to have a near-quadrupole field near trap center [97]. Traps of this geometry are used in antihydrogen and antiproton precision measurements for enabling laser or microwave access to a trap, for loading

particles, and for enabling particle transfer between stacked traps with different roles in a measurement, e.g., in [98, 99, 100, 101, 102]. The current-generation apparatus's positron accumulation trap, shown in Fig. 2.7, is an open-endcap trap.

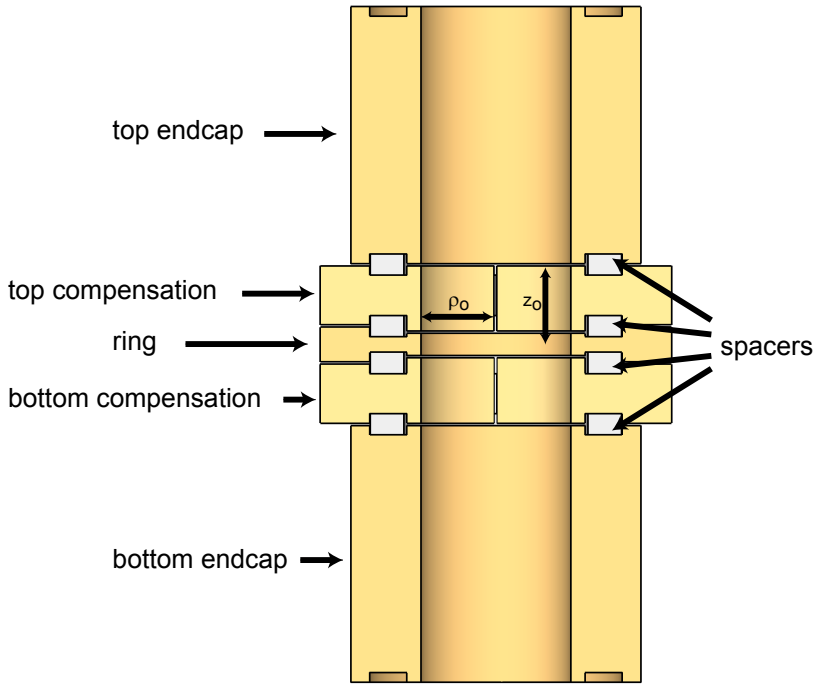

Figure 2.7: Cross section of the open-endcap positron accumulation ("loading") trap in the current-generation apparatus. Radius ρ_0 and half-height z_0 are given in Sec. 2.3.2. From [90].

Concentric rings of conducting material on a flat surface can also be configured to make electric fields sufficiently harmonic to form a Penning trap. The current-generation $g/2$ apparatus houses a novel planar Penning trap which is being investigated as a possible scalable, long-coherence-time platform for quantum information studies [93, 103, 104]. (Fig. 2.8) While the planar trap is not directly used in the $g/2$ experiment, the two experiments share infrastructure and manpower to maximize

scientific gain.

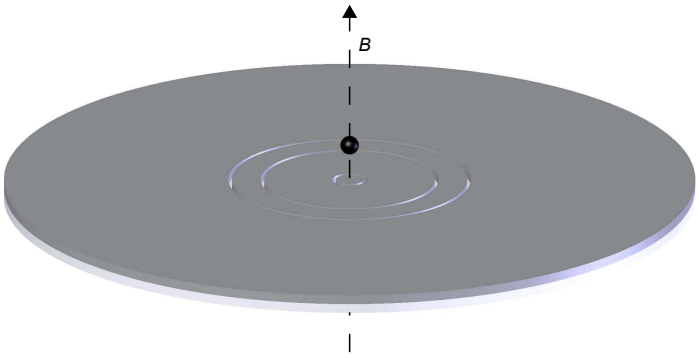

Figure 2.8: Planar Penning trap electrode geometry. From [93].

2.3.2 Penning Trap Electrostatics

Trap electrode design in general is covered in great detail in [96, 97, 105] and the designs of the current-generation precision measurement and positron accumulation traps are described in [71]. Here, only a brief review is included. In the following discussion, (ρ, z) are standard cylindrical coordinates and (r, θ, ϕ) are standard spherical coordinates. A trap can be characterized by dimension d, given by

$$d^2 = \frac{1}{2}\left(z_0^2 + \frac{\rho_0^2}{2}\right), \tag{2.15}$$

where z_0 and ρ_0 are a trap's half-height and radius. Near the center of a closed-endcap cylindrical trap, with $r \ll \rho_0$, the electric potential can be expanded in Legendre polynomials $P_k(\cos(\theta))$:

$$V = -V_R \frac{z^2 - \rho^2/2}{2d^2} - \frac{V_R}{2} \sum_{\substack{k=0 \\ \text{even}}}^{\infty} C_k \left(\frac{r}{d}\right)^k P_k(\cos(\theta)). \tag{2.16}$$

where V_R is the voltage applied to the ring electrode and $V_{EC} = 0$ is applied to the endcap electrodes. The "trap coefficients" C_k are given by

$$C_k = C_k^{(0)} + D_k \left(\frac{1}{2} - \frac{V_{Comp}}{V_R} \right), \tag{2.17}$$

where V_{Comp} is the voltage applied to the compensation electrodes. $C_k^{(0)}$ and D_k are defined by trap geometry; general expressions and specific values for the current-generation apparatus's precision measurement trap and positron accumulation trap are in [71]. Trap dimensions are chosen such that $D_2 = 0$, making C_2 depend only on V_R, not V_{Comp}; a trap with this property is referred to as "orthogonalized" [96]. This is useful because the frequency of axial oscillation ν_z is set primarily by C_2, with

$$\nu_z \approx \frac{1}{2\pi} \sqrt{\frac{eV_R}{md^2} (1 + C_2)}. \tag{2.18}$$

Nonzero $C_{k>2}$ coefficients lead to a dependence of axial frequency on A, the amplitude of the electron's axial motion, of

$$\frac{\Delta\nu_z}{\nu_z} = \left(\frac{3}{4} \right) \frac{C_4}{1 + C_2} \left(\frac{A}{d} \right)^2 + \left(\frac{15}{16} \right) \frac{C_6}{1 + C_2} \left(\frac{A}{d} \right)^4 + \cdots . \tag{2.19}$$

To minimize anharmonicity, $C_4 = 0$ can be set to zero by choosing V_{Comp} and V_R such that

$$\frac{V_{\text{comp}}}{V_R} = \frac{C_4^{(0)}}{D_4} + \frac{1}{2}. \tag{2.20}$$

Therefore, conveniently, axial frequency depends very little on either V_R or A in an orthogonalized trap. The open-endcap positron-accumulation trap potential can be analyzed with a similar expansion, though with different coefficients [97, 71]. Salient parameters for both $g/2$-related traps in the current apparatus are shown in 2.3.

[4] An error in the fabrication of the positron accumulation trap caused it to be slightly non-orthogonal. See [71] for details.

Precision Trap				Loading Trap			
ρ_0	0.3965 cm	$C_2^{(0)}$	0.077	ρ_0	0.2989 cm	$\bar{C}_2^{(0)}$	0.565
z_0	0.3879 cm	D_2	-3.73 $\times 10^{-4}$	z_0	0.3179 cm	$\bar{D}_2$	0.0987^4
z_c	0.2385 cm	$C_4^{(0)}$	-0.207	z_c	0.2695 cm	$\bar{C}_4^{(0)}$	-0.260
		D_4	-0.674	z_e	1.0306 cm	$\bar{D}_4$	-0.719
V_R	96.98 V	$C_6^{(0)}$	0.060	V_R	-8.537 V	$\bar{C}_6^{(0)}$	0.245
V_{comp}	79.19 V	D_6	0.326	V_{comp}	-7.567 V	$\bar{D}_6$	0.584
B	5.2 T			B	5.2 T		

Table 2.3: Dimensions, voltages, and fields for the precision measurement trap and the positron accumulation ("loading") trap.

2.4 Measuring $\bar{f}_c$ and $\bar{\nu}_a$

Sub-ppb measurements of the cyclotron and anomaly frequencies are at the heart of the $g/2$ measurement. To eliminate an unknown relativistic shift, as described in Sec. 2.1.1, cyclotron transitions are driven only between $|\uparrow, n=0\rangle$ and $|\uparrow, n=1\rangle$. Directly detecting 150 GHz photons from single cyclotron transitions would be prohibitively difficult. Therefore, the electron's cyclotron/spin state is monitored through a coupling to the axial degree of freedom, which is then directly detected. Many transitions are attempted with drives at different frequencies and the axial motion is used to assess the success of each attempt. The data are corrected for field drifts and binned into histograms to build up transition lineshapes (Fig. 2.9), from which $\bar{\nu}_a$ and $\bar{f}_c$ are extracted with modest linesplitting. The following subsections give more detail about each of these steps.

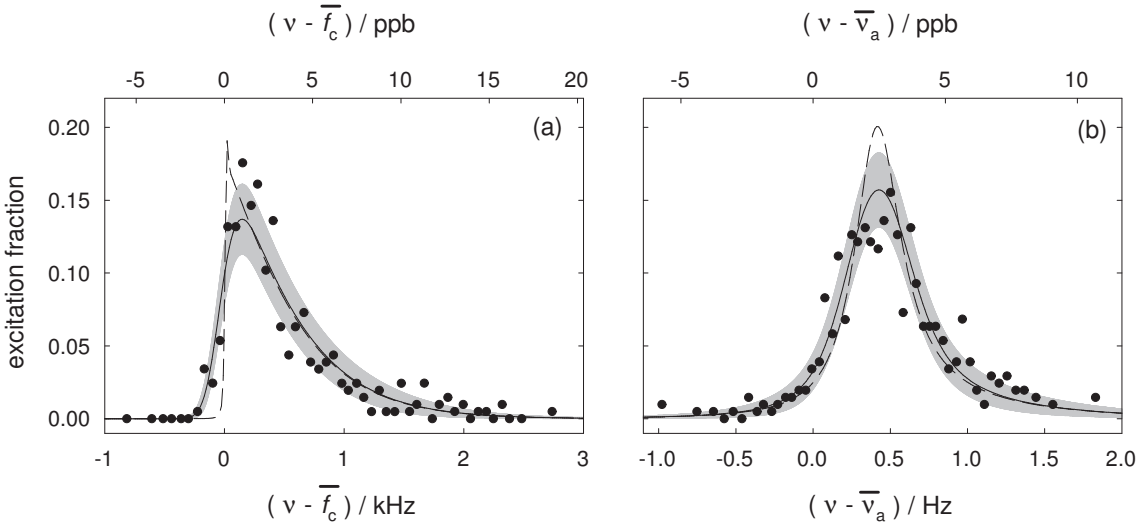

Figure 2.9: (a) Cyclotron and (b) anomaly lineshapes from data for the best electron $g/2$ measurement, taken with $\bar{f}_c$=147.5 GHz in the previous apparatus at Harvard. Black dots are data, dashed lines are ideal zero-noise lineshapes, solid lines are maximum likelihood fits to models assuming Gaussian-distributed noise, and gray bands show 68% confidence levels for expected point distributions. From [27].

2.4.1 Detecting the Cyclotron and Spin State

To couple the electron's cyclotron and spin state to its axial motion, two thin, precisely machined nickel rings are installed next to spacers in the precision trap electrode stack (Fig. 2.6) to create a magnetic field perturbation called the "magnetic bottle" [106]. Its zeroth-order effect is to shift the overall magnetic field by <1%. The second-order term adds a z^2 dependence to the magnetic field:

$$\Delta\vec{B} = B_2\left[(z^2 - \rho^2/2)\hat{z} - z\rho\hat{\rho}\right]. \tag{2.21}$$

This adds a perturbation term to the electron's axial Hamiltonian that depends on the electron's interaction with the magnetic field. The term is proportional to the electron's magnetic moment due to both spin and orbital angular momentum, and

also has the same z^2 dependence as the electric quadrupole. The electron's full axial Hamiltonian becomes

$$H_z = \left(\frac{1}{2}m\omega_{z_0}^2 + 2B_2\mu_B(n + \frac{1}{2} + \frac{g}{2}m_s)\right)z^2, \tag{2.22}$$

where ω_{z0} is the axial frequency in the absence of the magnetic bottle and a tiny magnetron contribution has been neglected. In the presence of the magnetic bottle, a cyclotron transition or spin flip thus shifts the observed axial frequency of the electron. It is this shift that is detected as described in Ch. 4 to determine that a transition has occurred. Because the perturbation Hamiltonian and the original Hamiltonian commute, this is a quantum non-demolition (QND) detection method.

The downside of this dependence of $\vec{B}$ on z is that it causes the electron to sample a range of magnetic fields. The anomaly frequency $\bar{\nu}_a$ and the cyclotron frequency $\bar{f}_c$ are both proportional to magnetic field, and the z^2 inhomogeneity in B widens the measured $\bar{\nu}_a$ and $\bar{f}_c$ lineshapes. This broadening causes the linewidth (Fig. 2.9), characterized by a linewidth parameter $\Delta\omega$ that is defined as [107, 105]

$$\Delta\omega \equiv \omega_0\frac{B_2}{B}\langle z^2\rangle = \omega_0\frac{B_2}{B}\frac{k_BT}{m\omega_z^2}, \tag{2.23}$$

where k_B is the Boltzmann constant. The anomaly and cyclotron lineshapes are different because $\Delta\omega$ for each of the two transitions compares differently to γ_z, the damping rate for thermalization between the axial motion and the amplifier. For the 150 GHz cyclotron transition, $\gamma_z \ll \Delta\omega$, so the axial motion remains in a single state during a transition, and $\langle z^2\rangle$ is a single value picked out of the thermal Boltzmann distribution of axial states. Combining data from multiple transitions leads to the exponential lineshape with width $\Delta\omega$ on the left in Fig. 2.9. The 170 MHz anomaly

transition on the right in Fig. 2.9 is closer to the $\gamma_z \gg \Delta\omega$ limit, where any given transition is affected by the magnetic field experienced in many axial states. In this limit, the lineshape is a Lorentzian with full-width $\gamma_c + 2(\Delta\omega)^2/\gamma_z$. The weighted-mean lineshape center, regardless of γ_z, is $\omega_0 + \Delta\omega$. Detailed lineshape derivations are done in [107, 105] and extended in [108, 27].

Because the axial coupling causes lineshape broadening, it is valuable to make this coupling as weak as is possible without making the axial frequency too small to be observable. As shown in the data in Sec. 4.7, the axial shift has been reduced from 4 Hz (20 ppb) in the previous apparatus to 1.5 Hz (8 ppb) in the current apparatus by designing a bottle with $B_2 = 622$ T/m^2 rather than the $B_2 = 1540$ T/m^2 of the previous apparatus [90].

To further reduce the range of fields the electron samples, it is also valuable to reduce the electron's axial amplitude as much as possible. The electron's axial temperature T, and therefore $\langle z^2 \rangle$, is set by the noise temperature of the axial amplifier. The amplifier is therefore turned off and allowed to cool toward the dilution refrigerator's 100 mK before cyclotron and anomaly transition attempts are made [27]. Methods under development for detuning the axial amplifier and cooling the axial motion below the thermal limit are discussed in Sec. 5.2.3.

The electron's axial amplitude must be deliberately increased from the 2 μm thermal amps-off value and 7 μm thermal amps-on value to 100 μm for quick assessment of axial frequency with the self-excited oscillator (SEO), described in Sec. 4.6.4. The tiny axial frequency shift due to the different fields experienced at these different amplitudes is taken into account for the 50 ppb $\bar{\nu}_z$ measurement for determining $g/2$.

2.4.2 Driving Cyclotron and Anomaly Transitions

Cyclotron transitions are electric dipole transitions driven by oscillating transverse electric fields. The microwaves used to drive cyclotron transitions are produced and delivered by a system described in Sec. 4.7. The drive strength is kept low, for a transition probability of around 10% or less for a 2 s drive time, in order to avoid the possibility of driving multiple transitions, which would lead to a more complex lineshape [108]. To control for systematic effects, a detuned anomaly drive is applied simultaneously.

Oscillating radial magnetic fields are required to drive anomaly transitions. Though these fields can be created by driving split electrodes to form two effective current loops (e.g., for [5]), in the previous Harvard apparatus and the current apparatus they are produced by driving the particle axially through the $z\rho\hat{\rho}$ magnetic bottle gradient at the 170 MHz anomaly frequency [109]. The relative proximity of the 200 MHz axial frequency to the anomaly frequency reduces the power needed to drive the anomaly transition (and possible power-dependent systematics), as described in Section 2.3.3 of [108] and in [27]. A detuned cyclotron drive is applied simultaneously during anomaly transition attempts.

2.4.3 Quantum Jump Spectroscopy Protocol

The procedure for a cyclotron transition attempt is as follows [27]:

1. The electron is prepared in the $|\uparrow, n = 0\rangle$[5] state. The electron's axial frequency is measured with the self-excited oscillator.

[5] for the positron, $|\downarrow, n = 0\rangle$

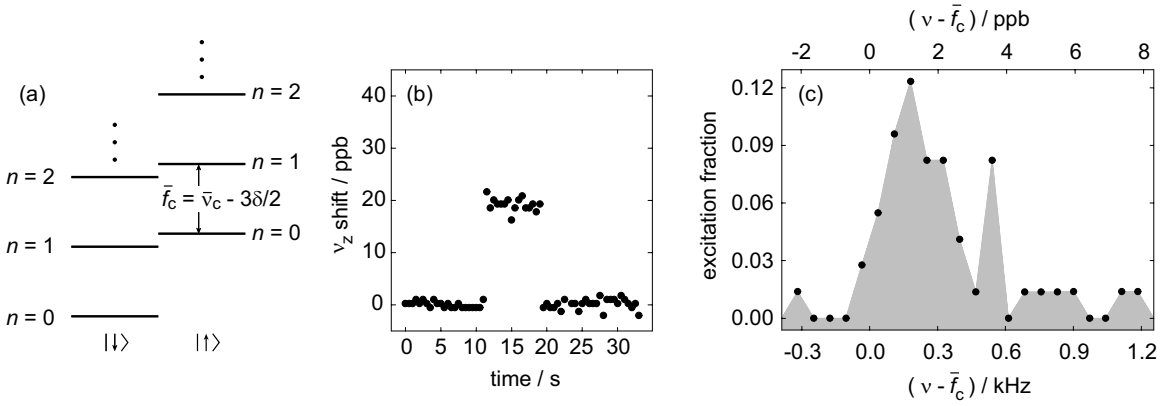

Figure 2.10: (a) Cyclotron transition driven for $g/2$ measurement. (b) Shift in axial frequency due to successful cyclotron transition attempt upward and then decay back to the ground state. (c) Histogram of cyclotron transition data over a range of frequencies. Data are from the best electron $g/2$ measurement, made in the previous Harvard apparatus. Figure from [27].

2. The self-excited oscillator (Sec. 4.6.4) is turned off and magnetron cooling (Sec. 4.6.1) is begun, followed by a 0.5 s wait.

3. The axial amplifier is turned off, followed by a 1.0 s wait to allow cooling of the axial amplifier toward the 100 mK dilution refrigerator base temperature.

4. A near-resonance cyclotron drive and an off-resonance anomaly drive are applied for 2.0 s to attempt to drive a transition to $|\uparrow, n = 1\rangle$[6]. (Fig. 2.10a)

5. The amplifier and self-excited oscillator are turned on and the self-excited oscillator is allowed to stabilize for 1.0 s.

6. The electron's axial frequency is measured to determine whether a transition has occurred. (Fig. 2.10b)

This procedure is then repeated for many near-resonant frequencies for the cyclotron

[6]for the positron, $|\downarrow, n = 1\rangle$

drive. Every few hours, an "edge-tracking" procedure finds the sharp low-frequency edge of the cyclotron line to measure the magnetic field [110]. Data are taken over the course of several hours and are combined with corrections for magnetic field drift provided by fits to the the edge-tracking data. Fig. 2.10c shows a histogram of such a combined data set from the best electron $g/2$ measurement, made at Harvard in the previous apparatus [27].

The procedure for an anomaly transition attempt is similar except that the axial frequency shift due to the anomaly transition itself is too small to be detectable. To make successful attempts distinguishable from failures, an end state with cyclotron quantum number $n = 1$ is chosen and the eventual transition from $n = 1$ to $n = 0$ is detected. Edge-tracking-corrected data for the anomaly lineshape are shown in Fig. 2.11c.

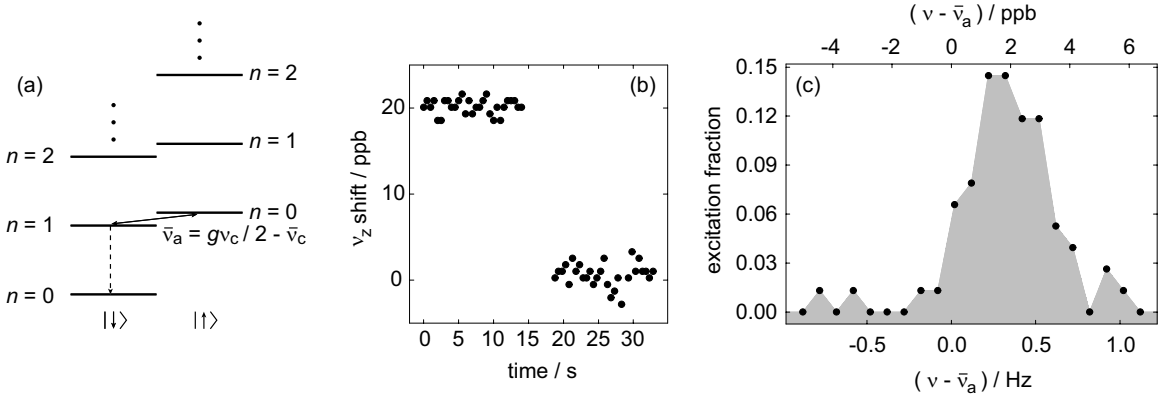

Figure 2.11: (a) Anomaly transition driven for $g/2$ measurement. (b) Shift in axial frequency due to cyclotron decay after a successful anomaly transition. (c) Histogram of anomaly transition data over a range of frequencies. Data are from the best electron $g/2$ measurement, made in the previous Harvard apparatus. Figure from [27].

1. The electron is prepared in the $|\uparrow, n = 0\rangle$[7] state. The electron's axial frequency is measured with the self-excited oscillator.

2. The self-excited oscillator is turned off and magnetron cooling is begun, followed by a 0.5 s wait.

3. The axial amplifier is turned off, followed by a 1.0 s wait to allow cooling.

4. A near-resonance anomaly drive and an off-resonance cyclotron drive are applied for 2.0 s to attempt to drive a transition to $|\downarrow, n = 1\rangle$[8]. (Fig. 2.11a)

5. The amplifier and self-excited oscillator are turned on and the self-excited oscillator is allowed to stabilize for 1.0 s.

6. The electron's axial frequency is monitored for up to several cyclotron lifetimes to detect the decay to $|\downarrow, n = 0\rangle$[9] that follows a successful anomaly transition. (Fig. 2.11b)

Cyclotron and anomaly data are taken for several nights at a given magnetic field value. From those data, $\bar{\nu}_a$ and $\bar{f}_c$ are extracted. Data for one magnetic field value for the best electron $g/2$ measurement, done at Harvard in the previous apparatus, are shown in Fig. 2.9. Lineshapes are blurred due to an unknown cause. Various lineshape models making different assumptions about the nature of the blurring were considered in extracting values in that measurement, as described in [27, 4]. The uncertainty in $g/2$ was determined by evaluating the range of $g/2$ values given by

[7] for the positron, $|\downarrow, n = 0\rangle$
[8] for the positron, $|\uparrow, n = 1\rangle$
[9] for the positron, $|\uparrow, n = 0\rangle$

different lineshape models. Then, to avoid artificially masking the uncertainty while combining data from different magnetic field values, the minimum disagreement at different magnetic field values was taken as a correlated error. These conservative assumptions limited linesplitting to a part in ten.

Data are taken at several magnetic field values (four in the best electron $g/2$ measurement). At each magnetic field value, the cavity shift correction $\Delta\omega_c/\omega_c$ derived from cyclotron lifetime data (described in Sec. 5.2.2, shown here in Fig. 2.12) is combined in Eq. 2.24 with measured $\bar{\nu}_a$, $\bar{f}_c$, $\bar{\nu}_z$, as well as δ from Eq. 2.6, to yield a measured value of $g/2$, given by

$$\frac{g}{2} \simeq 1 + \frac{\bar{\nu_a} - \frac{\bar{\nu_z}^2}{2\bar{f_c}}}{\bar{f_c} + \frac{3\delta}{2} + \frac{\bar{\nu_z}^2}{2\bar{f_c}}} + \frac{\Delta\omega_c}{\omega_c}. \tag{2.24}$$

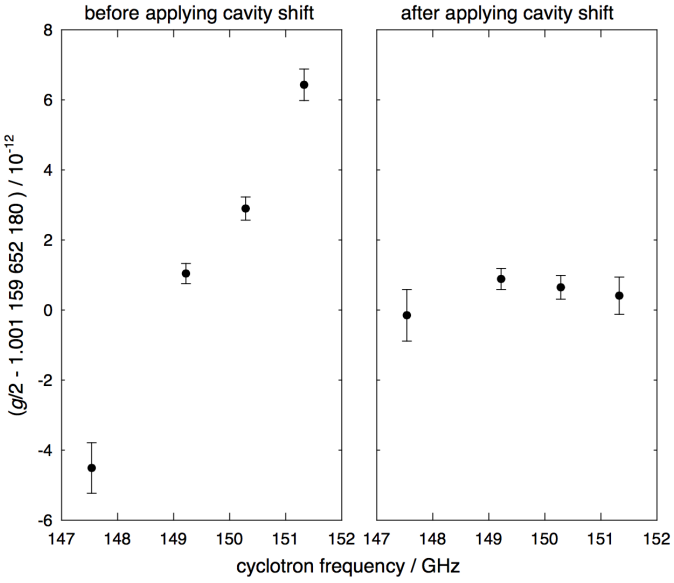

Figure 2.12: Electron $g/2$ as determined from data from the best electron $g/2$ measurement, taken at each of the four magnetic field values, before and after applying the cavity shift. From [27].

2.5 The Path to Improved Precision

$\bar{f}_c$ / GHz =	147.5	149.2	150.3	151.3
cavity shift uncertainty	0.13	0.06	0.07	0.28
statistical uncertainty	0.39	0.17	0.17	0.24
correlated lineshape model uncertainty	0.24	0.24	0.24	0.24
uncorrelated lineshape model uncertainty	0.56	0	0.15	0.30

Table 2.4: Summary of uncertainties from the best electron $g/2$ measurement. Adapted from [27, 4].

Table 2.4 shows the uncertainties in the best electron $g/2$ measurement. The dominant source of error was the lack of understanding of the lineshape. Though the cause of the lineshape blurring was not fully understood, its shape was consistent with magnetic field fluctuations on a timescale of 200 ms to several minutes [27]. Eliminating or reducing this uncertainty is necessary for improving measured electron $g/2$ precision.

The current-generation apparatus was designed with inherent stability improvements that are intended to reduce magnetic field fluctuations arising from any of several sources. These are described in Ch. 3. In addition, the aforementioned reduction in the strength of the magnetic bottle is expected to narrow lineshapes enough to determine $\bar{f}_c$ and $\bar{\nu}_a$ more precisely, even if blurring is not entirely eliminated. Improvements in trap cavity design, described in Ch. 5, create the possibility of further narrowing lineshapes through sideband cooling of the axial motion. These improvements, along with the positron-trapping capability of the current apparatus, provide a path to improved precision in both electron and positron $g/2$.

Chapter 3

A Highly Stable Apparatus

To push beyond the precision of the best electron $g/2$ measurement for both electrons and positrons, a new and improved apparatus has been built (Fig. 3.1). Because magnetic field noise is likely the dominant source of the lineshape blurring seen in the previous electron $g/2$ measurement, this current-generation apparatus was designed to reduce magnetic field fluctuations experienced by a trapped particle. This chapter describes the infrastructure of this apparatus, focusing on these improvements.

The precision, positron accumulation ("loading"), and planar trap electrode stacks are mounted within a vacuum enclosure called the "trap can" that is cooled to 100 mK by a dilution refrigerator. A high-stability, self-shielding superconducting magnet provides the Penning trap's overall magnetic field. A home-made gaseous ^{3}He NMR probe can be used to shim this cold-bore magnet to high field homogeneity. A vibration-isolated pulse-tube cryo-refrigerator is used to recapture boiled-off helium gas and control gas pressure in the >500 L helium dewar that cools the magnet and the exterior of the experimental insert. Efforts to mitigate vibrations from the cry-

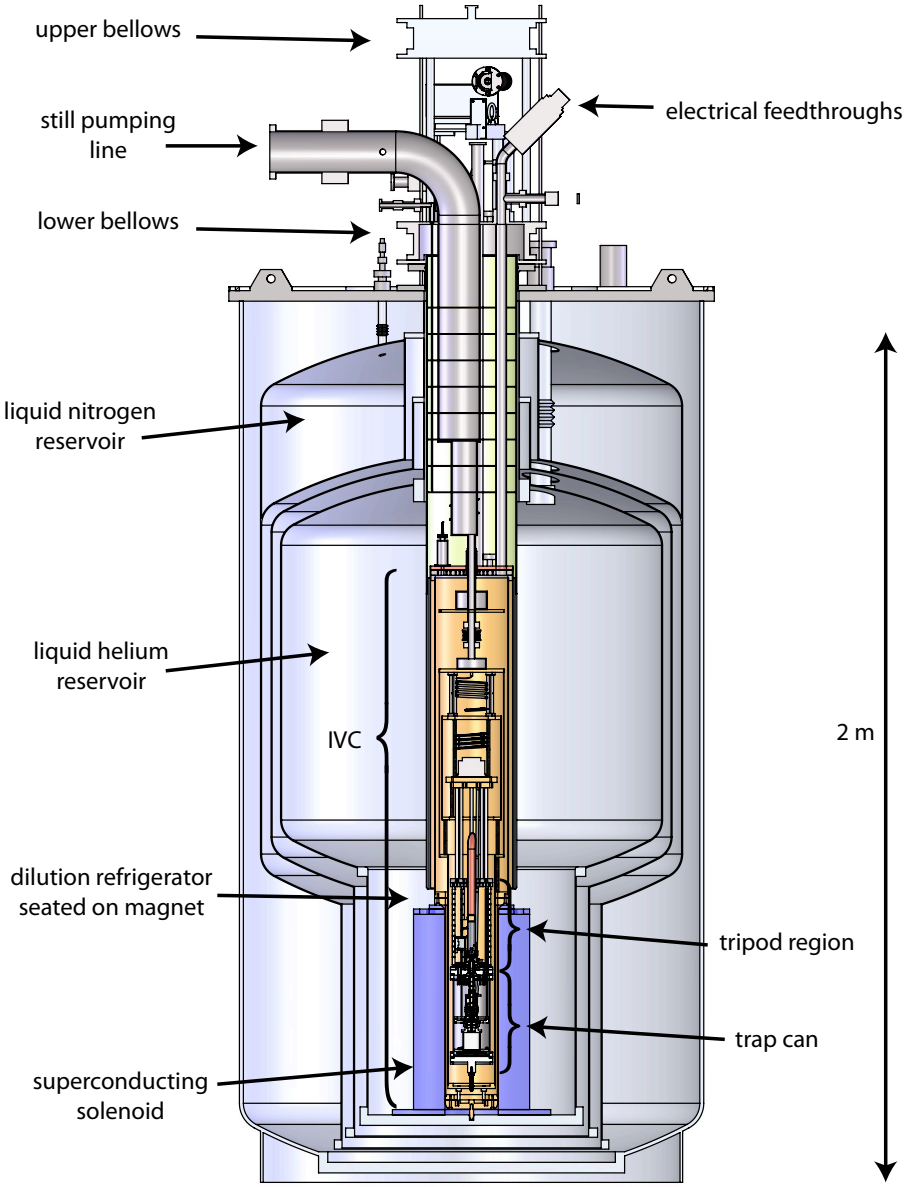

Figure 3.1: The current-generation electron/positron $g/2$ apparatus, showing dewar, superconducting magnet, and experimental insert with dilution refrigerator and trap can inside the inner vacuum chamber (IVC). From [90], adapted from [71].

orefrigerator inform potential future-generation cryogen-free systems. A low-activity, retractable positron source provides large numbers of trappable positrons without the inconvenient safety requirements of a larger source [89, 71, 90].

3.1 Electrodes, Dilution Refrigerator, and Dewar

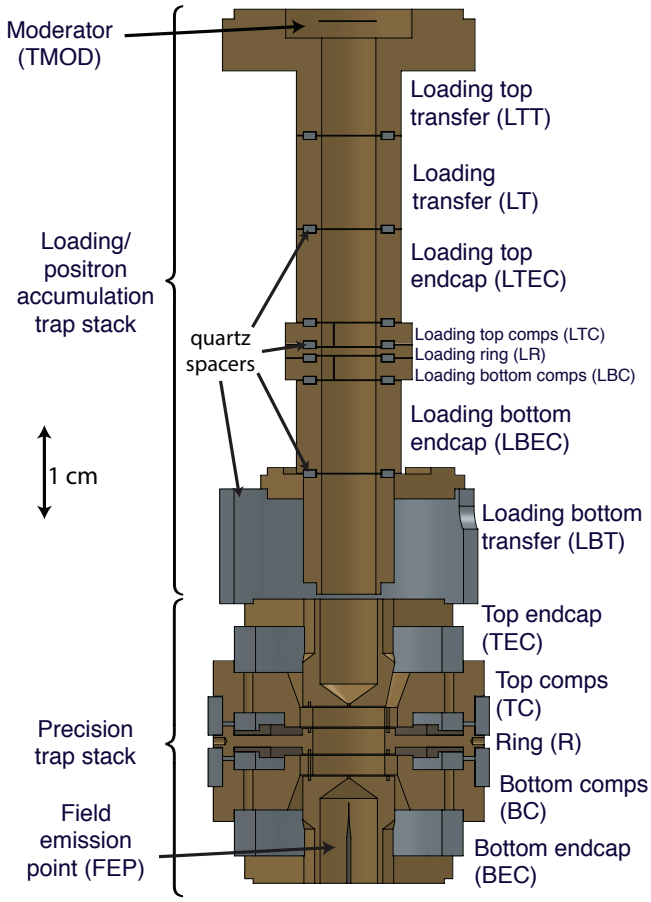

Figure 3.2: Cross section of the combined stack of Penning trap electrodes and spacers comprising the precision trap (bottom), the positron accumulation (or "loading") trap (center), and transfer electrodes (between traps and above positron accumulation trap). Adapted from [71].

Fig. 3.2 shows the combined precision/positron accumulation trap electrode stack.

Material choices in and near the trap electrodes are tightly constrained by the need to maintain an extremely stable and homogeneous magnetic field inside the trap; in a previous-generation apparatus, even copper electrodes' nuclear paramagnetism led to temperature-dependent 100 ppb shifts in magnetic field [110, 86]. High-purity silver, gold, titanium, molybdenum, quartz, and sapphire are among the few materials that are sufficiently nonmagnetic and also have desirable electrical and mechanical properties. Precision and positron accumulation trap electrodes are made from 99.999% pure silver. Spacers between electrodes are made of quartz. Split compensation electrodes, needed for sideband cooling of the magnetron motion (Sec. 4.6.1) are separated by 3/64" sapphire balls. A pair of thin nickel rings creates the symmetrical and well-understood magnetic bottle field needed for detection (Sec. 2.4.1 and Fig. 2.6).

Electrodes and nickel rings are machined by the Harvard SEAS Scientific Instrument Shop and spacers are ground by Insaco, Inc. Critical dimensions are specified to tolerances as tight as 0.0001", with electrodes designed to tighten against quartz spacers slightly as the electrode stack cools in order to precisely fix electrodes' relative positions. Trap dimensions in the current-generation apparatus have been chosen to enable cavity-assisted axial sideband cooling, described in Sec. 5.2.3. After machining, electron-facing surfaces are polished with a series of polishing papers of decreasing grit size, electrical leads are oven-brazed onto electrodes in a hydrogen atmosphere, and inner surfaces of electrodes are then coated in gold to prevent tarnishing. (See [71] for more electrode fabrication details.)

Fig. 3.3 illustrates some of the challenges of trap fabrication. The nickel layer typ-

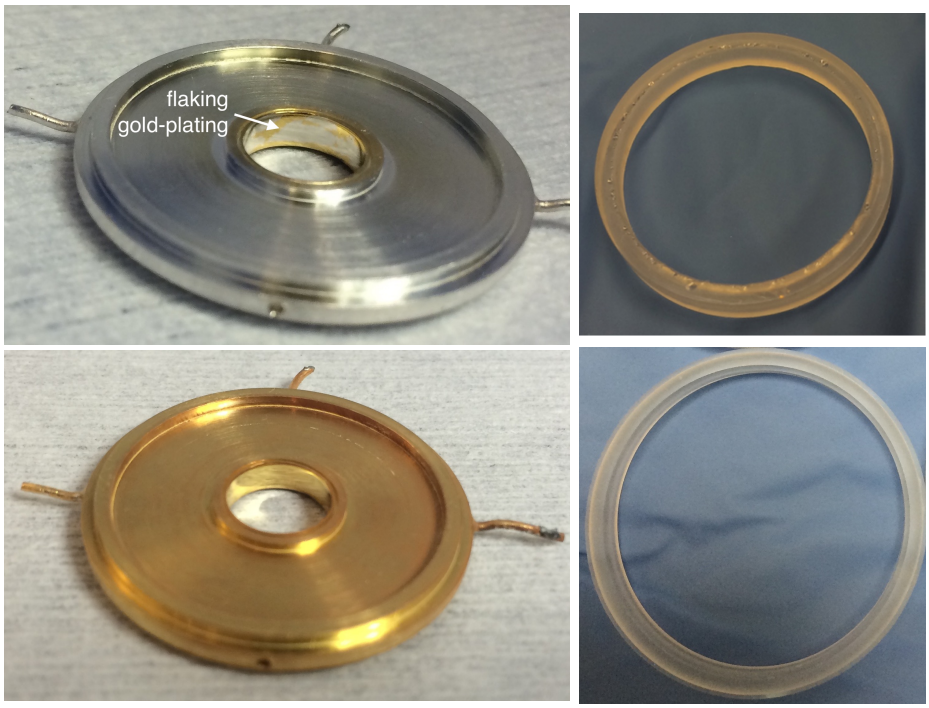

Figure 3.3: Flaking of evaporated gold layer on inside surface of precision ring electrode (top left). Same electrode after removal of flaking layer and gold electroplating (bottom left). Quartz spacer with chipping caused by inadequate chamfering (top right). Properly chamfered spacer (bottom right).

ically used to adhere a gold layer to a metal substrate is unacceptably magnetic, so gold is instead applied directly to the silver electrodes. Initially, thermal evaporation was used to apply the gold layers to precision trap electrodes because it was believed that this method would minimize patch potentials compared to electroplating [71]. However, after a few years and many thermal cycles, the gold layer began to flake off and had to be replaced. The remaining parts of the flaking gold layer were removed by hand with 0.5 μm grit polishing paste[1], taking care to avoid deforming the silver electrodes, which had been softened as they annealed while leads were brazed on. After thorough cleaning with soap and solvents in a sonicator, electrodes were electrocleaned[2] and then electroplated[3] to deposit a 200 nm gold layer. Gold surfaces are now in good condition and appear to be robust through thermal cycling.

Spacers also experienced unexpected damage after several cooldown/warmup cycles. Chamfers on outside corners of spacers were in several places insufficient to prevent interference with the mating inside corners of electrodes, causing chipping of the spacers on cooldown. Modifications to spacers' chamfers and in some cases outer diameters ameliorated the problem.

The combined trap electrode stack is mounted inside a CP-2 titanium[4] trap can vacuum enclosure (Fig. 3.4). The stack of cylindrical electrodes and spacers is sandwiched between silver plates and the top flange of the trap can (called the "pinbase"), held in gentle compression by springs and nuts on threaded rods. The pinbase contains DC feedthroughs and four indium seal flanges: one for the 200 MHz RF feedthrough

[1]Diamond Innovations DMSY SJK-5 0-0.50 MWS 5 with Hyprez W Lubricant

[2]Thanks to Ronald Alexander for introducing the electrocleaning procedure.

[3]Using Technic TG25 RTU gold plating solution at 42 mA/in^2 for 30 s. Thanks to Melissa Wessels and Ronald Alexander for improving the gold-plating procedure.

[4]Commercially pure titanium, grade 2

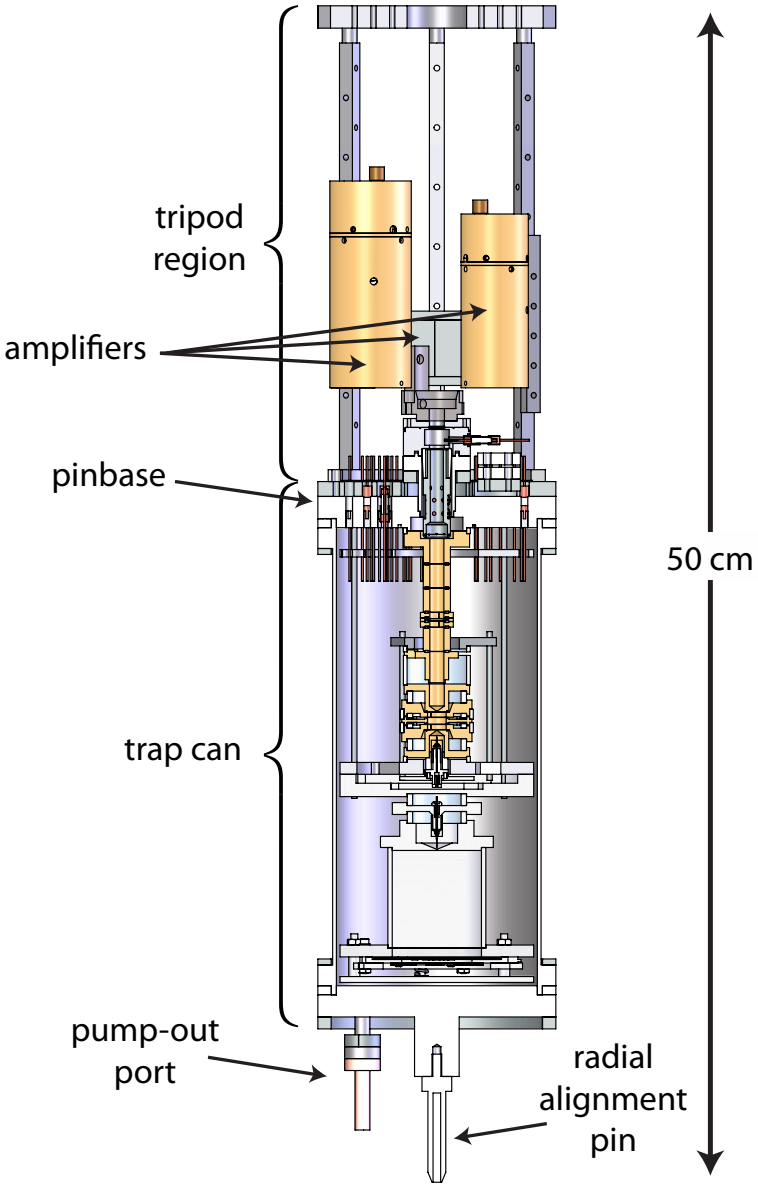

Figure 3.4: Cross section of the trap can and lower tripod region. The planar Penning trap is visible mounted below the precision/positron accumulation trap stack. From [90], adapted from [71].

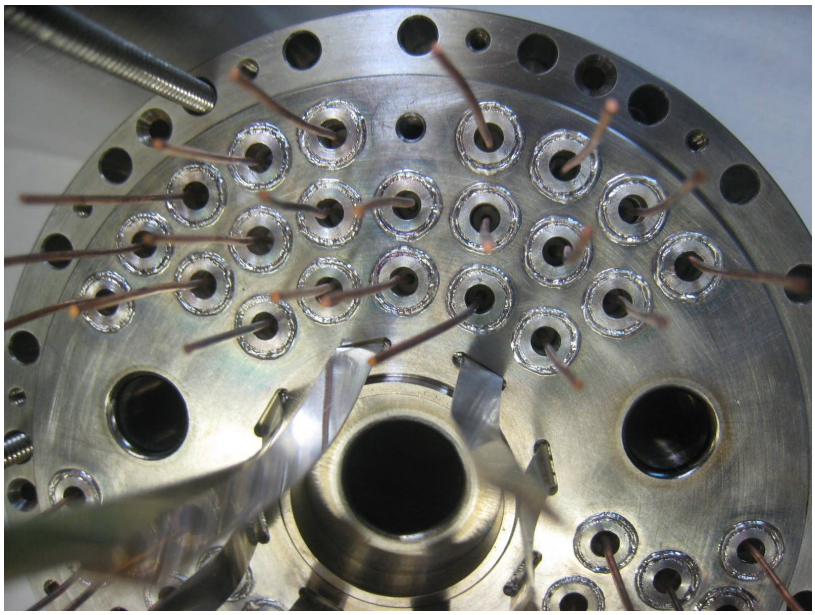

Figure 3.5: A silver plug and silver-to-titanium weld joint around each DC vacuum feedthrough is visible on this view of the bottom of the pinbase.

(Sec. 4.2), one for a sapphire microwave window (Sec. 4.7), one for a thin titanium window through which positrons enter the trap can (Secs. 3.4 and 4.5.1), and a spare. Creating vacuum seals around the DC feedthroughs was a particular challenge. The feedthroughs comprise a copper center conductor, a ceramic insulator, and a thin outer shell of copper (a small enough amount of copper and far enough from the precision trap that their nuclear paramagnetism is not a issue). The outer copper layers were oven-brazed into silver plugs, which then had to be e-beam welded to the titanium pinbase. After thermal cycling caused the original pinbase to develop leaks, optimization of plug geometry[5] and weld parameters yielded a recipe for robust weld joints, and an improved pinbase was fabricated that has had no leaks (Fig. 3.5). The trap can is pumped down to about 10^{-7} torr at room temperature and sealed by pinching off a copper tube. Vacuum within the trap can is much improved on cooling

[5]The silver protrudes 0.01" above the titanium surface.

to 100 mK (measured to be $< 5 \times 10^{-17}$ torr at 4 K with similar methods in [111]), sufficiently low to not interfere with trapping of antimatter on the months or longer timescale.

The trap can is connected by gold-plated silver posts (the "tripod") to the mixing chamber stage of the dilution refrigerator[6]. The trap can, tripod region, and higher temperature stages of the dilution refrigerator are contained within the inner vacuum chamber (IVC) of the dilution refrigerator (Fig. 3.6). Trap electronics, thermally anchored at each temperature stage by heatsink bobbins, are visible between the trap can and the IVC top plate in the photograph on the right. Radiation shields attached at the intermediate cold plate and the still, as well as the IVC enclosure, are visible in gold on the model on the left. Several tubes extend the vacuum space upward to electrical and microwave feedthroughs at the "hat," which is accessible from outside the dewar (Fig. 3.1). Thermally insulating PEEK centering pins (bottom) ensure correct radial alignment between the 100 mK trap can, the still shield, and the IVC. A centering pin in the bottom of the IVC mates with a divot in the bottom plate of the superconducting magnet to radially align the trap electrode stack with the magnet to better than 0.04". The cold-bore magnet and the IVC are immersed within the same liquid helium bath. This major design change from the previous Harvard electron $g/2$ apparatus enables improvements and also creates some challenges, summarized next.

[6]Janis Research Company Model JDR-500 custom ^{3}He-^{4}He dilution refrigerator system

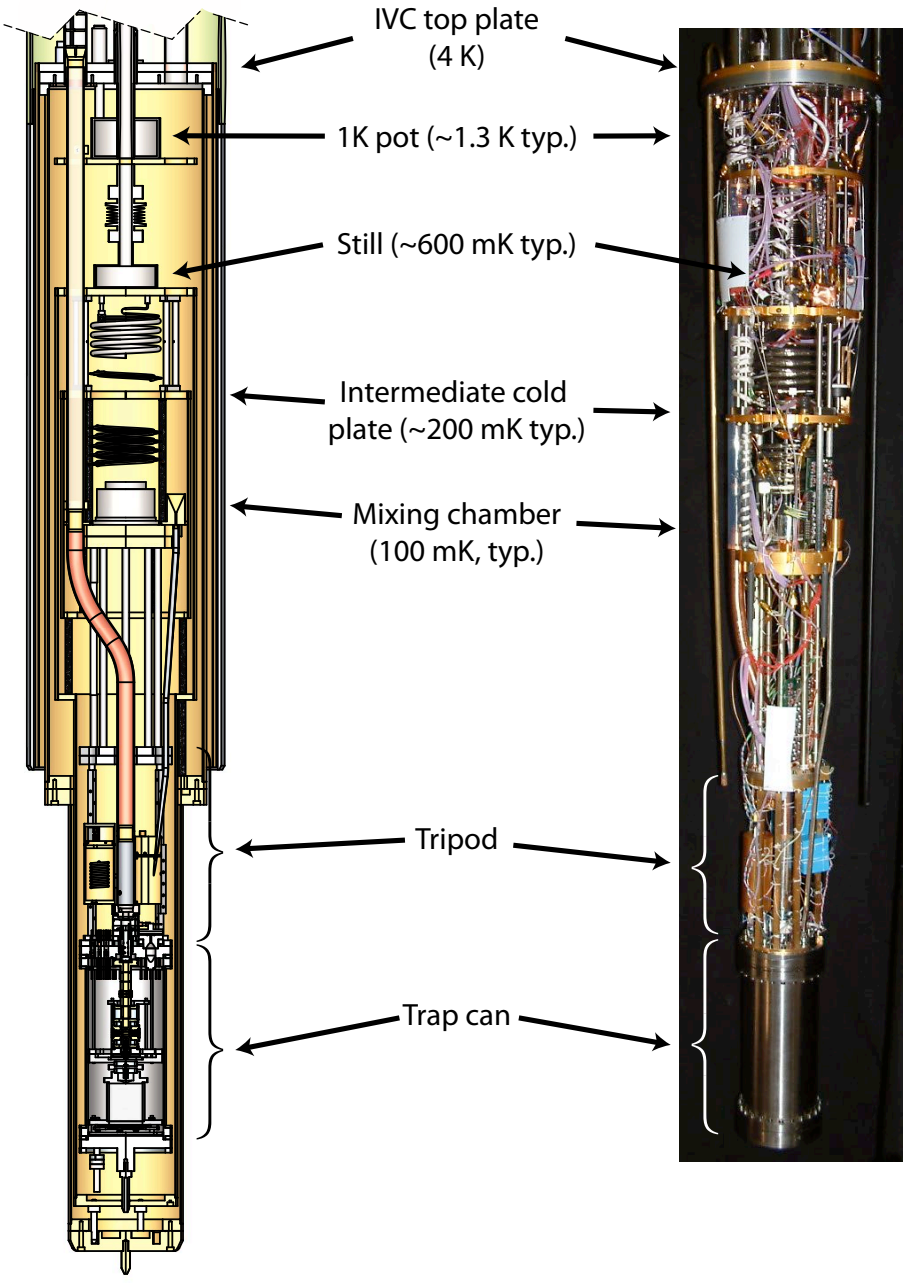

Figure 3.6: Views inside the inner vacuum chamber (IVC) of the dilution refrigerator, showing thermal stages, trap can, and instrumentation. From [71].

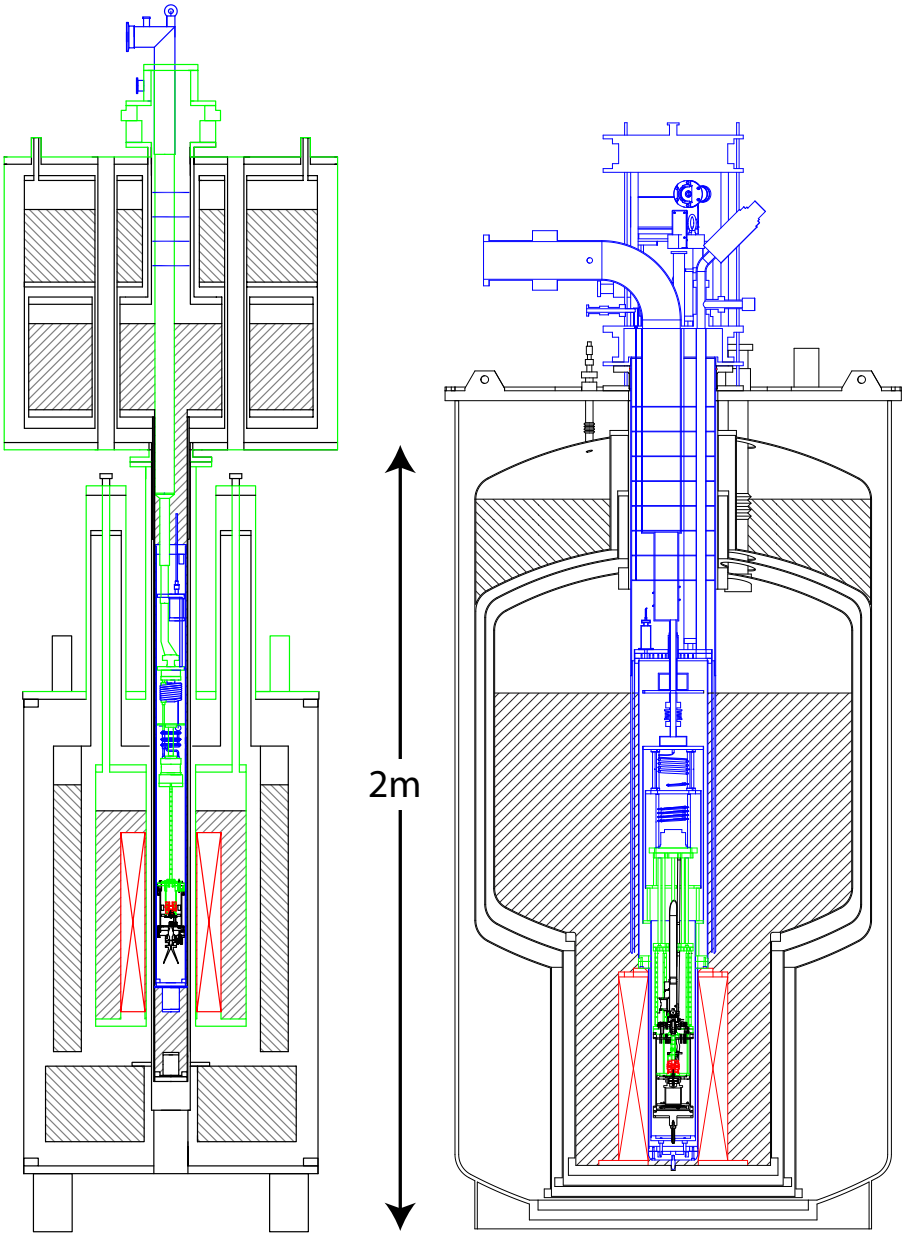

Figure 3.7: Apparatus used for the previous Harvard electron $g/2$ measurements (left) and current-generation apparatus (right). The mechanical support paths between magnets and electrodes are shown in green. From [71].

3.1.1 Mechanical Support of Trap Electrodes by Magnet

To ensure that a trapped particle experiences as homogeneous a magnetic field as possible, it is desirable to prevent the Penning trap electrodes from moving with respect to the magnetic field, which could translate spatial inhomogeneities into field fluctuations. However, in the previous Harvard electron $g/2$ apparatus, the Penning trap electrodes were suspended within the magnet bore at the end of a 2.2 m long insert, susceptible to being driven like a pendulum by externally transmitted vibrations. With a field homogeneity of 10^{-8} over a 1 cm diameter sphere, movements of the trap electrodes within a 100 μm range could cause the 0.5-1 ppb blurring observed in the cyclotron and anomaly lineshapes [27]. This corresponds to just a 0.0026° swing of the insert. Much of the support structure between the electrodes and magnet, shown in green in Fig. 3.7 on the left, was also at room temperature. A change of 1° C in room temperature caused relative position changes of the electrodes and the magnet due to thermal contraction, causing a 10 ppb cyclotron frequency shift; this effect made it necessary to build a temperature-controlled shed around the apparatus [110]. In contrast, in the current apparatus, the electrodes are supported directly on the magnet form, entirely at 4 K and below, shown in green in Fig. 3.7 on the right. A flexible section in the experimental insert decouples the electrode support structure from the dewar top, while thermally insulating carbon fiber posts mechanically support the electrodes on the magnet-resting lip of the IVC. A pair of large-diameter flexible bellows in the current apparatus (labelled in Fig. 3.1) allows a seal between the insert (blue in Fig. 3.7) and dewar top (black in Fig. 3.7) to contain the dewar helium space while mechanically decoupling the experimental insert from the dewar

top. The top of the upper bellows and the bottom of the lower bellows are rigidly connected to the dewar top, while the insert is rigidly connected to the top of the lower bellows and the bottom of the upper bellows. By connecting the interior of the upper bellows to the dewar helium space so the pressures equalize, the dewar top applies no net force on the insert. These changes are intended to greatly reduce any relative motion of a trapped electron or positron through spatial inhomogeneities in the magnetic field. Reduced vibration sensitivity should also increase the datataking duty cycle, which in the previous Harvard electron $g/2$ measurements was limited to 60% of each day by a noise source (likely vibrational) correlated with work hours [27].

3.1.2 Magnetic-field Shimming

The magnet's cold bore precluded use of a water NMR probe for magnetic field shimming. A new ^{3}He-based NMR probe was developed instead; see Sec. 3.2.1 for details.

3.1.3 Reduced Number of Cryogen Spaces

Gas pressure changes in a superconducting magnet's helium reservoir, including those caused by cryogen fills, can cause magnetic field fluctuations [112, 113, 114]. Field instability for the day after a helium fill has been observed in this apparatus [90]. While the apparatus used for previous Harvard electron $g/2$ measurements had five small cryogen reservoirs that needed frequent fills, the current generation's single $>$500 L liquid helium reservoir and surrounding 190 L liquid nitrogen reservoir can be

filled every two weeks and one week, respectively[7]. Helium reliquefication (see Sec. 3.3) extends the interval between fills to months or longer.

3.1.4 The Challenge of Cooldown

To cool down the experimental insert after having it open to work on the trap or its electronics, the initially room-temperature insert must be inserted into the 4 K helium bath and superconducting magnet bore without causing the magnet to quench. (To maximize field stability, the magnet is kept cold and running for months at a time.) Before cooldown, the insert is positioned above the dewar and a space created by a modified glove bag linking the insert and dewar top is flushed with helium gas. Then, the dewar top plate is removed within the glove bag and the insert lowered until a "sliding seal" is formed between a sheath covering the insert and a cryogenic o-ring in the dewar opening. Over several hours, the insert is cooled by helium vapor as it is slowly lowered toward and enters the liquid helium bath. The insert can be removed in just a few minutes, but ensuring good seals with well-flushed glove bags during removal is still critical; atmospheric gas must be prevented from condensing on the cold apparatus and dripping into the dewar. Before the glove-bag technique had been developed, magnetic ice (presumably oxygen, which is paramagnetic) tended to accumulate in the magnet bore over several cooldowns and warmups. More details about the cooldown procedure are in [90].

[7]The dewar was manufactured by Precision Cryogenic Systems.

3.2 Superconducting Solenoid

The 6 T superconducting magnet[8] consists of a main coil, a Z0 coil for small field adjustments, and 11 shim coils with Z, Z^2, Z3, X, Y, ZX, ZY, C2, S2, Z^2X, and Z^2Y geometry. The coils, made of single-filament NbTi, are run in persistent mode except when currents are being changed, and are charged using a removable charging wand to reduce thermal load when not being charged [71]. The main 210 H coil has a Gabrielse-style self-shielding solenoid design that screens out external magnetic field noise that is homogeneous over the volume of the magnet (e.g., from passing subway cars) [115]. Its shielding factor, measured by Cryomagnetics to be >1000, is an increase over the factor of 156 for the magnet used for the previous Harvard electron $g/2$ measurements [71]. Preliminary evidence from cyclotron excitation data has suggested that the magnetic field drift is under 0.3 ppb/hr and is probably much less, comparable to or better than the field stability in the previous apparatus [90]. The magnetic field at magnet center, where the precision trap volume is centered, is designed to be shimmable to a homogeneity of better than 1 part in 10^8 over a 1 cm diameter sphere.

3.2.1 ^{3}He NMR Probe

The magnetic field's spatial homogeneity is optimized by adjusting the current in the shim coils. To measure field homogeneity during the shimming process, the experimental insert is removed from the dewar and replaced with an NMR probe with a small spherical sample volume centered in the same position a trapped particle

[8] Cryomagnetics model 4983

would occupy in the experimental insert. Because the magnet bore is at 4 K, the signal from a typical water NMR probe such as that used in the warm-bore previous Harvard apparatus would suffer from freezing-induced broadening. An NMR probe using ^{3}He (which is gaseous at 4.2 K and, unlike ^{4}He, has a nuclear magnetic moment) was therefore designed and built.

The ^{3}He NMR probe is described in detail in [90] and only in brief here. It consists of a nonmagnetic 0.53 cm^2 glass bulb containing ^{3}He, an insert providing the mechanical support structure to hold it within the magnet, and an antenna near the bulb to induce and detect NMR signals. To increase the density of the ^{3}He gas in the sample volume, it is connected via a 1.65 mm inner diameter capillary to a warm 1 L ^{3}He reservoir, initially filled to a pressure of 1 atm. When the bulb is cooled to 4 K, almost all ^{3}He from both volumes becomes concentrated in the bulb, increasing the density of nuclei there by a factor of 63. (After constructing the probe, our group realized that this idea had been independently proposed elsewhere [116].) At 4 K, the 0.1% polarization of the spins in the 5.2 T magnetic field creates a magnetization of 9.0×10^{-9} A/m, similar to that of the previous-generation water NMR probe. To perform NMR measurements, first a 186 MHz RF drive is applied to the antenna to tip a small fraction of the spins within the sample volume into the x-y plane, and then the same antenna is then monitored for the free-induction decay (FID) signal produced by the spins' Larmour precession. In an inhomogeneous magnetic field, nuclei in different locations have different precession frequencies and their consequent relative dephasing can limit the duration of the FID signal to a timescale called T_2^*. To improve the field homogeneity, shim coil currents are adjusted to lengthen T_2^*.

The first-generation ^{3}He probe is a very successful proof-of-principle prototype which has enabled a demonstration of the shimmability of the magnet. An NMR signal size comparable to that of the previous-generation water NMR probe—sufficient for shimming purposes, and without using complex techniques like hyperpolarization—was demonstrated. The magnetic field was shimmed to 68 ppb within the sample volume, superior to the best shimming shown with the water NMR probe in the magnet used for the previous Harvard electron $g/2$ measurements [90]. However, the first-generation ^{3}He probe is not perfect. T_2^* degrades if the probe is rotated after shimming, which indicates some residual magnetism of the probe itself. This complicates efforts to optimize the field homogeneity that would be experienced by trapped particles in the insert[9]. The probe rotates on screw threads and probe angle is therefore coupled to height, limiting the precision with which rotation issues can be investigated. In addition, some soft- and hard-solder joints within the long capillary are not accessible for proper cleaning, and flux-corroded copper flakes have begun to fall from these joints into the NMR bulb. (Soft-solder flux is difficult to remove without access for mechanical scrubbing, and stainless-steel flux for torch-brazed joints must be boiled for proper removal.)

An improved second-generation probe (Fig. 3.8) was designed and is under construction[10]. Solder and braze joints that were not accessible for proper cleaning have been replaced by conflat and indium-seal flanges; these changes also make the capillary removable and serviceable. Independent vertical[11] and rotary[12] stages decouple

[9] Ultimately, a single trapped particle in the main apparatus must be used to perfect the shimming, but this process is time-consuming. The more shimming can be done with the ^{3}He probe, the better.

[10] Thanks to Marco Dembecki for his work on the new ^{3}He NMR probe.

[11] Manual Positioning Co., Ltd. T125Z-20B, 20 μm accuracy

[12] Edmund Optics 38-195, $\pm$60 arcminute increments

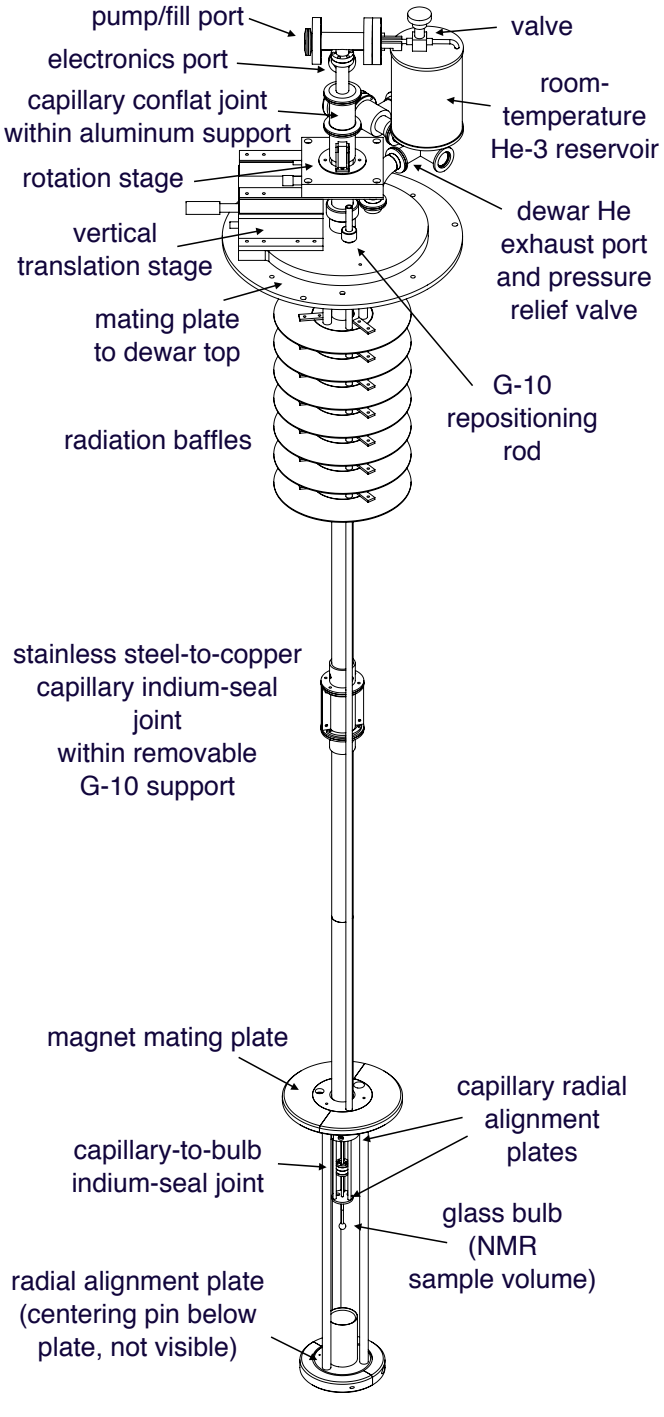

Figure 3.8: New ^{3}He NMR probe design. The probe's height is just under 2 m from dewar top mating plate to radial alignment plate. (Thanks to Marco Dembecki for his work on model featured in this figure.)

height and angle changes to allow precise positioning of the bulb. Rotatable guide plates near the bulb improve its radial alignment without compromising modularity. Optimization of top plate and room-temperature reservoir designs significantly reduce the probe's weight, making handling easier. Electronics near the antenna and bulb were also redesigned to eliminate a connector with a nickel layer, which might have been the cause of the magnetic field inhomogeneity that had been detected on probe rotation. These changes are expected to take the ^{3}He probe from prototype to functional tool in the next $g/2$ measurement.

3.3 Helium Recovery and Control

3.3.1 Helium Reliquefier

The 500 L helium dewar boils off 19±1.5 L of liquid helium per day while the dilution refrigerator is inserted and operating, or 9±1.5 L/day when the experimental insert is not within the dewar [89]. (Also, 24±3 L/day of liquid nitrogen from the surrounding reservoir are also boiled off in both cases.) To reduce this significant helium cost beyond the 50% discount from Harvard's institution-scale helium recycling system, a pulse-tube cryo-refrigerator configured as a helium reliquifier[13] is used to capture and re-liquefy helium gas. Compressors located in a closet in a separate room are connected via 25 m long flexible high-pressure helium lines to a remote motor suspended by rope from the ceiling. The remote motor is connected by 1 m flexible line to the thermally shielded cold head assembly installed over the

[13] Cryomech CP1010 configured as PT-415, 1.5 W cooling power at 4.2 K

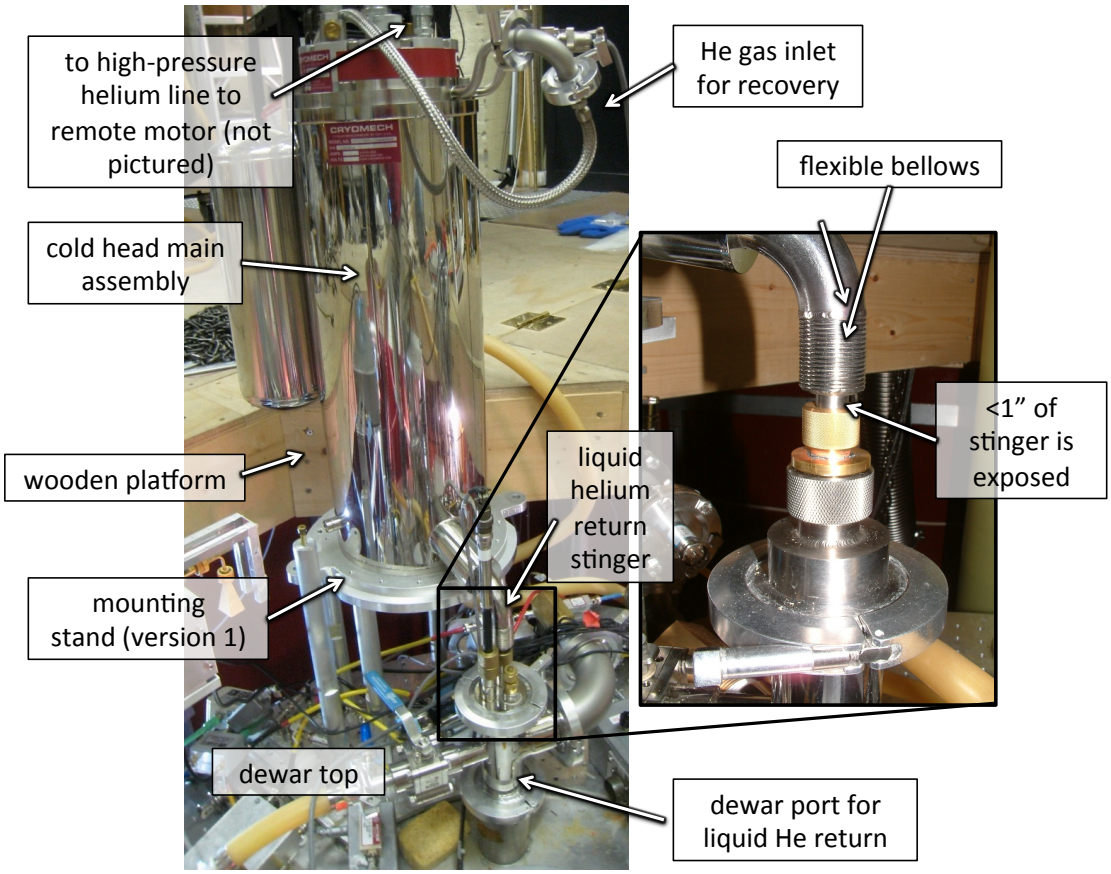

Figure 3.9: "Cold head assembly" portion of the helium reliquefier in place on "mounting stand version 1" on the dewar top. The inset shows the stinger entering the port into the liquid helium dewar just below the section of flexible bellows. "Mounting stand version 1" is discussed in Sec. 3.3.4. Inset photo is adapted from [90].

dewar, shown in Fig. 3.9 [90]. The reliquefier captures boiled-off helium gas from the exhaust ports of the dewar helium reservoir, recondenses the helium on the cold head, and drips it back into the dewar through a vacuum-insulated and radiation-shielded stinger inserted directly the dewar helium space through a port on the dewar top. The dilution refrigerator's 1 K pot sips liquid helium from this same main dewar, comprising about 3 L/day of the 19 L/day total. This exhaust helium from the 1 K pot can also recondensed and returned via the reliquefier, as shown in Fig. 3.10.

This recovery system enormously reduces the amount of liquid helium used by this apparatus. During one 22-day stretch, liquid helium boiloff was reduced to under 0.15 L/day. When care is taken to avoid leaks in the system, the reliquefier does not clog appreciably on a months timescale. When clogging does occur, a thermal cycling and flushing procedure that takes only a few hours is sufficient to restore the reliquifier to full capacity. In-situ heating with tape threaded through the stinger might enable faster de-clogging.

3.3.2 Pressure Control

Good pressure control of the helium gas above a liquid bath around a superconducting magnet has been shown to reduce magnetic field fluctuations [112, 113, 114, 86, 3]. Pressure changes cause temperature changes in the magnet, which affects the magnetic field through the temperature dependence of magnetic susceptibility of materials used in the magnet [113]. Therefore, the pressure in the helium space is kept steady by controlling the rate of helium reliquefication. The current through a 50 Ω resistive heater on the reliquefier's cold head is varied in response to precise pres-

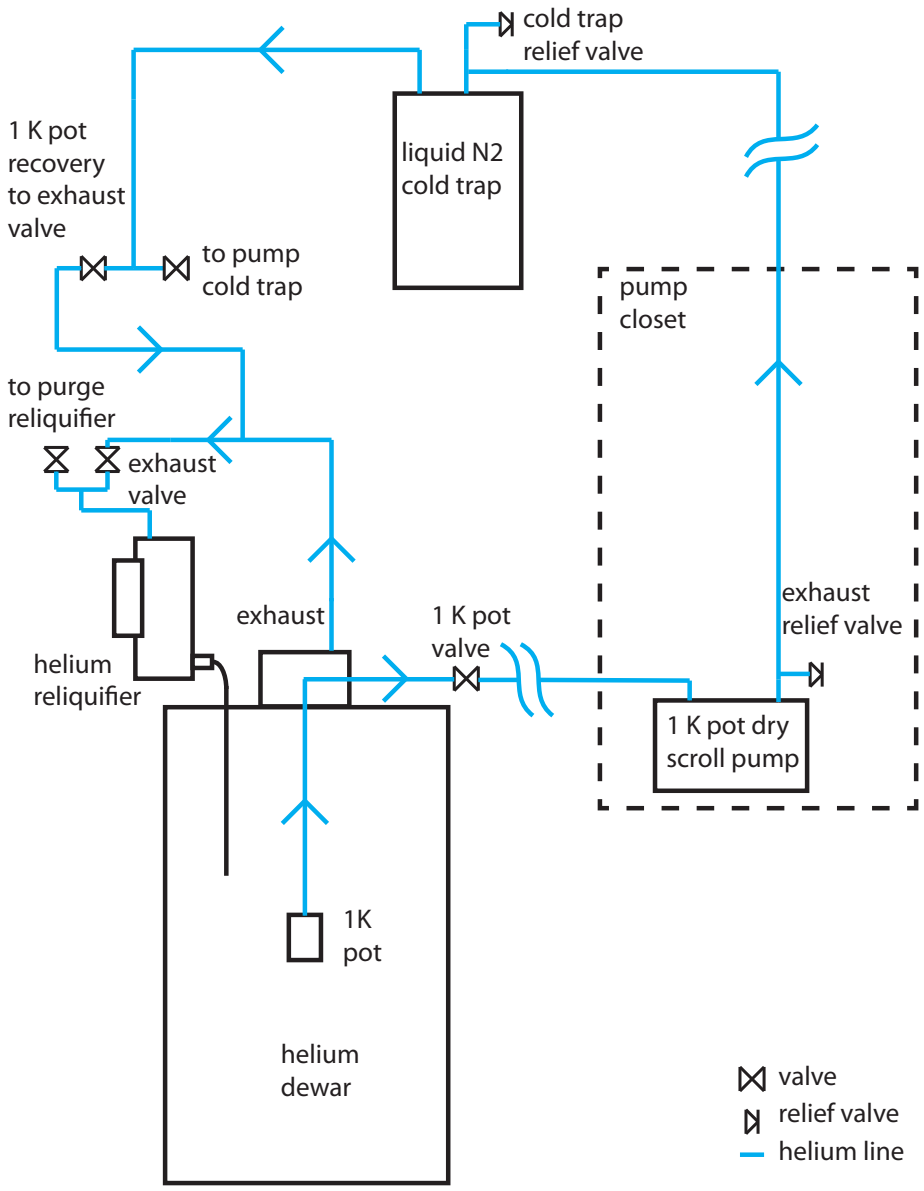

Figure 3.10: Helium gas recovery system including 1 K pot exhaust recovery. From [90].

sure measurements[14]. The cold head temperature is also monitored and heat input adjusted to prevent excursions of the cold head above 8 K, which have been found empirically to increase the rate of clogging. Despite this necessary asymmetry, an otherwise PID[15]-like control algorithm has been found to be sufficient to control pressure to within about a 0.2 mpsi range with only modest tuning efforts (Figure 3.11). This is comparable to or better than the vent-valve based, non-helium-recovering pressure control systems that were shown to reduce magnetic field fluctuations to less than 0.5 ppb in the apparatus used for previous Harvard electron $g/2$ measurements [110, 71]. Under some conditions, thermo-acoustic oscillations can occur, but these can generally be stopped by changing relative helium flow rates through different manual dewar-top valves. A hybrid hardware[16]/software interlock system shuts off the reliquefier's compressor in case of low pressure in the dewar, pressure monitoring failure, or computer failure.

3.3.3 Liquid Helium Level Control

In addition to controlling pressure in the main helium reservoir, it might be desirable to control the liquid helium level around the experimental insert to avoid systematics associated with variations in the temperature of instrumentation wiring. This proposed level control scheme works as follows. The cylindrical sheath that forms the sliding seal around the experimental insert extends downward partway into the liquid helium bath, dividing the helium gas space above it into two separate volumes:

[14]Digiquartz Absolute Pressure Transducer, Paroscientific, Inc, with digitizer built by Harvard Electronic Instrument Design Laboratory.

[15]Proportional-Integral-Derivative

[16]Hardware by Harvard Electronic Instrument Design Laboratory and National Instruments

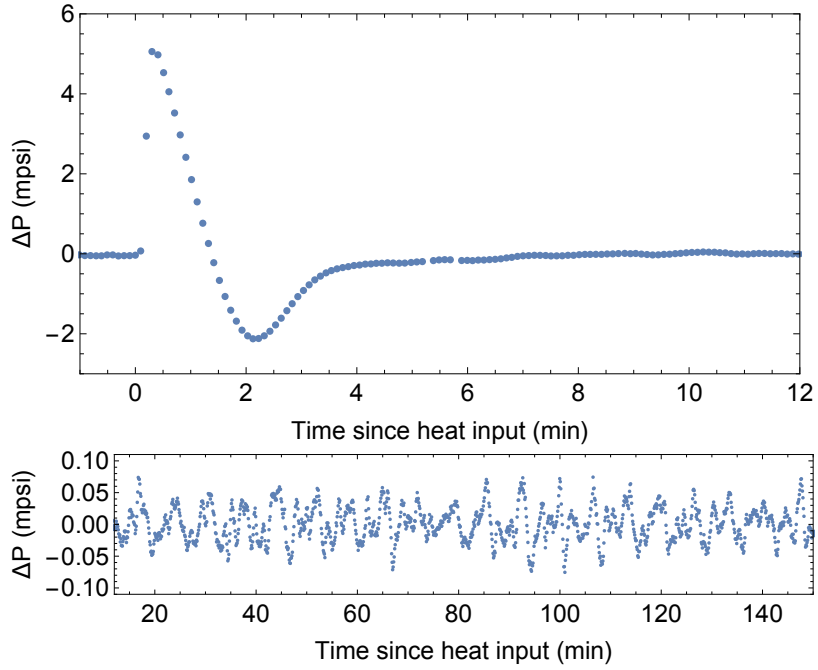

Figure 3.11: Helium gas pressure above the liquid helium bath in the main reservoir is shown during and after a fast heating pulse from a resistive liquid helium level monitor (top) and after the system has returned to close to the set pressure of 16.5 psi (bottom). The pulse lasts about 20 s and it delivers a few tens of J of heat. The pressure control system returns to set pressure within a few minutes and maintains it within a 0.2 mpsi range in the absence of external disturbance (e.g., change of flow rate of dilution refrigerator ^{3}He-^{4}He mixture). Due to clogging issues, 1 K pot exhaust helium was not being recovered when these data were taken.

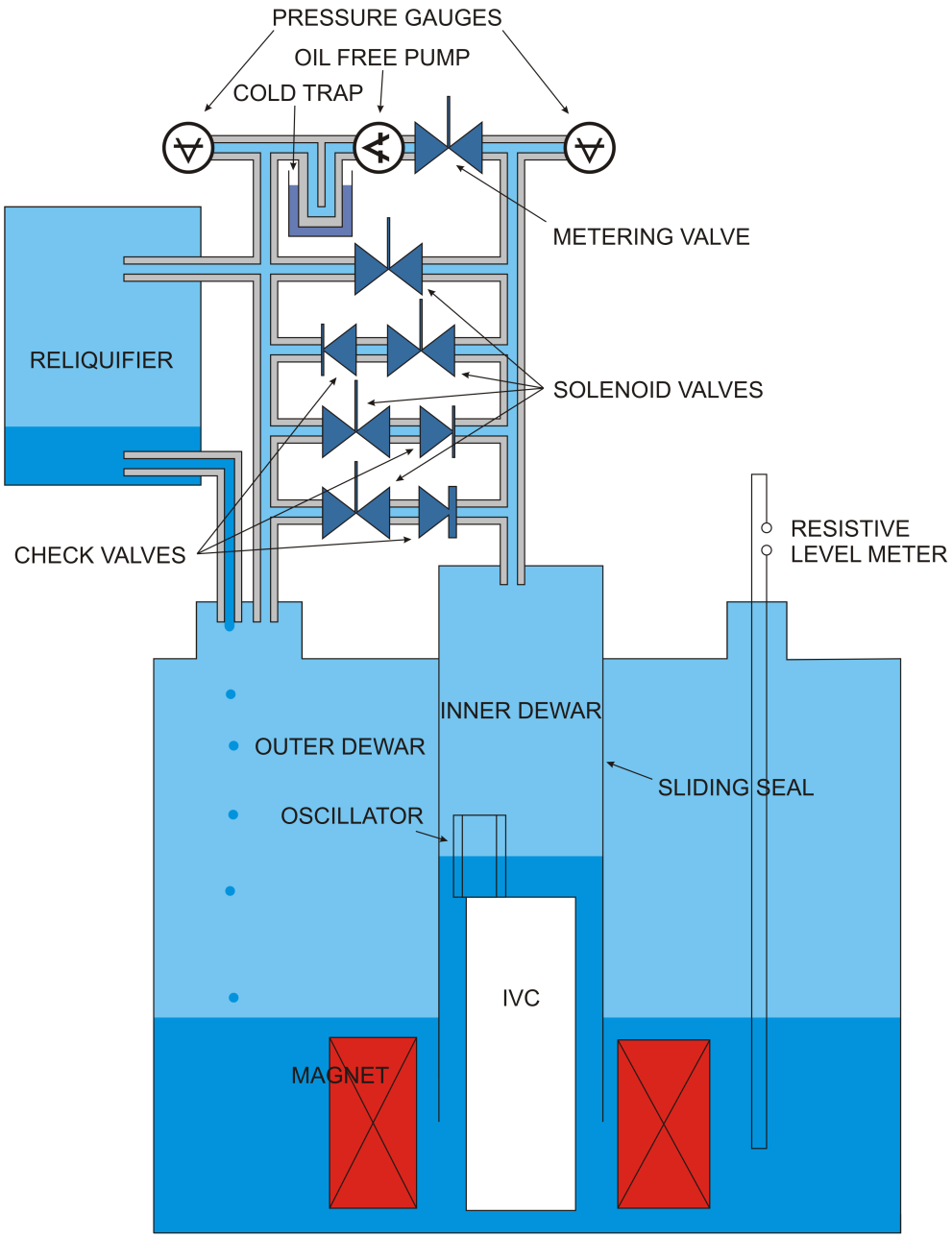

Figure 3.12: Simplified schematic of gas handling system for helium level control, omitting most infrastructure (e.g., that shown in Fig. 3.10.) Helium gas is shown in light blue, liquid helium is dark blue, and the magnet cross section is red. (Thanks to David von Lindenfels for making this figure.)

the "inner" and "outer" gas spaces. In the pressure-control-only scenario described in Sec. 3.3.2, these spaces are manually connected by external tubing to create one large gas space. If they are instead connected by a pump, one volume can be overpressurized compared to the other to change the relative liquid levels in the two spaces, and one of the levels can be controlled by changing pumping speed.

A proof-of-principle demonstration has shown that this level control system works[17]. The level sensor used is a 54 MHz Hartley oscillator[18] installed on the experimental insert just above the top of the IVC; changes in the liquid helium level change the capacitor's capacitance by almost 1 MHz over a 43 mm vertical range. A scroll pump[19] was installed as shown in Fig. 3.12 to pump from the inner to the outer gas space. To raise the liquid helium level in the inner space, a metering valve at the pump's input is opened, lowering perssure in the inner space. To lower the level, the valve is closed; the inner dewar's boiled off helium then raises the pressure in the inner space, while the reliquefier maintains a constant pressure in the outer space. Despite the asymmetry in response to changes in the valve openness, a simple PID-like control structure quickly enabled good control. The helium level can be raised at 11 mm/min or lowered at 1 mm/min. Level control at a setpoint that was demonstrated at the level of 0.3 mm with a first-guess set of PID parameters is expected to improve to 0.1 mm with optimized tuning. Studies of magnetic field stability will need to be done to determine whether this system improves $g/2$ data quality.

[17] Thanks to David von Lindenfels for his work on level control.
[18] Built by undergraduates Tova Holmes and Carl Hoffman.
[19] Edwards XDS35i

3.3.4 Vibrations

Starting in the previous Harvard electron $g/2$ measurement apparatus, the vacuum pumps for the dilution refrigerator were mounted on springs in a separate room 12 m away to isolate the main apparatus from the pumps' vibrations [27]. Though mechanical changes described in Sec. 3.1 should have greatly reduced the susceptibility of the apparatus to disturbance by external vibrations, the strong vibrations created by the reliquefier's pulse-tube cryo-refrigerator, new in this apparatus, are of concern. It is not feasible to separate the apparatus from the reliquifier by a long distance because of the thermal radiation shielding needed for transferring liquid helium to the main helium reservoir.

Vibrations originate in several parts of the reliqufier system. Those from the reliquefier's compressor and the remote motor are transmitted along flexible high-pressure helium lines to the cold head assembly. Along with vibrations originating in the cold head assembly, these can be transmitted to the dewar through the stinger and, depending on the details of the support structure for the cold head assembly, through other mechanical couplings as well. One decoupling mechanism built into the design of the reliquefier is the flexibility of the high-pressure helium lines between the remote motor and the main cold head. Another is a flexible bellows section built into the stinger (Fig. 3.9, inset). Despite these features, vibrations exceeding the magnitude of vibrations measured at the previous $g/2$ apparatus [27] have been detected by measuring surface velocity at the dewar top with a geophone[20] (Fig. 3.13a). In light of this, various strategies to reduce vibration transmission to the

[20]Geospace Geophone GS-11D

apparatus were tested.

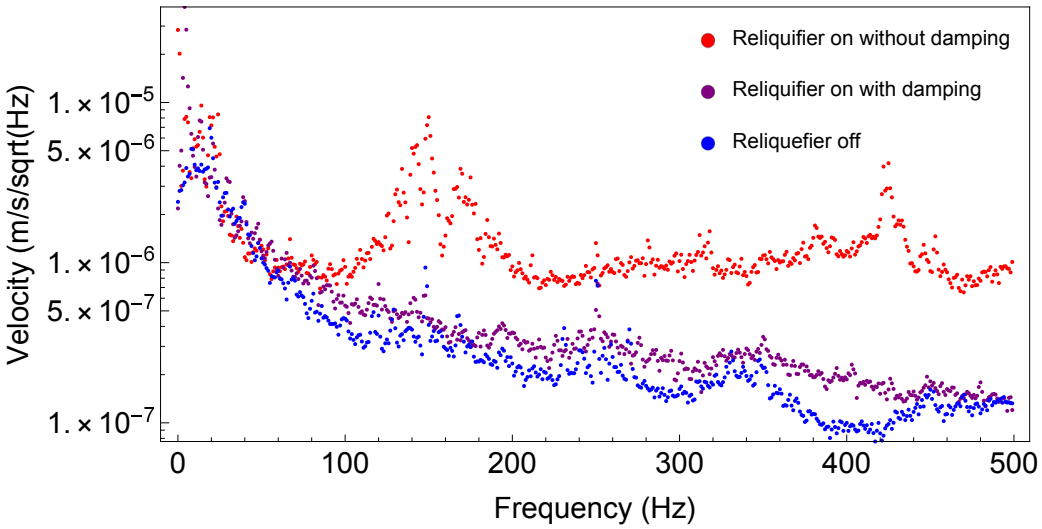

(a) Measurements with a geophone show that vibrations transmitted to the dewar can be reduced significantly by installing rubber "damping mounts" between the cold head assembly and a support stand on the dewar top.

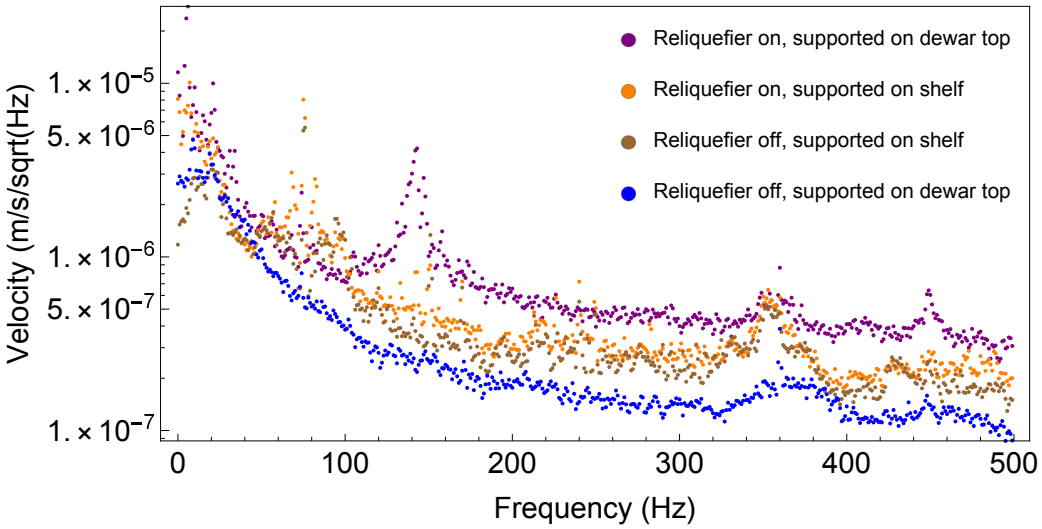

(b) Supporting the reliquefier on the dewar top transmits the most vibrations when the reliquefier is on (purple) but the least when it is off (blue). Mounting the reliquifier on a shelf from the wooden platform reduces vibration transmission when the reliquefier is on (orange) but creates an unwanted coupling to other sources of vibration through the wooden platfrom when the reliquefier is off (brown). Damping mounts are present for all four data sets.

Figure 3.13

When the reliquefier was first installed, it was supported on an aluminum stand sitting directly on top of the experiment dewar (labeled "mounting stand version 1" in Fig. 3.9.) To decouple the cold head assembly from the dewar, rubber vibration-damping mounts[21] were installed between the cold head assembly and its stand. Fig. 3.13a shows the resulting significant reduction in vibration[22].

To further decouple the reliquefier from the dewar (leaving the stinger as the only contact point), a shelf ("mounting stand version 2", Fig 3.14) was built to support the cold head assembly from a nearby wooden platform, which is itself supported by the ground floor of the building, one story above the pit floor on which the experiment dewar rests. The shelf, with damping mounts visible between the shelf and the cold head assembly baseplate, is shown in Fig. 3.14. Fig. 3.13b shows vibration data for both support mechanisms, both with the reliquifier running and with it turned off. When the reliquifier is on and running, the shelf-from-platform system achieves overall lower vibration levels than mounting on the dewar top, as would be expected. However, when the reliquefier is turned off, vibration levels are higher with the shelf-from-platform system. This indicates that the shelf couples in significant additional vibrations from the ground floor of the building.

These methods were somewhat successful in cutting down on transmitted vibrations. Several other methods of vibration control were tried but did not significantly reduce vibration levels at the dewar: up to 30 kg of lead shot was attached to the helium flex line between the remote motor and the cold-head assembly; dashpots were attached between this flex line and an external support; the cold head assembly

[21] KS44-50 from Karman Rubber Company

[22] Thanks to Olivier Simon for his work on vibration reduction.

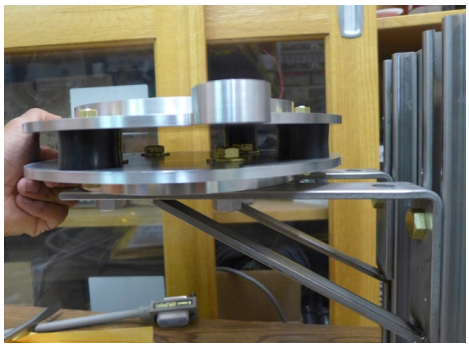

Figure 3.14: "Mounting stand version 2" for mounting the reliquifier cold head main assembly, which replaced the "mounting stand version 1" that was shown in Fig. 3.9. The vertical plate at the right attaches to the wooden platform that was also shown in Fig. 3.9. Black rubber damping mounts are visible between the bottom plate and the upper plate on which the reliquefier cold head assembly rests.

was suspended from the ceiling by latex hose. Significant further improvements to vibration-damping would likely require redesigning the reliquefier's stinger to be extremely flexible, encasing the cold head assembly in an enormous mass (ton-scale in order to effectively address Hz-scale vibrations), supporting the cold-head assembly on an active vibration-damping stage, or, if vibrations cannot be adequately controlled by these methods, supporting the reliquifier on the dewar top as in Figs. 3.9 and 3.13a and turning it off during critical datataking periods.

Though the geophone measurements presented above are useful for comparing vibration control methods, they only probe vibrations on the dewar structure, not at the position of the electron. Direct measurements of the reliquefier's effect on an electron's cyclotron frequency must instead be the final determination of whether the reliquefier can be run during $g/2$ datataking. These attempts at vibration control sound a cautionary note for any potential future $g/2$ apparatus designs incorporating a cryogen-free (and therefore pulse-tube-based) dilution refrigerator. Unless the

changes in electrode/magnet coupling render the apparatus extremely insensitive to vibrations, heroic vibration-damping measures might be needed, or in the worst case, might even be insufficient. It would be wise to carefully collect cyclotron lineshape data with the reliquefier turned on with this apparatus before proceeding with such a design.

3.4 Positron Source

Unlike the previous apparatus, the current-generation apparatus is equipped to measure positron $g/2$. Positrons or electrons can be loaded into the positron accumulation trap from a 6.3 μCi radioactive ^{22}Na source [89, 71]. This is a tiny source, about 77 times weaker than the smallest source previously used for trapping positrons [117]. Conveniently, its activity is below the 10 μCi threshold requiring special licensing and safety precautions for handling; its low activity also makes it less likely to cause the poorly-understood spontaneous electron loading that was observed in a previous apparatus that had a positron source fixed near trap electrodes [89]. The positron source and mechanical lowering system is described here, and the positron loading process and loading rates are covered in Sec. 4.5.1.

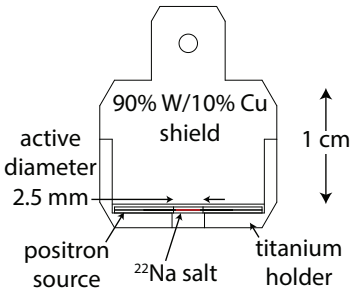

Figure 3.15: Positron source capsule. From [89], adapted from [71].

The positron trapping technique is adapted from methods developed by the ATRAP collaboration for mCi-scale sources [118]. ^{22}Na salt is confined in an electron-beam-welded titanium foil disc which is mounted inside an Elkonite-and-copper capsule shown in Fig. 3.15. During positron loading, the capsule rests on top of the trap can above a 10 μm thick titanium window through which emitted positrons enter the trap can. The positron trapping mechanism (which can also be used to load electrons) is described in Sec. 4.5.1. Though loading of secondary electrons can be blocked quite effectively by applying appropriate electric fields in the positron accumulation trap and transfer electrodes, it is desirable to move the source far from the trap can when it is not being used for loading in order to preserve a truly pristine environment for the precision measurement. Therefore, a system was built to make it possible to retract the positron source capsule far from the trap can and around a bend, shown in Fig. 3.16 [89, 71]. The source capsule is suspended on nylon string attached to a spool at the hat of the experimental insert. The spool is rotated via a rotational vacuum feedthrough to raise and lower the source. Four light-emitting-diode (LED)/photo-diode pairs along the source capsule's path allow verification of its position.

It was a cryogenic engineering challenge to make a path for the source while avoiding line-of-sight holes between different thermal stages; even a 0.8 mm diameter hole at 300 K would emit 200 μW of black-body radiation, consuming the majority of the dilution refrigerator's cooling power. To block this, a set of radiation baffles with offset holes rides on the source suspension line, catches on a slight narrowing of the guide tube at the top of the IVC, and delivers heat from room-temperature

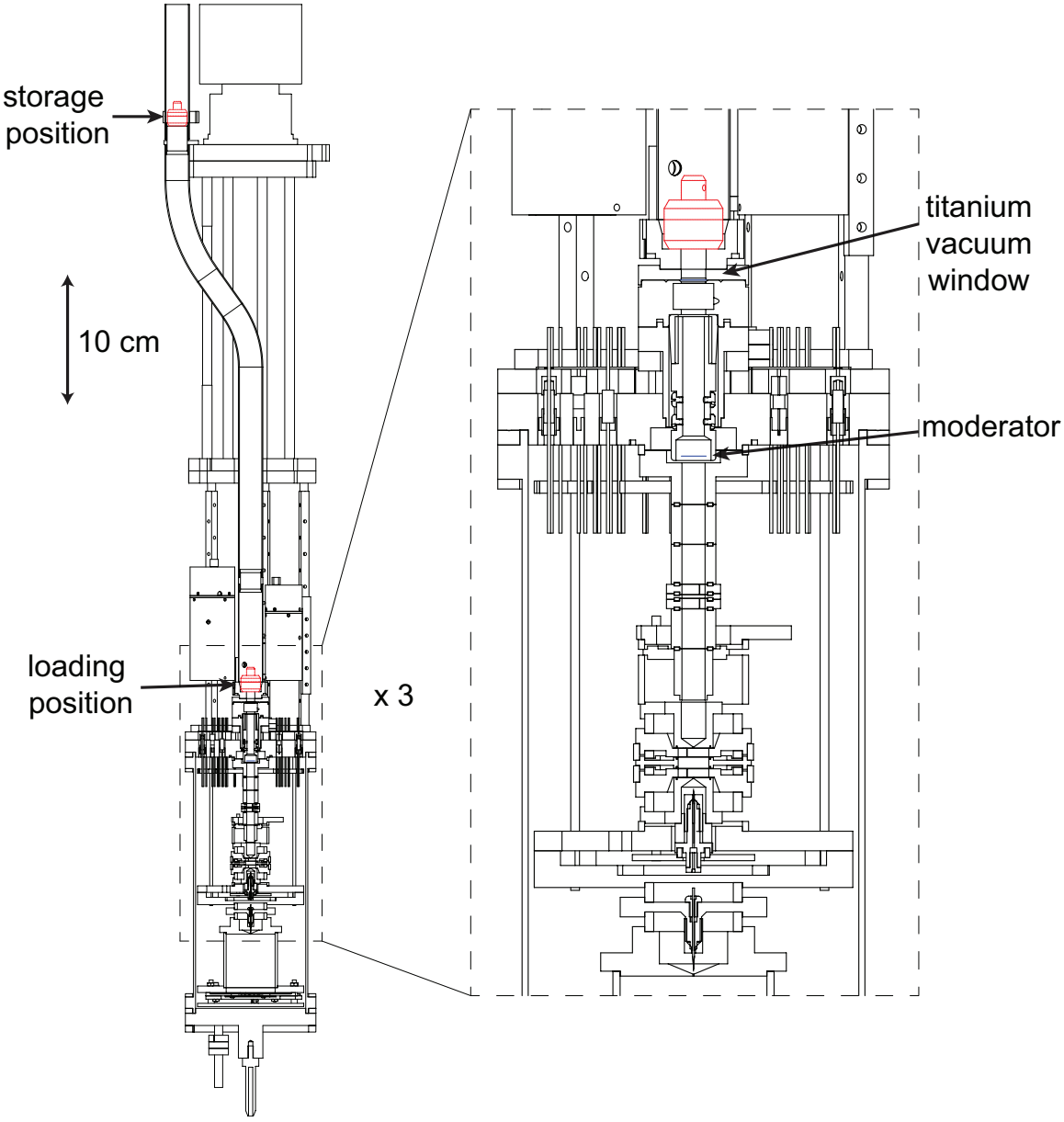

Figure 3.16: Positron source retraction system with source capsule storage and loading positions in red. From [89], adapted from [71].

black-body radiation to the main helium bath at 4 K.

To accommodate this source path, the current-generation dilution refrigerator and magnet bore (12.8 cm magnet bore inner diameter) are wider than those in the previous Harvard electron $g/2$ apparatus (8.6 cm magnet more inner diameter). This widening also creates additional volume within the dilution refrigerator that is needed for the electronics for the loading and planar traps. The dilution refrigerator also has more cooling power (330 μW) than the previous apparatus. This accommodates the increased heat load from the larger-diameter stages and additional electronics, and it improves temperature control of the electrodes to further reduce temperature-dependent magnetic field fluctuations from any residually magnetic materials.

Chapter 4

Trapping, Detecting, and Driving Particles

This chapter describes the electronics and techniques used for axial detection and control of particles in the precision measurement trap and positron accumulation ("loading") trap. Key components of the $g/2$ measurement protocol are discussed, including maintaining extremely stable axial frequencies, controlling a single electron in the precision measurement trap with the self-excited oscillator, sideband cooling particles' magnetron motion, loading of electrons into both traps from the field emission point (FEP), and loading positrons and electrons into the positron accumulation trap from the radioactive source.

A central challenge in developing the current apparatus has been coping with an unexpected conflict between the single-particle detection system, which is crucial for the $g/2$ measurements, and the positron accumulation trap, which is necessary for loading positrons. Sec. 4.2 describes this issue and its resolution. Ch. 7 uses lessons

from this problem to propose a design change that has the potential to improve single-particle detection beyond the standard set by previous electron $g/2$ experiments.

4.1 DC Electrode Biases

Wiring diagrams for the electrodes and amplifiers of the precision measurement trap and the positron accumulation trap, including cold RF and DC components and room-temperature filters mounted on the dilution refrigerator, are shown in Fig. 4.1 and Fig. 4.2. DC biases for electrodes in both traps are set by high-stability power supplies. Each pair of bias wires passes through room-temperature filters, enters the inner vacuum chamber (IVC), and goes through more filters and heatsinks. The choices of power supply and filter configuration for an electrode depend on the stability requirements for that particular electrode.

4.1.1 Power Supplies and Electrode Biasing Configurations

4.1.1.1 Ring electrodes

The axial frequency stability of particles in a Penning trap is primarily determined by the stability of the ring electrode voltage, so the ring voltages in both the precision and positron accumulation traps are set by extremely stable Fluke calibrators[1], followed by RC filters at the mixing chamber with large time constants. Measurements of the electron's axial frequency in the precision measurement trap showed a drift of 82 Hz on 201 MHz over 15 hours [90]. This drift of 5 μV/hr is slow enough to

[1] A Fluke 5270A, with a specified stability of 500 ppb over 24 hours, is used for the precision ring electrode and similar Fluke 5440B is used for the loading ring electrode.

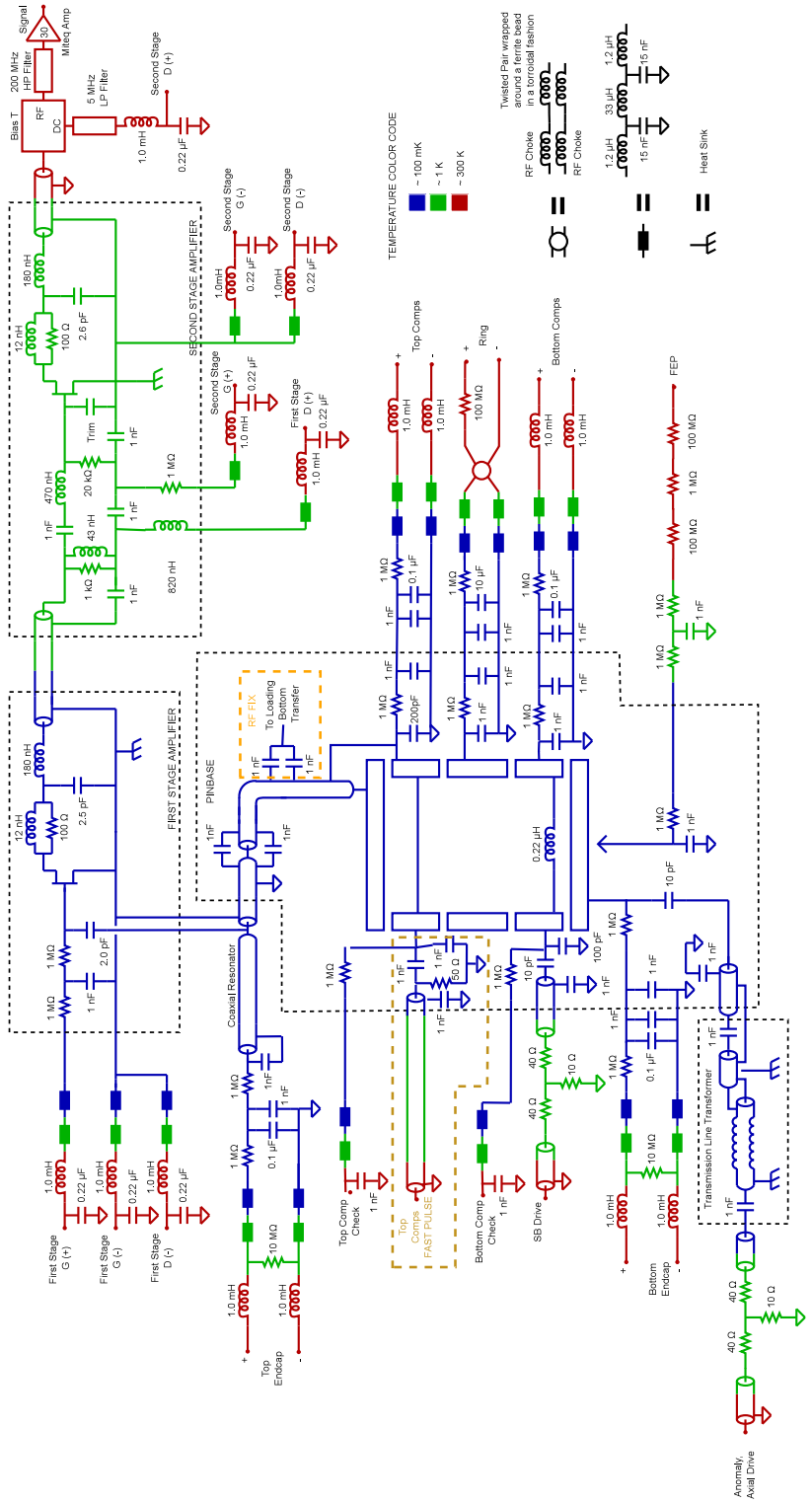

Figure 4.1: Precision measurement trap wiring diagram.

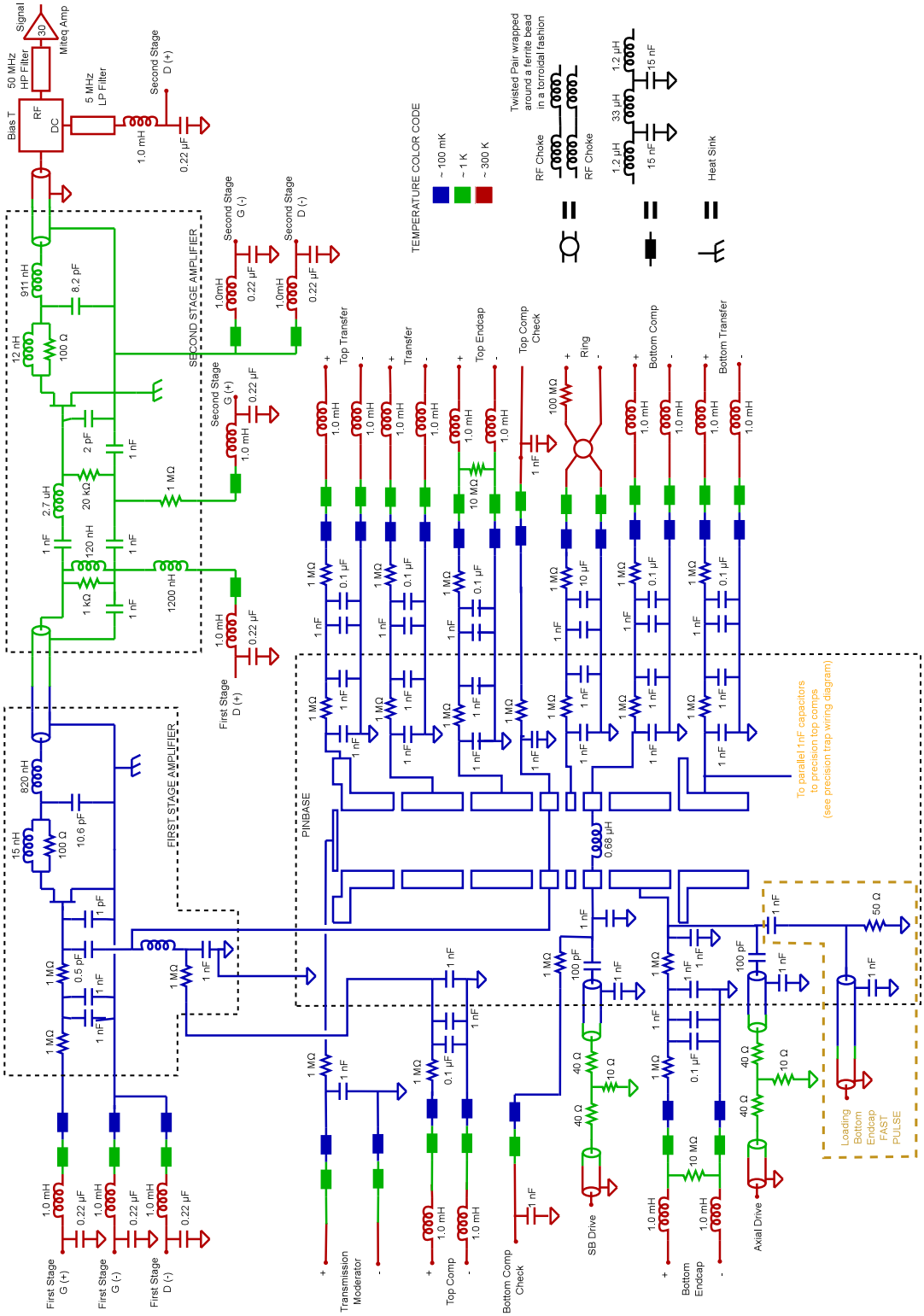

Figure 4.2: Positron accumulation (loading) trap wiring diagram.

be corrected between cyclotron and spin measurements. When a single particle is trapped in the precision trap and its frequency is being continuously monitored with the self-excited oscillator (described in 4.6.4), drifts in axial frequency can be actively corrected by charge-pumping the filter capacitor on the ring bias line with 50 ms pulses from a power supply whose ground is referenced to the non-ground side of the Fluke. The power supply used here is a BiasDAC, a ±10 V floatable supply designed and produced in the Harvard Electronic Instrument Design Laboratory (HEIDL).

4.1.1.2 Precision compensation electrodes

Though the stability requirements for precision compensation electrodes are not as stringent as for ring electrodes [87], the required voltages are larger than those available from BiasDACs and are set in either of two ways. To control the top and bottom compensation electrode voltages separately in the range of voltages necessary for pulsed particle transfer, described in Chapter 6, each is set by a separate Fluke calibrator. When particles are trapped in the potential wells used for detection and compensation electrodes, they only need to be adjusted within a small range for tuning and can be biased together by two BiasDACs stacked on top of the ring's Fluke.

4.1.1.3 Precision endcap electrodes

Precision endcap electrodes can also be biased in various configurations, several of which are shown in Fig. 4.3. For normal operation during a measurement, their 0 V biases are set by cold 10 MΩ resistors connected to pinbase ground. Endcaps can be biased antisymmetrically to offset particles axially in the trap for systematic

studies of trap cavity modes (see Chapter 5) [27]. To dump electrons (positrons), they are biased to $+(-)200$ V. Dumping could also be accomplished by reversing the potential on the ring electrode, but hysteresis in the large filter capacitors on the ring electrode line would cause nonreproducibility in axial frequency at a given ring voltage and require re-tuning of the trap harmonicity after each dump. Symmetric biases can be applied to the endcaps to quickly change the axial frequency of trapped particles without being affected by this hysteresis in the ring voltage.

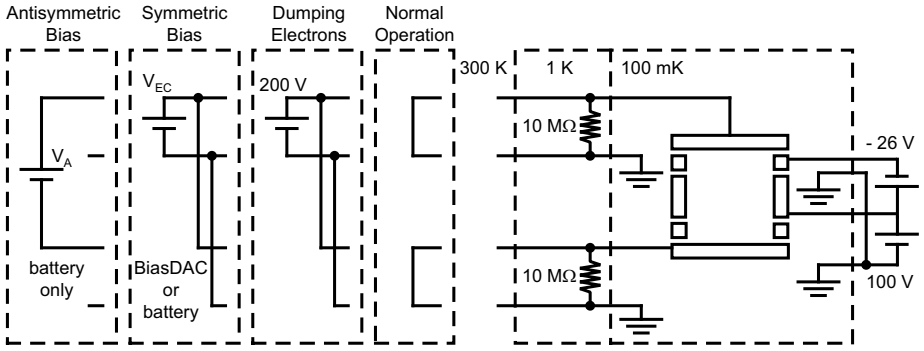

Figure 4.3: Precision endcap biasing configurations. From [27].

Remaining electrodes are set by DecaDACs, a multi-channel HEIDL product that is similar to a BiasDAC except for being explicitly ground-referenced (not "floatable"/"stackable"). For pulsed particle transfer, DecaDACs bias all electrodes except the precision ring and compensation electrodes.

4.1.2 Filtering, Vacuum Feedthroughs, and Cold Wiring

Each bias is carried from the power supply to the experiment on a twisted pair of wires. DC biases for cold amplifiers, most electrode voltages, temperature sensors, heaters, and LED/photodiode pairs go to one of four similar filter boxes, each of which connects through a home-made shielded cable to a 32-pin Fischer vacuum

instrumentation feedthrough[2]. In addition to maintaining vacuum, it is critical that these connectors have good leakage resistance characteristics, preserving the TΩ-scale resistances needed to prevent particle frequency drifts. High-stability ring and planar trap electrode biases and field-emission-point biases enter through separate filter boxes mounted directly on the insert of the dilution refrigerator ("fridge"). More details about filtering are in [90].

All DC lines are teflon-coated low-thermal-conductivity 0.003" diameter constantan wire from room temperature to the 1K pot stage and between all subsequent stages of the fridge. Constantan wires are wrapped around and epoxied to gold-plated copper heatsink bobbins at the 4 K plate, 1K pot, still, intermediate cold plate, and mixing chamber stages. At the 1K pot and at the mixing chamber, lines pass through LC filters on PCB boards.

At the mixing chamber, electrode biases pass through low-pass RC filters with time constants of 0.1 s for most lines and 10 s for high-stability ring and planar trap lines, utilizing large 0.1-10 μF polypropylene capacitors. Ground lines are soldered to a copper-clad teflon ground plane mounted on top of the vacuum feedthrough pinbase that forms the top of the trap vacuum can. Bias lines are soldered to feedthrough pins with the assignments shown in Fig. 4.4. Bias lines are also connected to the ground plane with 1 nF capacitors to short out undesirable RF paths to ground. Inside the trap can, low-inductance 3 mm wide silver straps, visible in Fig. 4.9d, carry the biases to the electrodes.

[2]These had a high vacuum failure rate and replacements provided by Fischer had an even higher failure rate than the originals provided by the dilution refrigerator. It is recommended that alternatives be found for future designs.

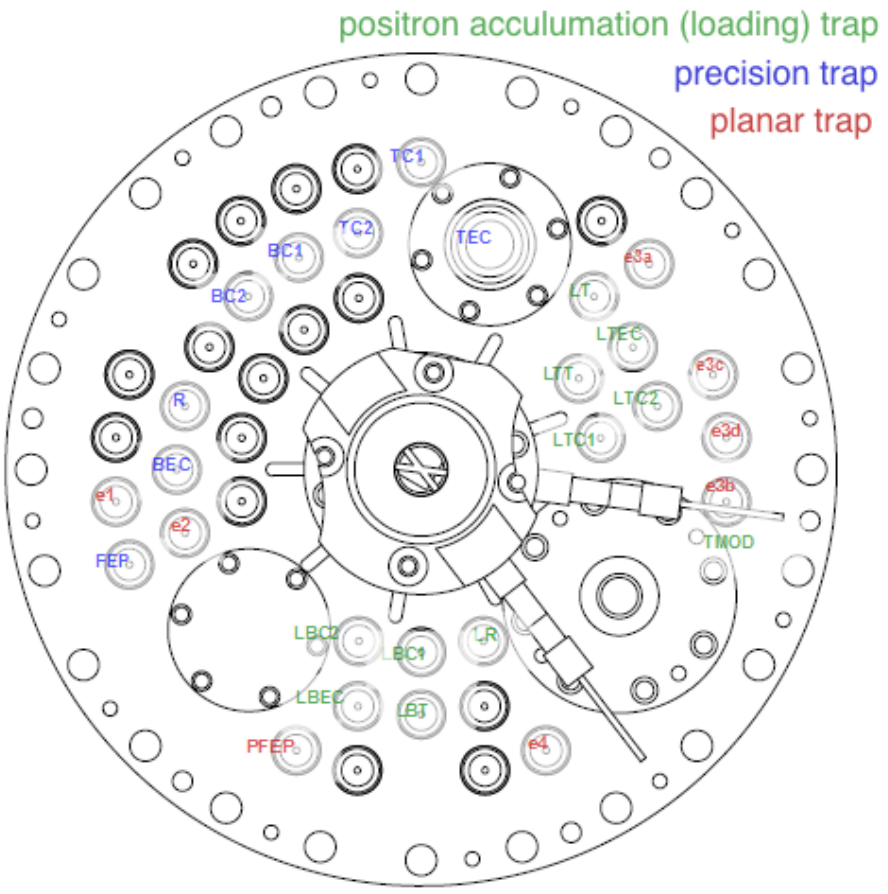

Figure 4.4: Map of electrode bias assignments to feedthrough pins on the pinbase, with electrodes identified by acronyms.

4.2 RF Detection: First Stage

In each trap, an electron or positron's axial motion is detected by coupling to a tuned circuit, hereafter referred to as the resonator, that forms the input to two stages of cryogenic amplification.

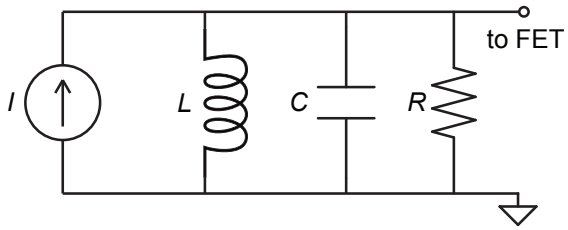

Figure 4.5: Effective circuit of the resonant input stage to the first-stage amplifier. From [90].

As the particle oscillates axially, it drives a tiny image current I in the nearby electrodes that is proportional to its velocity $\dot{z}$,

$$I = \frac{ec_1}{2z_0}\dot{z} \qquad [105], \tag{4.1}$$

where c_1 is a dimensionless constant of order one that is set by electrode geometry. An inductor L is placed in parallel with the capacitance C between trap electrodes, with its value chosen to create a real impedance R on resonance at the particle's axial frequency. This impedance is related to L, C, and the tuned circuit's quality factor Q by

$$R = \frac{Q}{\omega_z C} = Q\omega_z L. \tag{4.2}$$

The image current through this real impedance damps at a rate of

$$\gamma_z = \left(\frac{ec_1}{2z_0}\right)^2 \frac{R}{m}. \tag{4.3}$$

The voltage drop across the inductor and capacitor oscillates at the particle's axial frequency:

$$V = IR = \frac{ec_1}{2z_0}\dot{z}Q\omega_z L. \tag{4.4}$$

After the resonator, the signal is AC-coupled into a home-made cryogenic amplifier through a capacitive divider, as shown in Fig. 4.6. The divider reduces coupling between the resonator and input resistance of the amplifier's transistor. This limits the losses from loading by the transistor's input impedance to preserve high Q in the resonator.

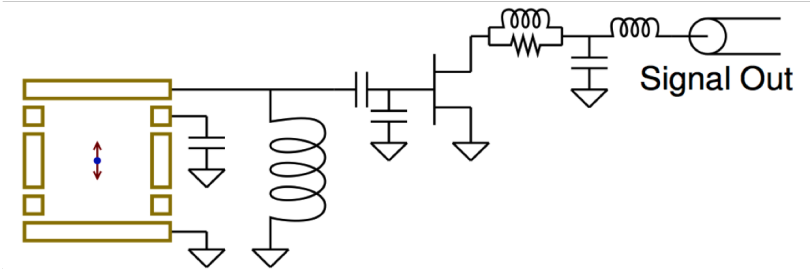

Figure 4.6: Schematic of resonant input stage and first-stage amplifier. Adapted from [108].

Within this basic framework, design details are different for resonators tuned to different axial frequencies in the two traps. In the positron accumulation trap, the 52 MHz frequency is low enough that a hand-wound coil can provide the L in the resonator. The detection electrode is connected with a silver strap to a standard vacuum feedthrough pin. The end of the feedthrough pin outside the trap can is connected to a lead into a custom metal enclosure—the 'amplifier can"—containing the coil and amplifier. The signal is divided down by "tapping down" on the coil: extracting the signal partway from the grounded end of the resonator to the signal end. The positron accumulation coil and amplifier are shown in Fig. 4.7.

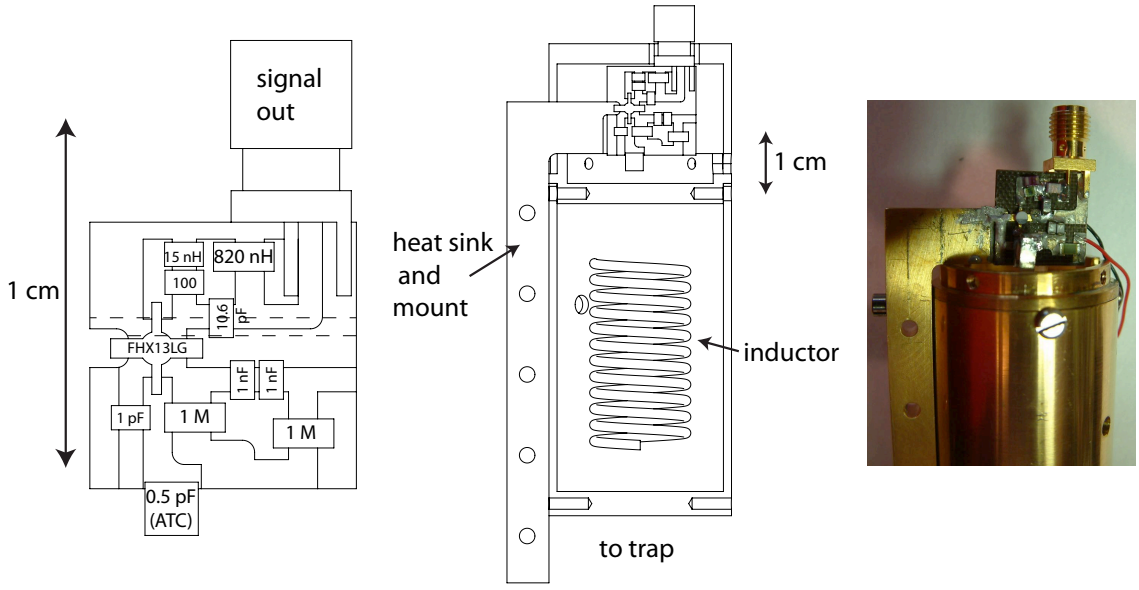

Figure 4.7: Amplifier circuit board layout, amplifier can cutaway view, and photograph of the first-stage amplifier for the positron accumulation trap. From [71].

Coil-type resonators for frequencies around 60 MHz have long been a standard tool in Penning trap experiments, but beginning in the 2006 Harvard electron $g/2$ measurement [86] (details in [110] and [108]) and continuing in the best measurement [3] (details in [4] and [27]), the precision measurement trap's axial frequency was increased to 200 MHz. This increases signal size, as shown in Eq. 4.4, and reduces the width of the cyclotron lineshape, as shown in Eq. 2.23, as well as reducing the power required to drive the anomaly transition and the size of the axial frequency shift in response to a cyclotron or spin transition [108, 27]. To achieve the higher 200 MHz axial frequency, LC must be reduced, and the combined inductance of a silver strap inside the trap can and a coil inside the amplifier can is prohibitively high. Instead, a length of home-made coaxial resonator plays the dual role of providing L while also carrying the signal out of the trap can via a custom coaxial vacuum feedthrough to

the input of the amplifier. This setup is shown for the previous Harvard electron $g/2$ apparatus in Fig. 4.8 and for the current apparatus in Fig. 4.9.

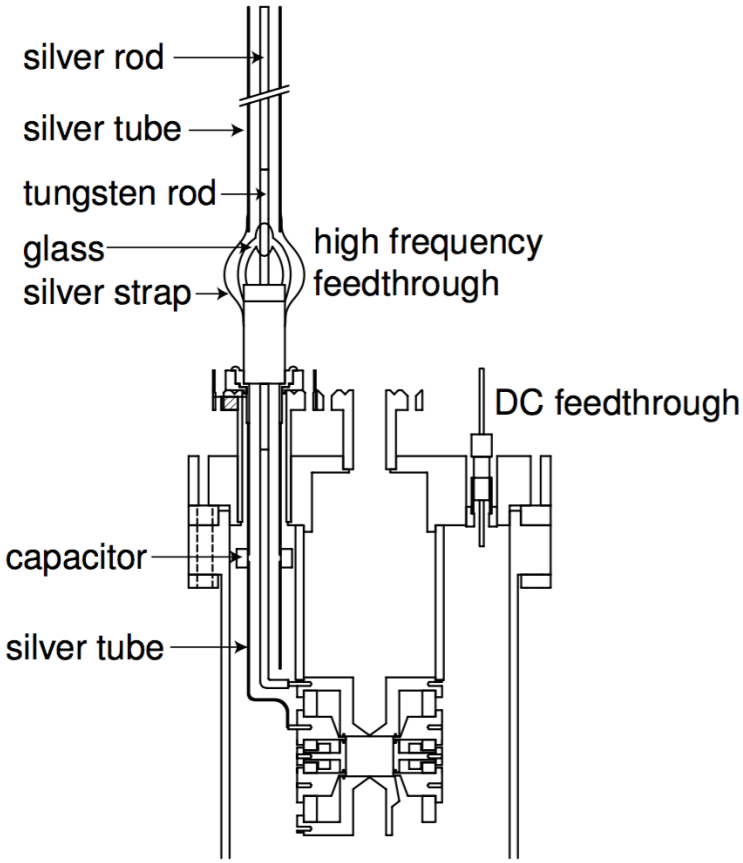

Figure 4.8: Cross section of the precision trap and 200 MHz resonator in the previous apparatus. From [108]. Compare to the relative positions of the trap and pinbase in the present apparatus (Fig. 4.9); proportionally less of 200 MHz feedthrough was inside the trap can in this earlier apparatus. See further discussion in Sec. 4.2.3.

The inner and outer conductors of the 0.25" diameter coax are separated by small teflon spacers to allow most of the inner volume of the resonator to be vacuum. The vacuum feedthrough has a copper outer conductor and a tungsten inner conductor connected by a glass-to-metal vacuum seal. The inner conductor is extended by

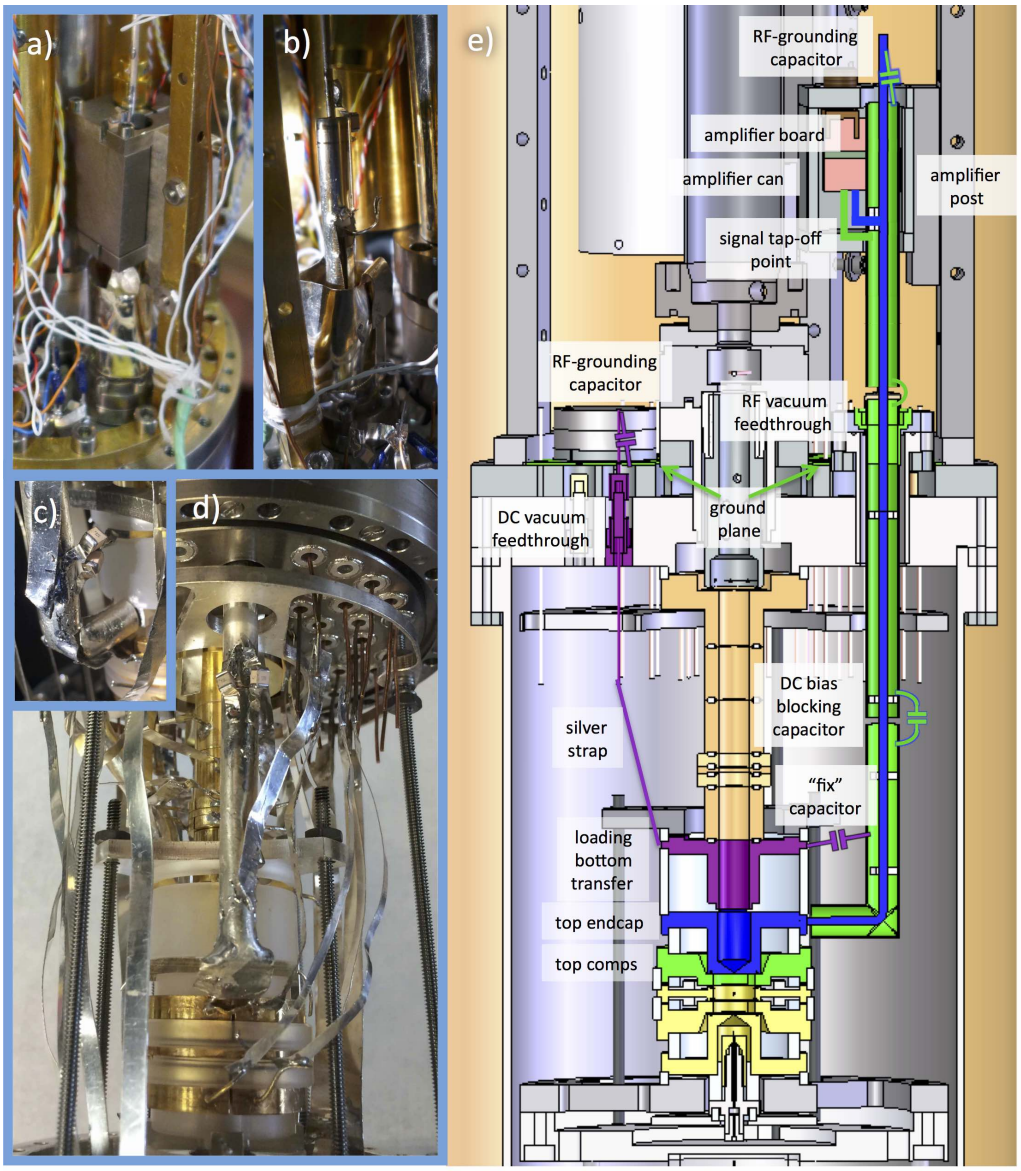

Figure 4.9: Pictures and cross section of the precision first stage 200 MHz resonator and amplifier. a) Amplifier can. b) Top portion of coax exposed before installation of amplifier can. c) Closeup of "L" at the bottom of coax length, with connection between coax and endcap and compensation electrodes. Capacitors to loading bottom transfer electrode are also visible. d) Portion of the resonator that is inside the trap can. e) Cross section with annotations.

lengths of silver wire attached to the tungsten section by torch-brazing. The outer conductor of the feedthrough is oven-soldered to a silver plug, which is e-beam welded to a titanium flange that mates to the trap can pinbase via an indium seal. The entire outer conductor of the resonator is RF-grounded, but the silver tube forming the remainder of the outer conductor is broken and rejoined by capacitors inside the trap can to allow the precision top compensation electrode to be DC-biased by a connection through a separate feedthrough pin. The length of the coax is chosen to be about a quarter-wavelength so that it presents an inductive load, allowing it to play the same role as a coil would in tuning out the trap capacitance and establishing the 200 MHz resonance. The signal is tapped off about 10% of of the way from the grounded end to the electrode end. The precision first-stage resonator and amplifier are shown in Fig. 4.10[3].

The first stage amplifier for each particle trap consists of a Field Effect Transistor (FET)[4] followed by a suppression circuit to create loss and prevent oscillation in the GHz frequency range and then an L-network to match the output to 50 Ω cable. To avoid positive feedback and regeneration, the center frequency of the output network is tuned slightly higher than the frequency of the input resonator [108]. The amplifier's mounting is designed to maximize the conductance of the thermal path to the mixing chamber and its cooling power; this is critical to enable the amplifier to cool quickly, reducing a single particle's axial amplitude and therefore its cyclotron and anomaly linewidths for a $g/2$ measurement. The amplifier is mounted to a silver post to which the source lead of the FET is directly soldered, using a special low-melting-point

[3]Thanks to Ronald Alexander for his work on constructing and testing 1st and 2nd stage amplifiers.

[4]Fujitsu FHX13LG High Electron Mobility Transistor

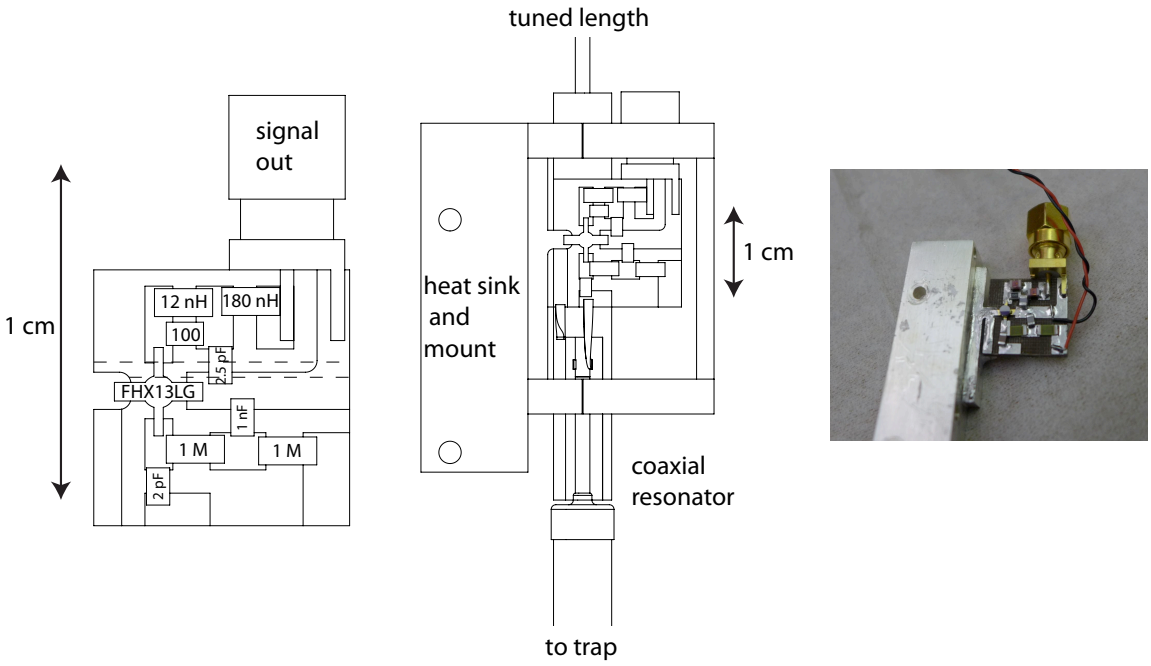

Figure 4.10: Amplifier circuit board layout, amplifier can cutaway view, and photograph of the first-stage amplifier for the precision measurement trap. From [90], adapted from [71].

indium-tin solder to avoid overheating the FET. DC biases for the FET's gate and drain are provided by BiasDACs and the similar BabyDACs.

4.2.1 Dissipation in First-Stage Resonators

As described in Eq. 4.4, the electron's axial signal is proportional to the quality factor Q of the resonant circuit that forms the input to the first-stage amplifier. Having sufficient axial signal is critical for detecting cyclotron transitions before decay back to the ground state. It is therefore important to understand and maximize the resonator's effective parallel resistance, $R = Q\omega L$, and thus both Q and L.

Quality factor Q is proportional to the ratio of stored energy in the resonator to energy lost per cycle. It is lowered by any dissipation. It is possible to determine Q of the resonator by fitting the resonator's response to a Lorentzian with amplitude A, width γ, and center frequency ν_0 as fit parameters:

$$V(\nu) \propto A\left(\frac{\gamma}{(\nu-\nu_0)^2+\gamma^2}\right), \tag{4.5}$$

then extracting Q from

$$Q = \frac{\nu_0}{2\gamma}. \tag{4.6}$$

Q for the 200 MHz resonator in the previous Harvard electron $g/2$ apparatus was 250 at room temperature and 600 at 4 K, where conductivities of silver and copper are higher [108]. In the current-generation apparatus, there was a period during which Q was significantly lower. Investigations conducted to understand and solve this problem are described in Secs. 4.2.2 and 4.2.3. These studies, along with concurrent studies done for lower-frequency amplifiers for the proton and antiproton magnetic

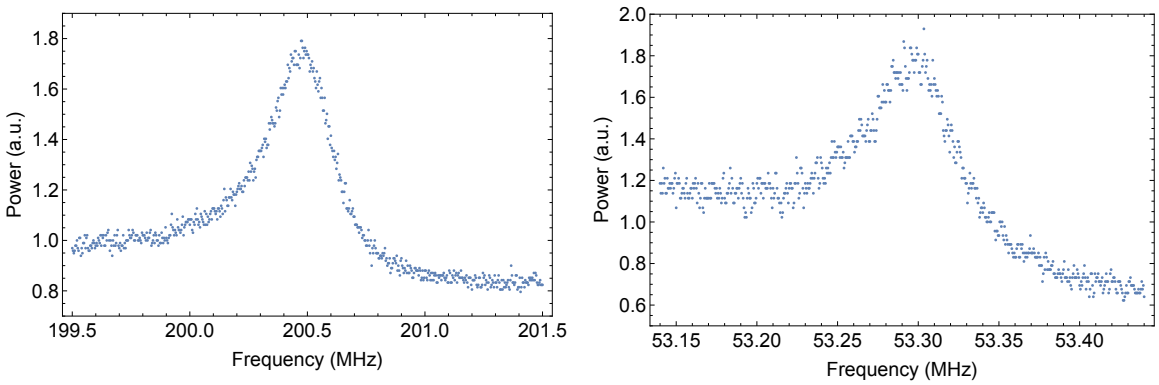

Figure 4.11: First-stage noise resonances at 4 K for the precision, left, and positron accumulation, right, traps. Adapted from [90].

moment experiments [119], have given a better understanding of sources of dissipation in these first-stage detection circuits.

4.2.2 Characterizing First-Stage Resonators

In the absence of a particle in the trap, the root-mean-square voltage due to Johnson noise across the real impedance R of the resonator in frequency bandwidth $\Delta\nu$ is

$$V = \sqrt{4k_B T(\Delta\nu)R}. \tag{4.7}$$

Fig. 4.11 shows the noise resonance as seen through the full detection chain.

It had been standard practice to use this noise resonance to measure Q as a tool for room-temperature amplifier troubleshooting. However, it was found that when the IVC was disassembled to expose the amplifiers and the IVC's function as a Faraday cage thereby lost, RF noise entering in later parts of the detection chain made this measurement method inaccurate. Reassembling the IVC to check Q after each change was too time-consuming to allow troubleshooting at a reasonable speed. Therefore,

a separate, lightweight aluminum Faraday cage that could be quickly assembled was constructed, which made room-temperature Q characterization by noise resonance useful again.

Another method of characterizing the resonator's Q is to inject a known signal on a different trap electrode, rather than relying on Johnson noise to drive the amplifier. This has the benefit of being affected less by external noise (particularly a problem with the experiment open at room temperature) and by the noise floors of later stages of amplification (a concern when the resonator is at 100 mK, when the Johnson noise voltage is reduced by a factor of 50 compared to room temperature.) The size of the injected signal must be carefully adjusted to not saturate any later stage of amplification, mixing, detection, etc. This driven method gives the most consistent results.

The two Q characterization methods just described use the first-stage amplifier. By using an alternative method of coupling to the resonator—magnetic coupling—information can be gained about whether the amplifier is loading down the circuit. The challenge in this lies in finding an alternative coupling method that does not itself load down the circuit. One method that proved to be useful was coupling through a simple antenna connected to a network analyzer. Several of the antenna designs used are shown in Fig. 4.12.

For the magnetic coupling method, an antenna is attached via a 50 Ω cable to a 50 Ω port on the network analyzer. The network analyzer is calibrated to compensate for the antenna's impedance profile, then set to sweep its output and detection through a range of frequencies. At each frequency, the signal is broadcast by the antenna,

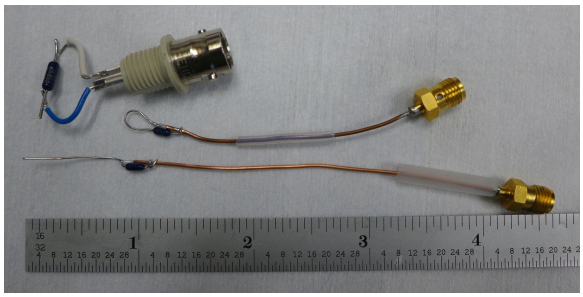

Figure 4.12: Antennas used for probing the resonator directly with a network analyzer. Copper-colored cables are microcoaxial 50 Ω cable. Each through-hole resistor is 50 Ω.

interacts with the resonant circuit, is picked back up by the same antenna, and is detected by the network analyzer. Coupling strength between the antenna and the resonator can be controlled by changing the orientation of the antenna and its distance to different parts of the resonator circuit.

This method proved to have significant drawbacks. With a strong couping, the antenna couples the 50 Ω network analyzer output/input too strongly to the resonator and loads it down, decreasing Q beyond loads already present in the system and masking differences between different system configurations, as shown in Fig. 4.13. With the antenna far enough away, signal-to-noise degrades, and fluctuations in ambient noise make it difficult to average long enough to produce a consistent Q measurement.

Despite these flaws, the antenna coupling method made it possible to exclude the amplifier as the cause of the 200 MHz resonator Q issues. This method also has the advantage of coupling in a relatively frequency-independent way in compared to our standard amplifiers, with which good impedance matching is limited to a narrow frequency range around the expected resonance. This frequency independence enabled

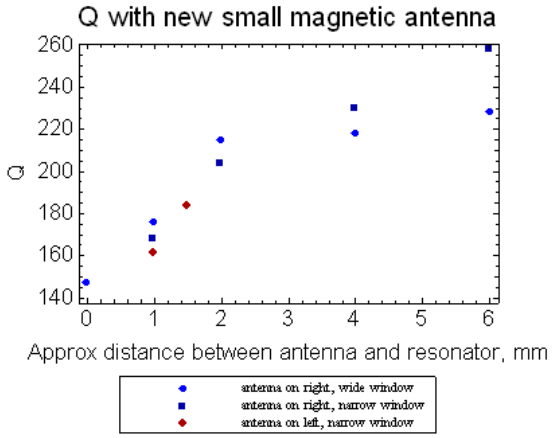

Figure 4.13: Measured Q of the precision first stage resonator using antenna placed at different positions and distances from a test resonator.

the discovery of unexpected additional resonances, a clue which hinted at the primary cause of the Q problem in the precision first stage resonator.

4.2.3 Understanding and Compensating for the Effect of the Positron Accumulation Trap

The degradation of the Q of the precision 200 MHz resonator became apparent around the time the positron accumulation trap was installed. Measurements on this apparatus at 4 K before the positron accumulation trap was installed had shown a Q of around 600, similar to the previous Harvard electron $g/2$ apparatus. New measurements were difficult to do because of the difficulty of deconvolving the characteristics of the very wide noise resonance from the effects of other frequency-dependent elements of the detection chain, but Q appeared to be 100 or lower. It was initially suspected that something had been broken during the handling of the pinbase and trap during routine maintenance or the dis-assembly and re-assembly of the trap elec-

trode stack that was required for the installation of the positron accumulation trap. The coaxial resonator, coaxial vacuum feedthrough, and amplifier were replaced, paying extremely careful attention to soldering technique and cleanliness, but it did not resolve the problem.

It was not clear whether the issue originated in the trap electrodes, the resonator's length of tuned coax, the coaxial vacuum feedthrough, the amplifier, or coupling to the amplifier can or something else nearby in the experiment. To disambiguate between these possibilities, a variety of test systems were constructed that omitted or altered one or more of these elements. All benchtop test systems indicated that Q in the system as designed should be adequate, including a test system that included an amplifier, coaxial resonator with feedthrough, and a ceramic capacitor playing the role of the trap electrodes. This suggested that the problem was related to elements present only on the experimental insert: the electrode stack, the pinbase, or the amplifier can.

To separate the effects of the amplifier and 200 MHz vacuum feedthrough from other effects, a test setup was constructed on the experimental insert in which a length of coax was mounted pointing horizontally outward from the trap electrodes rather than upward through the pinbase, and an antenna was used to couple to the system rather than looking through two stages of amplifiers. Not only did the primary resonance still look wide, but several other low-Q resonances were present within an 30 MHz range; before, they had been obscured by bad impedance matching of the amplifier output far from the center frequency. One by one the electrodes were disconnected from the the silver straps connecting them to the vacuum feedthrough

pins and the 1 nF grounding capacitors at the ground plane. As they were removed, the extra resonances began to disappear. Once all DC lines were disconnected except those for the top endcap (connected to the resonator inner conductor) and the top compensation electrodes (connected to the resonator outer conductor), only a single high-Q resonance was present. This made it clear that lossy RF paths through DC biasing straps were the primary culprit in lowering Q.

It is likely that this same mechanism also limited Q in the previous Harvard electron $g/2$ apparatus; however, the losses are worse in the current apparatus because of the additional electrodes in the new positron accumulation trap (compare Figs. 4.8 and 4.9). While the quarter-wavelength length of coax and the capacitance between the top endcap and top compensation electrode comprise the main current path in the 200 MHz resonator, capacitive coupling to other electrodes also affects the circuit. Fig. 4.14 shows the circuitry surrounding the resonator in more detail than Fig. 4.1 or Fig. 4.2, including some parasitic elements. Ideally, the vast majority of RF current in the resonator would follow a single path, shown as a green dashed line, with a tiny portion of current flowing toward the amplifier to carry the signal. In reality, there are pF-scale capacitances between all neighboring electrodes, shown in red, which couple them to the resonator. The straps connecting these electrodes to their DC-biasing feedthrough pins, and then the 1 nF grounding capacitors to the ground plane at the pinbase, then provide alternative paths to ground, shown as red dashed lines. There are also other lossy paths available, which might also be contributing to compromised Q. The outer conductor of the 200 MHz resonator is also connected to pinbase ground at its vacuum feedthrough, through a solder joint, a titanium flange, and an indium

seal. Finally, there is an RF ground path through the bolted connection between the first stage amplifier post and the tripod that could also be lossy.

These paths seem to be in an unfortunate middle ground of impedance and lossiness. They are not sufficiently high-impedance that they act as harmless open circuits, with no current flowing through them and therefore no added loss. Neither are they so low-impedance that they do not contain loss-causing resistances. Instead, they are low-impedance enough that some current flows though them and unintentional resistive components dissipate energy, lowering Q. Though only the precision top endcap, precision top compensation, and loading bottom transfer electrodes are pictured in Fig. 4.14, other electrodes also are coupled to this system through few-pF scale capacitances. This creates a complex RF environment with additional resonances and a shifted and lower-Q primary 200 MHz resonance, shown in Fig. 4.15. Because many of the "components" of this system are parasitic, distributed, and unintentional, it is extremely difficult to model the circuit exactly.

The lowest electrode in the positron accumulation/transfer stack—the loading bottom transfer (LBT) electrode—had the strongest effect on Q. Fortunately, this made it possible to remove the leading contributor of complexity and improve Q by providing a low-loss RF path (shown as a purple dashed line in Fig. 4.14 and within the orange box in 4.1) from the LBT electrode to the coax outer conductor, thereby shorting out the lossy path. As shown in Fig. 4.15, using a pair of 1 nF capacitors (doubled up as insurance against the possibility of damage on thermal cycling) to short the loading bottom transfer electrode to the length of tuned coax in the resonator simplifies the complicated set of resonances to a single large, narrow

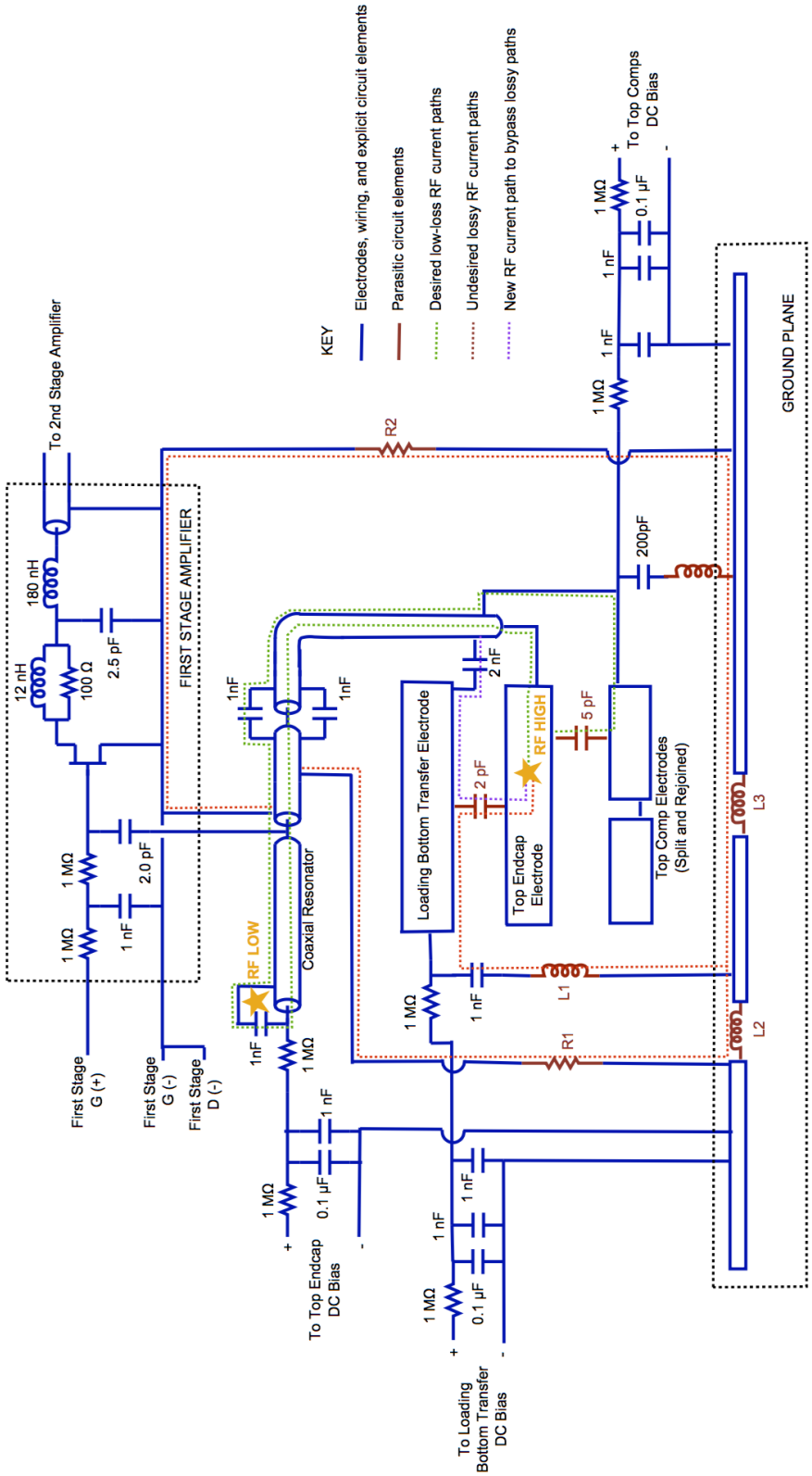

Figure 4.14: RF paths in and around the 200 MHz resonator, including through parasitic capacitances (red). The green dashed line shows the ideal path of RF current in the resonator. Red dashed lines are alternative, lossy paths. The purple dashed line shows the new path that shorted out the lossy paths and restored the resonator's good Q. R1 represents losses in the resonator vacuum flange ground path. R2 represents losses in the amplifier post ground path. L1 represents inductance in the silver strap through which the loading bottom transfer electrode gets its DC bias, estimated to be in the few 10s of nH. L2 and L3 represent inductance in the ground plane.

peak.

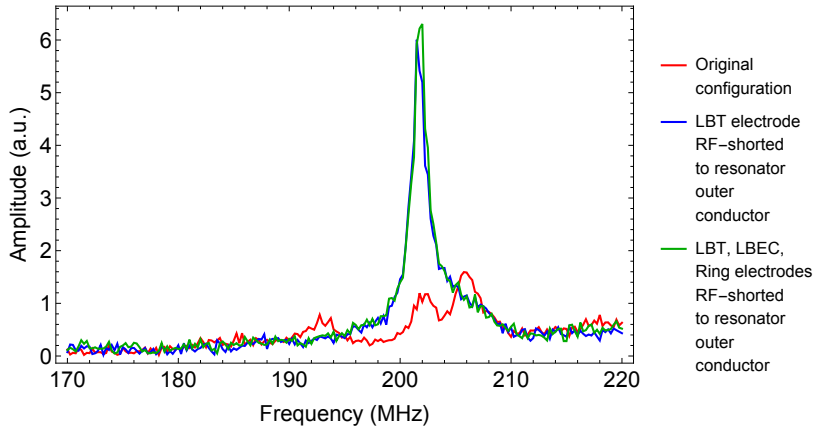

Figure 4.15: Response of a simplified 200 MHz resonator setup to excitation by a network analyzer, coupled to the circuit using an antenna. RF-shorting the loading bottom transfer electrode (LBT) to the outer conductor of the length of coax in the 200 MHz resonator removed spurious resonances, as well as frequency-shifting the main resonant peak, increasing signal size, and increasing Q. RF-shorting additional electrodes did not give substantial further gains.

In addition to extra resonant peaks appearing when the positron accumulation trap was added to the experiment, the capacitance between the top endcap and loading bottom transfer electrodes also shifted the frequency of the main, desired resonance downward. Once the capacitors to remove the extra resonances had been installed, it was possible to see this change and tune the frequency back upward (slightly overshooting 200 MHz on the first try, as shown by the frequency offset between the green and blue resonances in Fig. 4.16).

This tuning process was complicated by another constraint on the system that had been tightened by the positron accumulation trap: the positioning of the resonator's tuned coax length and tap-off point with respect to the pinbase. In order to accommodate the positron accumulation trap in the new apparatus, the pinbase

was moved up, away from field center (Fig. 4.9), with respect to the arrangement in the previous apparatus (Fig. 4.8 [108]) for which this resonator design had been created. The coaxial vacuum feedthrough also had to be moved radially outward to accommodate positron loading infrastructure at the center of the pinbase. These two changes together meant that the portion of the resonator inside the trap can had to be lengthened. However, the total length of the resonator is fixed by the desired 200 MHz frequency, so increase in length inside the trap can reduces the available coax length above the pinbase. The RF-grounded end of the resonator is at the top of the coax, and because of the FET's magnetism, the place where the signal is tapped off to go to the amplifier cannot be between the trap and the pinbase. The position along the resonator of the tap-off point is crucial because the single-electron signal is scaled down by the ratio of the tap-to-ground length to the whole coax length. The geometrical changes have made it so that the tap ratio, and therefore the size of the signal, is smaller by a factor 3 in the current generation apparatus than it was in the previous apparatus. Though this change can be partially compensated for by reducing the amount of division in the capacitive divider before the FET, parasitic capacitances limit the tunability of this stage. Ch. 7 contains a design proposal to increase the tap ratio and recover this lost signal.

RF-shorting the loading bottom transfer electrode (LBT) and paring the resonator to the correct length resulted in the noise resonance in blue in Fig. 4.16. Quality factor Q was measured in both driven scan and noise resonance scans to be 417 ± 17. Though much improved, this is still lower than the Q of 600 measured in the simpler system of the previous apparatus; it is not known for certain why this is. One possibility is

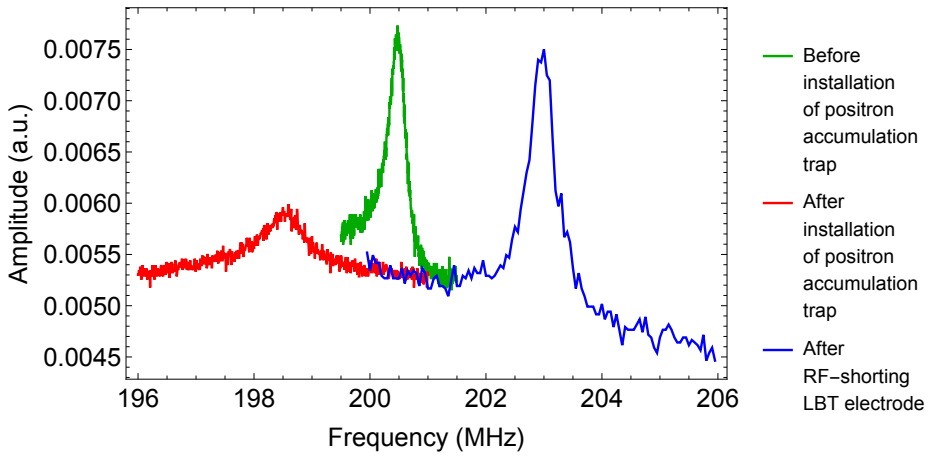

Figure 4.16: First-stage precision trap noise resonances at 4 K before installation of the positron accumulation trap, after installation of the positron accumulation trap, and after the fix. All plots are rescaled separately to compensate for differences in later stages of detection. Frequency changes are unimportant and are tuned away later in the process.

that some RF current is still flowing through undesired alternative paths involving the positron accumulation trap. Another, discussed next, is another possible lossy path through capacitive coupling to the microwave waveguide.

The microwave waveguide extends down into a notch in the top endcap (see Fig. 2.6). To allow shifting during thermal contraction on cooldown, the last section of waveguide is connected to the next-to-last by a sliding joint in gentle contact with grounded support plates in the pinbase. Capacitance between this waveguide and the top endcap has been measured to be about 3 pF, in the range of the capacitances to other electrodes whose ground paths matter.

Because the microwave waveguide was at the bottom of the electrode stack in the previous apparatus, far from the detection electrode, loss in this RF path might explain the residual Q degradation of the current apparatus compared to the previous apparatus. Improving RF-shorting of the microwave waveguide might cut off one

additional lossy return path, although this also has the potential downside of more strongly coupling the detection circuit to all the silver straps that pass near the microwave waveguide. This possibility is being investigated in the experiment as this thesis is being written. Th proposed reconfiguration presented in Ch. 7 would eliminate parasitic paths through both the microwave waveguide and the positron accumulation trap, thereby potentially improving signal-to-noise beyond the standard set in the previous Harvard electron $g/2$ measurement.

4.3 RF Detection: Second Stage

After the first-stage amplifier, the single-particle axial signal is carried up the fridge on segments of stainless steel microcoaxial cable between thermal stages of the fridge; these are interspersed with segments of copper microcoax epoxied to copper bobbins for heatsinking at each temperature stage. At the 1K pot stage, the signal goes through a second-stage amplifier, whose dual purposes are to amplify the signal with 20 dB gain with a still-cryogenic noise floor and to block RF noise from room temperature with greater than 20 dB suppression. The second-stage amplifier includes both input and output matching networks and passes the DC bias for the drain of the first-stage amplifier downward on the center conductor of their microcoax link. The precision trap second-stage amplifier is shown in Fig. 4.17.

In earlier iterations of positron accumulation and planar amplifiers for the new apparatus, the design of the second-stage amplifiers was based on the 66 MHz design that preceded the 200 MHz design on the previous Harvard electron $g/2$ apparatus [108]. In these amplifiers, unintentional positive feedback from the output back to

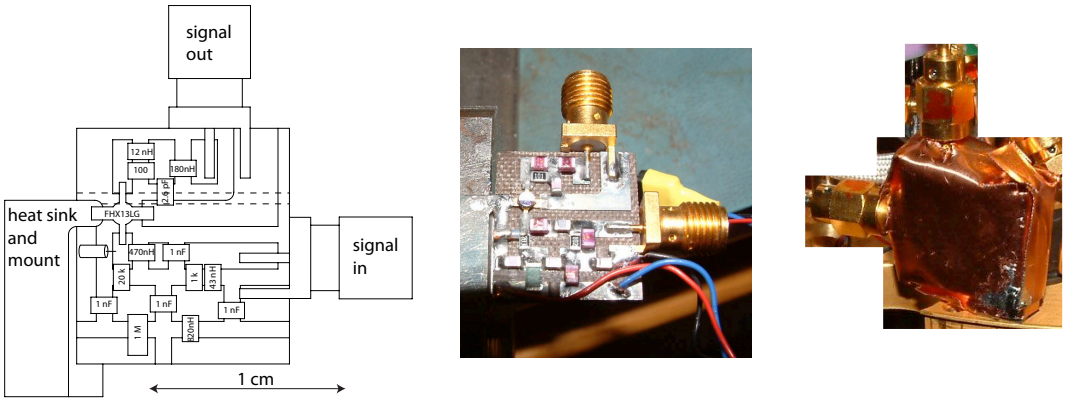

Figure 4.17: Amplifier circuit board layout and photograph of the second-stage amplifier for the precision measurement trap. From [90], adapted from [71].

input was avoided by tuning the output networks a bit lower in frequency than the input networks[5]. This solution created a tradeoff where stability came at the cost of decent impedance matching and signal transmission. The second-stage amplifiers for the positron accumulation and planar traps have now been redesigned[6] to take advantage of the fact that offsetting the output center frequency above the input center frequency presents a capacitive load and avoids positive feedback with a much smaller frequency offset and a much smaller cost in matching. Details of an analogous change during the original switch to 200 MHz for the precision trap are given in [108]. The new second-stage amplifier for the positron accumulation trap is shown in Fig. 4.18 and its gain characteristics are in Fig. 4.19.

[5]See Sec. 4.2.2 of [108] for a detailed description of the combination of Miller capacitance and drain loading that leads to positive feedback in this situation.

[6]Thanks to Melissa Wessels for her development work on 2nd stage amplifiers.

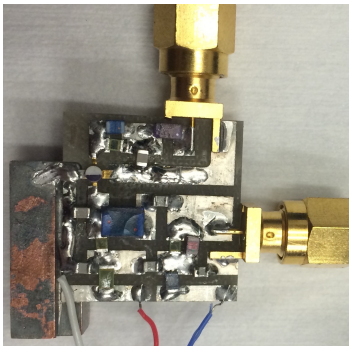

Figure 4.18: New second-stage amplifier for positron accumulation trap. Board layout is similar to Fig. 4.17 with component values shown in Fig. 4.2.

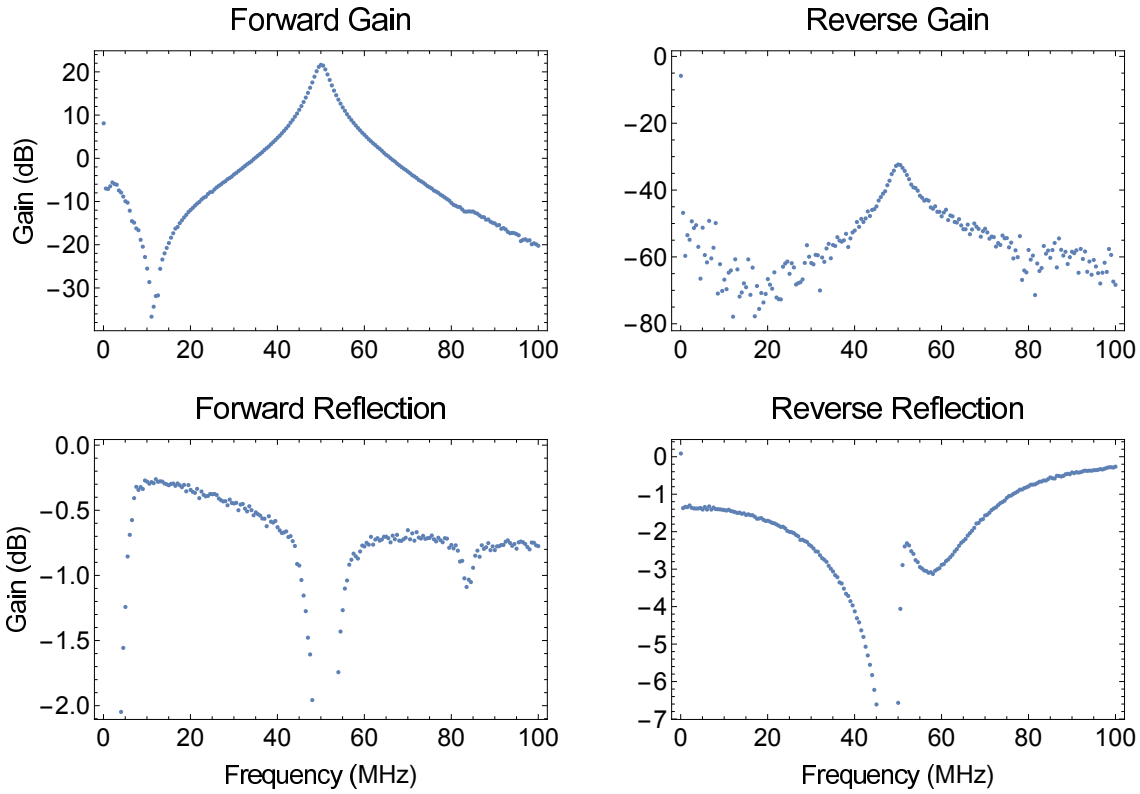

Figure 4.19: Gain characteristics of the redesigned second-stage amplifier for the positron accumulation trap, as measured using a network analyzer. Forward gain shows the amplifier's response at the output to a signal at the input. Reverse gain shows the suppression of noise going backward through the amplifier. Forward reflection is the reflection from the amplifier's input and reverse reflection is the reflection from its output.

4.4 RF Detection: Room Temperature

Fig. 4.20 shows the full RF detection chain for the precision measurement trap, including room-temperature components. The positron accumulation trap has a similar detection chain tuned to its frequency.

After the signal exits the dilution refrigerator insert, it goes through a series of filters and room-temperature amplifiers[7]. The signal is split off to a spectrum analyzer[8] for direct monitoring of the 200 MHz signal. After more filtering, attenuation, and amplification, it is mixed down with the signal from a low-noise frequency synthesizer[9] to 5.00005 MHz. The signal then goes through a narrow crystal filter, travels 2.5 m on double-shielded coax cable through a shielded trench to the instrumentation rack, and goes through a second narrow crystal filter. After one more stage of amplification, it is mixed down with a signal from another frequency synthesizer[10] to 5.05 kHz. After more filtering, attenuation and amplification, the signal is digitized by a high-speed PCI analog-to-digital converter (ADC)[11] mounted in the experiment data and control computer. The ADC also takes a signal mixed down from the same $\nu_z - 5$ MHz and 4.995 MHz sources as a phase reference.

[7] MITEQ AU-2A-0110-BNC

[8] Agilent 8564EC

[9] Frequency synthesizers for >5 MHz are PTS 250 and PTS 500 units from Programmed Test Sources Inc.

[10] Stanford Research Systems DS345

[11] National Instruments PCI-4462. Conversion from the previous experiment's PCI-4454 required rewriting all low-level LabView VIs to interface with NI-DAQ rather than Traditional DAQ drivers. The new ADC's truly differential inputs should offer superior noise rejection compared to the pseudo-differential inputs of the older ADC.

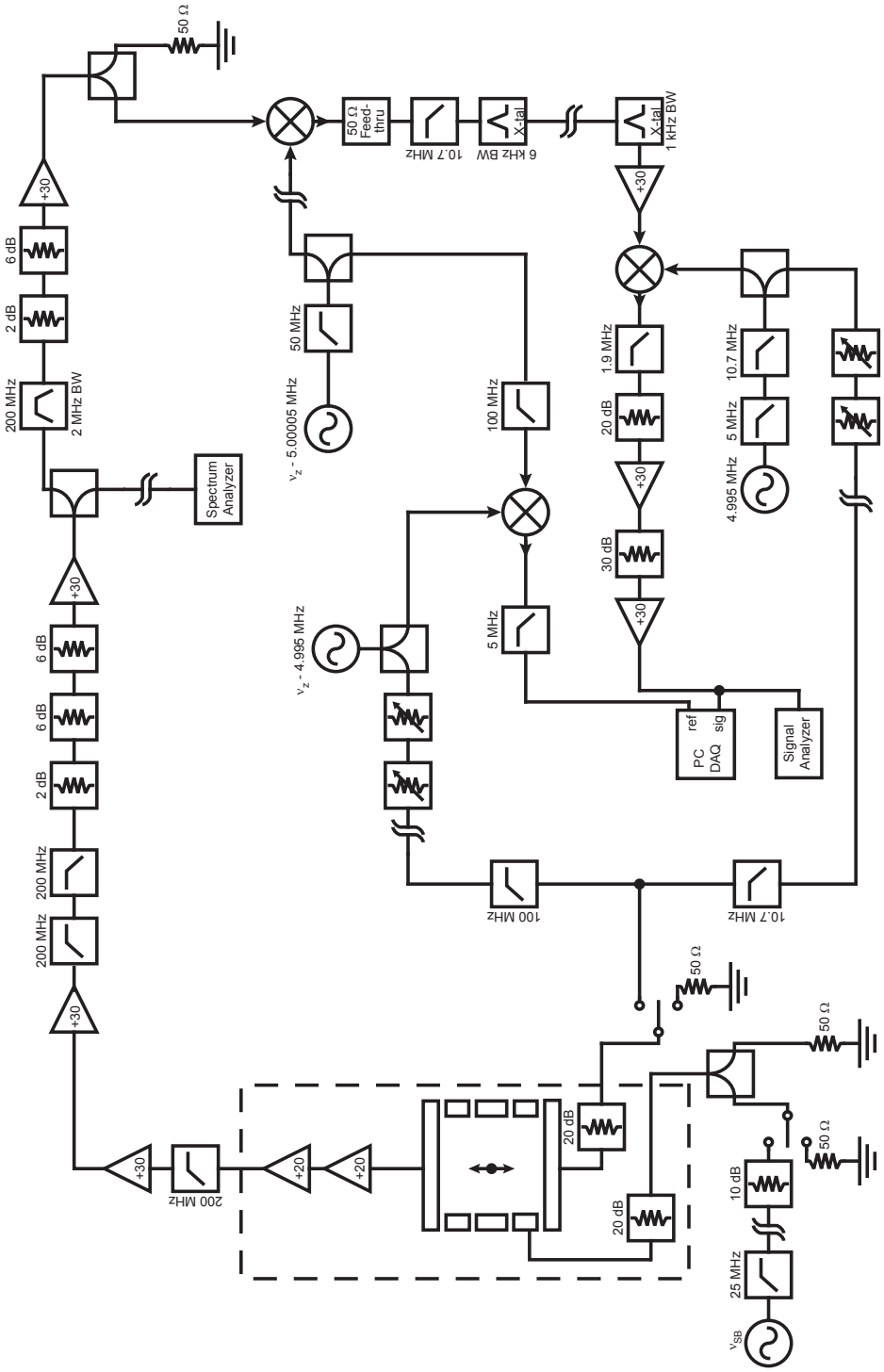

Figure 4.20: RF detection chain and direct-drive setup. From [90], adapted from [71] and [27].

4.5 Loading Particles

4.5.1 Loading from the Radioactive Source

The positron source is described in Sec. 3.4 and the loading technique (from [118]) is described here. Positrons are emitted from the source via beta decay, then travel along magnetic field lines to pass through first the 10 μm thick titanium window that forms part of the trap vacuum enclosure and then the 2 μm thick single-crystal tungsten moderator. Inside the moderator a small fraction of positrons pick up an electron to form loosely bound positronium, which continues downward into the positron accumulation trap [118]. Potentials shown in Fig. 4.21 are applied to loading and transfer electrodes to field-ionize the positronium and trap the positron, with the stripped electron carrying away the excess energy. Potentials may also be inverted to trap electrons.

A dip in the positron accumulation amplifier noise resonance from 160-320 positrons loaded during 2 hours in shown in Fig. 4.22. (See Sec. 4.6.2 for more information about dips.) Loading rates of 1-2 positrons per minute were demonstrated when the source activity was 6.3 μCi, giving a loading rate per unit activity of 3-6 positrons/s/mCi [89, 71]. This is comparable to ATRAP demonstrations of this loading method and over 150 times higher than the rate for a different method used in the last positron/electron $g/2$ comparison [118, 117, 5]. The loading rate for electrons is similar as long as "blocking" potentials are applied to prevent the loading of secondary electrons. Loading rates decrease after firing of the field emission point, which is believed to be the result of heating-induced changes in the amount of adsorbed gas

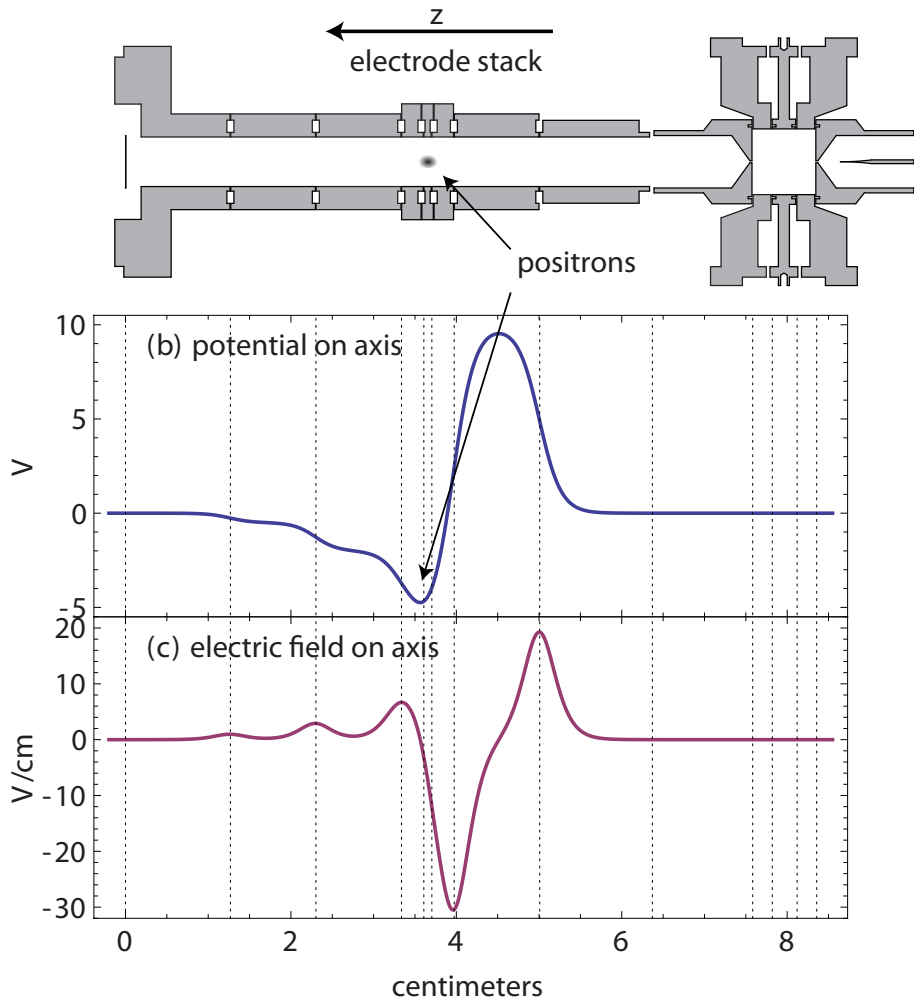

Figure 4.21: Trap potential and field profiles for positron loading. From [90], adapted from [71].

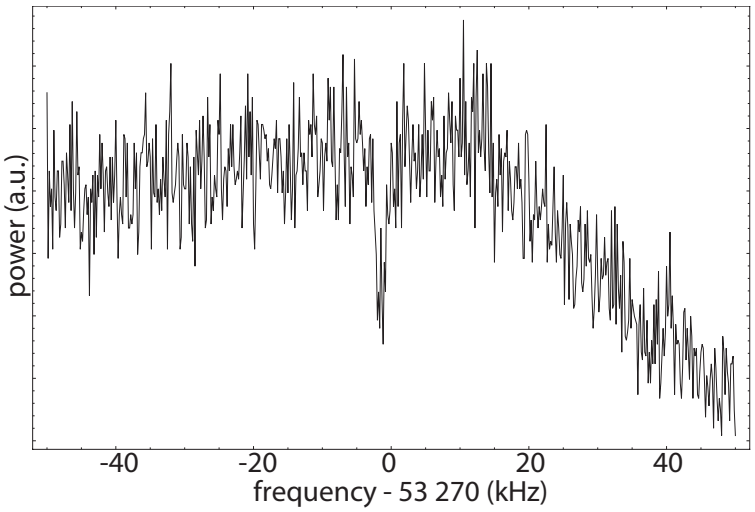

Figure 4.22: Dip in the positron accumulation trap noise resonance from about 160-230 trapped positrons. From [89], adapted from [71].

on the moderator. More details about positron loading are in [71].

Transfer of positrons to the precision measurement trap to perform the positron $g/2$ measurement is discussed in Chapter 6.

4.5.2 Loading Electrons with the Field Emission Point

Electrons can be loaded directly into either the precision or positron accumulation traps using the field emission point (FEP). The FEP is made by electrochemically etching a sharp point into a 0.018" diameter tungsten rod (see procedure in [108]). It is mounted directly below a 0.34 mm hole in the precision bottom endcap electrode, as shown in Fig. 2.6. To load electrons, a bias voltage is applied to the FEP and slowly turned up until field emission begins. The current increases exponentially above a threshold determined by the sharpness of the tip, typically 300-1000 V. Currents of tens of pA to 1 nA flow, monitored by a multimeter across the 1 MΩ resistor in series at room temperature. Emitted electrons follow magnetic field lines to go through the

hole in the precision bottom endcap and then either collide with the precision top endcap electrode or go through the hole in the precision top endcap and eventually collide with the tungsten moderator. This liberates residual gas molecules that had been cryopumped onto the electrode surface during cooling, which then interact with electrons in the continuing current from the FEP. These interactions leave behind some electrons that are low-enough energy to remain in the trap's potential well. The loading rate is approximately linear in time. FEP voltage can be adjusted to create a current such that loading times of 30 s to 2 min give anything in a range from one trapped electron to tens of thousands of trapped electrons. Electrons' axial motion quickly comes into thermal equilibrium with the axial amplifier. The radius of their magnetron motion can then be reduced by sideband cooling.

4.6 Manipulating Trapped Particles

4.6.1 Sideband Cooling of the Magnetron Motion

After being loaded from the field emission point or the radioactive source, particles are in unknown magnetron states. To move particles to the maximally harmonic and well-characterized region in the center of the trap, their magnetron motion is first "cooled"[12] to the smallest-radius state by sideband coupling to the axial motion [105]. A drive at $\omega_z - \omega_m$ reduces magnetron quantum number and raises axial quantum

[12]Smaller-radius, lower-quantum-number magnetron states have lower kinetic energy, but their total magnetron-state-associated energy is dominated by the potential energy of the particle's position in the quadrupole field, which increases with smaller radius. Therefore, though "magnetron cooling" increases total energy in the magnetron state, it reduces radius and decreases kinetic energy. Because of the extremely long magnetron lifetime, the "cooled" state is effectively stable on any experimentally relevant timescale.

number; excess axial energy is then quickly damped away by the amplifier. The cooling limit is given by

$$\frac{T_m}{T_z} = -\frac{\omega_m}{\omega_z}. \tag{4.8}$$

Magnetron-cooling transitions are driven in the precision trap by a PTS frequency synthesizer connected to half of the bottom compensation electrode, shown in the lower left corner of Fig. 4.20. The radial asymmetry of the split electrode enables the electric field created in the trap by the drive to have the radial-direction component needed for the sideband transition [105].

Successful magnetron cooling can be detected by observing the associated transient axial excitation and by watching as the axial dip and drive signals from trapped particle clouds (see following sections) shift and narrow in frequency as particles move toward the center of the trap.

4.6.2 Dips in the Noise Resonance

One method of characterizing trapped particles takes advantage of their interaction with Johnson noise in the resonator and does not require any external drive. When a particle or particles are trapped at a frequency within the noise resonance, the particles effectively short out the RLC circuit at their axial frequency. This creates a dip in the noise resonance with the power spectrum

$$P(\omega) \propto \frac{\omega_r^4(\omega_z^2 - \omega^2)^2}{[(\omega_z^2 - \omega^2)(\omega_r^2 - \omega^2) - \omega^2\Gamma N\gamma_z]^2 + \omega^2\Gamma^2[(\omega_z^2 - \omega^2) + \Gamma N\gamma_z]^2} \tag{4.9}$$

where ω is frequency, ω_r is the resonant frequency of the tuned input circuit (resonator), and Γ is the full width at half-maximum of the input circuit resonance [120].

For single particles and small particle clouds used in tuning the trap, $N\gamma_z \ll \Gamma$, and it is a good approximation that the dip is Lorentzian with a width of $N\gamma_z$. Dip width can therefore be used to assess the size of a cloud of trapped particles. Fig. 4.23 shows a dip in the precision first-stage resonance due to a cloud of trapped electrons.

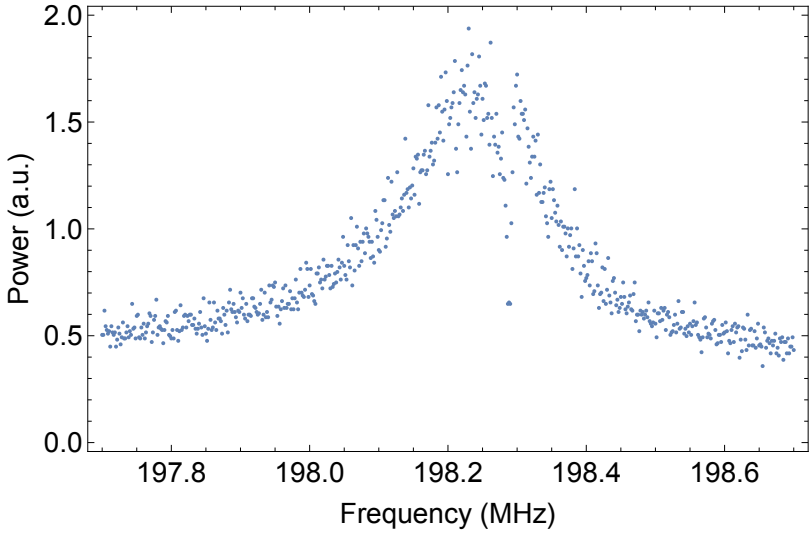

Figure 4.23: Dip in the noise resonance due to a cloud of trapped electrons in the precision trap. Adapted from [90].

4.6.3 Direct Drives

The amplitude of a trapped particle's axial motion and therefore the size of the signal it creates can be increased by applying a drive to the bottom endcap electrode. Axial drives are used to drive anomaly transitions for the $g/2$ measurement (see Sec. 2.4.2), to drive single particles or small clouds of particles to characterize and tune the trap, and to lock a single particle to a set axial amplitude in order to quickly measure axial frequency shifts for detecting cyclotron and anomaly transitions.

4.6.3.1 Two axial drive schemes for avoiding feedthrough

If an axial drive were applied to a single electrode at the axial frequency of trapped particles, the amplifier would also directly pick up the drive, obscuring the signal from the particle. Two methods are used for reducing this direct drive feedthrough.

1. The trapping potential is modulated at a frequency ν_i much lower than the particle's axial frequency and a drive is applied at $\nu_z - \nu_i$ to axially drive the particle [121, 86]. The setup for this method in the precision measurement trap is shown in Fig. 4.20.

2. Drives with the same frequency but different phase and amplitude are applied to two electrodes that create electric fields with different spatial profiles inside the trap (e.g., the bottom endcap and the bottom compensation electrode). The relative phase and amplitude of the drives are adjusted to interfere destructively and cancel as completely as possible at the amplifier but still have nonzero strength at the particle's position. This method is used for the self-excited oscillator described in Sec. 4.6.4.

The signal from axially driving a cloud of about 600 electrons is shown in Fig. 4.24. Drive and detection frequencies are swept together through the particles' axial frequency. Comparison to a global phase reference allows the separation of the signal into in-phase and quadrature components.

Driven axial signals can also be used for tuning trap voltages to create a more harmonic axial potential well. As described in Sec. 2.3.2, a trap's frequency is set primarily by the relative voltages on the ring and endcap electrodes, with voltages on

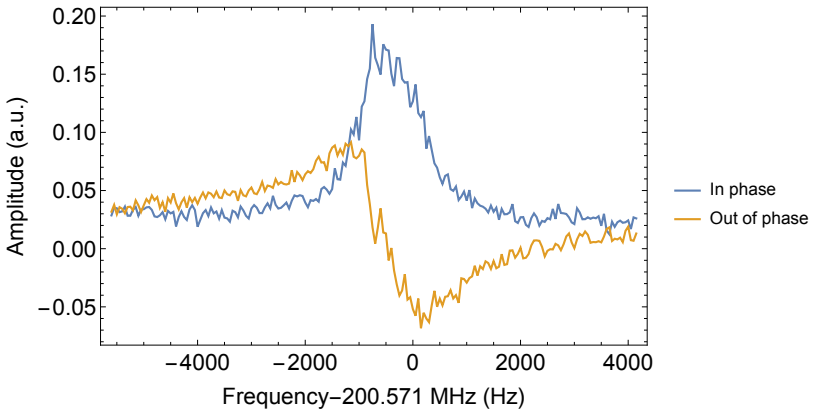

Figure 4.24: Driven axial scan. Adapted from [90].

the compensation electrodes set to tune out C_4 and thereby reduce the dependence of particles' frequency on axial oscillation amplitude [122]. The correct voltages for frequency-setting and tuning are not analytically predictable, given that small imperfections in set voltages and/or trap geometry produce anharmonicity, whereby particles respond to a drive at a range of frequencies wider than their damping width.

Particles' response to an axial drive in the presence of anharmonicity is described in detail in [105]. Anharmonicity causes the amplitude of the particles' response to depend on the drive frequency sweep direction, as shown in 4.25. By iteratively observing the effect on anharmonic resonances, adjusting compensation voltages to reduce anharmonoicity, and repeating the process with smaller particle numbers when a resonance begins to look symmetrical, the trap may be tuned until anharmonicity is not visible for even a single trapped particle.

4.6.4 Self-Excited Oscillator

As described in Sec. 2.4.1, detecting the excited cyclotron state before it decays relies on the ability to measure the axial frequency at the few ppb level on a 0.25 s

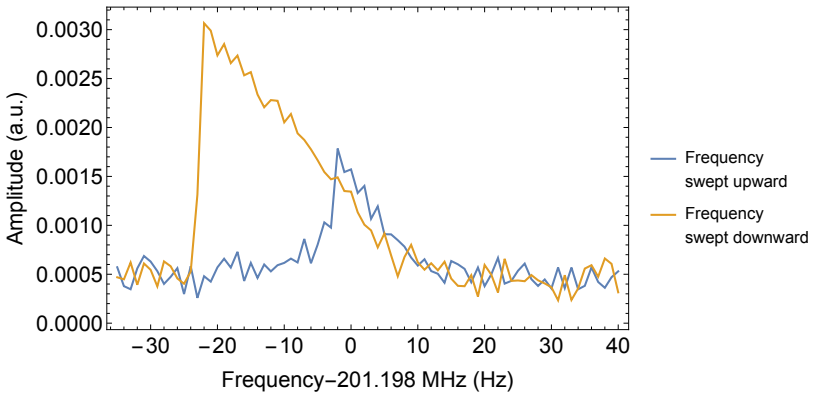

Figure 4.25: A driven axial scan in a trap tuned to have $C_4 < 0$ shows an anharmonic response, with excitation in the lower-frequency region depending on frequency sweep direction of drive and detection. Adapted from [90].

timescale. To achieve a sufficient signal-to-noise ratio, it is necessary to increase the particle's axial amplitude above its thermal amplitude. To accomplish this, a portion of the particle's axial signal is fed back to it as a drive in an arrangement called the self-excited oscillator (SXO), shown in Fig. 4.26 [123]. With this drive, the particle's equation of motion is

$$\ddot{z} + \gamma_z \dot{z} + [\omega_z(A)]^2 z = F_d(t)/m. \tag{4.10}$$

A phase shifter in the path back to the particle is adjusted such that the phase of the drive matches that of the particle and a voltage variable attenuator is used to set the gain, G, keeping

$$F_d(t)/m = G\gamma_z \dot{z}. \tag{4.11}$$

The amplitude is continually measured and the gain adjusted to exactly cancel damping due to the amplifier and maintain a stable oscillation amplitude A for which the trap is tuned to be maximally harmonic. Consistent $\omega_z(A)$ is thus maintained unless intentionally shifted by driving cyclotron transitions. The gain is controlled by a Digital Signal Processor based on Fourier-transformed input from the signal after it

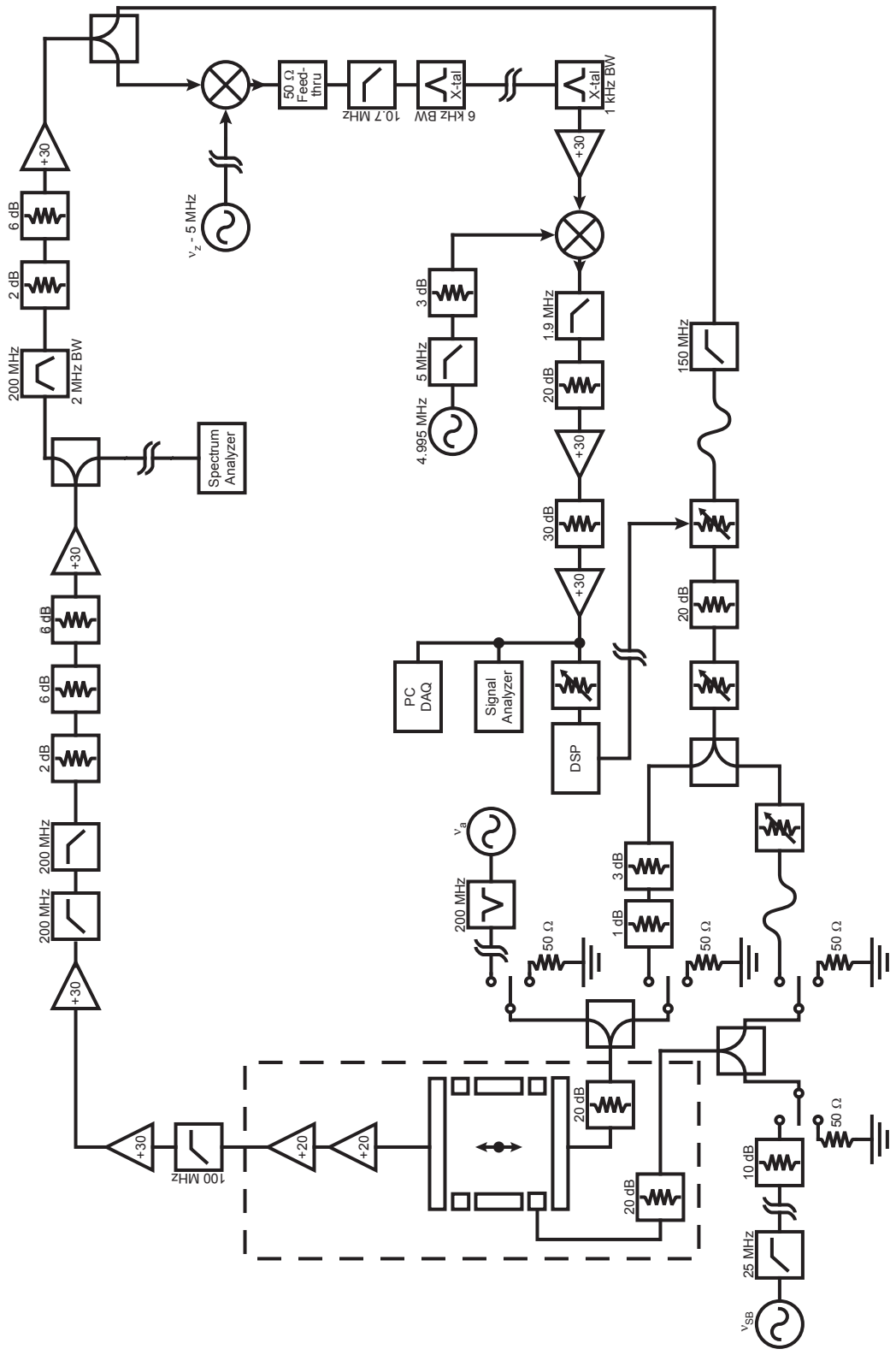

Figure 4.26: Schematic of self-excited oscillator drive scheme. From [71].

is mixed down to 5 MHz and then 5 kHz.

A self-excited oscillator signal from a single electron trapped in the current apparatus is shown in 4.27.

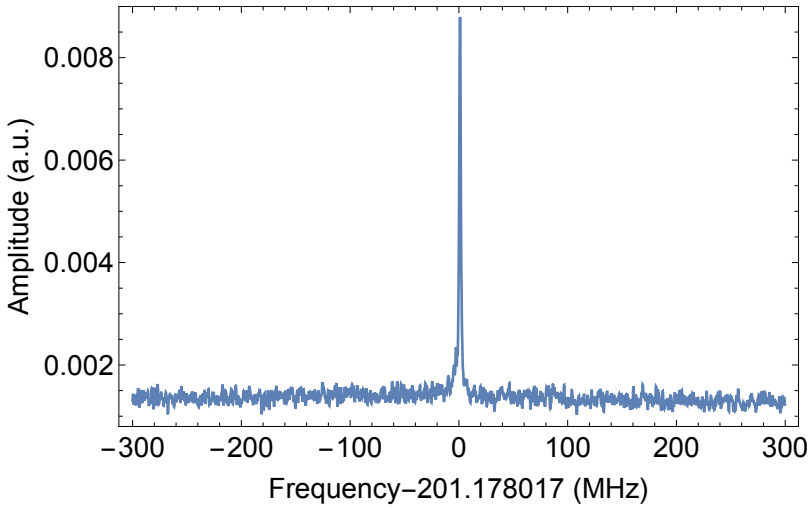

Figure 4.27: Self excited oscillator signal for a single electron. Adapted from [90].

4.7 Microwaves and Cyclotron Transitions

The microwave system used for driving cyclotron transitions is shown in Fig. 4.28. 15 GHz microwaves are produced by an Agilent E8251A signal generator. They propagate through cables and voltage-controlled attenuators to an ELVA microwave multiplier, which uses IMPATT diodes to multiply by 10 and produce 145.5 GHz microwaves. After going through another pair of attenuators, the microwaves propagate through a small section of waveguide around a bend to a horn pointing downward toward the experimental insert. The multiplier, waveguide, and horn are mounted on a rotatable support that is usually positioned above the insert but can be moved aside

to allow the insert to be removed. Once microwaves exit the horn, they propagate across a small gap and then enter the IVC vacuum space via a custom teflon flange. Two sections of thermally isolated waveguide guide the microwaves from the top of the inner vacuum chamber to the 4 K plate. Between the thermal stages of the dilution refrigerator, propagation occurs in free space between heat-sinked teflon lenses that focus the microwaves while blocking most black-body radiation. Microwaves enter a horn, go through another section of waveguide at the top of the mixing chamber, go through a sapphire vacuum window in the trap can, are guided through a final section of waveguide, and go through a horn into the precision measurement trap. The final section of microwave horn is visible in Fig. 2.6.

Driven cyclotron jumps between the ground and first few excited states have been observed in the current apparatus (Fig. 4.29). A microwave drive was applied at the cyclotron frequency while a single electron's axial frequency was monitored with the self-excited oscillator (Sec. 4.6.4) for shifts due to the coupling with the magnetic bottle (Sec. 2.4.1.) Individual states remain distinguishable even though the coupling between axial frequency and the cyclotron and spin states has been reduced to 40% of its value in the best electron $g/2$ measurement. As described in Ch. 2, this will allow for narrower lineshapes and improved $g/2$ measurement precision.

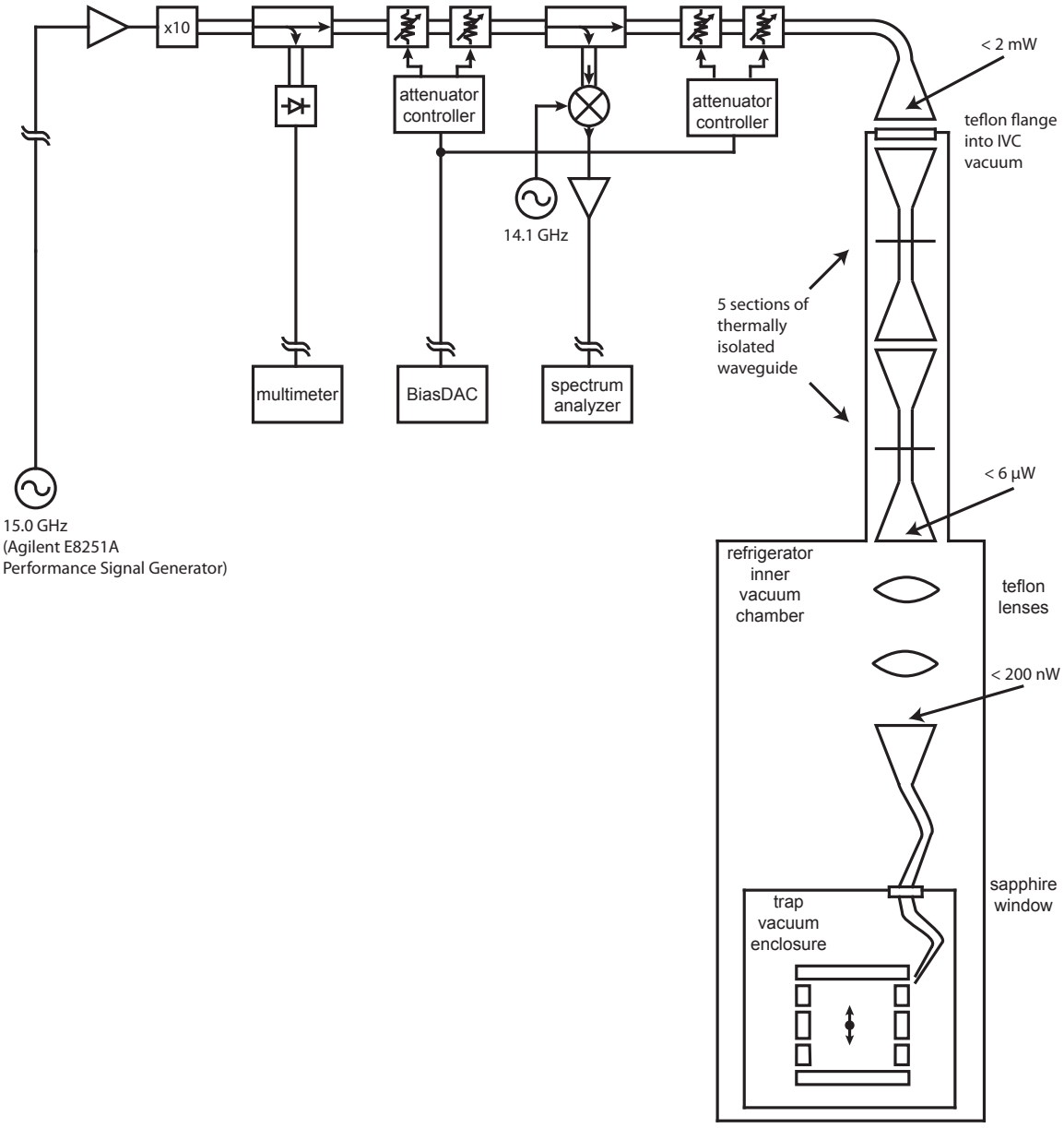

Figure 4.28: Microwave source and path to the precision measurement trap. From [71].

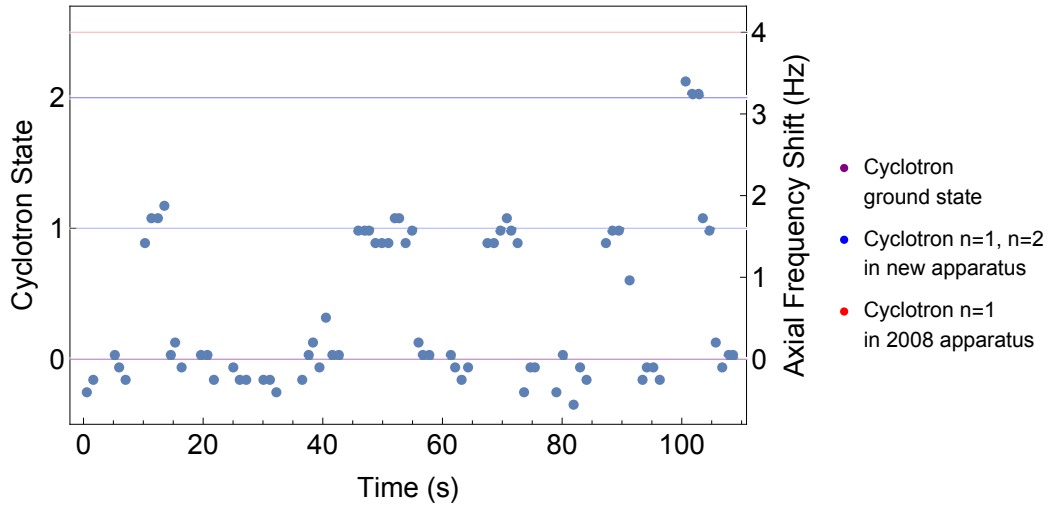

Figure 4.29: Single-electron cyclotron jumps (blue) in the new apparatus compared to jump size in the most recent Harvard electron $g/2$ measurement (red). Jump size has been reduced from 20 ppb to 8 ppb. Adapted from [90].

Chapter 5

Microwave Cavity Modes

The precision measurement trap electrodes form a microwave cavity that can inhibit spontaneous emission of a trapped electron's cyclotron motion [124] enough that individual quantum levels can be resolved. A particle's interactions with the cavity also shift its cyclotron frequency, an effect that must be understood and corrected for in the $g/2$ measurement [125, 86, 3]. Cavity modes' frequency-dependent enhancement of microwave transmission into the trap cavity might be harnessed to enable cavity-assisted axial sideband cooling, a proposed technique for improving $g/2$ measurement precision by cooling a particle's axial motion [105]. This chapter discusses cavity modes and their effect on $g/2$ measurements, describes preliminary steps toward characterizing cavity modes in the current-generation apparatus, and discusses trap design considerations related to cavity modes.

5.1 Penning Trap as Microwave Cavity

The cylindrical space inside the precision trap electrodes acts as a microwave cavity. At 7.76 mm high and 7.99 mm in diameter, it has several resonant modes near the 145.5 GHz cyclotron frequency (2 mm cyclotron wavelength). Allowed mode field geometries are determined by Maxwell's equations with boundary conditions of $\mathbf{E}_{\parallel} = 0$ and $\mathbf{B}_{\perp} = 0$ at the cylinder's walls and endcaps. The solutions can be classified as the familiar TE (transverse-electric) and TM (transverse-magnetic) modes for cylindrical waveguides [126]. Mode frequencies are given by

$$\begin{aligned} {}^{(E)}\omega_{mnp} &= c\sqrt{\left(\frac{x'_{mn}}{\rho_0}\right)^2 + \left(\frac{p\pi}{2z_0}\right)^2}, \\ {}^{(M)}\omega_{mnp} &= c\sqrt{\left(\frac{x_{mn}}{\rho_0}\right)^2 + \left(\frac{p\pi}{2z_0}\right)^2}. \end{aligned} \tag{5.1}$$

Electric and magnetic fields for TE_{mnp} modes are given by

$$\begin{aligned} \mathbf{E} =& E_0 \frac{{}^{(E)}\omega_{mnp}}{c}\left(\frac{\rho_0}{x'_{mn}}\right)^2 \sin(\tfrac{p\pi}{2}(\tfrac{z}{z_0}+1)) \\ & \left[\mp\hat{\rho}\,\frac{m}{\rho}\,J_m(x'_{mn}\tfrac{\rho}{\rho_0})\cos({}^{(E)}\omega_{mnp}t \mp m\phi)\right. \\ & \left. -\hat{\phi}\,\frac{x'_{mn}}{\rho_0}\,J'_m(x'_{mn}\tfrac{\rho}{\rho_0})\sin({}^{(E)}\omega_{mnp}t \mp m\phi)\right], \\ \mathbf{B} =& \frac{E_0}{c}\left[\hat{\mathbf{z}}\,J_m(x'_{mn}\tfrac{\rho}{\rho_0})\sin(\tfrac{p\pi}{2}(\tfrac{z}{z_0}+1))\cos({}^{(E)}\omega_{mnp}t \mp m\phi)\right. \\ & + \frac{p\pi}{2z_0}\left(\frac{\rho_0}{x'_{mn}}\right)^2 \cos(\tfrac{p\pi}{2}(\tfrac{z}{z_0}+1)) \\ & \left[\,\hat{\rho}\,\frac{x'_{mn}}{\rho_0}\,J'_m(x'_{mn}\tfrac{\rho}{\rho_0})\cos({}^{(E)}\omega_{mnp}t \mp m\phi)\right. \\ & \left.\left. \pm\hat{\phi}\,\frac{m}{\rho}\,J_m(x'_{mn}\tfrac{\rho}{\rho_0})\sin({}^{(E)}\omega_{mnp}t \mp m\phi)\right]\right]. \end{aligned} \tag{5.2}$$

Electric and magnetic fields for TM_{mnp} modes are given by

$$\begin{aligned}
\mathbf{E} =& E_0 \Bigg[\hat{\mathbf{z}}\ J_m(x_{mn}\tfrac{\rho}{\rho_0}) \cos(\tfrac{p\pi}{2}(\tfrac{z}{z_0}+1)) \cos({}^{(M)}\omega_{mnp} t \mp m\phi) \\
& - \frac{p\pi}{2z_0} \left(\frac{\rho_0}{x_{mn}}\right)^2 \sin(\tfrac{p\pi}{2}(\tfrac{z}{z_0}+1)) \\
& \quad \Bigg[\hat{\rho}\ \frac{x_{mn}}{\rho_0}\ J'_m(x_{mn}\tfrac{\rho}{\rho_0}) \cos({}^{(M)}\omega_{mnp} t \mp m\phi) \\
& \quad \pm \hat{\phi}\ \frac{m}{\rho}\ J_m(x_{mn}\tfrac{\rho}{\rho_0}) \sin({}^{(M)}\omega_{mnp} t \mp m\phi) \Bigg] \Bigg], \qquad (5.3) \\
\mathbf{B} =& \frac{E_0}{c} \frac{{}^{(M)}\omega_{mnp}}{c} \left(\frac{\rho_0}{x_{mn}}\right)^2 \cos(\tfrac{p\pi}{2}(\tfrac{z}{z_0}+1)) \\
& \quad \Bigg[\pm\hat{\rho}\ \frac{m}{\rho}\ J_m(x_{mn}\tfrac{\rho}{\rho_0}) \cos({}^{(M)}\omega_{mnp} t \mp m\phi) \\
& \quad + \hat{\phi}\ \frac{x_{mn}}{\rho_0}\ J'_m(x_{mn}\tfrac{\rho}{\rho_0}) \sin({}^{(M)}\omega_{mnp} t \mp m\phi) \Bigg].
\end{aligned}$$

In Eqs. 5.1, 5.2, and 5.3, the index m is the number of nodes as angular position ϕ is taken from 0 to π. The index n is the number of antinodes as ρ is taken from 0 to ρ_0. The index z is the number of antinodes between $-z_0$ and z_0. The constant x_{mn} is the nth zero of the mth-order Bessel function $J_m(x)$. The constant x'_{mn} is the nth zero of the derivative of the mth-order Bessel function $J'_m(x')$.

The interaction between a trapped particle and these resonant fields depends on the particle's location, given by (ρ, ϕ, z) in cylindrical coordinates. The interaction strength also depends on how close the mode frequency ω_m is to the particle's cyclotron frequency, as well as on the mode's width in frequency. The resonant frequency width depends on loss of energy due to dissipation in imperfect conductors or to leakage through holes or slits. A wider mode resonance affects particles in a wider frequency range but less strongly on resonance. A mode's full-width at half maximum Γ_M is related to its quality factor Q by $Q_M = \omega_M/\Gamma_M$.

By changing the current in the main superconducting solenoid, the magnetic field

and thus the particle's cyclotron frequency can be swept into and out of resonance with any given mode. The $TE_{1n(odd)}$ and $TM_{1n(odd)}$ modes have the azimuthal electric fields that couple most strongly to a trapped particle's cyclotron motion for a perfectly centered particle. Controlling particle interactions with these "strong-cyclotron-coupling" modes and other cavity modes is crucial for $g/2$ measurements for several reasons, covered in the following sections. Centering the trapped particle within the microwave cavity is also critical to reduce the importance of other modes.

5.2 Cavity Modes and $g/2$

5.2.1 Cyclotron Lifetime

A 100 mK electron in a 5.2 T magnetic field would have a free-space cyclotron lifetime of $\gamma_c^{-1} \approx 100$ ms. For the $g/2$ measurement, an electron must remain in the excited cyclotron state for an averaging time long enough to detect whether a transition has taken place. After a cyclotron transition is attempted, the 200 MHz axial amplifiers must be turned on and the signal averaged for at least 0.25 s to measure the axial frequency precisely enough to determine whether a cyclotron transition has occurred. Extending the cyclotron lifetime via cavity-inhibited spontaneous emission is thus crucial to a successful $g/2$ measurement.

Far from strong-cyclotron-coupling cavity modes, the cavity's boundary conditions reduce the density of states available for emitted radiation. This decreases γ_c, inhibits spontaneous emission, and extends the cyclotron lifetime [124]. The cyclotron damping rate γ_M for a trapped particle with cyclotron frequency ω_c' exactly on mode

frequency ω_M, is not shown here but is derived in [27, 4]. The cyclotron damping rate γ_c for a centered electron with its cyclotron frequency ω_c' near a mode is related to γ_M by the antisymmetric form

$$\gamma_c = \gamma_M \frac{\delta}{1+\delta^2}, \tag{5.4}$$

where δ is the normalized detuning

$$\delta = \frac{\omega_c' - \omega_M}{\Gamma_M/2} \qquad [127]. \tag{5.5}$$

By taking $g/2$ data at frequencies far from strong-cyclotron-coupling modes, inhibition of spontaneous emission was exploited in [86, 3] to lengthen the cyclotron lifetime to > 10 s. Fig. 5.1 shows γ_c as a function of cyclotron frequency in the vicinity of two strong-cyclotron-coupling modes in the best $g/2$ measurement (done in the previous apparatus at Harvard) [27]. Inhibition of spontaneous emission has also been observed in the current-generation apparatus. At 145.5 GHz, for example, the cyclotron lifetime has been measured to be 2.71±0.17 s, over 27 times the free-space cyclotron lifetime [90].

5.2.2 Cyclotron Frequency Shifts

Coupling to cavity modes also shifts a trapped particle's cyclotron frequency, causing a systematic effect in $g/2$ measurements [128, 129]. This "cavity shift" $\Delta\omega_c$ changes the cyclotron frequency to $\bar{\omega_c} = \omega_c\left(1+\frac{\Delta\omega_c}{\omega_c}\right)$, affecting $g/2$ as follows:

$$\frac{g}{2} = 1 + \frac{\omega_s - \omega_c}{\omega_c} \simeq 1 + \frac{\omega_s - \bar{\omega_c}\left(1-\frac{\Delta\omega_c}{\omega_c}\right)}{\bar{\omega_c}} = 1 + \frac{\bar{\omega_a}}{\bar{\omega_c}} + \frac{\Delta\omega_c}{\omega_c}. \tag{5.6}$$

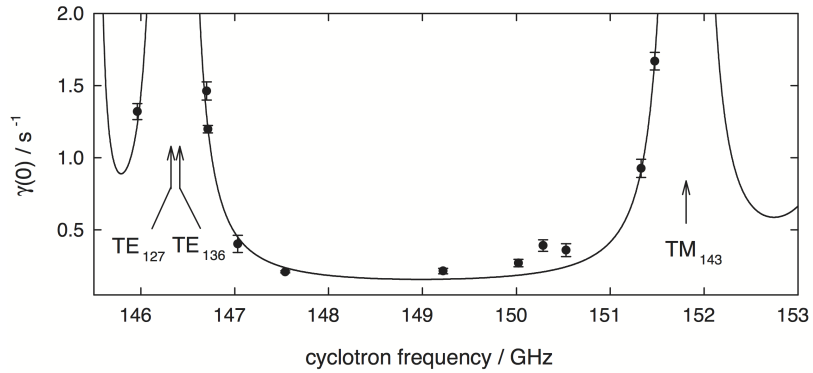

Figure 5.1: The zero-axial-amplitude cyclotron damping rate $\gamma(0)$ at various cyclotron frequencies, as measured in the previous Harvard electron $g/2$ apparatus. From [27].

The cavity shift due to coupling with a single mode is given by

$$\Delta\omega_c = \frac{\gamma_M}{2}\frac{\delta}{1+\delta^2} \qquad [127]. \tag{5.7}$$

Shifts from multiple modes must be summed using a renomalized method that removes the electron's self-field, covered in [27, 4].

Cavity shifts are believed to have been the leading source of systematic error in the 1987 electron/positron $g/2$ measurement, which was done in a hyperbolic trap [5]. The difficulty of machining hyperbolic trap electrodes precisely and the difficulty of controlling boundary conditions in gaps between electrodes made it impossible to quantitatively correct for cavity shifts. Cylindrical traps, however, can be made to have calculable, near-ideal modes with high Q [87]. By using mode frequency and Q information from wide-frequency-range mode maps (Sec. 5.3) and detailed single-particle cyclotron lifetime data (techniques described in [110, 27, 4]), in the Harvard electron $g/2$ measurements it has been possible to calculate the expected cavity shift at each magnetic field used and correct the g-value data accordingly, removing the cavity shift as the leading source of uncertainty.

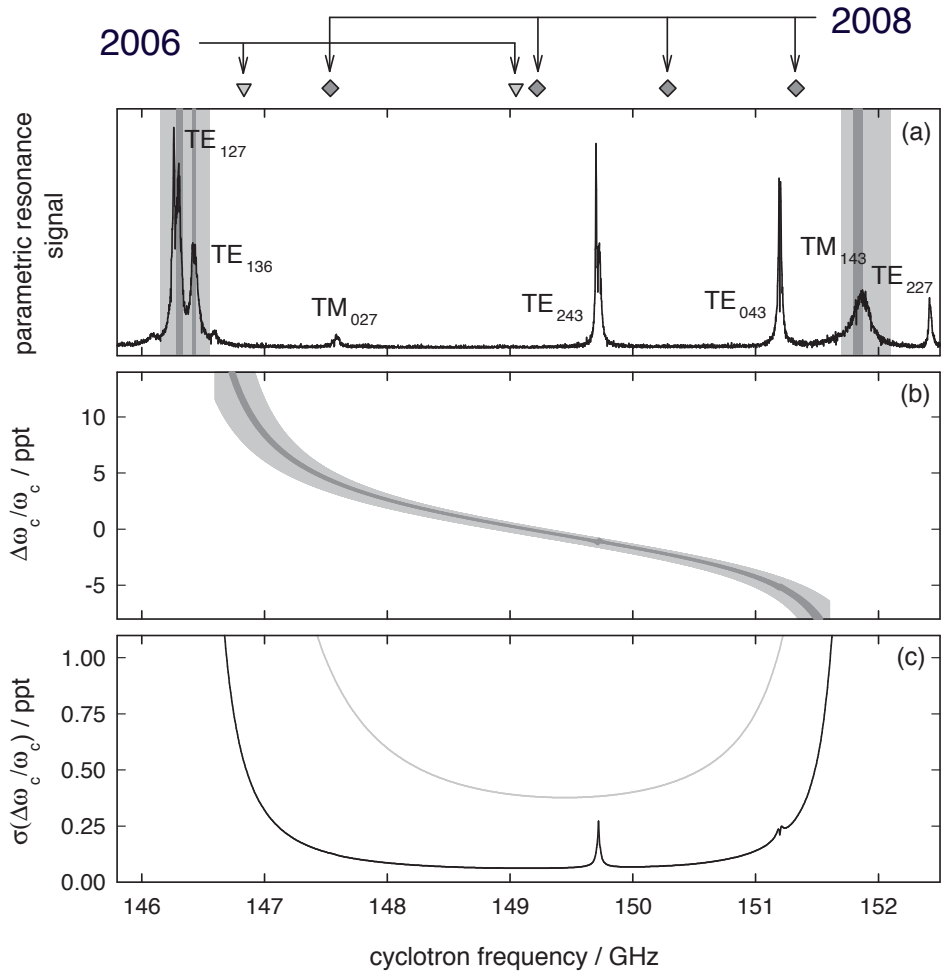

Figure 5.2: Cavity modes and their effect on cyclotron frequency in the previous $g/2$ experiments. At the top, triangles and diamonds indicate the magnetic fields at which g-value data were taken in the two Harvard electron $g/2$ measurements in the previous apparatus. (a) shows modes as detected by a method described in Sec. 5.3. (b) shows the cyclotron frequency shift caused by coupling to cavity modes. (c) shows the uncertainty on the cyclotron frequency due to the cavity shift. Uncertainty bands for the 2006 measurement are in light gray and for the 2008 measurement are in dark gray. From [27].

.

Fig. 5.2 shows the effect of cavity modes on cyclotron frequency in the previous apparatus as calculated from measured cyclotron lifetime data (e.g., Fig. 5.1). As is visible in Fig. 5.2c, both the magnitude of the cavity shift and the uncertainty due to the cavity shift are much higher close to strong-cyclotron-coupling modes. This is another reason (along with inhibition of spontaneous emission) that $g/2$ data must be taken far from these modes. Even far from cyclotron resonance with the strongly-coupled modes, however, frequency shifts must be carefully corrected, as is discussed next.

5.2.3 Cavity-Assisted Axial Sideband Cooling

Cavity modes might also enable a new method of narrowing cyclotron and anomaly lineshapes and increasing $g/2$ precision. One way to reduce the lineshape broadening caused by the coupling of the axial motion to the cyclotron and spin states is to reduce the amplitude of axial oscillations during transition attempts; this limits the range of fields from the magnetic bottle that are encountered by a trapped particle[1]. Feedback cooling, a technique in which the self-excited-oscillator system is used to deliberately reduce axial amplitude, has been shown to cool an electron from 5.3 K to 850 mK [130] and from 1.6 K to 700 mK [110]. However, amplifier noise and heat along with the limits on signal-to-noise ratio have so far kept this technique from achieving the 230 mK[2] achieved by using a dilution refrigerator to cool electrodes to 100 mK with the amplifier turned off [27].

Another route to cooling the axial motion is axial-cyclotron sideband cooling,

[1] See Sec. 2.4.1 for a discussion of the magnetic bottle.

[2] For details about this temperature, see [27].

an analog of the magnetron-axial sideband cooling used to reduce the radius of the magnetron motion [122, 131, 105]. A drive at $\omega_c' - \omega_m$ applying a force proportional to x or $\dot{x}$ in the $\hat{z}$ direction, a force proportional to z in the $\hat{x}$ direction, or any of these with y substituted for x, can cause transitions downward in axial state and upward in cyclotron state. The cyclotron motion could then be returned to its ground state either by allowing natural cyclotron decay or more quickly by taking advantage of the cyclotron motion's relativistic anharmonicity to drive adiabatic fast passage downward. This would leave the particle in the ground states of both cyclotron and axial motion, sampling a very small range of magnetic fields and ready for a cyclotron or anomaly transition attempt for a $g/2$ lineshape.

There are several challenges that must be overcome to use this technique in a $g/2$ measurement. One difficulty is that the axial motion is in thermal equilibrium with the amplifier, so cooling the electron to the sub-1 mK ground state requires decoupling it from the detection circuit. Efforts are underway to develop a piezoelectrically actuated RF switch 1) that can detune the resonant detection circuit without compromising Q and 2) that works at low temperature and high magnetic field. A switch of this type was developed by a group at Mainz [132], but further development is ongoing in our group to reduce capacitance enough to avoid disturbing our higher-frequency 200 MHz detection system[3].

Another challenge is driving the cooling transition at a high enough rate. Because the starting axial state is $n \approx 1000$, the sideband cooling sequence would comprise 1000 sideband transitions; afterward, the particle would need to decay or be driven

[3]Thanks to Jan Makkinje for his development of a first prototype RF switch in our group.

1000 cyclotron levels back to the ground state before an attempted transition for a lineshape. All this must happen between the two axial frequency measurements that are compared to determine whether a transition has occurred, but without allowing enough time for axial frequency drift to compromise detection fidelity.

The need to drive these sideband transitions at a high rate motivates efforts to increase the microwave drive power delivered to the trap. Cavity modes affect the impedance presented by the trap to the microwave drive system and therefore the deliverable effective drive power. Far from resonance with any cavity modes, most power is reflected back upward rather than being admitted into the trap cavity, which results in a low transition rate. In contrast, driving on a resonant mode with the correct field geometry (TE/TM$_{1n(even)}$ at trap center) for the sideband transition results in both high transmitted power and mode-dependent field enhancement factors. Driving on a resonant "cooling" mode may be necessary to make cavity-assisted sideband cooling practical.

In the previous Harvard electron $g/2$ apparatus, all of these "cooling" modes were too close to strong-cyclotron-coupling modes for their frequencies to be chosen as cyclotron frequencies for $g/2$ data, as shown in the top plot of Fig. 5.3. The preliminary attempts at axial sideband cooling were made far from cooling modes, so the cooling rate was too low to be useful (though some transitions were successfully driven) [108, 27, 71]. The current-generation apparatus was designed with a different trap cavity aspect ratio in order to make available several cooling modes that are far from strong-coupling modes, enabling axial cooling at frequencies where $g/2$ data can be taken.

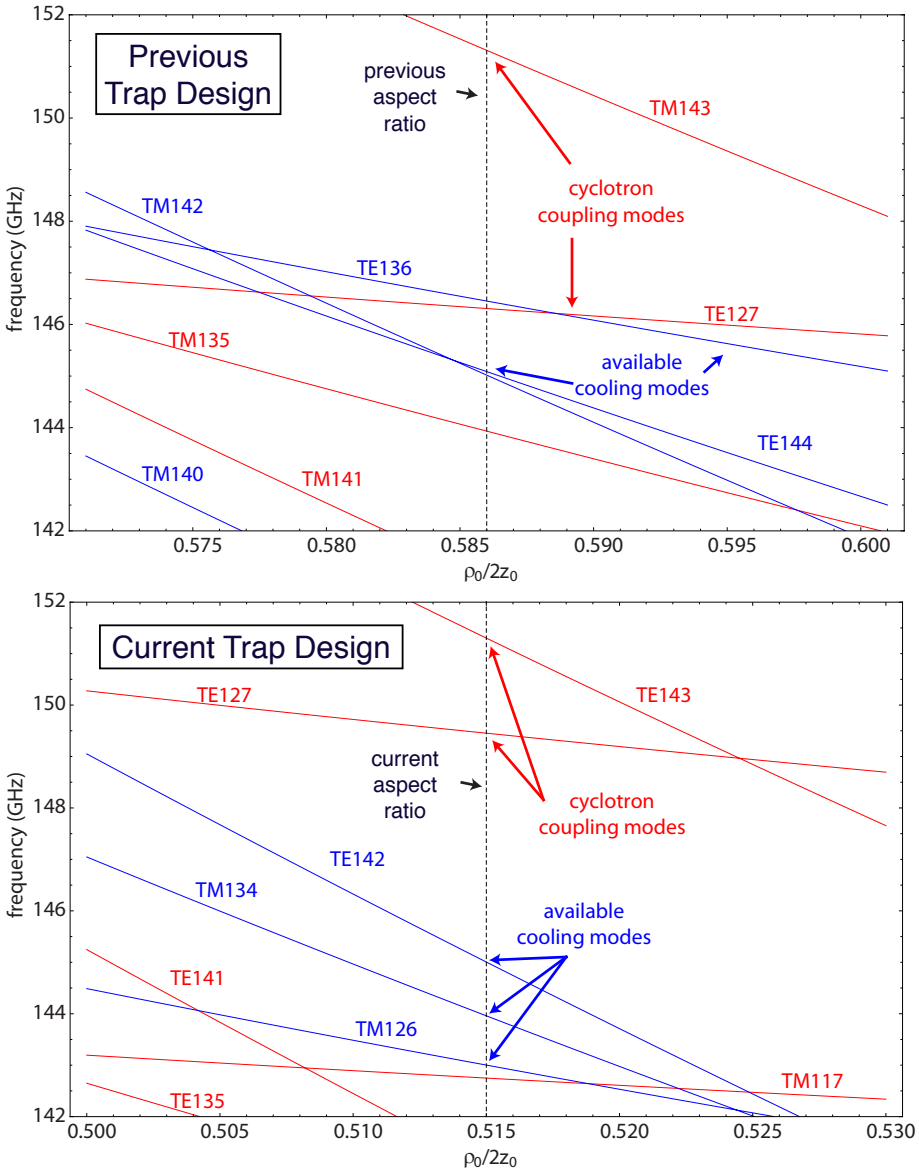

Figure 5.3: Frequencies of strong-cyclotron-coupling modes (red) and cooling modes (blue) in the desired $g/2$ cyclotron frequency region as a function of the ratio of trap radius ρ_0 to trap height $2z_0$. Trap aspect ratios in the previous Harvard electron $g/2$ apparatus and current apparatus are noted. Adapted from [71].

There are also other challenges to implementing cavity-assisted axial sideband cooling, such as remaining in resonance with the cooling transition despite the relativistic shift to the cyclotron frequency and enabling fast enough cyclotron transitions back to the ground state despite long cyclotron lifetimes [27]. However, with the trap design change implemented and an RF switch in development, cavity-assisted axial sideband cooling is a promising technique for eventual use in $g/2$ measurements in the current-generation apparatus.

5.3 Mode Mapping

To find good field values for taking $g/2$ data and to correct for mode-induced cavity shifts, it is necessary to know the frequencies and field geometries of cavity modes in the vicinity of the field values used for a measurement. (A 145.5 GHz cyclotron frequency seems like a promising choice of frequency based on Fig. 5.3.) Mode locations can be calculated analytically for a perfect cylinder, but slits between electrodes and holes in endcaps lead to small offsets in mode frequencies and lowered mode Q values. Therefore, the frequencies and widths of the many modes in a range of few 10s of GHz must be measured. A "map" of modes in frequency space is made using the "parametric mode-mapping" technique, described below, and modes are identified as $\mathrm{TE}/\mathrm{M}_{mnp}$ by comparison to the predictions for an ideal cylinder. Once $g/2$ datataking fields have been chosen, detailed measurements of the coupling of a single electron to cavity modes at those frequencies make it possible to correct for the cavity shift.

The parametric mode-mapping technique was introduced in [88, 133] and its ap-

plication to the best electron $g/2$ measurement is described in [4, 27]. This section reports preliminary parametric mode-mapping data in the current-generation apparatus.

5.3.1 Driven Parametric Oscillations

When a charged particle in a harmonic Penning trap is axially driven at twice its natural axial frequency (one example of a "parametric" drive), its motion is governed by the Mathieu equation (see, e.g., [134]):

$$\ddot{z} + \gamma_z \dot{z} + \omega_z^2 \left\{1 + h\cos\left[(2\omega_z + \varepsilon)t\right]\right\} z + \frac{2C_4}{1+C_2}\omega_z^2 \frac{z^3}{d^2} + \frac{3C_6}{1+C_2}\omega_z^2 \frac{z^5}{d^4} = 0, \qquad (5.8)$$

where h is drive strength, ε is drive frequency difference from $2\omega_z$, and all other variables are defined as in Ch. 2. Above a threshold parametric drive strength $h_T = 2\gamma_z/\omega_z$, the particle oscillates at ω_z. Successive cycles add energy to the particle's motion until its amplitude is limited by the anharmonic C_i-dependent terms proportional to z^3 and z^5. For a drive frequency that is twice the oscillation frequency, there are two stable phases of the excitation 180° apart, called the two "limit-cycles" (observed in [88]). Excitation is observed in a frequency range $\omega_z \pm \varepsilon_\pm$ that expands with increasing drive strength, with a boundary given by the hyperbola

$$\varepsilon_\pm = \pm\frac{1}{2}\omega_z\sqrt{h^2 - h_T^2}. \qquad (5.9)$$

Fig. 5.4 shows this boundary and describes how oscillation behavior differs in different parts of drive parameter space. No excitation occurs in region O and excitations always occur in region II. For $C_4 > 0$, region I is also quiescent, and both zero excitation and large excitations are solutions to Eq. 5.8 in region III. There, the

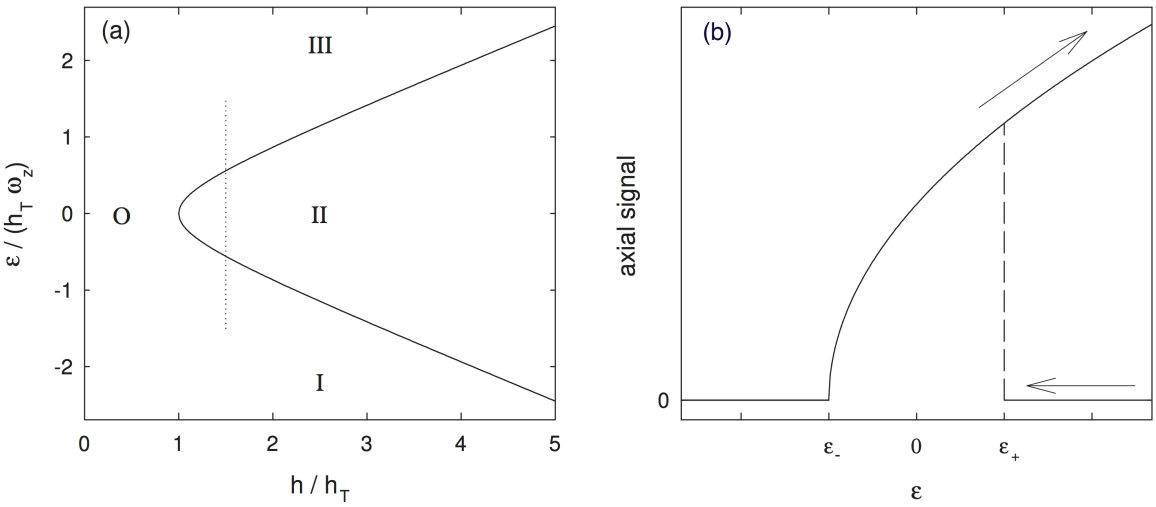

Figure 5.4: (a) Regions of varying behavior of parametric oscillations for varying drive strengths h and drive frequency differences ε from ω_z. (b) Hysteresis in oscillations for upward and downward frequency sweep directions on the slice through phase space marked by the dotted line in (a). From [27].

observed behavior shows hysteresis depending on how drive frequency and strength are changed over time (Fig. 5.4b). For $C_4 < 0$, regions I and III are switched.

These equations describe a single particle; behavior for a parametrically driven cloud of electrons is more complex. Naïvely, one might predict that in a cloud, the electrons would occupy each of the two 180°-separated phases in equal numbers, resulting in zero net axial signal. However, unequal occupation of the two states is observed [88]. The exact nature of the symmetry-breaking mechanism that enables this synchronization is not fully understood. It has also been empirically observed that in some parts of parameter space, the signal size is affected by the coupling strength of the electrons' cyclotron motion to microwave cavity modes [135, 88]. This is also poorly understood, but it is believed to originate from axial-radial coupling that arises within a cloud. Because energy can be exchanged between axial and cyclotron degrees of freedom, it is plausible that the faster loss of cyclotron energy via radiation

near a strong-cyclotron-coupling mode could affect the degree of synchronization of axial motion [136, 27].

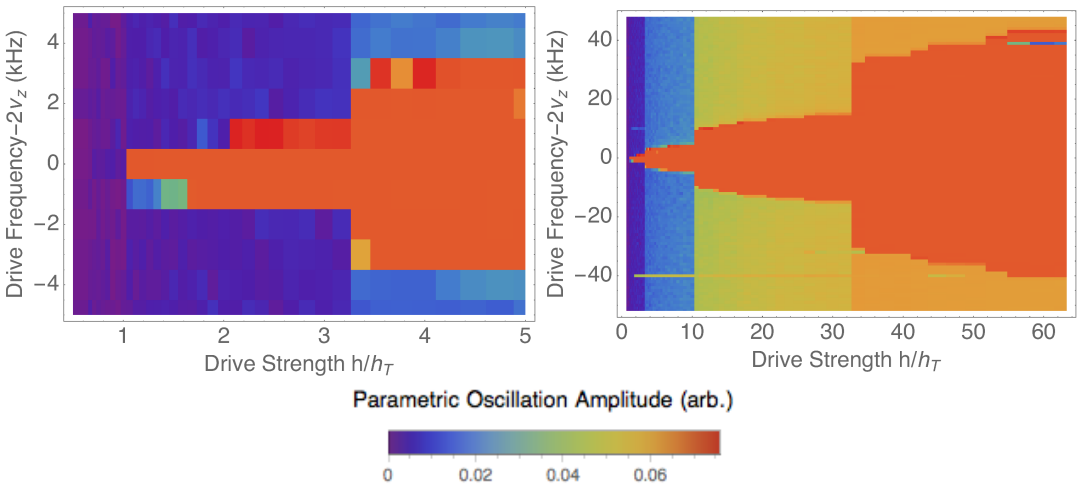

Figure 5.5: (left) Parametric oscillation amplitudes for a cloud of about 230 electrons are shown in the same region of h/h_T parameter space as Fig. 5.4a. (right) A dataset for a much larger range of drive strengths shows multiple "shoulders."

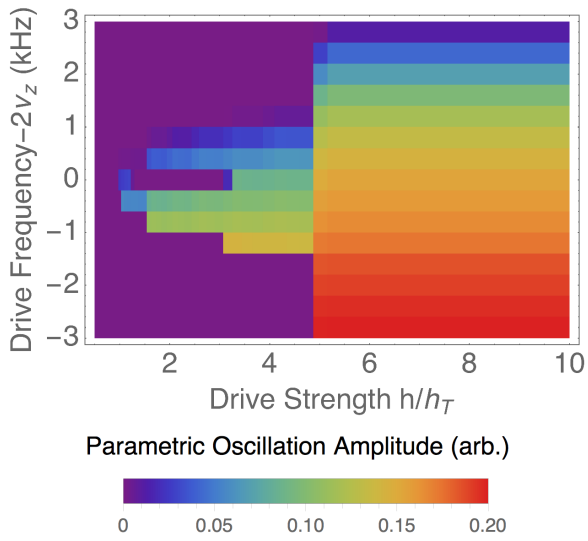

Figure 5.6: Parametric oscillations in the ∼50-electron cloud used for preliminary mode mapping, with one shouulder visible at $h/h_T \approx 5$.

Regardless of the exact mechanism, parametric oscillations' dependence on cavity

mode coupling can be exploited to map the trap's cavity modes in frequency space [137, 88]. As a first step toward mapping cavity modes in the current apparatus, parametric oscillations were driven in a cloud of about 230 electrons trapped in the precision trap, with observed oscillation amplitude shown in Fig. 5.5 for ramps upward in drive strength at multiple frequencies. The shape of the excited region appears to be locally hyperbolic in slices of parameter space, though with a "shoulder" at about $h/h_T \approx 3.2$ that marks both an increase in observed oscillation amplitude in the quiescent region and a widening in frequency of the excited region. Additional shoulders are observed at higher drive strengths (Fig. 5.5, right). Hysteresis as in Fig. 5.4b was observed when the drive frequency was swept (data not shown). Fig. 5.6 shows parametric oscillation amplitude in the electron cloud used for preliminary mode-mapping (described in the next section). Here, the amplitude variation within the excited region that was predicted in Fig. 5.4b is visible (with opposite frequency dependence because of opposite sign of C_4).

In the interest of time, and recognizing that understanding the details of parametric oscillations in clouds is a goal secondary to the main thrust of the $g/2$ measurement, saturation effects in the drive and detection systems were not systematically investigated and ruled out as causes of the shoulders. These data should therefore be considered preliminary; they are only a first observation of parametric excitations in this apparatus and a suggestion of possible future topics for exploration of these phenomena, particularly if difficulty is encountered in mode-mapping.

5.3.2 Parametric Mode-Mapping

By monitoring the amplitude of parametric oscillations of an electron cloud while sweeping the magnetic field, the electrons' cyclotron motion can be swept into and out of resonance with cavity modes, creating a parametric mode map. Mode maps made in the previous Harvard electron $g/2$ apparatus are shown in Fig. 5.7.

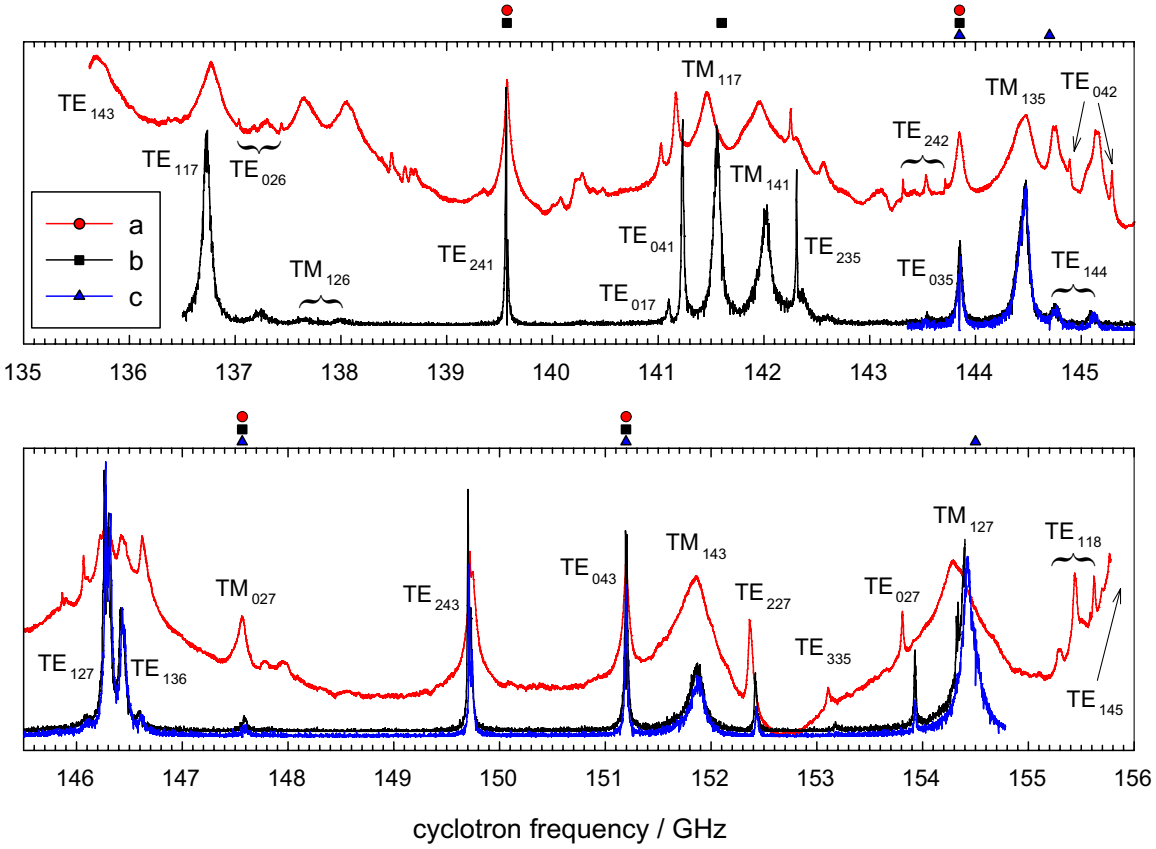

Figure 5.7: Parametric mode maps in the previous Harvard electron $g/2$ apparatus. From [27].

Modes are identified by comparison to the predicted mode structure for an ideal cylindrical cavity. Mode frequencies and Q are then extracted by fitting. Though detailed simulations to precisely predict the effect of trap imperfections on modes have not been done, observed frequency shifts are compatible with general expecta-

tions—for example, surface currents in TM_{1np} modes are interrupted somewhat by electrode slits, and these modes are indeed shifted more from the perfect-cylinder predictions than modes without these slit-impeded currents [27].

Though repeated parametric mode maps in a single apparatus agree on the frequencies of modes and are therefore reliable for the purpose of mode identification, the degree of parametric oscillation amplitude dependence on mode coupling has been found to be inconsistent. Mode maps made in an early 4.2 K apparatus reliably displayed this dependence [136, 133], but the majority of attempted mode maps in the previous Harvard electron $g/2$ apparatus, at 100 mK but with a nearly identical trap electrode stack design, showed no variation of parametric oscillation amplitude with magnetic field [135, 110, 27]. Efforts to create a high-success-rate mapping protocol were unsuccessful; subtle effects related to temperature, presence of electrical noise, electron cloud size, or location in the parametric excitation parameter space are possible contributors [27]. Because the cause of inconsistency in those mode maps is not understood, it was not known ahead of time how easy it would be to produce them in the much-changed current-generation apparatus. To assess this, a preliminary test of mode-mapping was done in the current-generation apparatus even before the apparatus was fully assembled and ready for a final, detailed mode characterization.

Several attempts were made at mode mapping using a variety of parametric drive strengths and magnetic field sweep directions and speeds. Most attempted maps showed some correlation with mode structure. Several maps are shown in Fig. 5.8. Though the maps at different drive strengths look quite different, all share common features that indicate the maps are indeed probing a consistent underlying mode

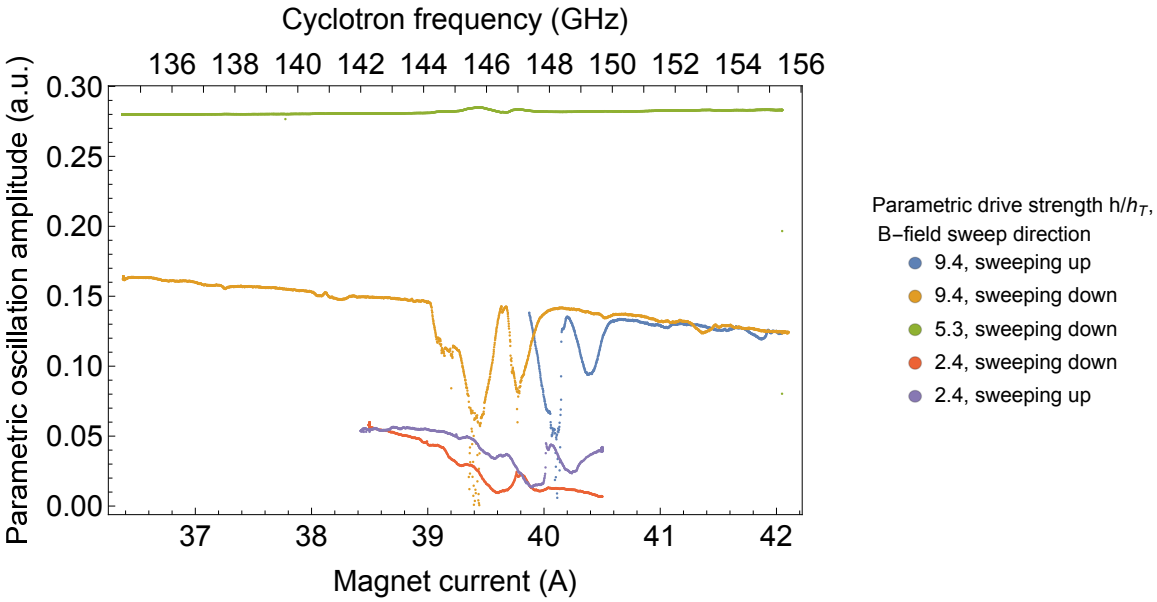

Figure 5.8: Results of the first attempts at mode mapping in the current-generation apparatus. Mapping was done with the ∼50-electron cloud of Fig. 5.6. (Magnetic field ramp speeds vary.)

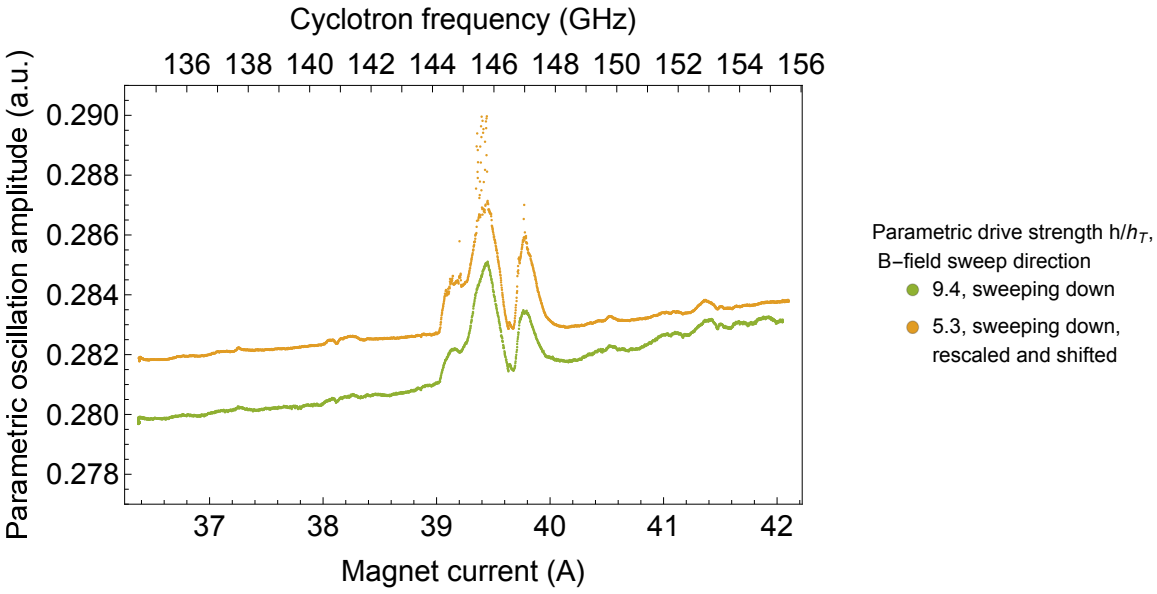

Figure 5.9: This plot shows the same data as in the yellow and green curves in Fig. 5.8, but with the yellow curve's amplitude inverted, rescaled, and shifted to allow visual comparison to the green curve. Despite the opposite sign of the amplitude dependence on cavity mode coupling, features large and small line up remarkably well between the two maps.

structure (Fig. 5.9). As expected, hysteresis in mode positions was observed between maps made by sweeping downward in frequency and those made by sweeping upward in frequency. This hysteresis will be reduced in the final mode maps by ramping the magnetic field much more slowly and will be taken into account in mode map interpretation. In all of these maps except the one with $h/h_T = 5.3$, the amplitude of parametric oscillations appears to decrease when in resonance with a mode, rather than increase as in the previous-apparatus maps in Fig. 5.7. These variations highlight the complexity of the interaction between cyclotron and axial motion in an electron cloud and the lack of understanding of the exact symmetry-breaking mechanism underlying mode-mapping. Further study of this phenomenon and of the shoulder features in the parametric excitation parameter space would be interesting, though tangential, side projects.

These preliminary mode-mapping data were taken in a single day between projects occupying apparatus time for work on positron loading, amplifier improvement, and pulsed particle transfer. Though the maps have fewer features than will be needed in a final map, the fact that correlation with cavity modes was observed on $>50\%$ of attempts on the initial day of tries is encouraging evidence that the conditions for parametric mode-mapping can be created in this apparatus. Once the trap electrode stack is in its final form, careful maps like those in Fig. 5.7 will be generated, individual modes will be identified, and final determinations of mode frequencies and Q values will be made.

5.4 Effect of Positron-Loading Hole on Cavity Modes

Slits between electrodes and holes in electrodes can allow microwave energy to leak out of the trap, lowering a mode's Q and broadening it in frequency. This, in turn, causes stronger coupling to an ostensibly detuned trapped particle, shifting its cyclotron frequency and lowering its cyclotron lifetime. To prevent these leaks, in both the previous Harvard electron $g/2$ apparatus and the current generation apparatus the 343 μm (0.0135") diameters of the FEP hole in the precision trap's bottom endcap and the positron hole in the top endcap were chosen to be significantly smaller than the 2 mm cyclotron wavelength. The existing holes have a depth of 245 μm (0.0096"). Also, $\lambda/4$ choke flanges were built into the 132 μm (0.0052") wide slits between electrodes to reflect microwave energy back into the trap cavity (Fig. 5.10 and Fig. 2.6).

However, the positron-loading hole's small radius might be an impediment to transferring particles from the positron accumulation trap to the precision trap (Ch. 6). Therefore, simulations and analytical calculations were used to explore how hole geometry could be changed without compromising mode Q.

5.4.1 3D Numerical Simulations

To explore the feasibility of using 3D electromagnetic simulation software to inform hole size choice, simplified models of the precision trap with varying hole sizes were created and the Eigenmode Solver in CST Microwave Studio 2013 was used to locate and compare the characteristics of resonant modes.

Fig. 5.11 shows the effect of increased hole size on a cavity mode near the cyclotron

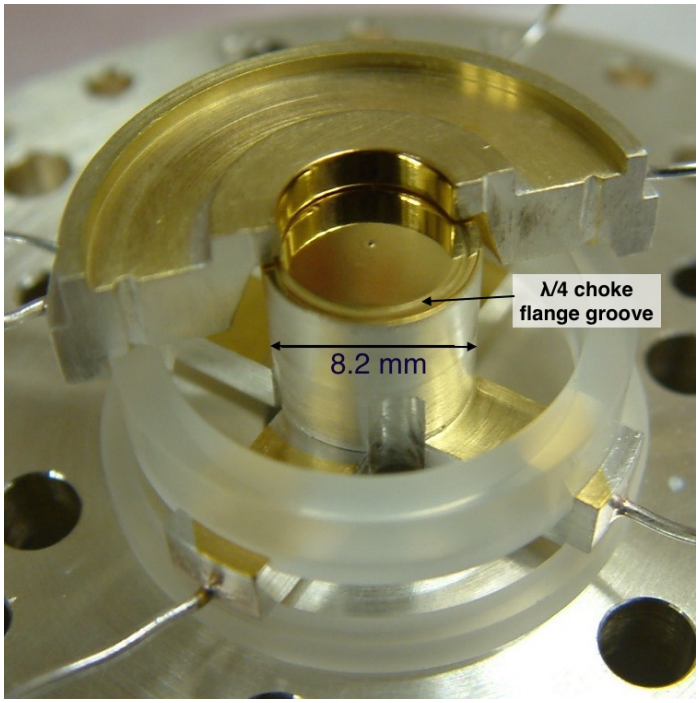

Figure 5.10: The partially-assembled precision trap with an endcap and half of one compensation electrode visible. A positron/FEP hole is at the center of the endcap's face. The $\lambda/4$ choke flange is on the edge of the top face of the endcap, in the gap between the endcap and the compensation electrode.

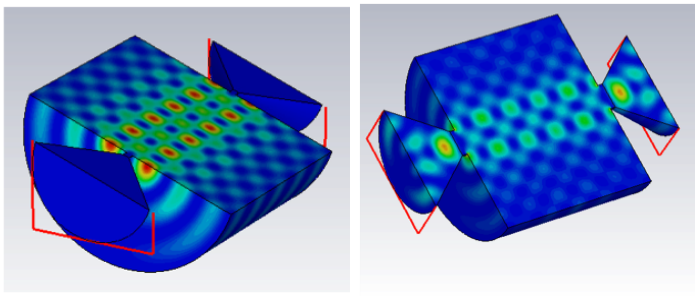

Figure 5.11: Energy density in a resonant mode's electric field along a cross section of the trap cavity, including the conical spaces just outside the positron-loading and FEP holes in the endcaps, as simulated by CST Microwave Studio's Eigenmode Solver.

frequency. While the model with the existing hole size has very low energy density outside the main cavity, increasing the hole size by a factor of five allows a lot of energy to leak out the hole, as well as modifying the calculated the mode field profile within the main cavity.

Simulation results for this and other strong-coupling modes confirmed predictions that any allowable hole size increase would have to be by less than a factor of five, i.e., subwavelength diameter. Ultimately, though, this software was found not to be the optimal tool for making precise design decisions. The Eigenmode Solver was not built to calculate Q, running the simulations for all relevant modes was time-consuming, and the boundary conditions allowed by the software were not sufficiently flexible to create realistic models. CST Microwave Studio's Frequency-Domain Solver allowed time variation, which made it more useful for calculating Q, but it also had serious boundary value constraints. It could also only do calculations for one frequency at a time, making it even more time-consuming than the Eigenmode Solver for covering the needed frequency range. With enough time and effort, a combination of these solvers or other 3D software could likely be made to work, but this was not a sensible investment given the cost-to-benefit ratio. 2D numerical simulations might also give similar results more quickly. However, to further decrease computation time and to develop intuition, we instead used an analytical model to assess the effect of hole size change on mode Q.

5.4.2 Analytical Calculations

The effect of hole geometry on radiation leakage depends on the transmission rate of microwaves through a hole with sub- but near-wavelength characteristic size. Transmittance of electromagnetic radiation through a hole with radius $r \ll \lambda$ in an infinitely-thin perfectly-conducting plate was calculated in [138, 139]. Others introduced corrections for finite plate thickness and larger apertures [140, 141]. An analytical treatment of transmission in this regime in [142] was adapted for analyzing the positron hole. In this calculation, the interior of the hole is treated as a waveguide and the coupling of incoming and outgoing radiation with its modes is calculated. In this regime, both hole depth h and radius r are $> \lambda_c/10$; this means that many modes contribute to transmittance. The normalized-to-area transmittance is given as

$$T = \left(\frac{2\pi r}{\lambda}\right)^4 e^{-2h\sqrt{\left(\frac{x'_{11}}{r}\right)^2 - \left(\frac{2\pi}{\lambda}\right)^2}} \times \left[C^\infty + (C - C^\infty)\, e^{-\frac{\delta h}{r}} + \left(\frac{2\pi r}{\lambda}\right)^2 \left(C_2^\infty + (C_2 - C_2^\infty)\, e^{-\frac{\delta h}{r}}\right)\right] \tag{5.10}$$

where x'_{11} is the first zero of $J'_1(x')$, $C = \frac{64}{27\pi^2}$ is analytically calcluated, and $C^\infty = 0.1694$, $C_2 = 0.33$, $C_2^\infty = 0.215$, and $\delta = 6$ are phenomenologically fitted from analytically calculated mode contribution sums in [142].

Fig. 5.12 shows the log of the ratio of transmitted (leaked) power for different possible combinations of hole radii and depths to the power leaked for the existing dimensions. The "0" contour corresponds to the power transmitted through the existing-size hole, which is known from the previous Harvard electron $g/2$ experiment to be compatible with a precise $g/2$ measurement. Constant transmitted power (and therefore constant effect of the holes on Q) can be approximately maintained in this

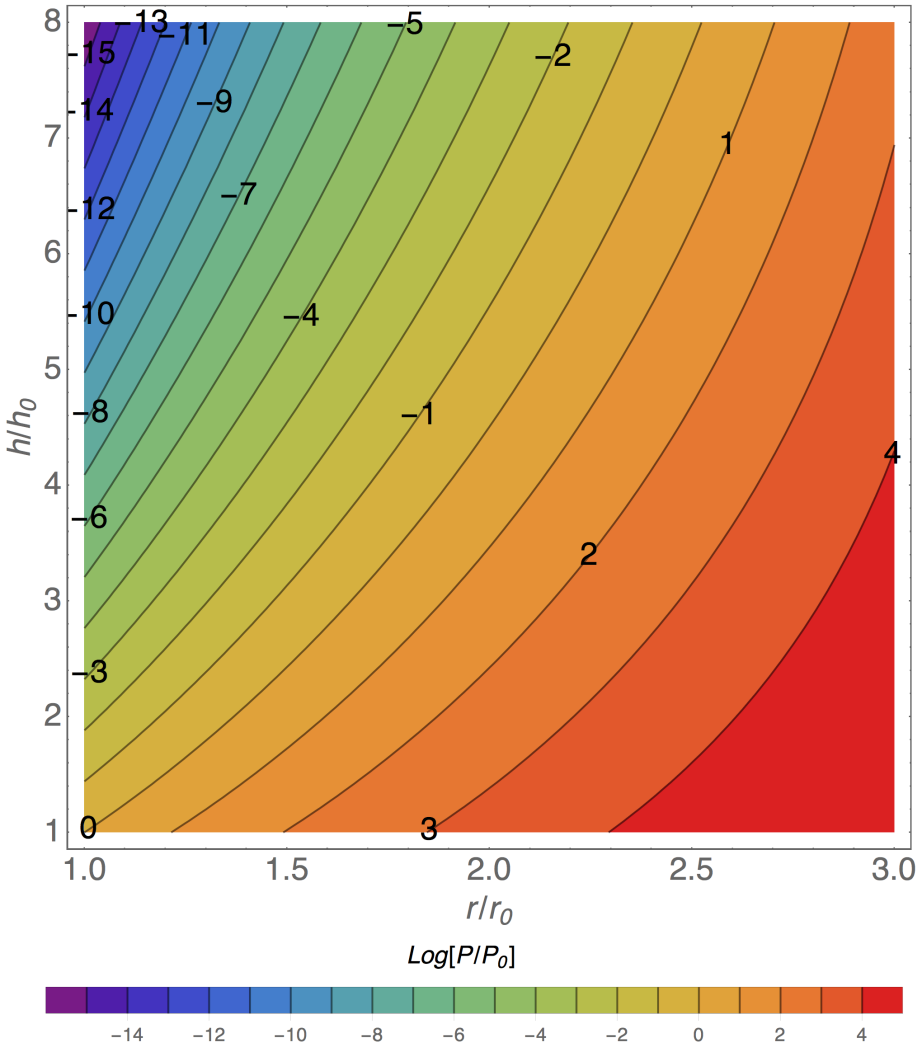

Figure 5.12: Map of the effect of positron/FEP hole geometry on energy leakage. The h/h_0 axis (hole depth in units of current hole depth) and r/r_0 axis (hole radius in units of current hole radius) are both on linear scales. The colors and contours represent P/P_0 (the total power transmitted through the FEP and positron holes) on a log scale. For example, the "0" contour line shows (h, r) pairs that preserve existing transmitted power ($10^0 = 1$). Combinations of depth and radius along the '0" line and in all areas "bluer" than this (e.g., the "-1" contour line, for which power transmission is $10^{-1} = 0.1$ times its current value) should not cause mode Q problems if chosen as the new hole dimensions.

region of parameter space by choosing h and r values obeying $h = 0.9r^{2.3}$. This relation gives a rough guide to the usefulness of increasing hole depth to compensate for increased hole radius. As covered in Sec. 6.4.3, the heating rate for a positron passing through the hole is expected to go like r^{-4} to r^{-2}, depending on which heating mechanisms are dominant. Total heating is approximately proportional to time spent in the hole, so assuming constant particle velocity, it should also go like h. Total heating therefore should go approximately like $r^{-1.7}$ to $r^{0.3}$, making it likely that increasing both hole radius and hole depth along a contour would result in less heating. In addition, the cross-sectional area available to a transiting positron goes like r^2, with larger radii reducing the detrimental effects both of magnetron heating and of any trap misalignments. These results suggest that a wider, deeper positron hole (and FEP hole, to preserve symmetry) should be implemented in the new trap design proposed in Ch. 7 if electrodes are remade.

It might also be permissible to increase hole radius without increasing depth. The effect of power loss through the holes on the Q of any given mode depends on that mode's particular field geometry in the local region of the hole. If the holes are not the factors limiting Q of the most important modes, slightly increased power loss could be acceptable. A rough estimate taking into account field enhancements at $\rho = 0$ of the strong-cyclotron-coupling modes near 145 GHz suggests that a hole radius increase to 1.5 times the existing radius—i.e. diameter $\leq \lambda/4$, with an area increase of only about a factor of 2.3—should not load down any mode to $Q < 10,000$, still well above Q of analogous modes in the previous Harvard electron $g/2$ apparatus. This improvement is modest and is not necessarily worth the trouble of modifying the electrodes, but the

calculation was also quite conservative in its approximations. To do more detailed, mode-specific calculations in the hope of finding slightly more leeway, useful references to follow could include [143, 142, 126]. However, also deepening the hole if it is widened is the best choice; this is the strategy recommended here. One final note about this design change is that it will be critical to assess how tight machining tolerances can realistically be made on both radius and depth and be accordingly conservative in choosing final dimensions.

Chapter 6

System for Pulsed Transfer of Positrons to Precision Trap

To measure positron $g/2$, a positron must be transferred from the positron accumulation trap ("loading" trap) into the precision measurement trap through the 0.34 mm diameter hole in the center of the precision top endcap electrode. This has proven to be very challenging because of tight constraints on geometry and RF electronics in the precision measurement trap. This chapter describes the development and installation of the hardware for pulsed positron transfer, the initial failed efforts to transfer between traps, and the experimental tests and computer simulations done to understand the cause of these failures. This sets the stage for a reconfiguration proposed in Ch. 7 that is expected to make particle transfer easier.

6.1 Techniques for Particle Transfer

Two techniques developed by the ATRAP experiment for moving particles axially in a stack of open-endcap Penning trap electrodes—the slow "inchworm" method and the fast "pulsed" method [144, 120, 145]—have been considered for use in transferring positrons to the $g/2$ precision measurement trap.

6.1.1 Slow "Inchworm" Method

The "inchworm" moving technique in a stack of open-endcap electrodes proceeds as follows [120]:

1. The particle(s) begin in a potential well that is established primarily by the voltage V_1 on a single electrode (e.g., the ring electrode of an open-endcap trap). For example, $V_1 = -5$ V where all surrounding electrodes have $V = 0$.

2. The voltage on the adjacent electrode, V_2, is set to a voltage $> V_1$ to make a deeper extension to the well, e.g., $V_2 = -8$.

3. V_1 is set to 0, leaving the particle(s) trapped only on the second electrode.

4. V_2 is set to the initial value of V_1.

5. The process is repeated with successive adjacent electrodes until the particle(s) are in the desired location.

In the current apparatus, this technique was tried without success for transferring positrons from the positron accumulation trap into the precision measurement trap. To determine whether the problem was related to the small top endcap hole, the

method was also used to move particles around the loading/transfer trap stack without going through the hole to the precision trap. Significant particle loss was noted, with larger losses for transfer processes with more steps.

Loss of particles confined in wells with very low axial frequency ("long wells") has been observed in ATRAP [146], and this is believed to have contributed to particle losses in these $g/2$ "inchworm" attempts. Long wells can come about when multiple adjacent electrodes are set to the same frequency, or if even a single electrode has a large length-to-radius ratio. In long wells, confining potentials are weaker and the magnetron frequency is reduced. This increases the particles' susceptibility to magnetron heating from any noise source that is stronger at lower frequency, including patch potentials on electrodes. Heating can be minimized by reducing time spent in long wells, but because of 0.1-10 s time constants on the low-pass filters for electrode voltage bias lines, there is a lower bound on the speed of this type of transfer.

6.1.2 Fast "Pulsed" Method

To avoid heating and loss in long wells—especially through a long, narrow electrode in which this well shape is inevitable—ATRAP developed a fast "pulsed" technique [144]. Fig. 6.1 shows the electric potential profile on-axis for pulsed transfer in the ATRAP apparatus, with cartoons of positron positions at different times. Electrode voltages are applied to create a double-well potential structure. A negative voltage pulse is applied to the two electrodes that form the inner walls of the wells, thereby releasing the positrons from the left well and opening the right well so that they can enter. When the particles are in the right well, the voltage pulse is ended to

reestablish the right well's left wall and trap the positrons in the right well ("shutting the door").

This pulsed method was chosen for positron transfer in the electron/positron $g/2$ experiment. Fast transfer in a single pass should minimize both the long-well effects in the transfer electrodes and any heating related to interaction with surface impurities within the small channel in the top endcap.

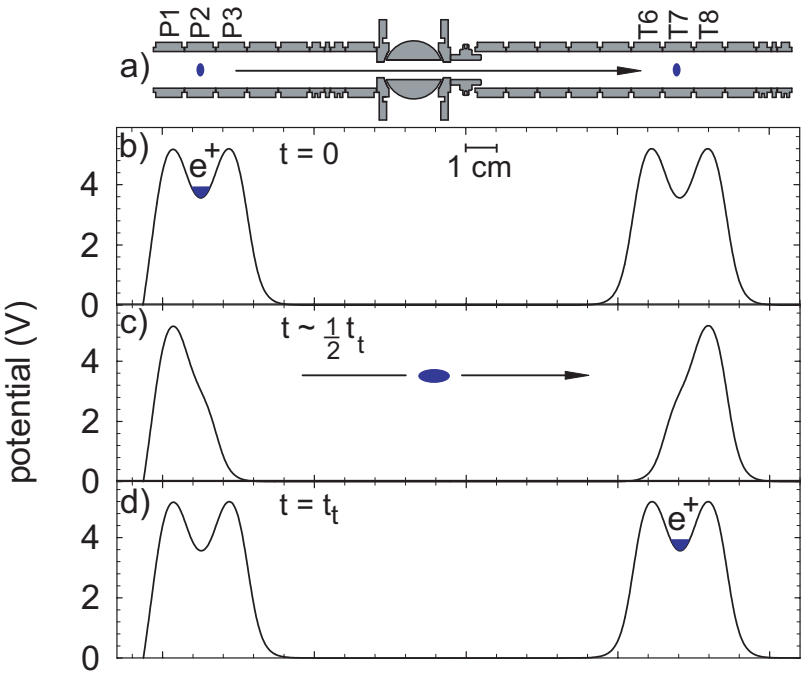

Figure 6.1: Pulsed transfer scheme in ATRAP apparatus. From [145].

6.2 RF Electronics Design Challenges

The tightly constrained geometrical and RF properties of the $g/2$ trap, crucial for enabling the precision measurement, complicated the design of a system for pulsed positron transfer.

6.2.1 Choice of Pulse Electrode

In the positron accumulation trap, the loading bottom endcap (LBEC) was chosen as the "pulse" electrode—the electrode whose voltage is briefly lowered to release particles. The two possible choices[1] for a "pulse" electrode in the precision measurement trap—for "shutting the door" to catch particles—are the top endcap (TEC) and the top compensation electrodes[2] (TC). (See Fig. 6.2 for a labeled cross section of both traps.) Fig. 6.3 shows possible potential landscapes for these two configurations.

Because trap geometry allows deeper wells to be created with TEC than with TC (Fig. 6.3b vs. 6.3d), it was originally chosen as the electrode for "shutting the door" in the precision trap [90]. However, this turned out to not work because of TEC's connection to the "high" side of the 200 MHz resonator for detection (Ch. 4), for the following reason. Ideally, the "pulse" voltage applied to an electrode would be a perfect rectangular function, turning on and off quickly. The relevant timescales are tens of ns for time-of-flight and about 10 ns for "shutting the door." A voltage pulse with such sharp edges has Fourier components near 200 MHz, which are severely disrupted by the 200 MHz resonator. This gives rise to unwanted ringing with an amplitude comparable to the total amplitude of the pulse. Any electronics to improve the matching and pulse shape—e.g., a 50 Ω resistor in parallel—create unacceptable loss in the resonator, degrading its Q. The resonator-caused ringing eliminated TEC from consideration as the "catching" electrode, leaving TC as the pulse electrode in

[1] Though it is possible to create a well on the bottom compensation electrode with the ring as the pulse electrode, it is both 1) undesirable to risk reducing axial frequency stability by installing additional electronics on the ring electrode and 2) difficult to create a well of the right shape using the bottom compensation electrode.

[2] The top compensation electrodes are tied together at RF.

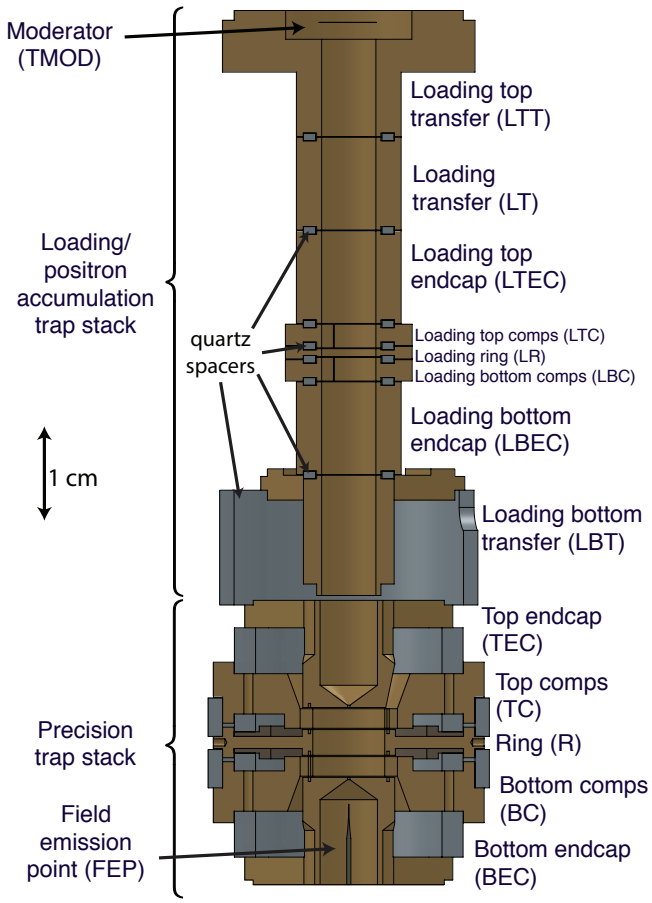

Figure 6.2: Cross section of the combined stack of Penning trap electrodes and spacers comprising the precision trap (bottom), the positron accumulation (or "loading") trap (center), and transfer electrodes (between traps and above positron accumulation trap). Repeated here from Fig. 3.2 for convenience. Adapted from [71].

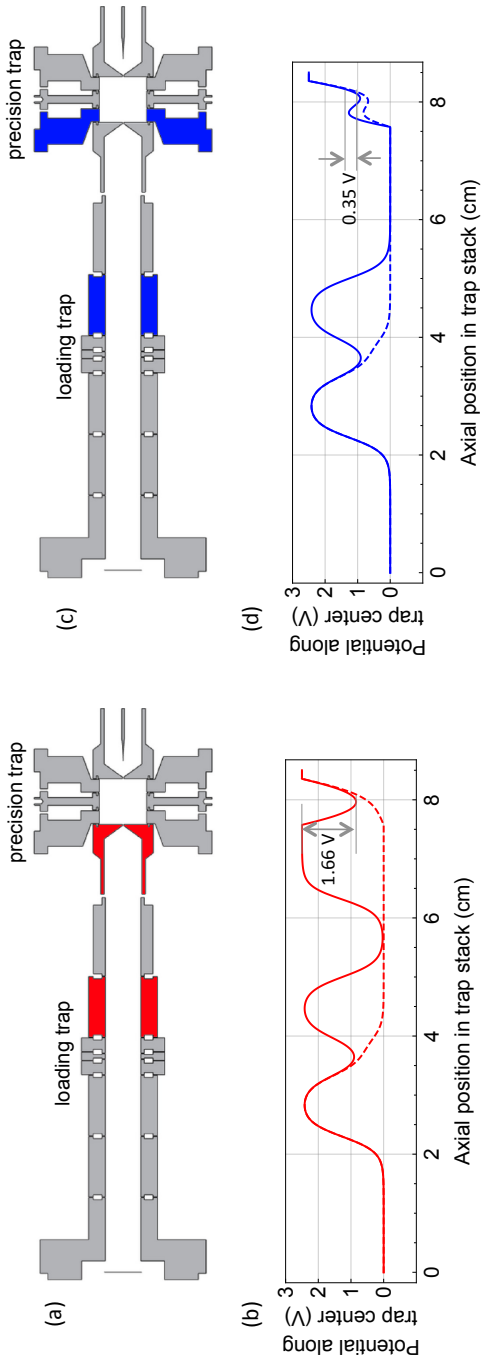

Figure 6.3: Two possible "pulsing" configurations. A 2.5 V pulse on the precision top endcap (TEC), shown in red along with the loading bottom endcap electrode in the rotated electrode stack cross section in (a), can lower the wall of a deep "catching" well (b). However, because of reactive electronic components connected to TEC, a rectangular pulse applied to TEC experiences severe ringing at the electrode. Applying a 2.5 V pulse instead to the top compensation electrodes (TC), shown in blue in (c), can lower the wall only of a shallower well (d), but pulse shape is much better.

the precision trap.

6.2.2 Pulsing Electronics

Matching electronics similar to those described in [145, 147] were installed at the pulse lines' terminations at the electrodes. These electronics are shown in Figs. 4.1 and 4.2. The matching is imperfect; especially in the case of the top compensation electrode with its additional reactive components, it would have been ideal to design the pulse electronics by beginning with a full knowledge of all circuit components and working backwards to the correct impedance-transforming circuitry. However, as with other wiring around the 200 MHz resonator (described in Sec. 4.2.3), parasitic capacitances between circuit elements and electrodes prevented the development of a fully accurate circuit model. Even with a model, the engineering required to adapt to such unusual reactive loads—and to be sufficiently tunable in case parasitic capacitances change on cooldown—would likely have been prohibitively time-consuming and expensive. Various values and configurations of resistors and capacitors in the pulse wiring at the electrodes were tested in situ, and the combinations shown in Figs. 4.1 and 4.2 gave matching that resulted in the best combination of pulse shape and size with a pulse amplifier designed for 50 Ω.

All electrodes are RF-grounded at the pinbase by at least 200 pF for detection reasons described in Sec. 4.2.3, which reduces pulse height and affects impedance matching. Because the top compensation electrode is part of the electrically "low" side of the 200 MHz resonator, it is RF-grounded by few-nF-scale capacitors. The resulting capacitive division means a larger pulse must be applied to have the same

effect on trap potentials. To increase the fraction of the pulse voltage at the hat that reaches the electrodes, it was necessary to exchange the 1 m section of lossy stainless steel microcoaxial cable between the room-temperature and 4 K stages of the experiment for copper microcoaxial cable, which increased the heat load on the helium bath in the dewar. It was also necessary to omit the cold voltage dividers that provide noise suppression on all other RF drive lines. To compensate, Johnson noise from room temperature can be reduced by shorting the pulse lines at room temperature when not in use rather than terminating them with 50 Ohm connectors as is sometimes done. Assuming a contact resistance of 0.1 Ω, this reduces the Johnson noise voltage by a factor of $\sqrt{50\ \Omega/0.1\ \Omega} \approx 22$.

Even with the changes described above, the division of the pulse due to the resonator's RF-grounding raises the input pulse voltage requirement beyond the capabilities of the 10 V saturated switch used to generate pulses in ATRAP. Therefore, two custom pulse amplifiers that take TTL (transistor-transistor logic) input from a pulse generator[3] and produce 100 V output were developed by Avtech Electrosystems, Ltd for this experiment. The Avtech AV-144B1-HUB and AV-144B1-HUC pulse amplifiers nominally have 2 ns and 10 ns rise/fall times, respectively. In practice, because the impedance presented by the pulse wiring and the trap is not 50 Ohms but is complex, pulse shapes at the electrodes are distorted. The "pulse-sharpening" electronics of the AV-144B1-HUB are more affected by this imperfect load during the pulse end (fall) than the start (rise), so this pulse amplifier is only useful on the loading bottom endcap, where the pulse end is not important. The AV-144B1-HUC is more symmet-

[3]Stanford Research Systems DG645

rical in rise and fall, and it is also less affected by the reactive load. It is therefore used on the precision top compensation electrode (TC), which 1) presents a more reactive load and 2) is where the pulse end shape matters for catching particles. For negative pulses, Avtech AVX-R2 inverters are used on the output of pulse amplifiers. Pulse size is controlled by installing in-line BNC attenuators. Both the inverters and the attenuators were tested and shown to have minimal effect on pulse shape.

The poor impedance matching described above causes distortion of pulse shapes and also creates frequency-dependent reflections in the pulse wiring that depend on cable length. Various cable lengths were varied while monitoring pulse shape, shown in Fig. 6.4. A length of 8.2 m was shown to optimize pulse shapes and was chosen for the final system design. Final pulse shapes on electrodes are shown in Fig. 6.5.

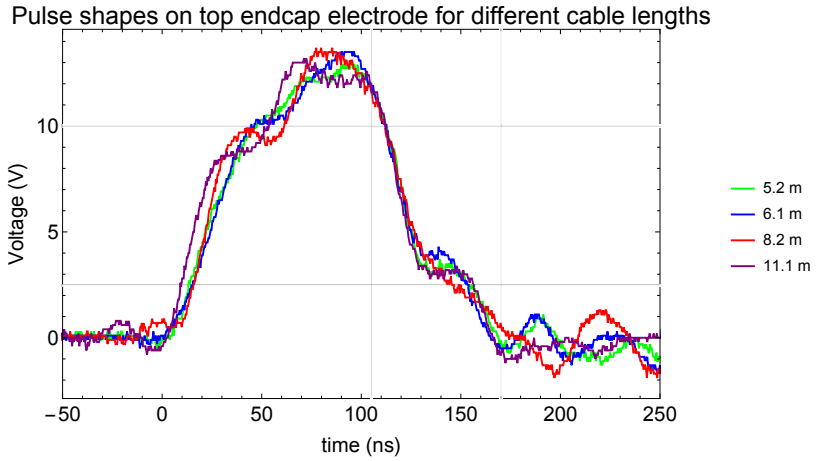

Figure 6.4: Pulse shapes for a variety of cable lengths. The 8.2 m cable (red) was chosen for the final design.

One final change in wiring was required to make pulsed positron transfer feasible. In previous $g/2$ experiments, top and bottom compensation electrodes had been tied together at DC. Simulations of the type described in the next section showed that

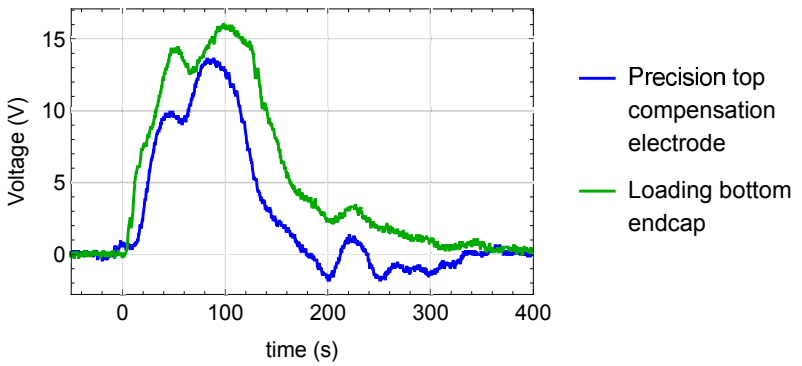

Figure 6.5: Voltage pulses on the precision top compensation and loading bottom endcap electrodes. Applied pulse height is 100 V for 110 ns. Measurement is done with 4 pF scope probe at room temperature. Pulse sizes are scaled in simulations to compensate for conductivity changes in microcoaxial cable at 4 K.

this constrains the parameter space available for pulsing far too tightly. Wiring was therefore redone to bias the top and bottom compensation electrodes separately, adding "comp check" lines (see Fig. 4.1) to make it possible to check that both halves of each of these two pairs of split electrodes remains properly DC-connected through cooldown.

6.3 Simulations of Pulsed Particle Transfer

Simulations of pulsed particle transfer were used to find good parameters—DC electrode voltages, pulse voltages, and pulse timing—for positron transfer. Simulations are built on Voltscalc, a C-language software package developed within this research group, which takes the geometry of an electrode as input and then calculates the spatial profile of the electric field it produces [148]. Results from Voltscalc were incorporated into a Mathematica program that takes the voltage applied to each $g/2$

trap electrode and sums the voltages to calculate the total electric potential at each axial position along the center of the trap [89]. A Mathematica implementation of the 4th-order Runge-Kutta algorithm was then used to simulate the dynamics of a charged particle in the presence of time-varying voltages applied to electrodes, including real measured pulse shapes. Parameter sets for which transfer between traps was successful were manually identified and optimized.

The result of a simulation for a locally optimal transfer parameter set is shown in Fig. 6.6 and Fig. 6.7. A positron begins in the precision trap. Pulses are applied to the loading bottom endcap and precision top compensation electrodes; the positron then moves to the precision trap, and the pulses end, leaving it trapped in the precision trap well. The voltages and pulse sizes and lengths applied to electrodes for these simulations are shown as Set A in Table 6.1.

6.4 Failure of Transfer Tests and Possible Causes

6.4.1 Transfer Attempts

Using the electron versions of the Set A positron-transfer parameters shown in Table 6.1, an attempt was made to transfer electrons from the positron accumulation trap to the precision measurement trap in the real apparatus. Electrons were used for transfer tests because they could be loaded from the field-emission point much more quickly than positrons could be loaded from the radioactive source, making each test faster and enabling more parameter sets to be tested. Transfer was attempted using the following procedure:

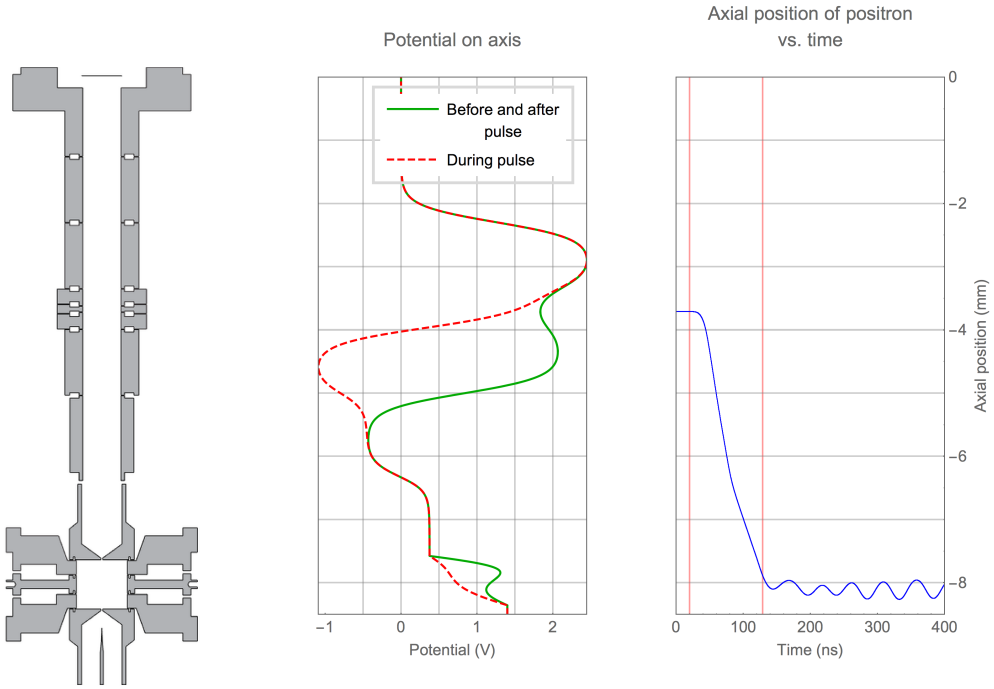

Figure 6.6: Cross section of electrode stack, potential on axis, and axial position of a positron vs. time for a successful simulation of pulsed transfer from the positron accumulation trap to the precision measurement trap. The position axis (vertical) is shared by all three subfigures. Pulse start and end times are marked by red vertical lines in the position vs. time plot.

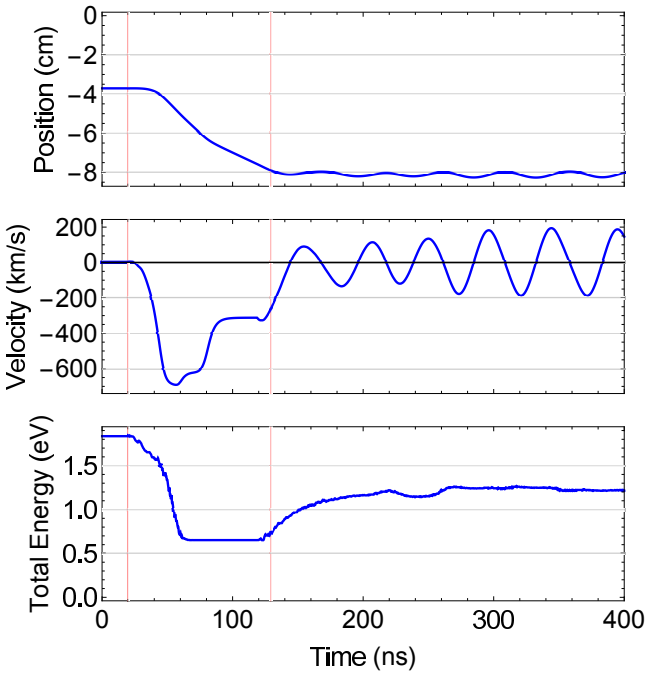

Figure 6.7: Position, velocity, and total energy of a positron vs. time for a successful simulation of pulsed transfer from the positron accumulation trap to the precision measurement trap. Pulse start and end times are marked by red vertical lines.

		Pre/post-pulse voltages			
	Measurement voltages	**Set A: transfer, pulsing on top comps, tested**	**Set B: pulse length tests**	**Set C: magnetron heating tests**	**Set D: transfer, pulsing on top endcap, proposed**
Pulse length	-	109 ns	varied	-	105 ns
Loading pulse voltage at electrodes	-	-3.45	-	-	-3.45
Precision pulse voltage at electrodes	-	-5.03	5.03	-	-3.56
TMOD voltage	0	0	-	-	0
LTT voltage	0	0	-	-	0
LT voltage	0	0	-	-	0
LTEC voltage	0	2.5	-	-	0
LTC voltage	7.215	1.755	-	-	-2.24
LR voltage	8.2073	1.755	-	-	-2.6
LBC voltage	7.215	1.755	-	-	-2.24
LBEC voltage	0	2.1	-	-	0
LBT voltage	0	-0.45	0.45	0.45	-3.5
TEC voltage	0	0.375	-3	-0.325	0
TC voltage	79.5	4.85	-4.85	-4.85	-2.5
R voltage	97.4779	0.5	-0.55	varied	-2.5
BC voltage	79.5	0.6	-0.6	-0.6	-2.5
BEC voltage	0	1.4	-1.4	-1.4	0
Pre-pulse wait	-	50	50	varied	-
Post-recovery wait	-	45	45	varied	-
Number of ramp steps	-	1	1	varied	-
Wait time between ramp steps	-	-	-	varied	-

Table 6.1: Parameter sets used for tests of the pulsed particle transfer system. "Pre-pulse wait" is the time waited in pre/post-pulse wells before applying pulses. "Post-recovery wait" is the time waited after ramping R and LR voltages back to measurement values before ramping other electrode voltages. Electrode acronyms correspond to names labeled in Fig. 6.2.

1. Particles were dumped from both traps.

2. A cloud of particles was loaded into the positron accumulation trap with electrode voltages in the "measurement" configuration in Table 6.1.

3. The dump procedure was repeated in the precision measurement trap and driven axial scans were done to check that dumping had been effective.

4. The magnetron motion of the particles trapped in the positron accumulation trap was cooled by several minutes of axial-magnetron sideband cooling.

5. Electrode voltages were changed ("ramped") to the values shown as "Set A" in Table 6.1 to create the (much shallower) "pre/post-pulse" wells.

6. A wait period allowed the ring electrode, which has a DC bias line with a longer RC time constant than the other electrodes, to come to the applied voltage.

7. Pulses were applied to the loading bottom endcap and precision top compensation electrodes to attempt to transfer particles.

8. The ring and loading ring voltages were ramped to their "measurement" values, and a wait period was observed[4].

9. The rest of the electrodes were ramped to their "measurement" values.

10. A sideband drive was applied in the precision-measurement trap to cool the magnetron motion of any caught particles.

[4]Because of the longer time constants on the ring and loading ring RC filters, ramping all electrodes simultaneously would cause the rings to lag and create shallow or even inverted well shapes.

11. A driven axial scan was done in the precision measurement trap to search for transferred particles.

Unfortunately, no electrons were found in the precision measurement trap in these tests. Additional tests were performed, varying the parameters that should most strongly affect the probability of transfer (Sec. 6.4.2.1), but electrons were not detected in the precision trap in any of these tests.

An unrelated problem in the positron accumulation trap at the time of the pulsed transfer tests might have caused the transfer failures. Though inconvenient, this problem is not complex; it was caused by a component that broke on thermal cycling. Once this issue is fixed, it is quite possible that transfer will succeed. The remainder of this chapter explores other possible causes for the failure and discusses ways that the system can be altered to increase the probability of future success.

6.4.2 The Effect of Imperfect Parameter Control

Though simulations are useful for choosing good transfer parameters, there are limitations to how well these desired conditions can be implemented in the real experiment, e.g., how precisely voltages can be set on electrodes. If the successful transfer region has too small a volume in parameter space, small imperfections in voltages could place the true experimental conditions entirely outside the "successful transfer" region of parameter space. If this were to happen, an experimental search in all 14 dimensions (electrode voltages, pulse lengths and pulse voltages) would likely be infeasible.

To determine whether this is a possible cause of the transfer failure, we now ask:

1. How large is parameter space predicted to be?

2. How large are real experimental parameters imperfections expected to be?

3. Can the answers to these questions be tested experimentally?

6.4.2.1 How large is the parameter space predicted to be?

Table 6.2 gives a first estimate of how sensitive the system is to voltage offsets. It shows the boundaries of the successful transfer region for each parameter varied alone, as predicted by simulations. Staying inside these boundaries is realistically achievable given expected offsets in power supply outputs, etc.

These simulations give a first piece of useful information: success is much more sensitive to some electrode voltages than to others. The most critical voltages are those on the loading ring (LR), loading bottom endcap (LBC), precision top endcap (TEC), and precision ring (R). Any exploration of parameter space could focus on varying those parameters, reducing from 11 to 4 the number of parameter space dimensions that are DC electrode voltages. A first set of exploratory transfer attempts was made in the experiment with variations on these parameters, but unfortunately, none was successful.

6.4.2.2 How sensitive is transfer predicted to be to variations in multiple parameters simultaneously?

While the parameter space boundary search described in the previous section is useful for identifying the most important parameters to tightly control for transfer, it does not give a quantitative prediction of how likely success is. Real offsets will

Control Parameter	**Optimized Value**	**Permissible Range**
Pulse length	109 ns	20 ns
Loading pulse voltage	-3.45	1.2
Precision pulse voltage	-5.03	1.7
LTEC voltage	2.5	2.6
LTC voltage	1.755	0.50
LR voltage	1.755	0.18
LBC voltage	1.755	0.19
LBEC voltage	2.1	0.85
LBT voltage	-0.45	0.77
TEC voltage	0.375	0.17
TC voltage	4.85	1.5
R voltage	0.5	0.35
BC voltage	-0.6	1.1
BEC voltage	-1.4	0.52

Table 6.2: Size of parameter space for pulsed particle transfer in simulations from locally optimal parameters. All units are V except for pulse lengths. Each controllable parameter varied while keeping the others constant at their values for a set of locally optimized successful transfer parameters. Fig. 6.2 is a key to electrode acronyms (LTEC, etc).

occur in multiple conditions simultaneously. It is not feasible to thoroughly explore the full parameter space of possible offsets, even just in simulations. However, an ensemble model of many simulations with different combinations of random offsets can sample this space. Fig. 6.3 shows the compiled results of simulated transfer attempts where random offsets have been added to DC and pulse voltages. Success rates varied depending on the maximum ranges of these offsets. Success rates are as high as 98% for tightly controlled conditions. Success rates fall below 40% if electrode voltage offsets of ±200 mV and pulse voltage variations of ±20% are permitted.

	Range of Pulse Voltage Offsets		
Range of Electrode Voltage Offsets	±5%	±10%	±20%
±10 mV	98	96	75
±50 mV	92	83	68
±100 mV	68	65	55
±200 mV	33	35	33

Table 6.3: Success rates of pulsed transfer simulations given random offsets in electrode voltages and pulse voltages. Table entries are in percentages, with 95% confidence intervals of approximately ±2%.

6.4.2.3 How large are real experimental parameter imperfections expected to be?

How likely is it that tight enough control can be achieved? Voltage offsets can arise from several sources. Offsets and drifts in power supply output can be measured and compensated for at room temperature. Voltage division from unwanted leakage

resistances and in-line filter resistors is minimized by choosing high-leakage-resistance vacuum feedthroughs and filter components and maintaining appropriate cleanliness. Both causes of offsets should be controllable to the needed precision.

One other cause of voltage offsets might be more pernicious: hysteresis in the large polypropylene filter capacitors in the RC filters on DC electrode bias lines. This hysteresis causes the voltage on an electrode to depend on its history, including both previous voltages and times spent at those voltages. The effect is stronger for larger capacitors; therefore, ring electrode voltages are affected most. Hysteresis was tolerable in previous electron $g/2$ measurements because large voltage changes were infrequent. Particle frequencies were also always within a range visible through amplifiers, making it possible to observe the resulting shifts in particle frequency and readjust voltages as necessary. However, pulsed particle transfer happens in non-detection wells where particle frequencies are far from amplifier frequencies, so tuning and direct in-situ measurement of the potentials in the pulse wells will not be possible. Hysteretic variations of up to 1.2 V out of 97 V on the precision ring electrode and up to 84 mV out of 8.2 V on the positron accumulation ring electrode have been observed in the current apparatus. If hysteresis-induced offsets are proportional to total voltage, then these 1% imperfections are modest on the scale of Table 6.3.

It is possible to reduce hysteresis by overshooting and then "ringing in" to the desired voltage whenever making a large voltage change [27]. However, it might be necessary to limit time spent in shallow pulse wells in order to limit magnetron heating (Sec. 6.4.3.2), limiting the usefulness of ringing in.

6.4.2.4 How well do simulations correspond to real experimental conditions? Comparing simulation to experiment in single-trap experiments.

To assess how well simulations correspond to experimental conditions, simulations and experiments were compared for matching parameter sets. Positron transfer attempts could have failed for many reasons; to disambiguate between a cause related to the small hole in the precision top endcap and other possible causes (voltage offsets, heating in "pre/post-pulsing" wells, issues with the simulations), it is valuable to test the pulsing system in a way that involves only one trap and so is not limited by effects related to the hole.

A set of experimental tests were done in which DC electrode voltages and voltage pulses were used to control electrons in the precision trap alone. All parameters were the same for each test except pulse length, which was varied. The parameters used are listed as Set B in Table 6.1. The procedure used for these tests was similar to that described in Sec. 6.4, but occurred entirely within the precision trap. After each trial, electrons were sideband-cooled and an driven axial scan was done to assess how many remained in the trap. Electrons were dumped and reloaded from the field emission point between trials.

For comparison, simulations with the same electrode voltages, pulse sizes, and pulse lengths were also performed. Each simulation predicted whether electrons would be retained in the trap and, if so, with what energy. Fig. 6.8 shows an example of differences in predicted electron behavior for two different pulse lengths.

In these simulations, the electron begins very close to the the center of the trap

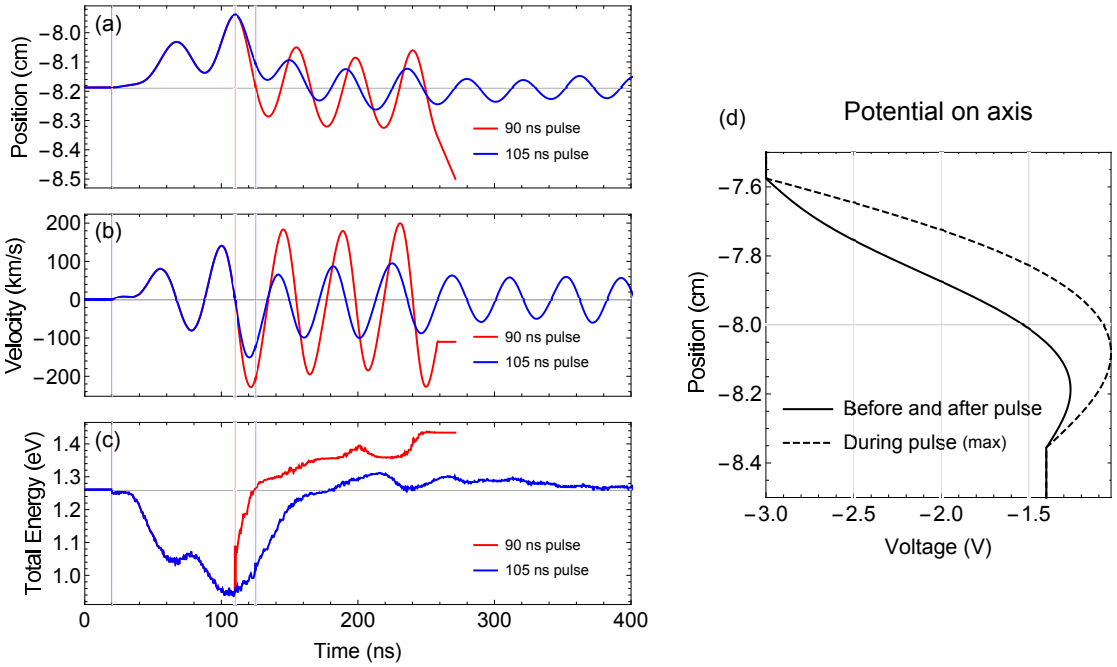

Figure 6.8: Position (a), velocity (b), and energy (c) vs. time for an electron for simulations in which a 90 ns or 105 ns pulse was applied to the precision trap. Purple vertical lines are the start time of both pulses; the red vertical lines mark the end time of the 90 ns pulse and the blue vertical lines mark the end of the 105-ns pulse. The electron is ejected from the trap by the 90 ns pulse but remains in the trap for the 105 ns pulse. (d) Electric potential on axis in the precision trap before and after the pulse (solid line) and during the pulse (dashed line).

with low kinetic energy. The pulse deepens the well asymmetrically, most strongly affecting the potential closest to the pulse electrode (the top compensation electrode, in the upper half of the trap.) When the well is deepened by the pulse, the electron's axial oscillations grow in amplitude. If a particle happens to be as close as possible to the pulse electrode at the time the pulse is ended (red vertical line), as in the 90 ns pulse, the potential energy change at the electron's position as the pulse ends is greater than the potential energy change the electron experienced at the beginning of the pulse. The electron thus gains net energy, and it is no longer trapped. If at the end of the pulse the the electron is closer to where it started, as in the 105 ns pulse (pulse end at blue vertical line), then the net energy given to the electron is much smaller and it remains trapped.

Fig. 6.9 compares the results of simulations and experiments for many pulse lengths. Fractions of particles retained experimentally are shown in blue. It is expected that simulations in which final particle energies are predicted to be the lowest are those in which particles are most likely to be retained in experiment. Therefore, in Fig. 6.9, the electrons' final energies in the simulation are shown in green, with a scale that goes from highest energy at the bottom (because these particles should be least likely to be retained) to lowest energy at the top. The relative scaling between the green and blue points is chosen only to display all points on the same plot, not set from first principles; in a sense, it is a fit parameter, and it predicts the maximum final energy a particle can have and still be caught in experiment. Red dots show parameter sets where, in simulations, particles are not retained in the precision well. (Though these dots are displayed at the "0" line for fraction retained on the plot,

there is no information contained in their position on the vertical axis because there are no meaningful final-state energy data.)

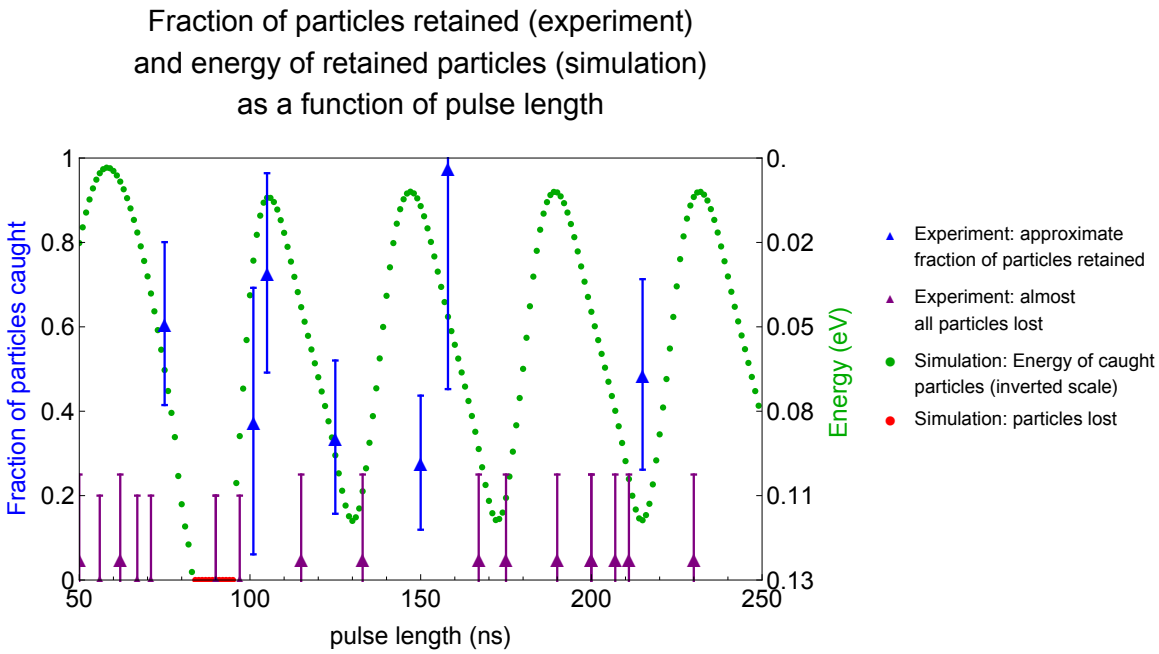

Figure 6.9: Results of simulations and experiments in which pulse length was varied. The vertical axis shows the fraction of particles retained for experimental data, and for simulations it shows energy (lower energy at top of plot.) Purple experimental points at zero represent conditions in which there was no evidence of retained particles and those just above zero represent conditions in which very small numbers of particles were present but their quantity could not be measured due to harmonicity issues.

There are clear differences between simulations and data in Fig. 6.9. If the disagreement is caused by an offset in a parameter (e.g., an electrode that is supposed to be set to 1 V is actually at 0.9 V), it could be possible to adjust the simulation to compensate. It is unfortunately not possible to search all of parameter space to fully understand the effects of all offsets. However, it is possible to learn about which offsets can cause which types of imperfect matching, which could conceivably narrow

the search for the cause of the disagreement. For example, Fig. 6.10 shows the same experimental data superimposed with a simulation in which a 50% larger pulse was applied.

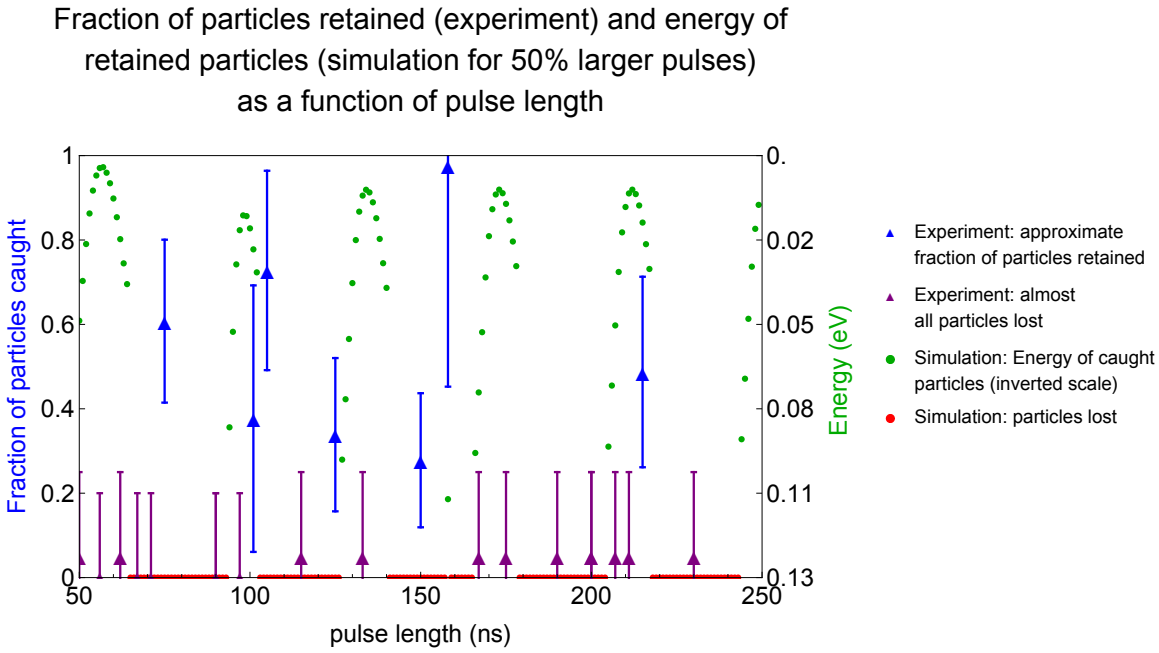

Figure 6.10: Same experimental results as in Fig. 6.9 but displayed with simulations in which a 50% larger pulse voltage was applied.

This simulation predicts that all particles are lost for most pulse lengths, which is a better qualitative match for the data than the simulation in Fig. 6.9. The fit is still poor, however. Similar simulations were done for offsets in many individual electrode voltages, but none yielded an excellent match. Given that there is a continuum of possible voltage offsets and that offsets likely are present on multiple electrodes simultaneously, the search for a good match might not be feasible. Even if a better fit were found, it would not be possible to be certain that it was unique.

6.4.2.5 Imperfect parameter control: conclusion

It is not yet understood why pulsed particle transfer has been unsuccessful so far. The transfer process is expected to be quite robust in the presence of variations of electrode voltages and pulse heights (Sec. 6.4.2.1, Sec. 6.4.2.2). No known cause of DC electrode voltage offsets (Sec. 6.4.2.3) is large enough to explain the failure of pulsed particle transfer between traps (Sec. 6.4.1) or the disagreement between data and experiment in single-trap experiments (Sec. 6.4.2.4).

This leaves a couple of possible explanations for the disagreement between predicted and observed behavior of the pulsing system.

1. There could be electrode or pulse voltage offsets present that are larger than expected offsets.

   (a) Create new ways to measure electrode voltages and verify that offsets are not present. This could be accomplished by the installation of additional "comp-check"-like lines on all electrodes, allowing a direct check of electrode voltages. This strategy has the disadvantage of creating new routes for noise to get into the trap, as well as introducing the complexity and bulk of additional filtered lines in the volume-limited, thermally cycling environment of the dilution refrigerator.

   (b) Increase the transfer system's robustness in the presence of offsets. This could be done by deepening the "pre-pulse" wells so that any small voltage offsets are proportionally smaller. This change would be expected to increase the ranges in Table 6.2 and the percentages in Table 6.3. Ch. 7

presents such a proposal for deepened "pre-pulse" wells and shows that it does indeed increase the likelihood of transfer in the presence of offsets.

2. There could be another factor, entirely unaccounted for in simulations, that is causing the disagreement with experiment. Magnetron heating in the relatively shallow "pre-pulse" wells is a strong candidate for such an effect. Sec. 6.4.3 presents an analysis of the effect of magnetron heating and other considerations related to radial motion on pulsed particle transfer. Ch. 7 presents a proposed reconfiguration of the pulsed transfer system that will make it possible to create "pre-pulse" wells that are:

   (a) deeper and therefore less susceptible to magnetron heating, and

   (b) harmonic, which might allow for pre-pulse magnetron cooling to counter the effect of heating.

Without knowing for certain whether large voltage offsets or magnetron heating is responsible for the failure of transfer, both of these possibilities are being addressed. Tests continue in the pulsed transfer system as installed. In parallel, the hardware for the improved system of Ch. 7 is being built.

6.4.3 The Role of Radial Motion in Particle Transfer

Analysis in previous sections has considered only the axial motion of particles. Taking into account magnetron motion and off-axis position raises several additional complications, examined one by one in the following subsections.

6.4.3.1 Magnetron radius and hole size

A particle with a magnetron radius greater than the 0.18 mm radius of the top endcap hole will not be able to go through the hole in the top endcap electrode. To determine the magnetron radius of positrons in the "pre-pulse" accumulation trap well, it is assumed that they are cooled to the axial-magnetron sideband cooling limit in the normal measurement potential well for the positron accumulation trap, and then voltages are adiabatically changed such that energy in the magnetron motion is conserved. The cooling limit for the magnetron motion is given by

$$\langle E_m \rangle = -\frac{\omega_m}{\omega_z} k_B T \qquad [105]. \tag{6.1}$$

The energy of the magnetron motion is primarily potential rather than kinetic:

$$E_m \approx -\frac{m\omega_z^2 \rho_m^2}{4}. \tag{6.2}$$

Solving for the magnetron radius gives

$$\rho_m = \sqrt{\frac{2k_B T}{m\omega_z \omega_c}}, \tag{6.3}$$

where T is the temperature of the axial motion during cooling. Conservatively assuming an axial temperature of 4 K, this gives a magnetron radius in the normal 52 MHz positron accumulation trap well of $\rho_m \approx 600$ nm.

The axial frequency in the "pre-pulse" accumulation trap well in the successful transfer simulation in Sec. 6.3 is 12.5 MHz. Assuming an adiabatic ramp process from the "measurement" well to the "pre-pulse" well, energy in the magnetron motion is conserved, giving a magnetron radius of 3 μm that is much smaller than the 0.17

mm radius of the hole[5]. As long as the particle remains well magnetron-cooled, the magnetron radius should not be an issue in pulsing.

6.4.3.2 Magnetron heating in the "pre-pulse" well

The potential wells used for transfer are much shallower and trapping forces weaker than for typical "measurement" wells. This could expose particles to "long-well" heating (Sec. 6.1) before they are launched, which could increase their magnetron radius beyond the radius of the hole or even cause the loss of particles from the trap.

Preliminary trials done on electrons trapped in the positron accumulation trap suggest that this could be a problem. The procedure for each trial was similar to that described in Sec. 6.4.2.4, but the pulses were not applied. When wait time in the "pre-pulse" well was less than 1 minute, electrons were magnetron-heated but not lost from the trap. For a wait time of 5 minutes, about half of the electrons were lost. The cause is presumed to have been "long-well"-type magnetron heating in the shallow "pre-pulse" wells. Ideally, more detailed tests would have been performed to learn more about the extent and cause of the heating. Unfortunately, the broken component in the accumulation trap wiring that was mentioned in Sec. 6.4 made further study impossible in the positron accumulation trap in the data collection period.

Because the precision "pre-pulse" wells are similar to the positron accumulation "pre-pulse" wells, it was possible to do analogous heating tests in the precision trap as a substitute. The "pre-pulse" well parameters used for these tests are listed as Set C in

[5]Though magnetron radius is larger still in the effective "long well" present during pulsing, the pulses and transit are so fast that the magnetron radius does not expand appreciably on the timescale of the transit.

Table 6.1. The procedure used was similar to the procedure in Sec. 6.4.2.4, but with the pulsing step omitted. The final magnetron sideband cooling step was omitted so that magnetron heating could be detected in the final axial scan. Because particles in high magnetron states are far from trap center, they sample different electric and magnetic fields from cool, centered particles and so they appear at different axial frequencies. A magnetron-heated cloud of many particles therefore appears to be spread out and shifted in frequency compared to a well-cooled cloud.

To determine which parts of the procedure were associated with magnetron heating, the following parameters were changed between trials: number of steps in each voltage ramp, wait times between ramp steps, depth (and therefore frequency) of "pre-pulse" well, wait time in the "pre-pulse" well, and termination on RF pulse lines when pulses were not being applied. Results for varied wait times in the "pre-pulse" wells are in Fig. 6.11.

A decrease in amplitude of the driven axial signal along with significant spreading and shifting upward in frequency, indicating magnetron heating, was observed in all trials. The conditions most strongly correlated with more magnetron heating were shallow "pre-pulse" wells and long wait times in the "pre-pulse" wells. This supports the hypothesis that the observed magnetron heating is primarily "long-well"-type heating. Magnetron heating was especially bad in wells with 0.5 V on the ring electrode; particle clouds were spread out so much in axial frequency that they were undetectable without sideband cooling. The ring voltage therefore had to be increased to 5 V in the central parameter set, around which other parameters were varied, in order to be able to discern differences in non-cooled clouds.

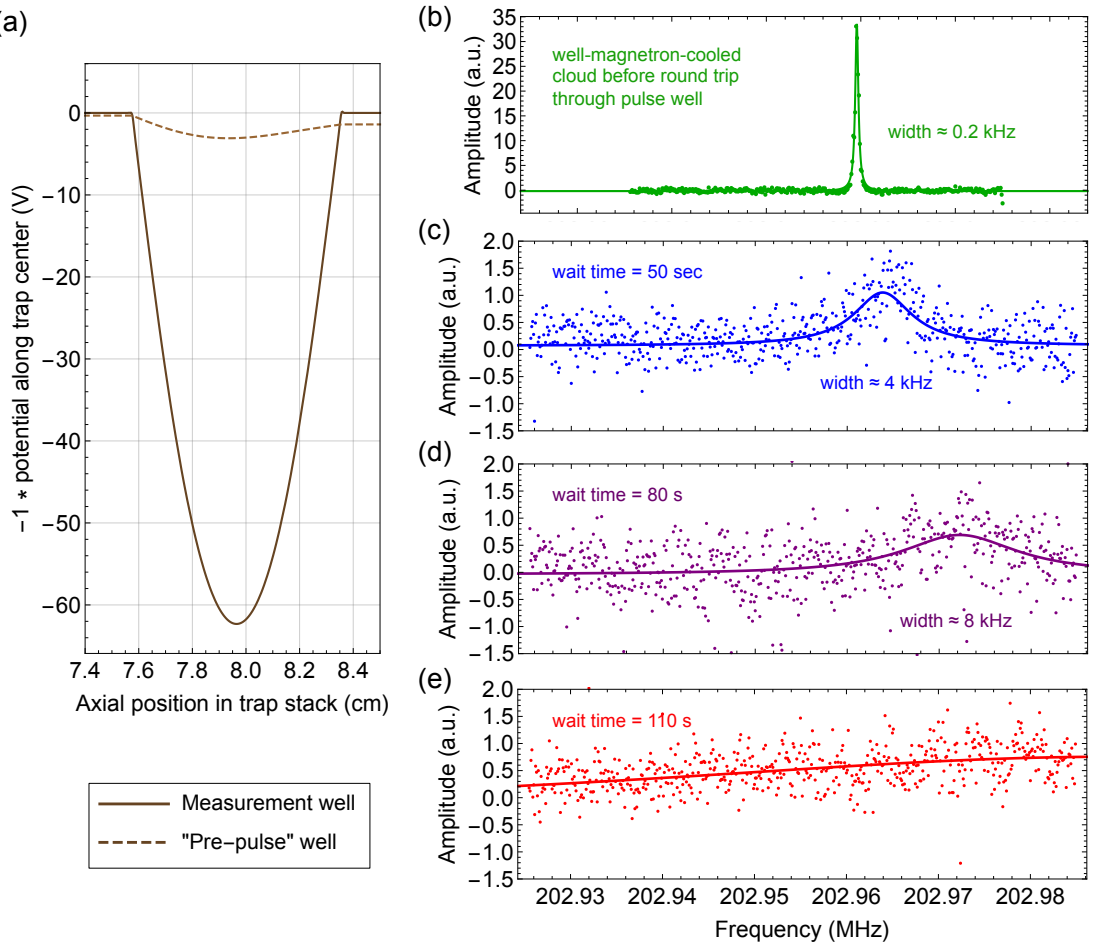

Figure 6.11: Tests showing that time in "pre-pulse" wells is correlated with magnetron heating. A cloud of electrons is first cooled in the measurement well, and then the potentials are ramped to the "pre-pulse" well. After a variable wait time, potentials are ramped back to the measurement well for assessment. (a) shows potentials in the measurement well (solid brown line) and the "pre-pulse" well (dashed brown line). The remaining plots show the driven axial signal from a cloud of electrons (b) after magnetron cooling in the measurement well, (c) after a round trip with a 50 s wait in the "pre-pulse" well, (d) after a round trip with a 80 s wait in the "pre-pulse" well, and (e) after a round trip with a 110 s wait in the "pre-pulse" well.

Because the pulse RF lines lack attenuators, it is possible that they transmit a room-temperature noise source into the trap, which could have contributed to the magnetron heating. However, no difference in heating was observed whether pulse lines were shorted, shielded without shorting, or left connected to the switched-off pulse amplifier. Noise coming down the pulse lines was therefore ruled out as the leading cause of heating.

Understanding and reducing magnetron heating in "pre-pulse" wells is likely to be critical in ensuring the success of pulsed particle transfer. Avenues for improvement include:

1. If the heating mechanism were understood, it could be reduced, e.g., if there is an RF leak from room temperature or if imperfect trap electrode surface quality or cleanliness is causing heating.

2. Sideband cooling of the magnetron motion could be performed in the "pre-pulse" well. This would require that the "pre-pulse" potentials be harmonic. One difficulty with this approach is that there is not currently an amplifier in the positron accumulation trap at the "pre-pulse" well particle frequency, so the cooling would need to be done without certain knowledge of the particles' axial frequency and without directly observing the cooling. If cooling were critical enough, it could be worth installing an additional amplifier for this purpose.

3. The "pre-pulse" well could be modified to be deeper. The extent to which this is possible is limited by the size of pulse that can be applied; the barrier to the particles' escape must be lowerable by a pulse. There is some room for optimization of this within the current "pre-pulse" parameter set. It could be

further improved with any changes to the pulsed transfer system design that allowed for bigger pulses, as described in the proposal in Ch. 7.

6.4.3.3 Surface heating within the precision top endcap channel

A particle that makes it into the precision top endcap electrode (TEC) hole will come within 0.17 mm of the surface for about 1 μs, exposing the particle to heating mechanisms from surface imperfections. Heating of charged particles near surfaces in ion traps has been investigated by many groups, with possible heating mechanisms including fluctuating electric fields from patch potentials and diffusion of adsorbed atoms. Orders-of-magnitude differences in heating rates have been observed in ostensibly similar systems. The ion-trapping community has not yet come to a consensus about which mechanisms dominate, what absolute heating rates can be expected, and what the scaling with surface-to-ion distance d should be in a range of d^{-2} to d^{-4} [149]. Most data also deal with trapped ions rather than electrons and Paul traps rather than Penning traps, limiting their relevance. However, a comparison to the planar Penning trap within the current electron/positron $g/2$ apparatus suggests that heating in this hole is unlikely to be an issue [93]. Clouds of small numbers of electrons trapped 1 to 2 mm from the surface of the planar trap remain trapped and drift in frequency only modestly due to magnetron heating over timescales of hours. Even with worst-case distance scaling of heating, the pulsed electron or positron going through the hole should experience less heating than an electron trapped in the planar trap for 1 s.

6.4.3.4 Misalignment

If there is a misalignment between the electrostatic center of the positron accumulation trap and the center of the hole in the precision top endcap electrode (TEC), even well-magnetron-cooled particles might not make it through the hole.

The stack of precision trap electrodes is held between two plates connected by three threaded rods 120 degrees apart. Nuts on these threaded rods tighten down on springs to gently press the plates together and hold the trap stack in place. Three threaded rods then go through one of these plates and screw into the pinbase to gently compress the positron accumulation trap stack between the pinbase and the precision trap stack, using a similar system of nuts and springs. To optimize alignment, nuts are adjusted until total height of the trap electrode stack as measured with calipers is as consistent as possible between six angular positions around the trap stack, which has been achievable with a standard deviation of under 0.05 mm. How bad could misalignment be within these constraints? In the worst-case scenario, the precision trap would be flush with the pinbase and square with the magnetic field but the positron accumulation trap would be tilted to cause the whole 0.05 mm height imbalance. Then, the tilt would be 3° and the positron accumulation trap center would be offset from the hole center by 0.2 mm, slightly greater than the hole radius. In practice, any tilt is likely to be shared by the electrode stack as a whole, reducing the maximum radial offset by a factor of 2 and bringing the positron trap center once more in line with the hole.

Realistically, because the precision trap electrodes are mounted against the accumulation trap electrodes and depend on them to remain parallel to the face of

the pinbase (perpendicular to the magnetic field), a lack of tilt in the precision trap electrodes is good evidence that accumulation trap electrodes are also well aligned. Design choices and tight machining tolerances on radial concentricity should also ensure that there are not significant offsets in the center axes of electrodes in the stack, since electrodes are built to gently tighten down on spacers as the electrode stack cools.

Alignment can be probed experimentally by loading electrons directly into the positron accumulation trap from the field emission point (FEP), as described in Sec. 4.5.2. FEP electrons follow magnetic field lines, just as particles do during a pulse; because electrons from the FEP make it to the tungsten moderator on the far side of the positron accumulation trap, it indicates that the FEP and the TEC hole are well aligned for transfer. The FEP electrons hitting the moderator can be detected directly as a current; their effects are also observed indirectly through changes in the positron loading rate after FEP firing [89].

6.4.3.5 Off-axis potential

Having a nonzero magnetron radius affects the electric potential experienced by a particle, which affects axial forces from electric fields. The particle transfer simulation code neglects this effect, assuming that particles are on-axis to calculate electric potential. This is a very good approximation; at the magnetron radii in question, this offset affects axial forces by much less than 1%, a smaller effect than, e.g., expected electrode voltage offsets. Upgrading the simulations to consider off-axis fields is not necessary for understanding pulsed particle transfer.

6.4.3.6 Interactions between particles

The transfer simulations have so far considered a single particle at a time, neglecting interactions between particles. Is this a good enough approximation for modeling pulsed particle transfer, given that clouds of many positrons rather than single positrons are expected to be "thrown" from the loading trap? It is useful to keep in mind that only a single positron is needed for the $g/2$ measurement, so 100% transfer efficiency is not necessary.

Following [150], a coupling parameter Γ for a non-neutral plasma can be defined as

$$\Gamma = \frac{1}{4\pi\epsilon_0}\frac{q^2}{ak_BT}, \tag{6.4}$$

where k_B is the Boltzmann constant, q is the charge of the particles comprising the plasma, a is the Weiner-Stiglitz radius

$$a = \left(\frac{e}{4\pi n}\right)^{(1/3)}, \tag{6.5}$$

and n is the plasma density. For $\Gamma \ll 1$, interactions between nearby particles are typically weaker than the energy in other degrees of freedom, and cloud effects are relatively unimportant. The density of positron clouds in a trap and potential similar to the positron loading trap was measured in [145]; for a cloud of about 50,000 positrons, n was found to be about $7 \times 10^{12}/m^3$, giving $\Gamma < 0.2$. Positron transfer in this apparatus is unlikely to use clouds this large or dense, which gives a yet-smaller Γ. This indicates that interactions between particles are relatively unimportant in their effect on axial motion in pulsed transfer simulations. While it would be interesting to develop a more detailed model of cloud effects, it should not be necessary for simulating the axial motion of particles during pulsed particle transfer.

However, it is also interesting to note that the radius of the 50,000-positron cloud described in [145, 144] was just under 3 mm. A significant fraction of particles of a cloud this large would not make it through the small precision top endcap hole; 99.6% of the projected cloud area would be blocked by the electrode. This has a couple of implications for the strategy used to attempt transfer. First, if alignment is good, increasing cloud size beyond 50,000 particles is unlikely to increase the particle transfer rate. Second, poor alignment could be rendered unimportant by using a fairly large-radius cloud. 50,000 positrons can be loaded in less than a day, and a 3 mm radius more than compensates for any possible misalignment.

6.4.3.7 Radial effects: conclusion

This section has considered many aspects of the pulsed transfer system that could conceivably impede pulsed particle transfer and found that almost all are unlikely to be important. A particle's (well-cooled) magnetron radius is sufficiently small to make it through the small channel in the precision top endcap, and the simplification of using on-axis potentials in the transfer simulation should not affect outcomes. Vertical trap alignment should be adequate, but if it is not, "throwing" larger clouds could mitigate the effect of misalignment on transfer.

Magnetron heating in the "pre-pulse" well is the only effect that was found to be likely to compromise particle transfer. Next steps to combat magnetron heating are discussed in Ch. 7.

6.5 Outlook

After overcoming significant design challenges, hardware for pulsed transfer of positrons into the precision trap is in place. Though pulsed particle transfer might be possible with the existing setup, it remains to be seen whether it will be possible to limit magnetron heating and control all parameters as tightly as necessary. Ch. 7 contains a proposal for a modified system that would significantly expand the available parameter space for pulsed particle transfer, limit magnetron heating, and improve the probability of successful transfer of positrons to the precision trap for an improved positron $g/2$ measurement.

Chapter 7

Next Steps: A Proposed Reconfiguration

Chapters 1 through 6 have described many design improvements and successfully demonstrated $g/2$ measurement techniques in the current apparatus. However, a few challenges also remain on the path to an improved positron $g/2$ measurement. As described in Ch. 4 and Ch. 6, the system for transferring positrons into the precision measurement trap conflicts with the single-particle axial detection system crucial for the $g/2$ measurement. The current configuration of the apparatus is a compromise between these two purposes; signal-to-noise is suboptimal (Sec. 4.2.3) and positron transfer has not yet been achieved (Ch. 6). This chapter presents a proposed trap reconfiguration that should remove this conflict, enabling far easier positron transfer, improving single-particle axial detection, and ultimately making possible an improved positron $g/2$ measurement.

7.1 Challenges in RF Detection and Pulsed Particle Transfer

The top two electrodes in the precision trap play crucial, but fundamentally conflicting, RF roles in detection and in particle transfer. The precision top endcap electrode (TEC) would be the most useful electrode for "closing the door" behind positrons being "pulsed" into the precision trap, but the 200 MHz resonator connected to TEC for single-particle detection destroys the voltage pulse shape (Sec. 6.2.1). Unfortunately, pulses on the other electrodes that can be used for "catching" particles—the precision top compensation electrodes (TC)—are weaker than pulses on TEC and are also adversely affected by the 200 MHz detection circuit (Sec. 6.2.2). This makes pulsed transfer so difficult that it might not be achievable in the current configuration (Sec. 6.4.2, Sec. 6.4.3.2).

Meanwhile, the 200 MHz single-particle axial detection system also suffers from several geometry-related imperfections that degrade signal-to-noise (Sec. 4.2.3). Parasitic capacitances to physically close objects (e.g., the positron accumulation trap and the microwave waveguide) couple lossy elements into the 200 MHz resonator. The 200 MHz resonator's configuration, bisected by the feedthrough pinbase (Figs. 4.9 and Fig. 7.1), also causes several problems. The resonator's direct electrical connection to the pinbase couples lossy elements into the detection circuit (Fig. 4.14). The resonator's mechanical connection between the electrodes and the pinbase creates mechanical stresses that may be causing unwanted electrical shorting on thermal cycling. Geometrical constraints (Sec. 6.2.2) on the 200 MHz resonator, imposed by

the presence of the positron loading trap and the positron source flange, also force the single-particle signal to be divided down more than desired.

7.2 Brief Overview of Proposed Solution

This section explores the possibility of moving the 200 MHz resonator to the precision bottom endcap electrode and moving the 200 MHz resonator and amplifier to be entirely within the trap vacuum can. This will allow the bottom endcap to be optimized for detection and the top endcap to be used for pulsed positron transfer. This should solve the aforementioned problems, enabling easier positron transfer and improving detection beyond the level of the best existing electron $g/2$ measurement. Fig. 7.1 shows the current and proposed configurations. Though these changes are nontrivial, they could be implemented within the basic framework of the current apparatus.

The next two sections take the challenges described in Sec. 7.1 one by one and explore how this proposal could address each of them.

7.3 Advantages for Detection

Problem: Single-particle 200 MHz axial detection in the precision trap is adversely affected by lossy elements, parasitically coupled alternative RF ground paths, mechanical strains, and geometrical constraints (Ch. 4).

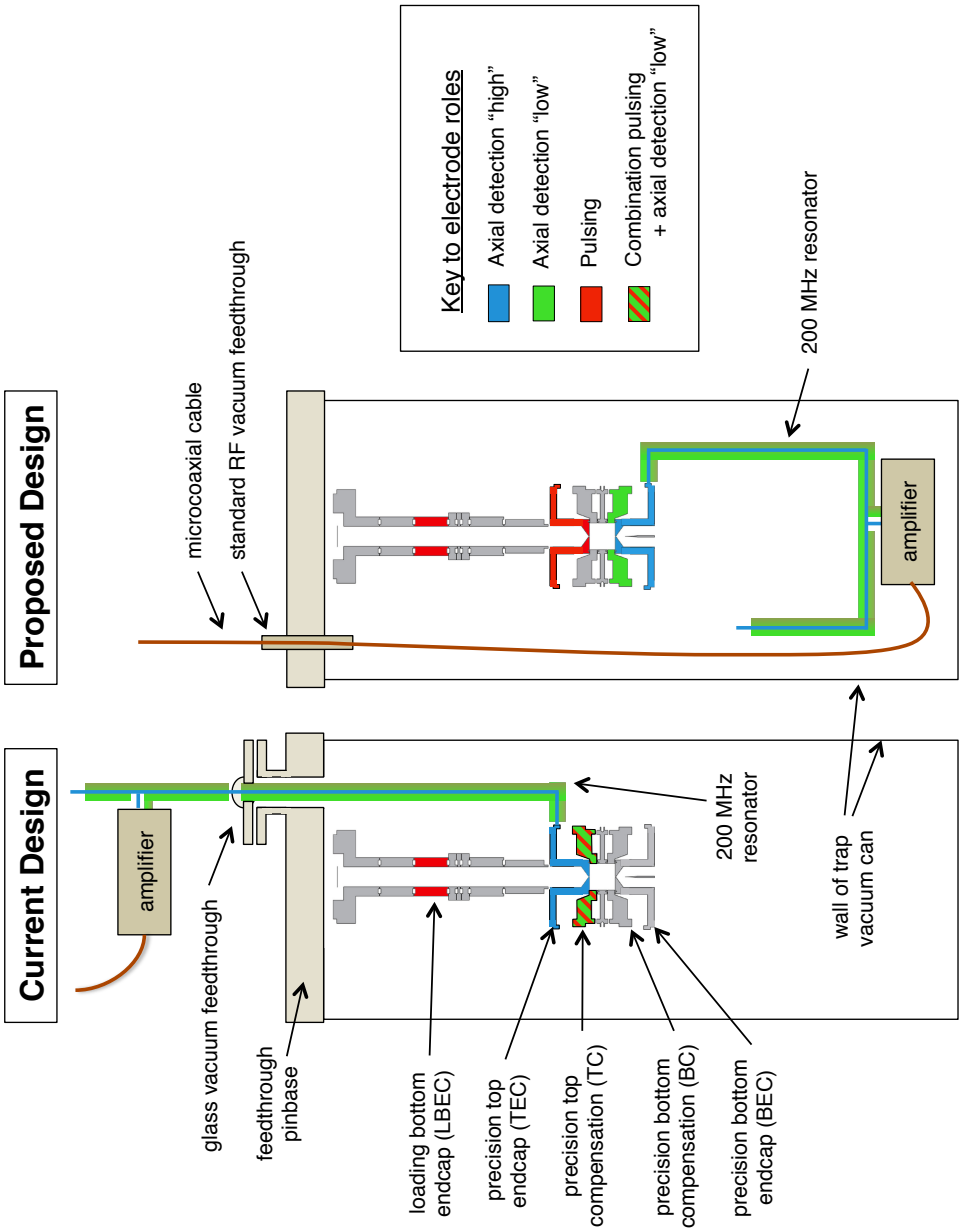

Figure 7.1: Physical configurations and roles of various trap electrodes in detection and pulsed particle transfer currently (left) and in a proposed reconfiguration (right).

Improvement 1: Separating the detection electrodes from the microwave waveguide, positron accumulation trap, and pulsed transfer electronics will eliminate parasitic capacitively-coupled RF ground paths. As described in Section 4.2.3, pF-scale capacitive couplings to objects that are physically close to the top endcap electrode (the microwave waveguide and an electrode in the positron accumulation stack) are believed to be among the leading sources of loss in the first stage of the 200 MHz detection circuit. The new detection electrode—the bottom endcap—is not close to either of these objects, which would eliminate these parasitic capacitances and likely improve resonator Q and therefore signal-to-noise.

Improvement 2: Moving the 200 MHz resonator and first-stage amplifier inside the trap can will physically disconnect lossy components from the detection system. Removing the vacuum feedthrough in the 200 MHz resonator eliminates the RF ground path through the 200 MHz feedthrough indium seal, shown as a red dashed line in Fig. 4.14. It also removes a section of inner conductor made of tungsten, which is less conductive than the silver that comprises the rest of the resonator. These changes are likely to increase resonator Q and signal-to-noise.

Improvement 3: Removing the 200 MHz feedthrough will reduce mechanical strain that can cause electrical and other problems. In the present design, the top endcap electrode is mechanically connected to the pinbase both symmetrically through the electrode stack and asymmetrically by the silver-and-tungsten rod that forms the inner conductor in the 200 MHz feedthrough. If these two paths contract different amounts on thermal cycling, the resulting mechanical stress on the

top endcap could cause various problems, including stress on the top endcap electrical lead and torquing of the top endcap. Those in turn could lead to intermittent, temperature-dependent electrical shorts and/or breaks in the detection circuit. Such problems have in fact been observed. Repeated several-day warmup/cooldown cycles to troubleshoot these issues are presently the primary factor limiting the progress of the electron/positron $g/2$ experiment. Locating the 200 MHz feedthrough entirely within the trap can will fix this problem. It will also increase the mechanical robustness of the trap vacuum enclosure by eliminating the feedthrough's glass section, which is relatively delicate.

Improvement 4: Moving detection away from the loading trap electrodes will allow for a larger tap ratio and signal size. As described in Sec. 4.2.3, the inclusion of a positron accumulation trap in the current-generation apparatus changed the relative positions of the detection electrode and the feedthrough pinbase in a way that physically obstructed the optimal position of the amplifer. In the new design, there would be no physical limitations on the position of the amplifier, so the position could be chosen to optimize tap ratio and increase signal size, with the constraint that the FET should be located as far away as possible within the trap can (see Sec. 7.5.1.)

Improvement 5: Moving the first-stage amplifier inside the trap should cut down on noise. Noise can presently enter the detection circuit before the first stage amplifier because shielding is imperfect around the glass portion of the 200 MHz resonator. By keeping all of the input to the first-stage amplifier within the

trap vacuum can in the new design, the single-electron signal will be better shielded from any noise that comes into the experiment through leads that do not come inside the trap can, e.g., temperature sensor and heater wires.

The upshot: Re-envisioned and improved detection. Though the issues presented here have caused painful delays, the reconfiguration they have inspired should enable improvements in detection over what was possible in the most recent previous Harvard electron $g/2$ apparatus. The new design is expected to have superior resonator Q, noise floor, and single-particle signal size. This would reduce the averaging time needed to determine whether a cyclotron transition had been driven, and would therefore reduce the system's vulnerability to axial frequency drifts.

7.4 Advantages for Pulsed Positron Transfer

Problem: Voltage pulses are too small and have a poor shape, making pulsed positron transfer very difficult (Ch. 6).

Improvement 1: Separating the precision pulse electrode from the detection electrodes will allow for larger and cleaner pulses. As described in Sec. 6.2.1 and Sec. 6.2.2, the top endcap (TEC) and top compensation electrode (TC) connections to the the 200 MHz resonator cause pulse division and pulse shape imperfections. Removing the detection circuit from TEC and TC would eliminate these problems.

Improvement 2: Pulsing on the precision top endcap (TEC) will enable larger pulses. Due to geometrical factors, a voltage change on TEC has an over-five-times-larger effect on the electric potential experienced by a trapped particle than does a voltage change on TC (Fig. 6.3). This means that a pulse on TEC, as in the proposed design, will be effectively bigger than one of the same voltage on the presently-used TC.

Improvement 3: Larger pulses will make the parameter space for pulsed particle transfer larger. Having larger pulses will make transfers work under a broader range of conditions (electrode voltages and pulse sizes and timing). This will make the transfer system more robust in the presence of experimental imperfections. An ensemble model of simulations, as described in Sec. 6.4.2, was used to get a first estimate of how much easier transfers will be when the top endcap electrode is used for pulsing. First, one possible set of good transfer parameters in the proposed new configuration was identified; this is shown as Set D in Table 6.1. The results of simulated positron transfer with this parameter set are in Fig. 7.2.

Parameter Set D was found manually. Significantly less time was spent optimizing this Set D than Set A (for pulsing on TC). To build the ensemble model, simulations were run for many sets of random electrode voltage offsets and pulse height offsets from Set D. The percentages of transfer attempts that were successful for different maximum allowed offsets are shown in Table 7.1. (Analogous data for the existing pulse-on-TC configuration are in Table 6.2.) With random offsets of up to 200 mV for electrode voltages and up to 20% in pulse voltages, successful transfer is expected to be almost twice as likely in the new configuration as it is in the existing

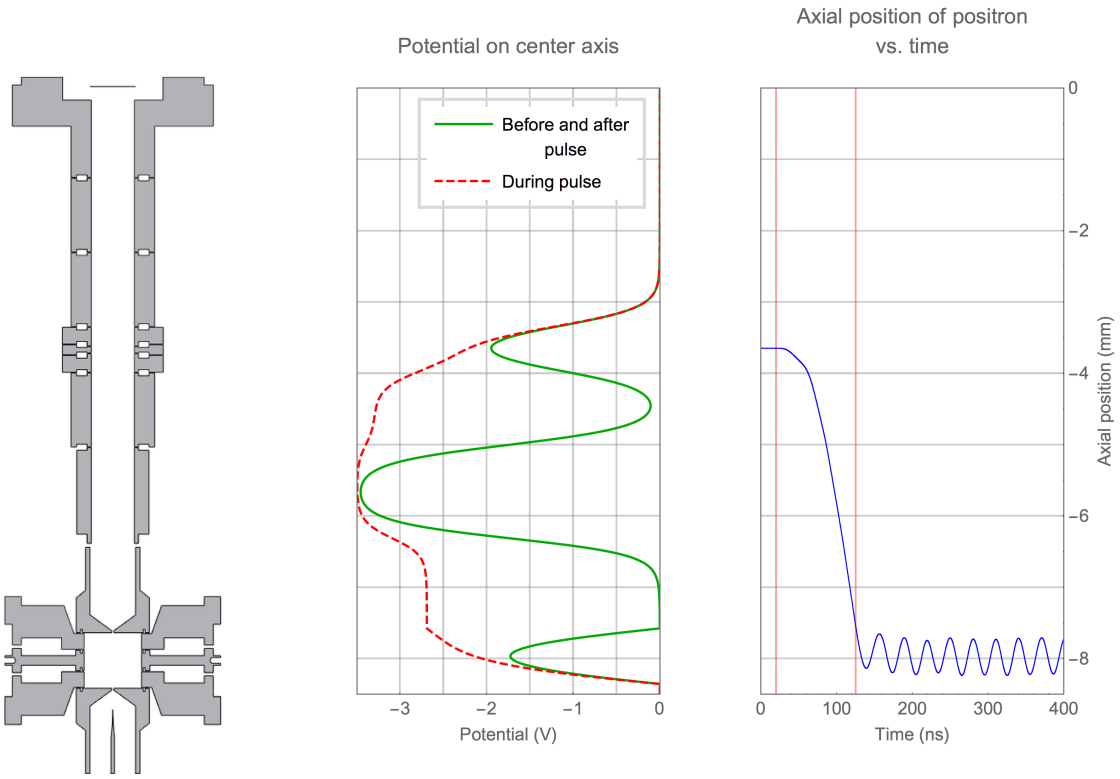

Figure 7.2: Cross section of electrode stack, potential on axis, and axial position of a positron vs. time for a successful simulation of pulsed transfer from the positron accumulation trap to the precision measurement trap, "closing the door" with the top endcap electrode (TEC). The position axis (vertical) is shared by all three subfigures. Pulse start and end times are marked by red vertical lines in the position vs. time plot. "Pre-pulse" wells are much deeper than is possible when pulsing on the top compensation electrodes (TC), shown in Fig. 6.6.

configuration—despite using a less carefully optimized set of parameters for the new configuration than the old configuration for this test.

	Range of Pulse Voltage Offsets		
Range of Electrode Voltage Offsets	±5%	±10%	±20%
±10 mV	100	97	71
±50 mV	100	96	71
±100 mV	100	93	73
±200 mV	94	86	62

Table 7.1: Success rates of pulsed transfer simulations given random offsets in electrode voltages and pulse voltages from a good parameter set; similar to Fig. 6.3 but for pulsing on TEC, the precision top endcap electrode. Table entries are in percentages, with 95% confidence intervals of approximately ±2%.

Improvement 4: Larger transfer parameter space will make magnetron heating issues more addressable. With increased freedom in parameter choice, it will be possible to create deeper "pre-pulse" wells, in which particles are less susceptible to the pernicious magnetron heating detected in Sec. 6.4.3.2. It will also give the flexibility to create more-harmonic "pre-pulse" wells, which could enable sideband cooling of the magnetron motion in "pre-pulse" wells. In the Set D parameters for pulsing on TEC, the "pre-pulse" well in the positron accumulation trap is harmonic and is 1.9 V deep, compared to the 0.23 V depth of the "pre-pulse" well for pulsing on TC. This leads to a factor of about 3 higher frequency for the new configuration, with accompanying reduced magnetron heating rate. Set D is only a first iteration of

pulsing parameters in the new configuration; pulses can be made twice the amplitude of those used in Set D, so much deeper wells are likely to be usable.

The upshot: A transformed landscape of pulsed positron transfer. In the existing configuration, pulsed particle transfer can be achieved only in tightly controlled, inconvenient conditions. In the proposed configuration, transfer will be much more flexible and robust. The proposed changes could be the deciding factor in the ultimate success of pulsed positron transfer.

7.5 Other Considerations

7.5.1 Drawbacks

Drawbacks of the proposed design changes include:

1. It will be necessary to break the trap electrode vacuum space in order to adjust or repair the first-stage amplifier.

2. The vacuum within the trap can will be exposed to possible outgassing from materials in a PCB board in the first-stage amplifier.

3. The amplifier will be mounted lower on the dilution refrigerator, further from the mixing chamber where the heat is being removed. A low-thermal-impedance heatsinking path from the amplifier to the mixing chamber must be included without introducing mechanical constraints that could stress the trap electrodes.

4. The field emission point, which can be biased up to 1 kV, will be mounted close

to the detection electrode and shock-susceptible FET.

5. The FET is ferromagnetic, so care must be take to locate it as far as possible from the precision trap center to avoid distorting the magnetic field within the trap. However, because of the larger trap can in this new apparatus, even within the trap vacuum can the amplifier can be placed as far away from the precision trap center as it was outside the trap vacuum can in the previous Harvard apparatus, in which the best electron $g/2$ measurement so far was made.

Though these problems must be addressed in the details of the new design, the inconveniences associated with them are far outweighed by the advantages described in previous sections.

One other significant barrier to the reconfiguration is that the planar trap might need to be modified in order to make space for the resonator and the precision first-stage amplifier. There is space in the magnet bore to make the trap can slightly longer, which could provide the necessary space.

7.5.2 Other RF Wiring

Pulsing and detection are not the only RF processes that need to be accommodated in the precision trap. Table 7.2 shows the present and planned connections for all precision RF drive lines. None of these should present a significant problem.

7.5.3 Electrode Modifications

The proposed reconfiguration does not require modifying any trap electrodes. This is a good feature because electrode fabrication is an expensive and time-consuming

Electrode	**RF connections in current configuration**	**RF connections in proposed configuration**
Precision Top Endcap	200 MHz resonator signal	Precision axial/anomaly drive, Precision pulse line
Precision Top Comp	200 MHz resonator ground, Precision pulse line	Precision sideband drive
Precision Bottom Comp	Precision sideband drive	200 MHz resonator ground
Precision Bottom Endcap	Precision axial/anomaly drive	200 MHz resonator signal

Table 7.2: RF connections in current and proposed configurations.

process (Ch. 3). A positron $g/2$ measurement can likely be accomplished more quickly without electrode modifications. However, if the resources were available for a more extensive trap overhaul, there are several minor modifications that would be modestly beneficial.

1. As covered in Sec. 5.4, the positron-loading hole in the top endcap of the precision measurement could be made slightly larger, or significantly larger if it were also made deeper. This could increase the efficiency of pulsed positron transfer into the precision measurement trap (Sec. 6.4.3).

2. Sec. 3.1 described the failure of gold plating on the evaporatively plated precision trap electrodes. Electrodes on which flaking was observed have been re-plated or replaced, but it is possible that plating on the remaining precision measurement trap electrodes could fail in the future. If precision trap electrodes were remade, they could be plated using the more reliable optimized electroplating procedure.

3. As described in [71], an error in the fabrication of the positron accumulation trap led it to its being imperfectly orthogonalized. Installing slightly taller

loading compensation electrodes would allow this error to be corrected, making it easier to tune the positron accumulation trap to see small numbers of trapped particles.

7.6 Outlook

The modifications proposed in this section are relatively minor changes to the current apparatus. Once the amplifier and the 200 MHz resonator have remade in their new locations, the RF properties of the resonator and pulse system will need to be carefully refined and characterized, and the pulsing procedure will need to be tested. These tasks should all be achievable on a timescale of months. With these last major hurdles cleared, the path will be clear to use the many improved features of the current apparatus to make a precise new measurement of positron $g/2$.

Chapter 8

Quench Protection in ATRAP

The ATRAP experiment aims to use precision spectroscopy of trapped antihydrogen to set the most precise limit on CPT symmetry violation in a lepton-baryon system. This chapter describes quench detection and quick turnoff systems for the magnet coils of the Ioffe neutral-particle trap in the ATRAP's current-generation CTRAP apparatus. These systems are used both to enable the detection of trapped antihydrogen and to protect the Ioffe coils in case of a quench. Trap turnoff 25 to 90 times faster than in the previous-generation apparatus and effective protection during quenches have been demonstrated.

8.1 Brief Introduction to ATRAP

The original TRAP collaboration started low-energy antiproton and neutral antihydrogen physics [151, 152], and the current ATRAP collaboration remains a leader [101, 153] in what has developed into a dynamic field of fundamental physics [154,

155, 156, 157]. Comparison at the 1 part in 10^{-12} level or better of the $1S-2S$ line in antihydrogen to existing measurements in hydrogen might be feasible [158].

To make antihydrogen, ATRAP accumulates positrons and antiprotons. The 5.3 MeV antiprotons come from CERN's Antiproton Decelerator [159]. These antiprotons are slowed further via interaction with a 100 μm beryllium degrader foil and an energy-tuning gas cell. They are then trapped in a cryogenic, open-endcap Penning trap, the electrodes of which are nested within a Ioffe trap capable of trapping neutral atoms in a magnetic field minimum [160, 161, 152]. Positrons are emitted from a 20 mCi source, go through a neon moderator [162], undergo buffer-gas cooling [163], go through a long magnetic guide to a room temperature accumulation Penning trap at a rate of 2.4×10^4 e^+/s/mCi [164], and are then transferred to the cryogenic Penning trap stack with near-100% efficiency. Within the Penning-Ioffe trap [100], the positrons and antiprotons are combined into antihydrogen via either three-body recombination [99, 165, 166] or Rydberg cesium charge exchange [167], and low-field-seeking neutral antihydrogen atoms are magnetically confined with the Ioffe trap [101]. Trapped antihydrogen can be detected by applying electric fields that sweep charged particles out of the trap, then turning off the Ioffe trapping field and using scintillating fibers and paddles to detect the pions produced when antiprotons annihilate on the electrode walls. The cosmic ray background of around 41 Hz can be reduced to 1.7 Hz with coincidence information between detectors [101]. Laser systems are under development for laser cooling and precision spectroscopy for the CPT symmetry test [168].

Experiments by the ATRAP collaboration with their first-generation Penning-Ioffe

trap, BTRAP, produced antihydrogen within a Penning-Ioffe trap [100], studied methods for controlling and cooling charged particle plasmas to increase the antihydrogen production rate [169, 170, 171, 172], and culminated in trapping of ground-state antihydrogen [101]. However, the passive quench protection diodes within BTRAP Ioffe magnets made a well-controlled turn-off of trapping fields with external power supplies take at least ten minutes. Only by deliberately quenching the Ioffe magnets—with its concomitant timing nonreproducibility, risk of damage due to local heating, and waste of liquid helium—could the trap be turned off quickly enough to detect antihydrogen above the cosmic ray background. Detection sensitivity of $12/\sqrt{N}$ antihydrogen atoms in N trials with a 1-second turnoff time was demonstrated [101].

8.2 Ioffe Trap Improvements for CTRAP

The design of CTRAP, the ATRAP collaboration's new second-generation Ioffe trap apparatus, incorporates several changes that improve its utility for the study of antihydrogen over previous generations of apparatus that are described in detail in [173]. To accommodate larger plasmas, CTRAP has a much larger trapping volume than BTRAP, the previous-generation apparatus. As in BTRAP, the CTRAP Ioffe trap includes quadrupole coils with $\vec{B}_\perp \propto \rho$ for radial confinement and pinch coils for axial confinement. New in this generation are octupole coils with $\vec{B}_\perp \propto \rho^3$ that can be used for radial confinement in place of the quadrupole coils, as well as bucking coils that cancel out the undesired effect of the pinch field near trap center. The geometry of the octupole field makes it likely to interfere less with charged-particle trapping, which makes it a good candidate for use as the initial trapping field dur-

ing antihydrogen creation. The quadrupole field will confine neutral particles more tightly, a possible advantage for laser cooling and spectroscopy. Both the quadrupole and octupole traps (see Table 8.1) have trap depths greater than BTRAP's 0.57 T (380 mK) quadrupole trap depth, which will enable trapping of a larger fraction of produced antihydrogen.

Magnet	**Inductance**	**Operating Current**		**Dump Resistor**
		Octupole trap	**Quadrupole trap**	
	(mH)	(A)	(A)	(Ohms)
Octupole	14	680	0	1.17
Quadrupole	113	0	470	1.99
Pinch	117	210	310	3.94
Bucking	20	-179	-264	1.90
Trap Depth		0.60 T (405 mK)	0.76 T (526 mK)	

Table 8.1: Measured inductance, dump resistor values, and highest achieved operating currents for both trapping modes of the CTRAP Ioffe trap. Trap depths are listed in Tesla and also as the energy, $-\mu_B\|\vec{B}\|$, in mK for ground-state antihydrogen.

The most important changes between BTRAP and CTRAP are those that allow faster magnet turnoff without quenching the Ioffe magnets. To improve to single-atom detection of antihydrogen over the cosmic ray background, the new trap makes it possible to remove the Ioffe trapping fields on the timescale of tens of ms rather than BTRAP's 1 s. By constructing them with many fewer turns (Fig. 8.1), CTRAP coils have been made to have much lower inductances (Table 8.1) than BTRAP

quadrupole's 3.3 H. This allows for much faster magnet charging and turnoff[1]. In order to create deep enough traps, however, much higher currents—up to 680 A rather than up to 80 A—must be used, which increases demands on hardware used to rapidly remove the current. The remainder of this chapter describes the Ioffe magnet turnoff and quench protection systems for CTRAP.

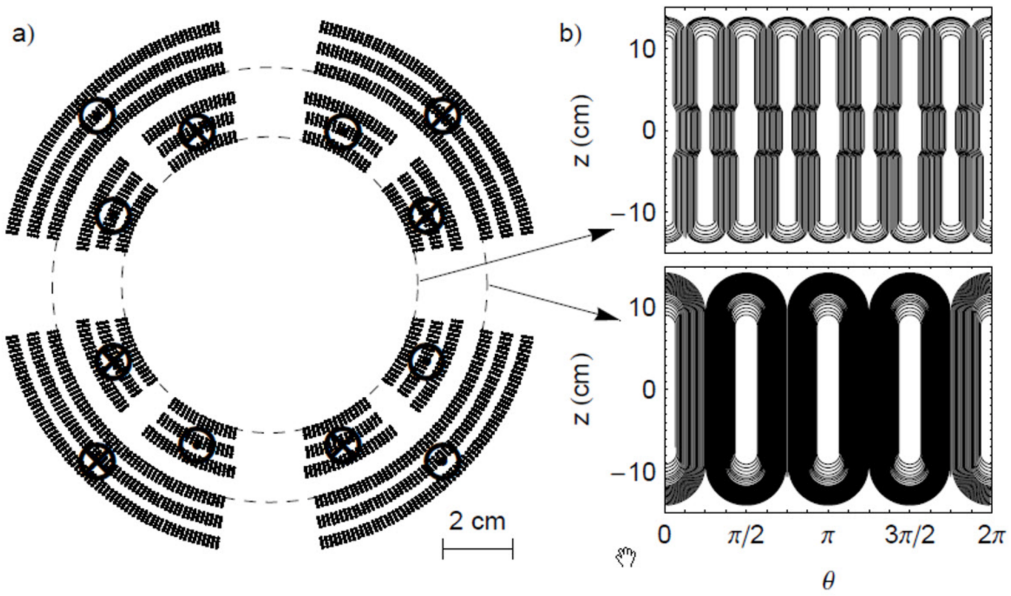

Figure 8.1: (a) Cross section of the Ioffe windings that contains the center axis of the trap. The quadrupole racetrack, which has $2n = 4$-fold symmetry, sits outside the octupole windings, which have $2n = 8$-fold symmetry. The $\odot$ and $\otimes$ signs indicate the current direction and the four side-access ports are visible. (b) An unfolded side view of the quadrupole and octupole windings shows how the octupole windings are slightly spread near the center of the trap to permit 4-fold side access. The quadrupole has a total of 744 "vertical current bars" and the octupole has 216, compared to the 2930 for BTRAP's quadrupole. CTRAP also has a much larger inner diameter than BTRAP, creating a larger trapping volume.

The considerable apparatus required for such fast current dumps, along with pre-

[1]Because the Ioffe field reduces the stability of the charged particles confined by the Penning trap, the reduced charging time enabled by these lower inductances is also a valuable improvement. Faster charging times are described in [173].

dictions and data about the behavior of the system, is described in Sec. 8.3. The need for fast, non-quench-triggered turnoff also changes the design requirements for quench protection. Incorporating passive quench protection diodes, as in BTRAP, would create the same unacceptable limit on the speed of non-quench-induced magnet current ramp-down. Also, enough energy is stored in the coil that a quench could destroy coil windings. Therefore, an active quench protection system was designed for CTRAP. Sec. 8.5.1 describes predictions of temperature rise during a quench and the effect of quench protection, with further calculations and predictions in Ch. 9 and comparisons to observational data in Sec. 8.5.3. Sec. 8.5.2 describes the hardware and software of the implemented quench detection system.

8.3 Energization and Turn-off (Dump) Circuits

Fig. 8.2 shows the generic plan of each Ioffe coil energization and dump circuit, with voltage taps for quench monitoring. Each magnet is energized by a dedicated high-current power supply or pair of such supplies. Current flows through copper bus bars at room temperature, through vapor-cooled current leads upon entry to the cryogen space, and through bus bars made of high-temperature superconductors near 4 K. Voltages V_A through V_G are monitored to detect quenches (see Sec. 8.5.2). To quickly stop current flow through a magnet, the leg of its circuit containing the power supply is interrupted using an Integrated Gate Bipolar Transistor (IGBT). This redirects the current through an external dump resistor R, where the magnet's stored energy is safely dissipated outside the magnet.

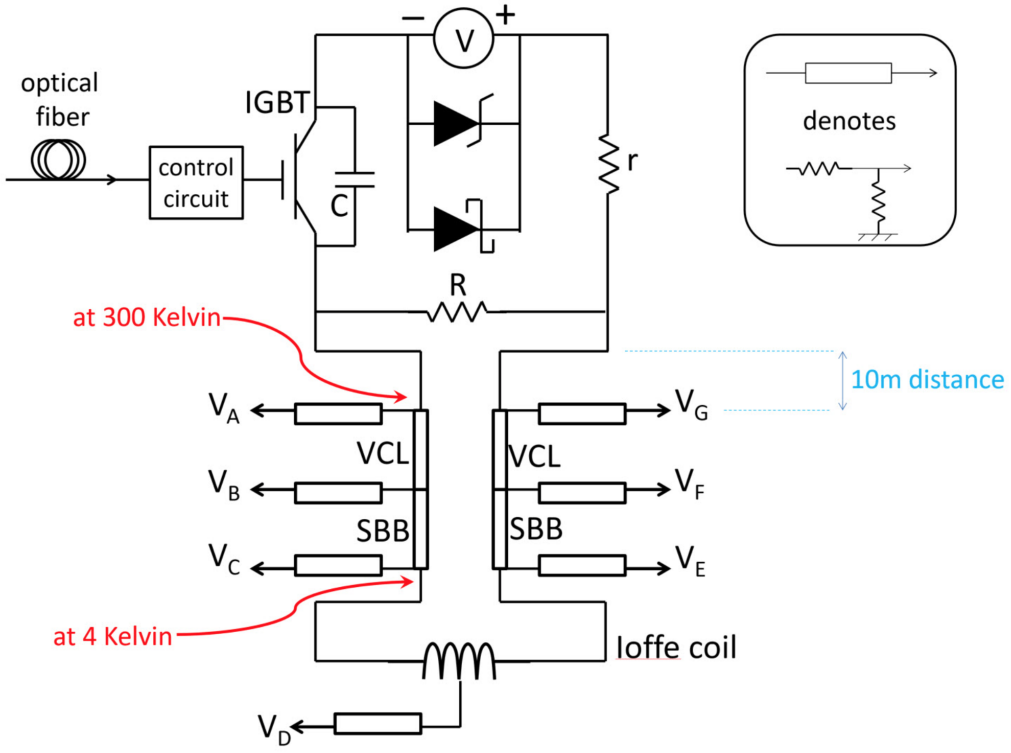

Figure 8.2: A room temperature power supply, IGBT, and dump resistor connect to a 4 K Ioffe coil through vapor cooled leads (VCL) and superconducting bus bars (SBB). Tap voltages (V_A through V_G) are monitored for quench detection.

8.3.1 Switching with IGBTs

To interrupt current in the Ioffe coils, a switch was needed which could conduct 1000 A when closed, withstand 1000 kV when open, and reliably switch faster than the desired 10 ms turn-off timescale. Mechanical contactors are available with these current and voltage ratings, but not with both in a single device; in addition, they take 20-40 ms to open and have delays that are not reproducible. Metal-oxide-semiconductor field-effect transistors (MOSFETs) are fast enough but barely reach high enough currents and cannot survive 1 kV. IGBTs can withstand higher voltages than MOSFETs, have lower losses at high currents, and also switch on a 1 μs timescale [174]. The chosen IGBTs are produced by Semikron, Inc and are intended for use in DC to AC converters at power plants and in other industrial applications. They are rated to 1500 A and 1700 V.

Because of inductance in the high-current bus bars that carry the steady-state current, current briefly continues to flow in the IGBT's leg of the circuit even after the IGBT has opened. Therefore, to avoid charge pileup and the development of damaging voltages spikes across the IGBT, a capacitor must be placed in parallel with the IGBT. The IGBTs sit within a custom assembly[2], pictured in 8.3, that includes a bank of four 420 μF propylene capacitors in parallel, an integrated IGBT gate driver controlled by 15 V CMOS logic, bus bar terminals, and a cooling fan. The DC voltage rating of the assembly is limited by the capacitors' limit of 1100 V.

[2]Semikron SKiiP 1513GB172-3DL

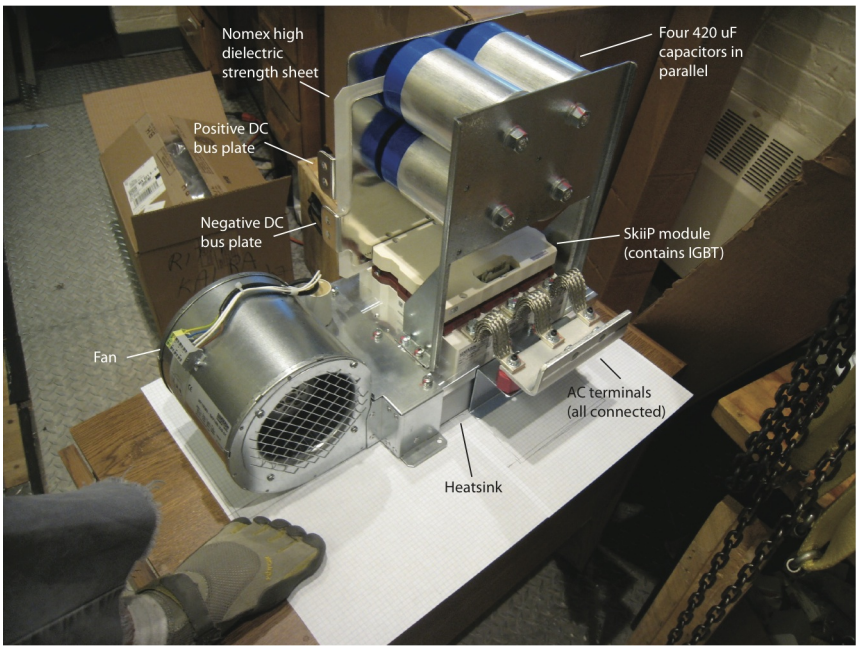

Figure 8.3: Semikron SkiiP IGBT module with women's US size 7 foot for scale.

8.3.2 Power Supplies and Protection

Agilent 6681A power supplies energize the coils. The pinch and bucking coils each use a single supply configured for up to 580 A and 8 V. The quadrupole uses a supply configured for 650 A and 7 V. The octupole uses two 580 A, 8 V supplies in parallel.

Like the IGBTs, the power supplies must be protected during the dump process. After a dump is triggered, the IGBT-protection capacitors initially charge up, then discharge. During this discharge, current briefly flows backward through the power supply's leg of the circuit. The power supplies' current-sinking capabilities might not be sufficient to protect them from damage in this case: they cannot sink enough current and they cannot be placed in the current-sinking mode quickly enough. As a precaution, each power supply is thus protected by a Transient Voltage Suppression

(TVS) diode[3] in parallel to clamp reverse voltages. Out of an abundance of caution in case of unexpected transients, Schottky diodes[4] are also placed in parallel to limit forward voltage drops. For redundancy, several of each type of diode are connected in parallel across each power supply.

8.3.3 High-Current Bus Bar Assembly

To carry the necessary currents, a combination of solid copper bus bars and tin-plated, insulated flexible copper braid[5] with cross sections of at least $1/2" \times 2"$ is used. The bus bar connection surfaces are prepared with the industry-standard procedure: cleaning, sanding, and the application of a thin layer of petroleum jelly [175]. The jelly itself is non-conductive, but as the bolts are tightened, the jelly is squeezed out from between all the points of contact on the rough bus bar surfaces and therefore has no negative effect on overall conductivity of the joint. The jelly occupies the interstices between these points of contact to prevent air from entering and oxidizing the copper, which reduces the rate of degradation of the joint over time [175].

8.3.4 Dump Resistors

A dump resistor's role is to harmlessly dissipate its magnet's stored energy far from the magnet. The higher its resistance, the faster the energy is removed and the more effectively heating is prevented. However, the $V = I_L R_{dump}$ voltage spike across the terminals of the dump resistor (and therefore the magnet, and the power

[3] Littelfuse 5KP5.0A, 2kW power rating for 10 ms pulse

[4] GeneSiC 905MBRH20045, voltage drop of 0.65 V, surge current rating 3 kA and GeneSiC 905MBRT40060, forward voltage 0.8 V, surge current 3 kA

[5] Storm Copper HVDFB-82310A and HVD-82310B

supply plus IGBT circuit leg) shortly after the switch happens is also higher for higher resistance. Each circuit's dump resistance was chosen to maximize energy dissipated outside the magnet while limiting the voltage spike to under 1 kV to prevent damage to the IGBT assembly. Resistance values are listed in Table 8.1.

Dump resistors were machined into long zigzags with a water-jet from 1/8" thick 304 stainless steel sheet. This design provides ohm-scale resistances spread over a large area for better heat dissipation. Each dump resistor is mounted separately on ceramic spacers inside its own fan-cooled 19" rack-mounted box. A stainless-steel-and-ceramic assembly model is shown in Fig. 8.4.

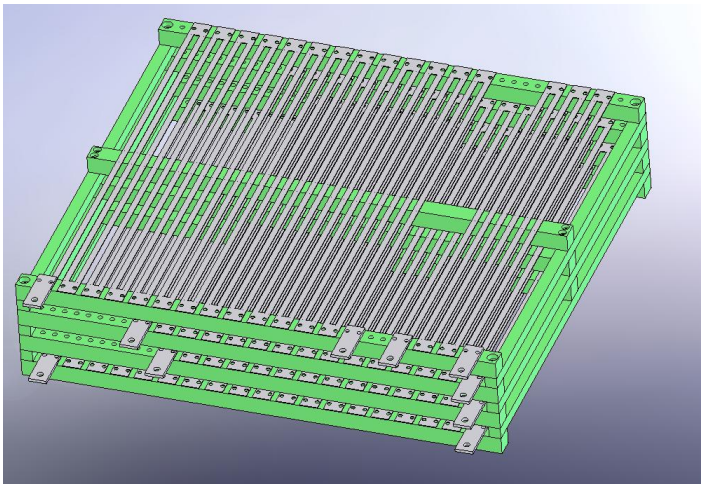

Figure 8.4: CAD model of a dump resistor, where the assembly shown fits inside a standard 19"-wide rack-mount box.

8.4 Dump Progression Predictions and Data

The effective circuit after a dump is triggered and current through the IGBT has been interrupted (which happens very quickly) is shown in Fig. 8.5. The evolution of

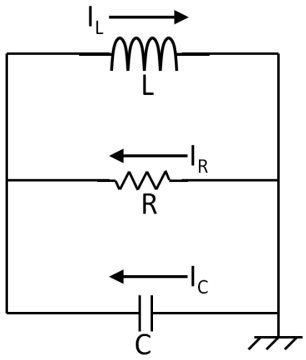

Figure 8.5: The effective circuit during a turn-off (dump) of one of the coils of the Ioffe trap. At $t = 0$, $I_L = I_C$ and $I_R = 0$.

current through the magnet I_L is determined by

$$\tau_{RC}\tau_{LR}\ddot{I_L} + \tau_{LR}\dot{I_L} + I_L = 0 \tag{8.1}$$

where $\tau_{RC} = RC$ and $\tau_{LR} = L/R$ (so $\frac{\tau_{RC}}{\tau_{LR}} = R^2C/L$), C is the 1.68 mF in parallel with the IGBT, and R is the resistance of a given circuit's dump resistor. Given the boundary conditions of $I_L(t = 0) = I_0$ and $\dot{I}_L(t = 0) = 0$ and defining $s \equiv \sqrt{1 - 4\tau_{RC}/\tau_{LR}}$, $I_L(t)$ is predicted to be

$$\begin{aligned} I_L &= I_0 \left[\frac{1+s}{2s} e^{-\frac{t(1-s)}{2\tau_{RC}}} \frac{1-s}{2s} e^{-\frac{t(1+s)}{2\tau_{RC}}} \right] \\ &\approx I_0 \left[\left(1 + \frac{2\tau_{RC}}{\tau_{LR}} \right) e^{-t/\tau_{LR}} - \frac{2\tau_{RC}}{\tau_{LR}} e^{-t/\tau_{RC}} \right]. \end{aligned} \tag{8.2}$$

Predicted tap voltages across sections of the magnet coils are given by $V = L\dot{I_L}$, allowing a comparison to data available from voltage taps on the Ioffe coils. Fig. 8.6 shows predictions and experimental data for intentionally triggered current dumps (not dumps automatically triggered by a quench.) Voltage differences shown are across each coil, $V_E(t) - V_C(t)$.

These voltage data can be used to reconstruct the I_L and therefore magnetic trap

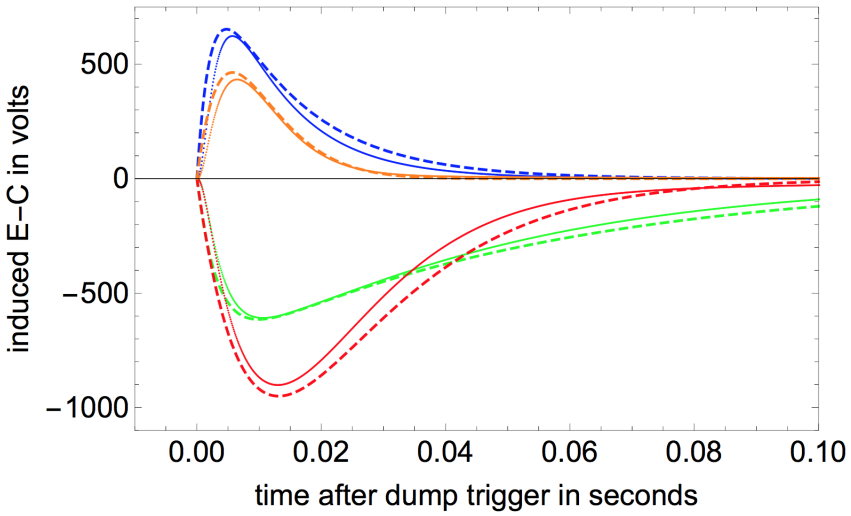

Figure 8.6: Measured (solid/dotted) and predicted (dashed) voltages induced across Ioffe trap coils for the octupole (blue), quadrupole (green), pinch (red) and bucking (orange) coils, respectively.

turnoff times as follows:

$$I_L(t) = I_0 + \int_0^t \frac{V(t)}{L} dt. \tag{8.3}$$

These yield the data in Fig. 8.7. Current that appears to persist after the initial dropoff, most notably for the octupole magnet, does not indicate a physical persistent current but instead energy dissipation (e.g., heating of the magnet enclosure by eddy currents) not included in the model of Eqn 8.1. The solid/dotted lines may therefore be treated as an upper limit to current. Our paper [173] explores imperfections in the match between data and theory in more detail. It is clear from these data, however, that $1/e$ turnoff times are well under 0.1 s for all magnets and under 0.03 s for the octupole magnet. After these data were taken, direct monitoring of the currents in the Ioffe coils was implemented using Hall current sensors that enclosed the current-carrying wires. These data confirmed the fast turnoff, with time constants of 11 ms for the octupole, 40 ms for the quadrupole, 18 ms for the pinch coil, and 7 ms for

the bucking coil [173]. This is an enormous improvement over BTRAP's 1 s turnoff time and is expected to improve antihydrogen detection sensitivity to the single-atom level.

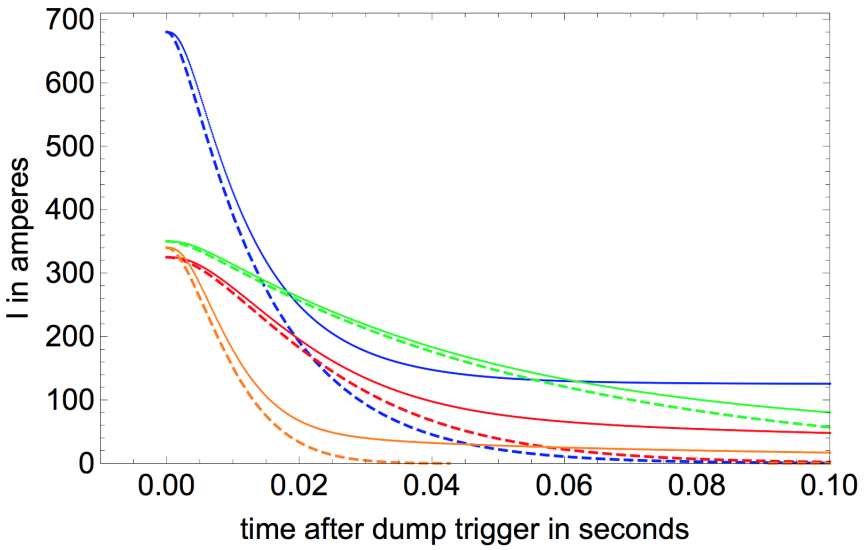

Figure 8.7: Measured (solid/dotted) and predicted (dashed) currents through Ioffe trap coils for the octupole (blue), quadrupole (green), pinch (red) and bucking (orange) coils, respectively.

8.5 Quenches and Quench Protection

8.5.1 The Need for Active Quench Protection

If any section of superconducting wire inside one of the superconducting magnets warms to above its critical temperature, its resistance suddenly increases, triggering a positive feedback loop of heating and resistivity increases called a quench. Whether or not the temperature rises to a damaging level depends on the material properties, geometry, and operating current of a given magnet, motivating a study of the progres-

sion of quenches in these specific magnets to evaluate whether a quench protection system is needed, and if it is, how quickly it must be activated to prevent thermal damage.

The maximum temperature reached by a section of quenched coil depends on the local interaction of electrical current with properties that are highly nonlinear with temperature, such as thermal conductivity, heat capacity, and electrical resistivity. Though numerical simulations are the most accurate way to predict the progression of a quench [176], in some conditions analytical calculations are predictive enough to be useful in the design process, for example to determine the need for and help in the design of an active quench protection system. Ch. 9 extends a treatment by Wilson [177] and adapts it to the CTRAP octupole and quadrupole coils. This analytical calculation predicts the progression of the quench resistance, magnet current, voltage drop, and maximum hot spot temperature associated with a quench. A small subset of these results—the predicted maximum temperatures of the hottest spots during an octupole or quadrupole quench, with and without a quench protection system as described in Sec 8.5.2—are quoted here in Table 8.2.

	Maximum temperature (K)	
	Octupole	**Quadrupole**
Prediction without quench protection	488	750
Prediction with quench protection	24	26

Table 8.2: Predicted maximum temperatures reached by octupole and quadrupole magnets during a quench with and without quench protection. Quench detection and dump systems are described in following sections. Table 9.4 is an expanded version of this table.

Without quench protection, both the octupole and quadrupole magnets are at

risk of charring of insulation. (The pinch and bucking coils have lower currents, current densities, and stored energies than the octupole and quadrupole, but they still are at risk during quenches. It is also useful to have the option of dumping the current from the pinch and bucking coils as an alternative way to remove the trap.) Each of the four Ioffe coils is therefore protected by a quench protection system that watches for asymmetries in the voltage drops that arise across sections of the magnets during a quench [177]. When a quench is detected, the detection system electronically activates the quick magnet turnoff system and redirects each magnet's current through an external dump resistor, where the magnet's stored energy is harmlessly dissipated externally.

8.5.2 Quench Detection Hardware and Software

The basic quench detection protocol follows the lead of previous groups in comparing voltage drops across analogous sections of a solenoid [178, 177, 179]. Voltages are tapped off at junctions between different sections of the magnet circuit and at the center of each Ioffe coil, at positions labeled V_A through V_G in Fig. 8.2. The middle five voltage tap lines from each magnet must emerge from the cryogen space on a 32-pin hermetically sealed electrical vacuum feedthrough with pins spaced 3 mm apart. Because voltage drops across the magnets can reach 1 kV (see Sec. 8.3) and the breakdown voltage in the gaseous helium atmosphere in this cryogen space is less than 1 kV per 3 mm [180], these voltages are scaled down by a factor of 5 using a voltage divider inside the cryogen space, before they reach this connector. Voltage dividers are made from five 150 kΩ resistors each, using large resistor case sizes and

designing trace layouts carefully to avoid breakdown.

The seven divided-down voltage tap voltages from each of the four magnets are fed to a custom-built quench detector that determines whether a quench has happened and triggers a current dump if it has. The dump circuit can also accept a TTL pulse input to trigger a dump intentionally. Fig. 8.8 shows a schematic of the first version of the quench detector.

To determine whether a quench has occurred, the quench detector subtracts $V_C - V_D$ from $V_D - V_E$, $V_B - V_C$ from $V_E - V_F$, and $V_A - V_B$ from $V_F - V_G$. In the first version of the quench detector, analog logic was used to add these differences with adjustable weighting factors into a weighted sum. If this weighted sum's absolute value exceeded an adjustable threshold for a time exceeding a set threshold, a quench was considered to have been detected and a dump of the current in the magnet was triggered (see Sec. 8.3 for details of the dump process). In a newer version of the quench detector, the time delay has been eliminated and dumps can be triggered directly by an imbalance in any single pair of differences rather than combining all differences into a single weighted sum. Thresholds are typically set at 1 V for differences between voltage drops over vapor-cooled current leads (for the full voltage at the coils, not post-division) and 0.5 V for bus bars. Because the Ioffe magnet coils are the easiest to damage and more difficult to repair, thresholds for differences between these halves are set lower, to 0.25 V, over a noise threshold of approximately 0.15 V.

One advantage of comparing symmetrical parts of the magnet to each other over comparing each voltage drop to an externally defined threshold is that it automatically ignores the voltages that develop during normal charging and discharging of the

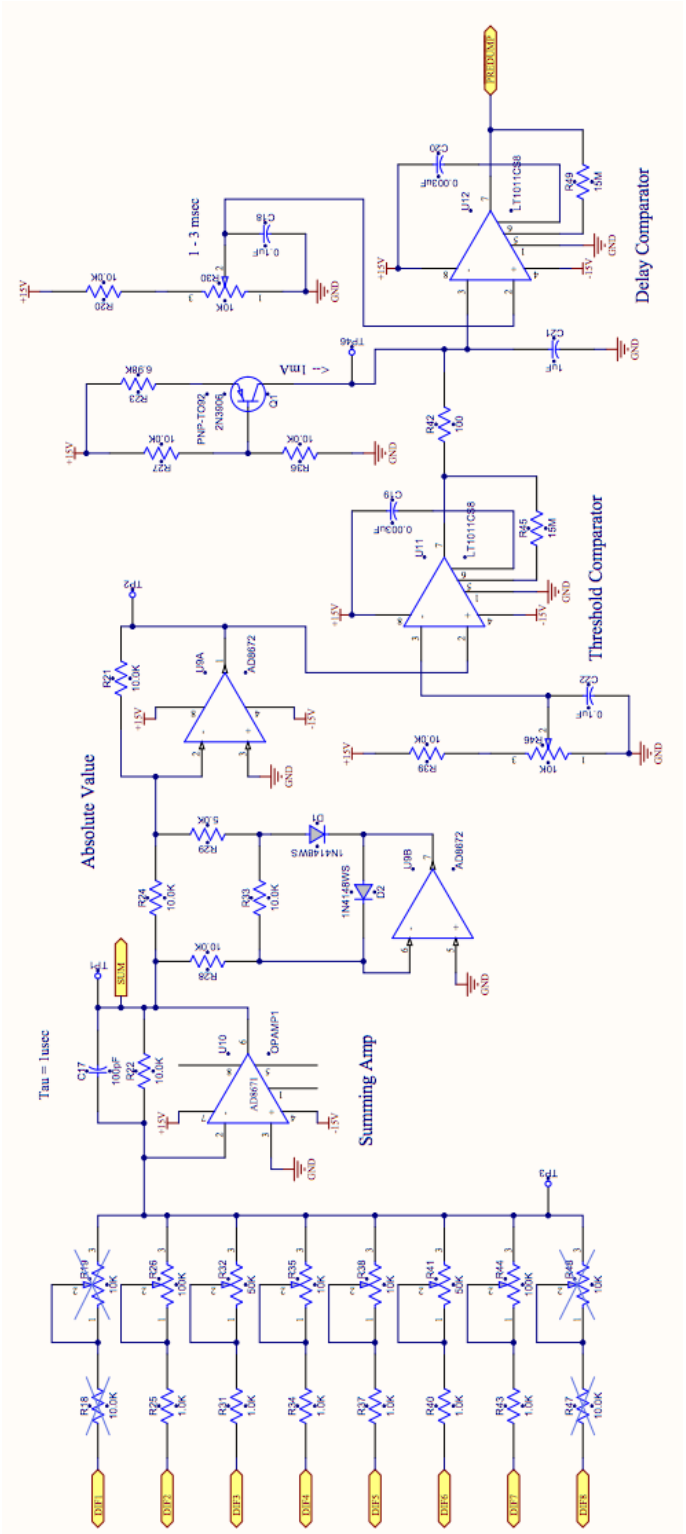

Figure 8.8: The first-generation quench detector takes in the divided-down tap voltages and takes differences between neighboring taps (schematic not pictured; these differences are shown as inputs on the left). Then, it adds weighted differences to determine whether a quench has happened and a dump should be triggered.

magnet. This doesn't result in missed quenches as long as the following assumptions hold: 1) a quench is unlikely to nucleate in the exact center of a magnet and propagate perfectly symmetrically, and 2) it is extremely unlikely that multiple identical quench events will occur simultaneously in different sections of the magnet.

In the event of a dump, the quench detector sends out the following signals:

1. A fiber optic output signal received by an independently powered "daughter board" at the IGBT, which then converts the dump command to 15 V CMOS levels to control the IGBT gate driver. It is this signal that causes the current in the magnet to be quickly redirected to the dump resistor.

2. A TTL signal that is monitored by a dedicated quench datalogging computer to determine when to save detailed data.

3. A relay switch to send the power supplies into "Inhibit" mode, which turns off their output. This prevents the power supplies from continuing to push current through a dump resistor and quenched magnet. It also provides a modest degree of protection for the power supplies against voltage transients.

In addition to being monitored by the quench detector, each tap voltage is also monitored with an input channel on a National Instruments 9220 analog-to-digital converter, then displayed and saved using National Instruments' LabView software on the datalogging computer. The voltage tap data are saved at a rate of 10 kHz during an adjustable period before and after a quench or an intentional dump, triggered on the quench detector's dump command and using Labview's producer/consumer loop data structures. Data are saved at a lower rate during magnet charging, steady-state

operation, and slow discharging.

8.5.3 Quench Progression Predictions and Data

The quench protection system has been a great success, protecting the magnets from harm. With it in use, no damage has been noted from the quenches that have been observed in the octupole and quadrupole magnets. Once, the quench protection system was mistakenly turned off, and a quench burned through a section of the quadrupole magnet's superconducting lead. Fortunately, the lead was outside the epoxied magnet form, so it was repairable. This experience validates the analysis in Sec. 8.5.1 and Ch. 9: quench protection is required, and the detection and dump systems implemented as described here are sufficient to prevent damage to the magnets.

However, this does not give any finer-grained quantitative sense of the accuracy of, e.g., the maximum local hot spot temperatures in Table 8.2. For a more detailed test of our understanding of quench propagation dynamics, voltage rise predictions can be compared to voltage tap data from initial period of a quench, before a dump is triggered. The details of these predictions are described in Ch. 9.

8.5.3.1 Interpreting voltage tap data

This section discusses the voltages that are predicted to arise in the period between quench nucleation and the triggering of the quench detection system. Voltage tap data are compared to the voltage rise predictions from Ch. 9.

Before a quench, voltages V_C and V_E at taps at either end of a given supercon-

ducting Ioffe magnet are approximately equal to each other and to the voltage V_D at the center tap[6]; the tiny differences observed come only from static resistances in wiring between the tap points and the the quench detector and/or instrumentation offsets within the quench detector. Corrected versions of the tap voltages can be defined where these uninteresting offsets have been measured in pre-quench data and subtracted so that until the onset of quench, $V_{C,adj} = V_{D,adj} = V_{E,adj}$. As the quench begins, a resistive voltage drop ΔV_{RQ} develops across the quenched region. As illustrated in Fig. 8.9, across the terminals of the magnet this voltage drop is virtually entirely canceled out by ΔV_{LQ}, the EMF induced by the changing current and inductance of the magnet [177][7]. The voltage spike therefore appears only within the magnet, not across its terminals, and it remains the case that $V_{C,adj} = V_{E,adj}$. However, $V_{D,adj}$ decreases if the quenched region is centered between taps C and D and increases if it is centered between taps D and E.

To test Ch. 9's prediction of ΔV_{RQ}, the voltage drop due to the resistance of the quenched section, it must be related to the measured voltage tap differences. First, we derive an expression for voltage as a function of position. Define x as the position

[6]Though there are 2-3 V across the terminals of the power supply during normal operation [173], this is balanced by the voltage drops across resistances in the normal-conducting parts of the magnet energization circuit (bus bars and joints, IGBT, etc). Because the V_C, V_D, and V_E voltage taps probe points on a continuous stretch of superconducting wire, during normal operation the voltages at these points in the Ioffe coils are equal.

[7]The rest of the magnet energization circuit does have some inductance (e.g., in the normal-conducting bus bars) and across which some small voltage drop does develop due to the changing current. However, this inductance is tiny compared to the inductance of any of the Ioffe coils and this voltage drop can therefore be ignored. As before the quench, the voltage difference across power supply terminals is canceled by voltage drops across resistances in the normal-conducting parts of the magnet energization circuit. Therefore, it is expected to still be the case that $V_{C,adj} = V_{E,adj}$, and the data (Figs. 8.10 and 8.12) support this. In the words of [177]: "A common misapprehension is that large voltages appear across the terminals of a magnet during a quench. In fact almost all of the potential drop occurs within the coil where the inductive and resistance voltages are opposed to each other."

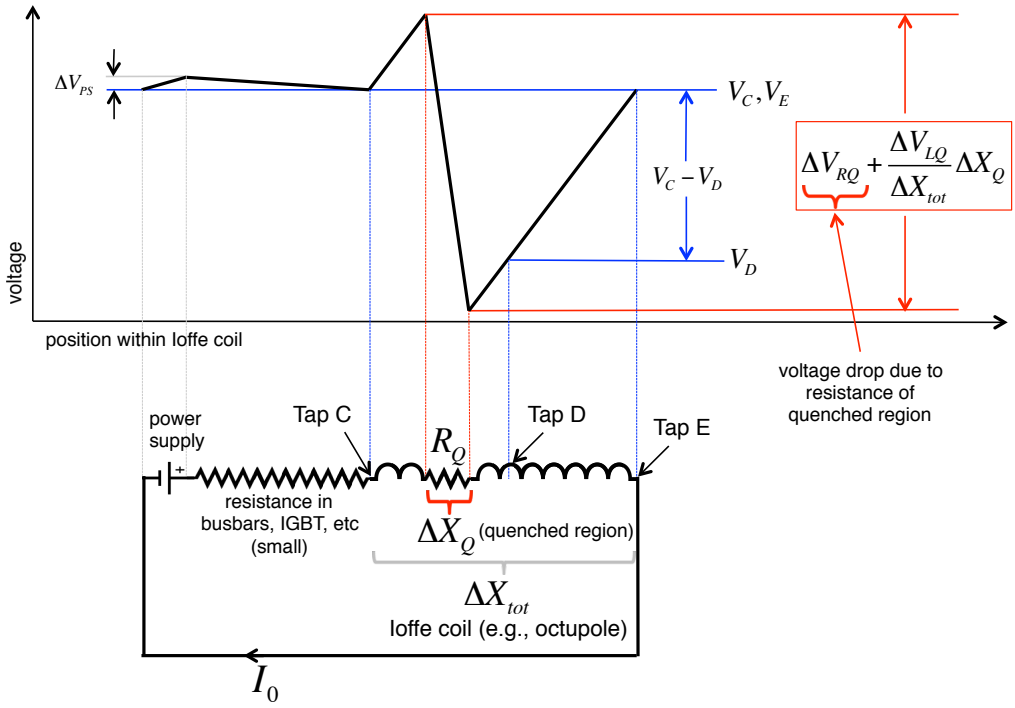

Figure 8.9: Voltage drops within a magnet during a quench. V_C, V_D, and V_E are voltages at the voltage taps, R_Q is the resistance of the quenched region, ΔV_{RQ} is the voltage drop due to resistance across the quenched region, ΔV_{LQ} is the magnet's inductive kickback voltage in response to the quench, and ΔV_{PS} is the voltage across the power supply terminals. ΔX_{tot} is the length of the superconductor in the magnet. ΔX_Q is the length of the quenched region.

along the coil, with tap C at $x = 0$ and $x_{Q,0}$ as the position of the quench origin. Define ΔX_{tot} as the total length of the coil and ΔX_Q as the length of the quenched region. Taking the inductance per unit length to be uniform along the length of a Ioffe coil, the voltage at a position x from tap C is given by

$$V(x) - V_{C,adj} = \begin{cases} \dfrac{\Delta V_{LQ}}{\Delta X_{tot}} x & 0 < x < x_{Q,0} - \frac{\Delta X_{tot}}{2} \\ \dfrac{\Delta V_{LQ}}{\Delta X_{tot}} x + \dfrac{\Delta V_{RQ}}{\Delta X_Q}(x - (x_{Q,0} + \dfrac{\Delta X_Q}{2})) & x_{Q,0} - \frac{\Delta X_{tot}}{2} < x < x_{Q,0} + \frac{\Delta X_{tot}}{2} \\ \dfrac{\Delta V_{LQ}}{\Delta X_{tot}} x + \Delta V_{RQ} & x_{Q,0} + \frac{\Delta X_{tot}}{2} < x < \Delta X_{tot}. \end{cases} \tag{8.4}$$

Without knowing whether the D tap at position $x = \frac{\Delta X_{tot}}{2}$ is within the quenched section, the relationship of V_D to ΔV_{RQ} cannot be known with certainty. However, quenches are detected on a <15 ms timescale, much shorter than the >1 s timescale on which they would spread along a cable axis through an entire magnet (Ch. 9, [177]). Due to cable winding geometry, a transverse quench propagation is also likely to involve cable sections on the same side of the center tap. Therefore, as long as quenches are not more likely to nucleate near the center of a magnet than the edges, a given quench will rarely cross the center D tap before the quench protection system kicks in. First consider the case where the quenched section is entirely between taps C and D, as in Fig. 8.9. In this case,

$$V_{D,adj} - V_{C,adj} = \frac{\Delta V_{LQ}}{\Delta X_{tot}} \frac{\Delta X_{tot}}{2} + \Delta V_{RQ} = \frac{\Delta V_{LQ}}{2} + \Delta V_{RQ}. \tag{8.5}$$

Because $\Delta V_{LQ} = -\Delta V_{RQ}$, this simplifies to

$$V_{D,adj} - V_{C,adj} = \frac{\Delta V_{RQ}}{2}. \tag{8.6}$$

Also remembering that $V_{C,adj} = V_{E,adj}$, the voltages on voltage taps can therefore be combined in the following way to get

$$(V_{D,adj} - V_{E,adj}) - (V_{C,adj} - V_{D,adj}) = \Delta V_{RQ}, \tag{8.7}$$

which is positive. Similarly, for a quench between taps D and E,

$$(V_{D,adj} - V_{E,adj}) - (V_{C,adj} - V_{D,adj}) = -\Delta V_{RQ}, \tag{8.8}$$

which is negative. In the following two sections, this is used to compare analytical predictions to data from quenches in the octupole and quadrupole magnets.

8.5.3.2 Octupole quench

The voltages at taps C, D, and E from a quench in the octupole magnet from a starting current of 594 A are shown in Fig. 8.10. As described in Sec. 8.5.3.1, the D tap's voltage increase during the pre-dump part of the quench shows that the quench originated between taps D and E. After the dump is triggered, the voltage drop across R_{dump} is much greater than the voltage drop across R_Q and the voltage at tap D is once again between those of taps C and E.

Fig. 8.10 superimposes predicted $-\Delta V_{RQ}(t)$ from the voltage tap data with Ch. 9's analytical predictions for various boundary conditions, with the prediction for this system shown as a solid blue line. Because the exact time of quench initiation in the experimental data is not known, there is an unknown time offset between data and

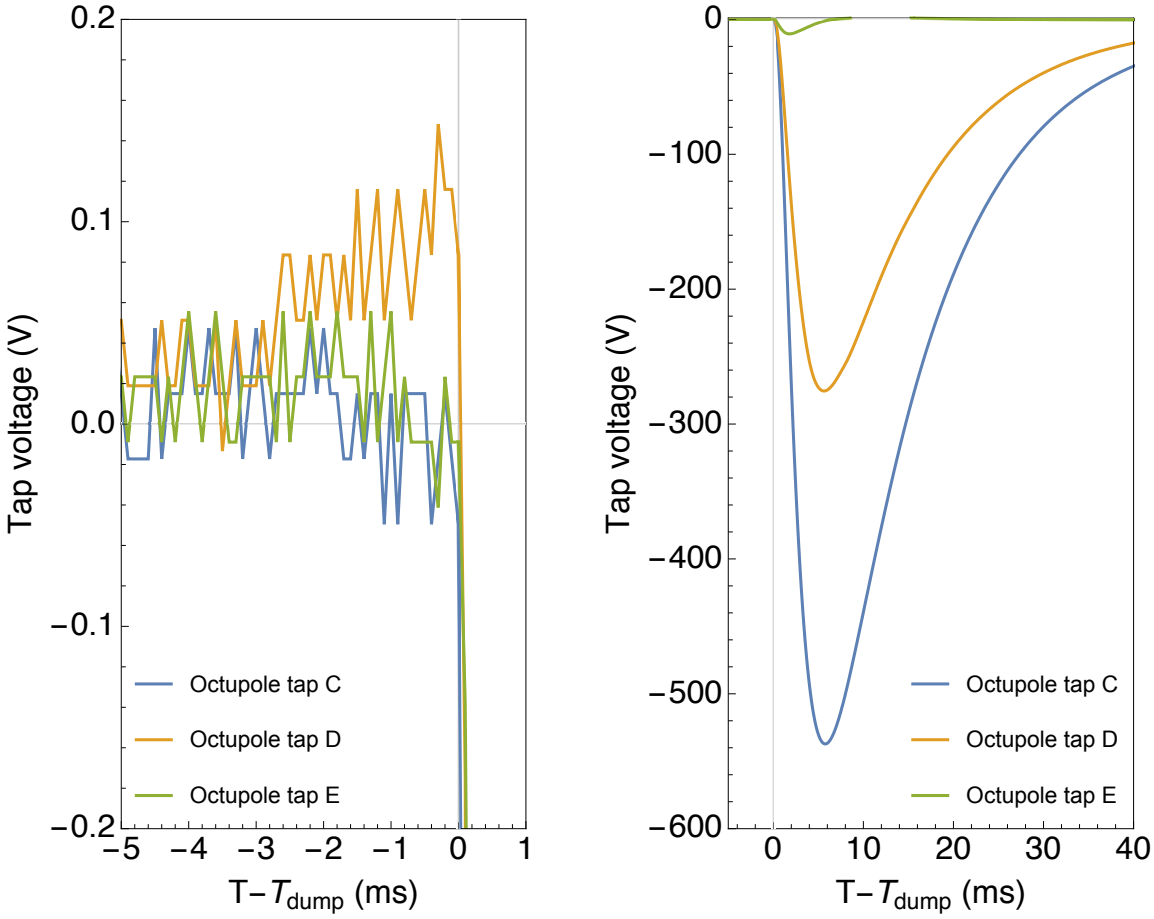

Figure 8.10: Adjusted voltages $V_{C,adj}$, $V_{D,adj}$, and $V_{E,adj}$ on the octupole voltage taps during the beginning of a quench and dump trigger (left) and the resulting dump (right).

theory. The relative timing chosen for for the plot was set by eye. This $T_Q - T_{dump}$ is the only free parameter in this plot. The quench protection system triggers a dump at a time marked by a vertical gray line, and after this point the curve deviates sharply from the no-protection prediction (as expected).

Signal-to-noise is intentionally low because the quench protection system thresholds are set close to noise thresholds to be maximally conservative in protecting the magnets. However, the curve appears to be between the blue curve, which this prediction for for the CTRAP octupole geometry, and the red curve, which is the prediction for a slightly altered geometry in which propagation of a quench transversely between neighboring coils is a more important effect[8]. The deviation from the predicted blue curve could be caused by imperfections in any of a number of aspects of the model, e.g., the estimate of the transverse quench propagation velocity across a set of four cables, or the constant-current assumption. This agreement is impressive considering the simplifications that had to be made to analytically describe the highly nonlinear quench process.

8.5.3.3 Quadrupole quench

The voltages at taps C, D, and E from a quench in the quadrupole magnet from a starting current of 500 A are shown in Fig. 8.12. The direction of the current is opposite to that in the octupole magnet with respect to the labeling of the voltage taps, so the D tap's voltage decrease during the quench shows that the quench originated between taps D and E. Fig. 8.12 is the analog of Fig. 8.10 for this quadrupole

[8]See Ch. 9 for more details on the differences between the boundary conditions for the different curves. The data are clearly incompatible with the predictions for an unbounded quench (orange curve) or a quench that does not propagate transversely at all (green curve).

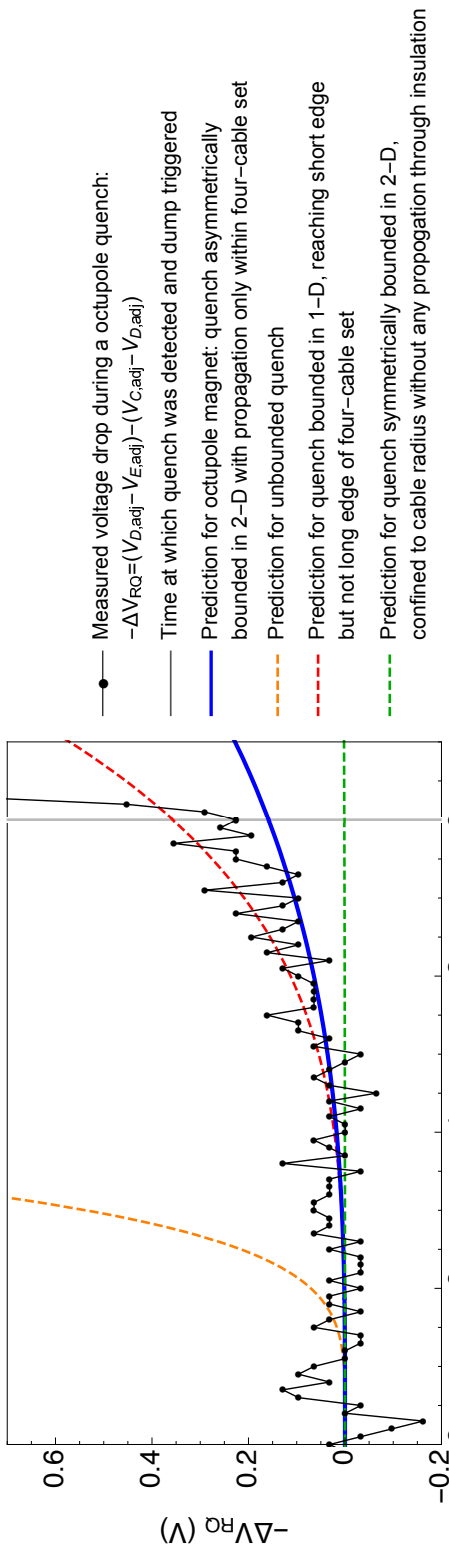

Figure 8.11: Measured voltage drop difference $(V_{D,adj} - V_{E,adj}) - (V_{C,adj} - V_{D,adj}) = -\Delta V_{RQ}$ vs. time during an octupole magnet quench (black), with predictions for CTRAP octupole boundary conditions (blue) and various other boundary conditions for comparison (other colors; see Ch. 9 for details). Because the exact time of quench initiation in the experimental data is not known, the quench initiation time $T_Q - T_{dump} = -8$ ms of the theoretical curves is set by eye with estimated error of ± 1 ms.

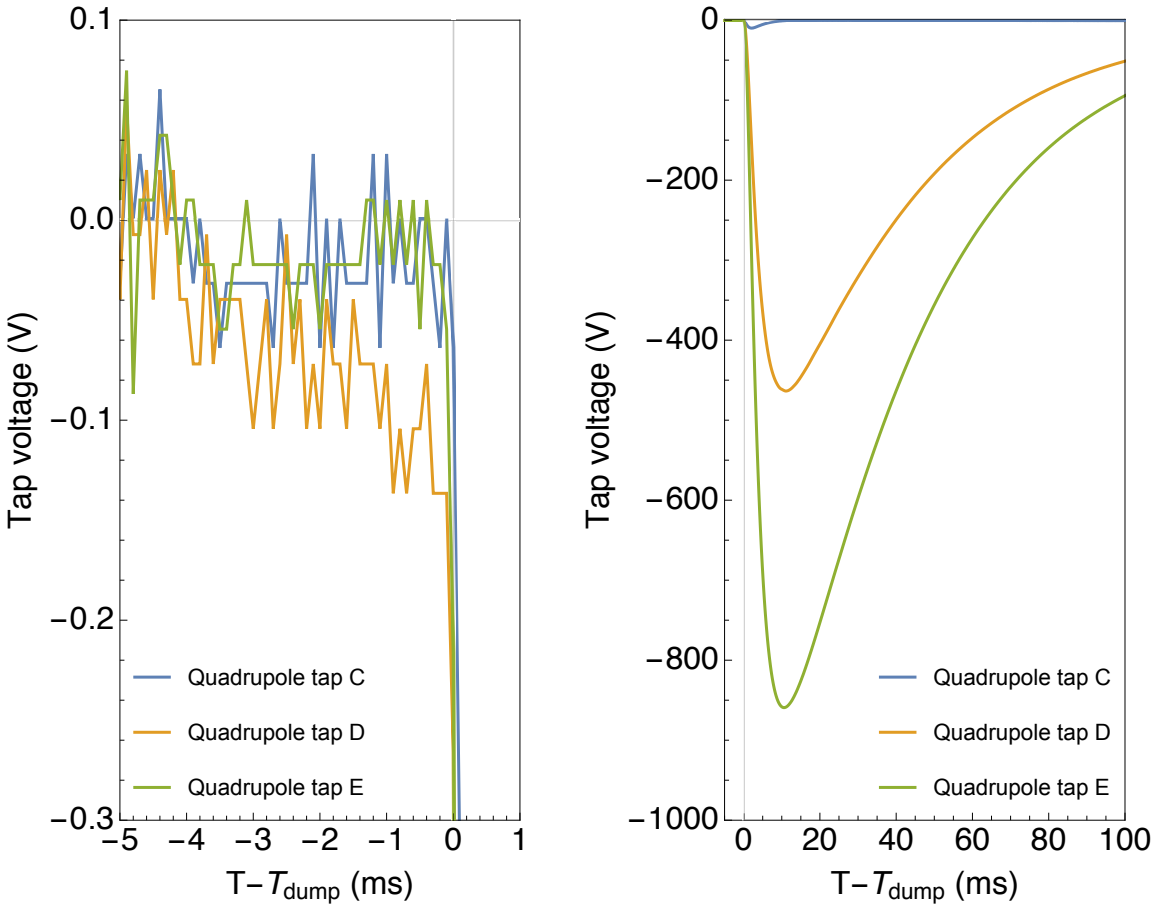

Figure 8.12: Adjusted voltages $V_{C,adj}$, $V_{D,adj}$, and $V_{E,adj}$ on the quadrupole voltage taps during the beginning of a quench and dump trigger (left) and the resulting dump (right). The feature at $T \approx -4$ ms is common-mode noise which does not appear in the differences used for dump triggering.

quench. Its slope also appears to be between the predicted blue curve and the red curve.

The red curves yield lower maximum temperatures (Table 9.4, first row) than the dark blue curves (Table 9.4, fourth row); therefore, the bound between the red and dark blue curves implies that the addition of quench protection (cyan, Table 9.4, second row) to the conditions of the dark blue curve holds temperatures at or below these safe, sub 30-K values.

8.6 Conclusion

An improved CTRAP Ioffe trap with quench detection and quick turnoff systems has been designed, built, and tested. An analytical model has been shown to describe early quench progression quite well, and the quench protection system has been shown to activate and trigger a current dump in response to quenches, protecting the Ioffe coils from damage. Quick magnet turnoff has been achieved, setting the stage for improved detection rates for trapped antihydrogen.

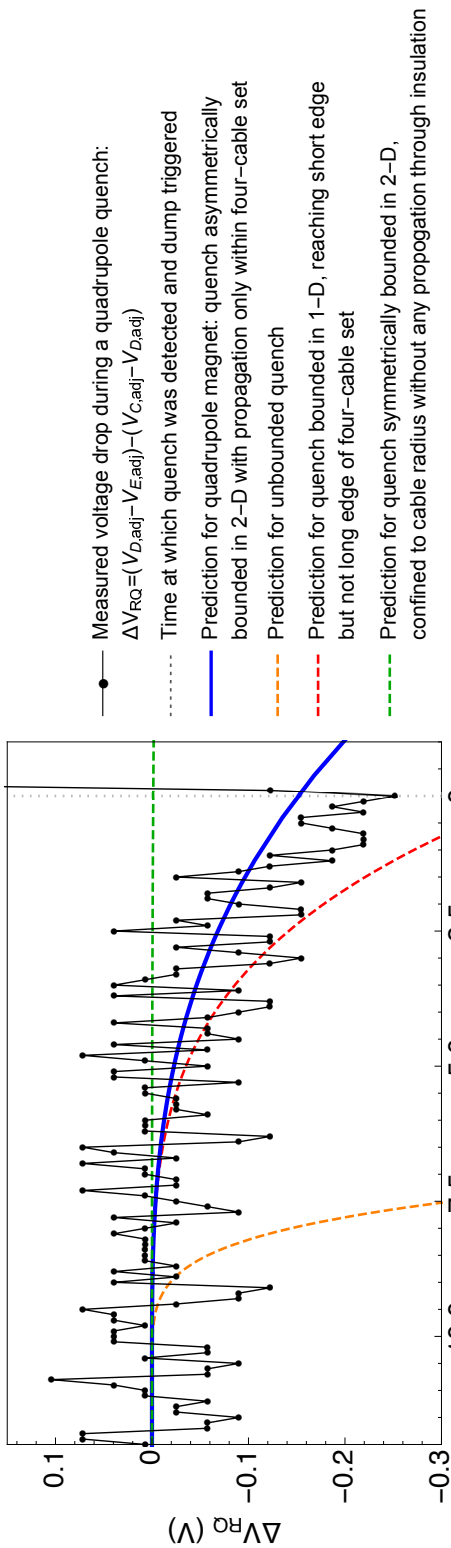

Figure 8.13: Measured voltage drop difference $(V_{D,adj} - V_{E,adj}) - (V_{C,adj} - V_{D,adj}) = \Delta V_{RQ}$ vs. time during a quadrupole magnet quench (black), with predictions for CTRAP quadrupole boundary conditions (blue) and various other boundary conditions for comparison (other colors; see Ch. 9 for details). Because the exact time of quench initiation in the experimental data is not known, the quench initiation time $T_Q - T_{dump} = -11$ ms of the theoretical curves is set by eye with estimated error of ± 1 ms.

Chapter 9

Quench Propagation Calculations

This chapter presents an analysis of the progression of a quench in the Ioffe trap magnet windings in the ATRAP experiment. First, the evolution of a quench is discussed generally to give an intuitive picture of the factors affecting quench propagation. Then, an analytical calculation is done to predict how resistances, currents, voltages, and temperatures change during the course of a quench in the Ioffe trap octupole and quadrupole magnets of Ch. 8. This section includes the derivations for the predictions that are quoted and compared to measurements in Sec. 8.5.3. The Ioffe trap results are compared to calculations for slightly different boundary conditions, leading to discussions of the effect of Ioffe coil design on quench behavior and of the accuracy of the analytical calculation.

9.1 Introduction to Quench Propagation

The current-carrying cables in many superconducting magnets, including the CTRAP Ioffe trap magnets in the ATRAP experiment, are composed of multiple strands of superconducting wire in a copper matrix. To mechanically anchor the cables, they are epoxied into place on an insulating form of the desired geometry. We assume that when a quench begins, a tiny spot in one of the cables becomes normal-conducting. Current flowing through the nonzero resistance of the normal section dissipates heat, which then causes more of the superconductor to become normal-conducting, repeating in a chain reaction. The "quench front," as the boundary of the normal-conducting volume is called, expands in three dimensions until it hits the radius of the cable, then continues to propagate longitudinally along the cable in both directions. It is a good approximation that the longitudinal quench propagation velocity is constant near the beginning of a quench, before the current has decayed substantially [177].

Simultaneously, the heat generated in the normal volume also begins to flow transversely to the cable axis. The insulator between magnet windings is a poor thermal conductor, so heat propagates much more slowly transversely through the insulation than it does longitudinally along the cable. Still, if neighboring windings are close enough to each other, the quench can propagate cable-to-cable before all energy is dissipated. In these cases, understanding transverse quench propagation can be important for understanding the time course and maximum temperature reached during a quench. To get a sense of the effect of transverse propagation, we briefly discuss two extreme cases.

9.1.1 No Transverse Propagation

In a quench where neighboring cables are separated by a thick enough layer of insulator, the quench propagates only longitudinally after spreading radially to the radius of a single superconducting cable. As the quench evolves, the energy $\frac{1}{2}LI^2$ (where I is steady-state current and L is magnet inductance) that was originally stored in the magnet is dissipated. This energy is deposited throughout the section of cable that eventually becomes normal conducting, but the quench nucleation point, because it is resistively generating heat for the longest time, reaches the highest temperature and is in the greatest danger of being damaged. The faster the quench propagates, the more cable becomes involved in the quench and shares the load of absorbing the dissipated energy.

9.1.2 Significant Transverse Propagation

When a quench can propagate transversely, more of the magnet can quench quickly, spreading the heat dissipation across the magnet's volume and reducing the maximum temperatures reached. Fast enough transverse propagation can be sufficient to limit the maximum temperature, at the nucleation point, to a safe level[1]. However, the drawback of significant transverse propagation is that it also causes a quench to happen much faster. If the transverse propagation alone is not enough to limit temperatures, the faster quench can make it more difficult to activate a quench protection system in time to prevent damage.

[1]Some active quench protection systems rely on this effect, switching on heaters to cause the transition from superconducting to normal in multiple locations throughout a magnet as soon as a quench is detected, e.g., in the ATLAS toroids described in [181].

9.1.3 How Simple Can a Model of Quench Propagation Be?

To determine the maximum temperature reached during a quench in one of the CTRAP Ioffe trap magnets—and assess how a quench detection system must be activated to avoid magnet damage—it is necessary to understand the spatial pattern of heat energy deposition. It is tempting to estimate maximum temperature by simply comparing $\frac{1}{2}LI^2$ to the heat capacity of a section of wire whose length is calculated from rough quench time and quench propagation velocity estimates. However, this does not take into account the crucial asymmetry of the heat distribution within the quenched region. It is then tempting to make a simple, perhaps linear, guess about the pattern of heat distribution. However, heat distribution is strongly affected by the extreme nonlinearity with temperature of heat capacity and electrical resistivity, belying attempts to use any back-of-the-envelope model. The simplest model that could be expected to be reasonably accurate therefore takes into account the temperature dependence of these properties in the materials from which the cable is constructed. These minimal concessions to complexity, combined with some well-motivated approximations (e.g., that a quench propagates along a wire at a constant velocity), bring us to the basic analytical model of quench propagation described in [177]. The next sections apply this model to the CTRAP Ioffe trap magnets, extending it to accommodate the fact that transverse quench propagation is predicted to be important in this system, but only in one transverse dimension. Throughout the calculation, the properties of interest (temperature, resistance, current, and voltage drop across the quenched region) are calculated both for the CTRAP Ioffe trap and for hypothetical magnets with different boundary conditions (e.g., ones in which

transverse propagation is not important). This builds intuition about how magnet geometry affects quench propagation.

9.2 Introduction to Analytical Quench Calculation

This analytical calculation is built on Wilson's treatment in [177][2], adapted both by modifying and extending derivations for the case of asymmetrical propagation and boundary conditions and by using improved material property data from [182, 183, 184, 185, 186, 187, 188].

The calculation proceeds as follows: first, the velocity of propagation of the boundary of the quenched region (the "quench front") in each of the three dimensions is determined. Then, these velocities and coil geometry information are used to predict the time at which the quench front hits various boundaries (in this case, thick layers of insulation through which little heat will propagate on the timescale of the quench.) This allows the calculation of the quench resistance as a function of time, which can be used to predict voltage, current, and maximum coil temperature as a function of time.

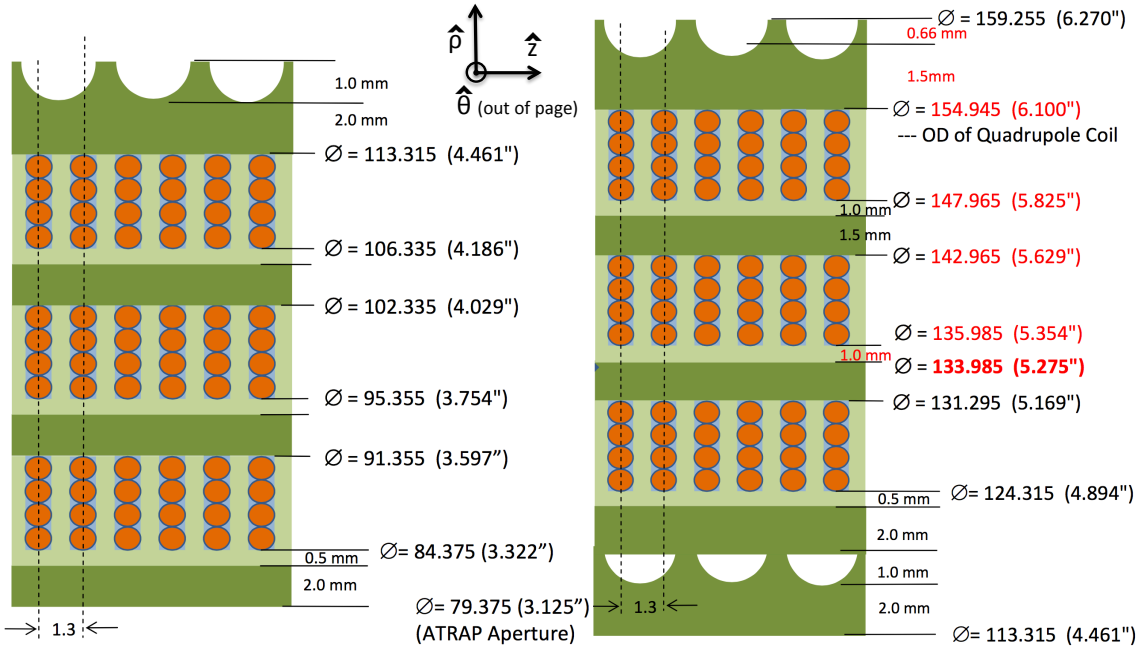

Figure 9.1: Octupole (left) and quadrupole (right) coil cross-sections. Red circular cross-sections are cables of 50% NbTi, 50% Cu cable by volume. Dark green represents G-10 and light green represents similar composites. Light blue areas around the cables are epoxy. Distances are radii from the trap's central axis.

9.3 Coil Geometry and Directional Quench Propagation Velocities

Cross-sectional diagrams of small portions of the octupole and quadrupole coils in Fig. 9.1 show the structure of four-cable groups that is critical for understanding quench dynamics in this system. (For further details of coil construction, see [173].) The quench front first spreads in three dimensions. The approximate longitudinal quench velocity, v_l, along the cable ($\pm\hat{\theta}$ direction in Fig. 9.1)[3] and from the center of a cable to its radius (within a red cable in the $\pm\hat{z}$ direction in Fig. 9.1) is given by

$$v_l = \frac{J}{\gamma C}\left(\frac{\rho k}{\theta_s - \theta_0}\right) \tag{9.1}$$

where J is current, ρ is resistivity (dominated by the copper component), and k is thermal conductivity (also dominated by the copper component). Density is represented by γ and C is specific heat, so γC is volumetric specific heat. C, ρ, and k are averaged over the range from the starting temperature θ_0 to the critical temperature θ_c, and are also averaged over both cable components. θ_s is the mean of the field-dependent NbTi critical temperature θ_c with θ_g, the temperature at which power generation begins. θ_g is calculated as described in [189] using fits from [190] to the data in [191]. For calculating v_l, J is approximated to be constant throughout the quench (which is empirically justified; see [177].)

[2]All labeled equations in the text of Secs. 9.3 and 9.4 are from [177]. The first three entries in Table 9.2 and the first two in 9.3 are altered slightly from [177] to account for asymmetrical transverse quench propagation. Remaining entries in the tables are newly derived to allow for arbitrary, asymmetrical boundary conditions.

[3]Though the orientation of a cable with respect to the standard cylindrical $\hat{\rho}$, $\hat{\theta}$, and $\hat{z}$ axes changes as it winds in an octupole or quadrupole shape, for convenience in the discussion in this chapter, the axes will be defined relative to the local cable, e.g., $\hat{\theta}$ is always along the cable axis.

The longitudinal quench velocity v_l in the octupole magnet at full current was calculated to be 46 m/s and in the quadrupole magnet at full current to be 34 m/s. These are larger values than more typical velocities of 10-20 m/s in many superconducting magnets [181], which reflects the minimal cooling allowed by the epoxy impregnation of these magnets and their high current density.

In the direction of transverse propagation between neighboring cables in a four-cable set ($\pm\hat{\rho}$ direction in Fig. 9.1), quench propagation is slowed significantly by the epoxy insulation between cables. The approximate transverse quench propagation velocity is given by

$$v_t = \frac{(\gamma C)_{avm}}{(\gamma C)_{avtot}} \left(\frac{k_t}{k_l}\right)^{\frac{1}{2}} v_l \equiv \zeta v_l \tag{9.2}$$

where $(\gamma C)_{avm}$ is averaged over the cable, $(\gamma C)_{avtot}$ is averaged over a full unit cell including insulation, k_l is the longitudinal thermal conductivity (dominated by copper), and k_t is the transverse thermal conductivity averaged over the unit cell (limited by the insulation). A unit cell in this case is defined as one-quarter of a four-cable set, including the red and blue regions in Fig. 9.1. The prefactor relating transverse and longitudinal velocities is referred to as ζ in the remainder of this chapter.

The octupole magnet at full current has a calculated transverse quench velocity v_t of 1.7 m/s; for the quadrupole magnet at full current, it is 1.3 m/s. It would be possible to define another transverse velocity to describe the propagation between four-cable sets, for which green regions in 9.1 would be included in material property averages. In practice, however, the magnet's stored energy dissipates before heat can spread significantly in this low-thermal-conductivity direction, and the quench instead is effectively bounded within the red and blue regions in Fig. 9.1.

Given these velocities and the coil geometry, a quench progresses as follows. After initiation and the initial period of expansion in three dimensions with velocity v_l, it hits a boundary in the $\hat{z}$ dimension at a time T_A at the short width of a four-cable set (a cable radius). The quench propagates between cables in a four-cable set along the $\hat{\rho}$ dimension with average velocity v_t until it hits the edge of a set at time $T_B > T_A$. The quench front also continues to propagate along cables in the $\hat{\theta}$ dimension with velocity v_l. In these magnets, most energy has already been dissipated by the time T_C at which the quench would become bounded in this dimension, but derivations for this case are included for reference in the tables below. Approximate timescales are shown in Table 9.1. The separate treatment of boundaries and propagation velocities in the two transverse dimensions is an important deviation from [177] that is needed to account for the properties of the CTRAP magnets.

	Dimension	**Time (ms)**	
		Octupole	**Quadrupole**
Ta	short dimension of four-wire set	.01	.02
Tb	long dimension of four-wire set	1	2
Tc	along cable axis	30	40

Table 9.1: Characteristic timescales on which a quench hits boundaries in three dimensions. T_C is the time it takes the quench to proceed once longitudinally around the magnet, where it hits the place where the quench has spread transversely within a four-cable set. The characteristic time for longitudinal propagation throughout the entire magnet is much longer, but is not relevant because most current has been dissipated by this time.

9.4 Time Evolution of Quench Resistance, Current, and Voltage

The total resistance of the quenched portion of a superconducting magnet depends on time in two ways: the resistance of any given quenched unit of volume increases over time as its temperature increases, and the volume of the quenched region increases over time. The total quench resistance is given by

$$R_Q(t) = \int_0^{V_{tot}(t)} \frac{\rho(\theta)}{A^2} dV. \tag{9.3}$$

where θ is temperature, $\rho(\theta)$ is resistivity, A is cross-sectional area, and $V_{tot}(t)$ is the volume of the quenched region at time t.

It is a good approximation that

$$\rho(\theta(\tau)) = \frac{\rho_0 J_0^4}{U_0^2 A^2} \tau(\vec{x})^2 \tag{9.4}$$

where J_0 is initial current density, ρ_0 is resistivity at a reference temperature θ_0, and τ is the time the quench front reaches a given dV at position $\vec{x}$. J_0, ρ_0, and U_0 are all averaged over a unit cell of winding. $U(\theta_0)$ is a material property defined below that describes the temperature rise of a material during a quench; it takes into account both changes in dissipative power input as resistivity changes with temperature and the temperature dependence of heat capacity that governs the effect of this input heat on temperature. It is given by

$$U_0 = U(\theta_0) = \int_0^{\infty} J^2(t) dt = \int_{\theta_0}^{\theta_0} \frac{\gamma C(\theta)}{\rho(\theta)} d\theta. \tag{9.5}$$

$U(\theta)$ can be approximated as $U_0\sqrt{\frac{\theta}{\theta_0}}$. Combining these, the quench resistance is

$$R_Q(t) \approx \int_0^{V_{tot}(t)} \frac{\rho_0 J_0^4}{U_0^2 A^2} \tau(\vec{x})^2 dV. \tag{9.6}$$

The details of the integration depend on the nature of any boundaries encountered by the quench front. Before the quench front hits boundaries, dV are spherical shells. Once boundaries in one dimension have been encountered, dV are approximated as elliptical cylindrical shells. After boundaries have been encountered in two dimensions, dV are approximated as elliptical discs. (See figures in [177] for illustrations.) Even after a given boundary has been encountered, the resistance of the region inside the boundary continues to increase in resistance as its temperature increases. Therefore, the total quench resistance at any give time (say, for t between T_A and T_B) is the sum of incremental contributions from each region from each time period since quench onset. Table 9.2 shows the contributions to R_Q for various geometries and time limits. These expressions can be combined to predict the total resistance at a given time for a quench that hits boundaries at times T_A, T_B, T_C in succession, shown in Table 9.3.

From $R_Q(t)$, current $I_L(t)$ can be derived:

$$I_L(t) = I_0 e^{-\int_0^t R_Q(T)dT/L} \tag{9.7}$$

where I_0 is initial current and L is magnet inductance. The total voltage drop across the quenched region due to resistance (so, not including the inductance of the quenched region) is then given by

$$\Delta V_{RQ}(t) = R_Q(t) I_L(t). \tag{9.8}$$

Because the quench spreads between coils, this voltage drop will be split unevenly between up to four resistive sections that are separated by still-superconducting sections.

Progression type	**Time window**	**Contribution to R_Q**
Unbounded	t_0 to t	$6t^5$
Unbounded	t_0 to T_A	$60T_A^3t^2 - 90T_A^4t + 36T_A^5$
1-D bounded	T_A to t	$15T_At^4 - 90T_A^3t^2 + 120T_A^4t - 45T_A^5$
1-D bounded	T_A to T_B	$90T_AT_B^2t^2 - 90T_A^3t^2 - 120T_AT_B^3t + 120T_A^4T + 45T_AT_B^4 - 45T_A^5$
2-D bounded	T_B to t	$-90T_AT_B^2t^2 + 90T_AT_B^3t + 30T_AT_Bt^3 - 30T_AT_B^4$
2-D bounded	T_B to T_C	$90T_AT_BT_Ct^2 - 90T_AT_B^2t^2 - 90T_AT_BT_C^2t + 90T_AT_B^3t$ $+ 30T_AT_BT_C^3 - 30T_AT_B^4$

Table 9.2: Expressions that when multiplied by a prefactor of $\frac{4\pi\zeta\rho_0 J_0^4 v_l^3}{180U_0^2A^2}$ describe the contribution to total quench resistance of regions that encounter boundaries at different times. The number of factors of ζ is equal to the number of dimensions in which the quench travels through insulation with a reduced transverse velocity—in our case, one.

Time	**Components of $R_Q(t)$**	**Sum of components for total $R_Q(t)$**
$t_0 < t < T_A$	Unbounded 0 to t	$6t^5$
$T_A < t < T_B$	Unbounded 0 to T_A +1D bounded T_A to t	$15T_A t^4 - 30T_A^3 t^2 + 30T_A^4 t - 9T_A^5$
$T_B < t < T_C$	Unbounded 0 to T_A +1D bounded T_A to T_B +2D bounded T_B to t	$-30T_A {T_B}^3 t + 30T_A T_B t^3 - 30T_A^3 t^2$ $+ 30T_A^4 t + 15T_A T_B^4 - 9T_A^5$
$T_C < t$	Unbounded 0 to T_A +1D bounded T_A to T_B +2D bounded T_B to T_C	$90T_A T_B T_C t^2 - 90T_A T_B T_C^2 t - 30T_A T_B^3 t$ $+ 30T_A T_B T_C^3 + 15T_A T_B^4$ $- 30T_A^3 t^2 + 30T_A^4 t - 9T_A^5$

Table 9.3: Expressions that when multiplied by a prefactor of $\frac{4\pi\zeta\rho_0 J_0^4 v_l^3}{180 U_0^2 A^2}$ give the total quench resistance as a function of time.

Using the definition and approximation for $U(\theta)$, the maximum temperature reached by the point in the coil the gets the hottest is given by

$$\theta = \theta_0 \left(\frac{\int_0^\infty I_L^2(T) dT}{A^2 U_0} \right)^2 . \tag{9.9}$$

9.5 Approximations

In addition to the assumptions mentioned above about the form of $U(\theta)$ and the constancy of J_0 and v_l during the quench, there are many other approximations used in this analysis. The magnetic field at the coils, which affects the critical temperature of NbTi and the resistivity of copper, are approximated by values at the inner boundary of the inner coil. To calculate boundary-hitting times, quenches are assumed to begin centrally and hit boundaries symmetrically. Quench propagation between cables in a four-cable set is calculated using material properties averaged over the unit volume rather than taking into account the geometry of the insulation that provides the main impedance to heat transfer.

9.6 Predictions for CTRAP Octupole and Quadrupole Magnets

Predictions for quench resistance, current, and sum of voltage drops due to resistance across the quenched region are shown for the CTRAP octupole magnet in Fig. 9.2 and the CTRAP quadrupole magnet in Fig. 9.3. Table 9.4 shows predicted maximum temperatures for all the various boundary conditions, as well as additional

descriptions of the boundary conditions. Sec. 8.5.3 compares predicted voltages at early times to experimental voltage tap data.

In each plot in Figs. 9.2 and Fig. 9.3, the dark blue line shows the prediction for a given CTRAP magnet without quench protection[4]. The cyan line shows the prediction for the CTRAP magnet but also includes the quench protection system described in Secs. 8.3 and 8.5.2. The dashed lines of other colors show what would be predicted to happen if boundary conditions were different from those in CTRAP, but all other aspects of the system remained the same. These other conditions are included 1) to aid in developing an intuitive understanding of how design choices affect the system, and 2) in the case of an imperfect fit between the main prediction and the data, to generate hypotheses about how the model might be inaccurate. The curves in order of increasing importance of transverse propagation through insulation are green, blue (actual CTRAP magnet geometry), red, and orange, with green corresponding to the case of no transverse propagation as described in Sec. 9.1.1, orange to significant transverse propagation as in Sec. 9.1.2, and red and blue to intermediate cases.

9.7 Discussion

Comparing predictions for different boundary conditions illustrates the well-known fact that the more strongly geometrically bounded a quench is—either by hitting a given boundary condition sooner or by hitting more boundaries—the more slowly the quench proceeds. A more-bounded quench causes a slower rise in resistance, a

[4]For both the CTRAP quadrupole and octupole magnets, quenches are predicted to propagate into the time period where they are bounded in 2D at the edges of a four-wire set.

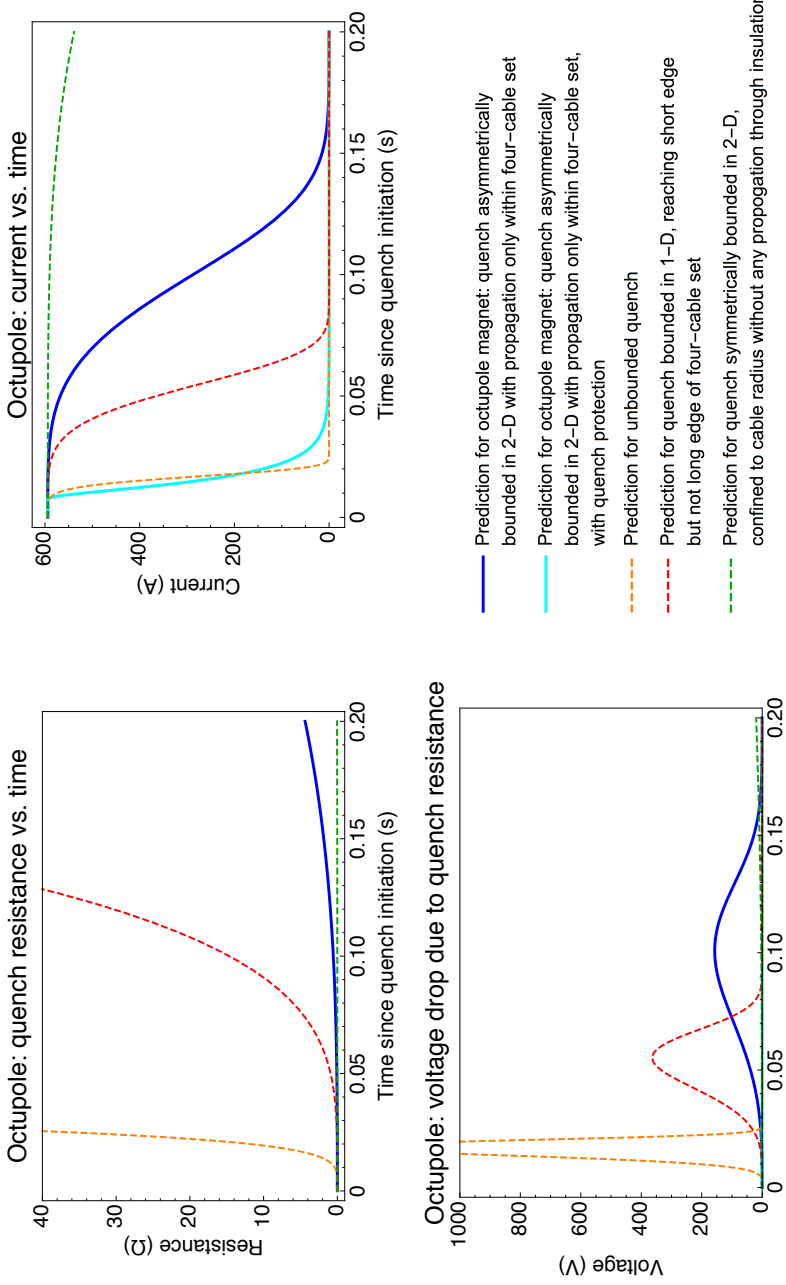

Figure 9.2: Predicted total resistance of quenched regions, current, and maximum voltage drop vs. time for the CTRAP octuple magnet. Fig. 8.11 shows a zoomed-in view of voltages in the first 15 ms, with the same color coding of boundary conditions.

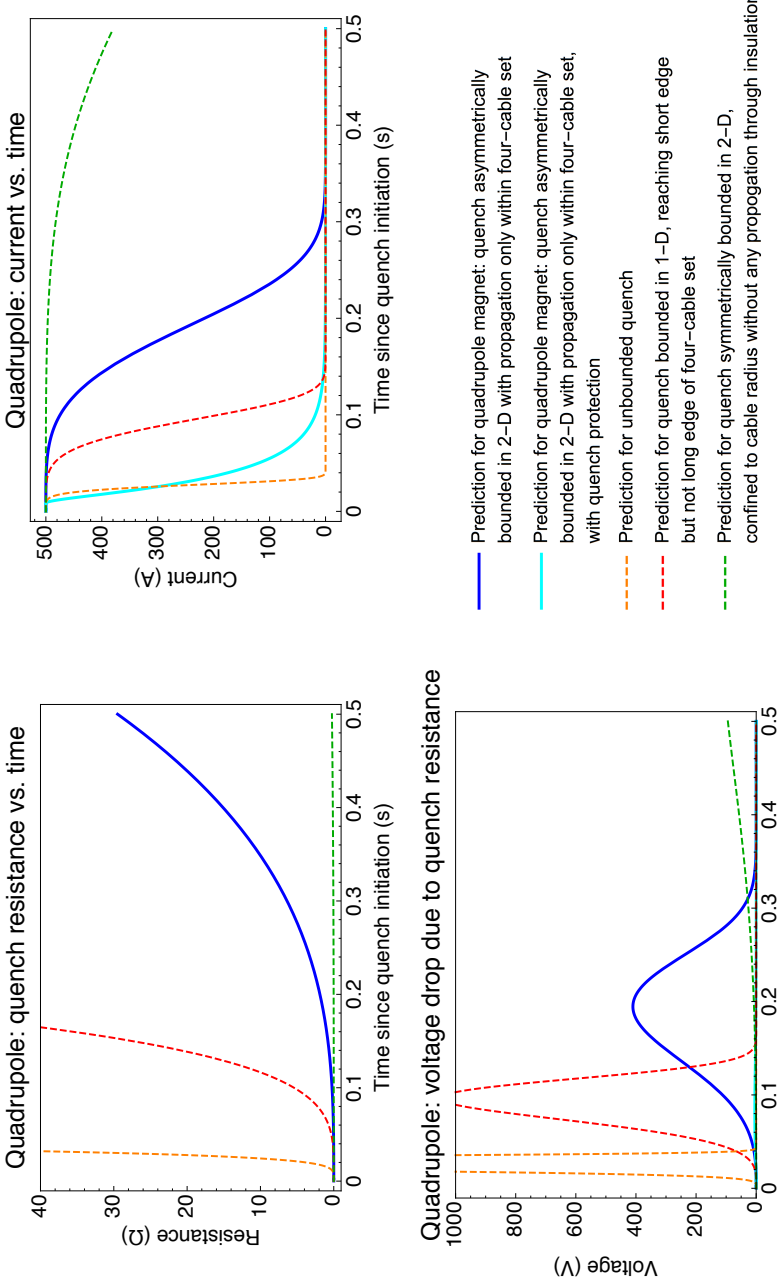

Figure 9.3: Predicted total resistance of quenched regions, current, and the maximum voltage drop vs. time for the CTRAP quadrupole magnet. Fig. 8.13 shows a zoomed-in view of voltages in the first 20 ms, with the same color coding of boundary conditions.

	Differences in boundary conditions from unprotected CTRAP Ioffe coils	Color, style in figures	Max. temp. (K)	
			Oct.	Quad.
Quench asymmetrically bounded in 2-D with propagation only within four-wire set	**No change; conditions for unprotected CTRAP Ioffe coils**	**Blue, solid**	**488**	**750**
Quench asymmetrically bounded in 2-D with propagation only within four-wire set, with quench protection	**CTRAP Ioffe coils with quench protection**	**Cyan, solid**	**24**	**26**
Quench symmetrically bounded in 2-D confined to cable radius	Neighboring cables have no thermal coupling; no quench propagation through insulation	Green, dashed	5095	7860
Quench bounded in 1-D, reaching short edge but not long edge of four-cable set	Instead of four-cable sets, sets have many more cables, so slow quench propagation continues in $\hat{\rho}$ dimension	Red, dashed	136	170
Unbounded quench	As in 1-D bounded case, but also with increased NbTi/Cu cable width, so fast propagation continues in $\hat{z}$ dimension and slow propagation continues in $\hat{\rho}$ dimension	Orange, dashed	17	18

Table 9.4: Predicted maximum temperatures reached by octupole and quadrupole magnets during a quench (top two rows in bold, with other rows describing different conditions for reference). Quench detection and dump systems are described in Chapter 8. Table 8.2 is an abbreviated version of this table. Colors are defined as in this table for Figs. 8.11, 8.13, 9.2, and 9.3.

slower decay of the current, and a slower and lower-maximum voltage spike across the quenched region. Temperature rise is highest in the most strongly bounded quenches because dissipation is proportional to the square of current, and current in these cases decays very slowly. The voltage spikes from less-bounded quenches could cause damaging arcs between coils within a magnet, while the temperature rise from a quench that could not propagate transversely through insulation at all would be extremely damaging.

The CTRAP quadrupole and octupole magnets are shown by the data in Sec. 8.5.3 to be close to their predicted dark blue curves, indicating that quenches propagate between neighboring coils in a four-coil set. These magnets might encounter both dangerous voltage drops across the tiny gaps between neighboring coils and possibly dangerously high temperatures during a quench if they were not protected by the quench protection system[5]. Increasing insulation thickness between coils would prevent voltage spikes within the magnet but make temperatures worse; decreasing insulation thickness would do the opposite. This suggests that small design changes alone would be insufficient to create inherently safe magnets of this general design. The quench protection system, however, is predicted to be effective at protecting the magnets.

In conclusion, analytical calculations of the progression of a quench were extended to a system with less symmetry. In Sec. 8.5.3, results were shown to be impressively

[5]It must noted here that the vast majority of the voltage drop measured after a dump (e.g., in Fig. 8.6) is across the dump resistor, and therefore across the leads of the magnet, which is connected in parallel with the dump resistor. In contrast, the voltage drops shown in quench-related figures (Figs. 9.2 and 9.3) are the sums of voltages drops across the quenched regions of magnet winding, potentially in adjacent sections of coil separated from each other by a fraction of a millimeter of epoxy. The difference in geometry makes the similar-scale voltage drop less dangerous in triggered-dump case than the quench-resistance case.

consistent with (admittedly limited) data in the CTRAP octupole and quadrupole magnets, despite the many approximations needed to simplify the highly nonlinear quench process enough for an analytical calculation. This agreement strongly suggests that the quench does indeed propagate between neighboring windings through insulation. The quench protection system was predicted and shown experimentally to be necessary and sufficient to protect the CTRAP Ioffe trap. This analysis is thereby validated as a useful design tool in the context of these high-current-density, epoxy-impregnated magnets.

Chapter 10

Conclusion

10.1 Electron and Positron $g/2$

A next-generation apparatus has been developed for measuring $g/2$, the magnetic moment in Bohr magnetons, of the positron and electron. The apparatus is designed for precision better than the 0.28 ppt uncertainty of the best existing measurement of electron $g/2$. The comparison of an improved electron or positron $g/2$ measurement with $g/2$ determined from Standard Model calculations and an independently measured fine structure constant α will improve on the most precise test of the Standard Model. An improved positron $g/2$ will improve on the best test of CPT symmetry in leptons.

To measure $g/2$, quantum jump spectroscopy is performed on a single electron or positron held in a cylindrical Penning trap. The new apparatus contains a positron source to enable a positron $g/2$ measurement, and it is also designed to eliminate the leading sources of uncertainty seen in the best electron $g/2$ measurement. Its smaller

magnetic bottle and stability improvements are expected to narrow the previously precision-limiting cyclotron and anomaly lineshapes. Pressure control around the superconducting solenoid helps to maintain a very stable magnetic field. A helium recovery system using a pulse-tube cryo-refrigerator nearly eliminates helium loss from the large liquid helium dewar, and pulse-tube vibrations are damped by careful mounting. A ^{3}He NMR probe for shimming the magnetic field in the cold-bore solenoid to excellent spatial homogeneity has been demonstrated, and a more robust second-generation probe has been designed and is under construction. An improved trap cavity design and a cold RF switch in development are expected to make cavity-assisted cooling of the axial motion possible; this could further improve precision of the cyclotron and anomaly frequency measurements.

Key $g/2$ measurement techniques—axial-magnetron sideband cooling, single electron axial detection and control with the self-excited oscillator, resolution of single cyclotron transitions of a single electron—have been demonstrated in this apparatus. Understanding the microwave cavity mode structure of a trap is critical for inhibiting spontaneous emission and eliminating the cavity shift to $g/2$; using the parametric mode-mapping technique, the cavity mode structure of the new apparatus has been probed for the first time. Positrons from a small, convenient source that requires no special licensing have been trapped in the positron accumulation trap, and a system is in place for transferring these positrons through a tiny hole into the precision measurement trap for a positron $g/2$ measurement. There have been challenges in integrating the positron trapping and transfer systems with the sensitive and tightly constrained precision measurement trap. These challenges have

been largely overcome. In addition, a planned reconfiguration of the detection and transfer systems should eliminate the last vestiges of the conflict between detection and transfer. This is expected to enable positron transfer into the precision measurement trap and improve the single-particle detection beyond the standard of previous electron $g/2$ measurements.

These achievements in apparatus and technique development have yielded a much-improved platform for precise $g/2$ measurements. Adjustments in the near future should remove the final obstacles on the path to higher-precision electron and positron $g/2$, and with them improved fine-structure constant α and improved tests of CPT symmetry and the Standard Model.

10.2 ATRAP

The ATRAP experiment aims to make the most stringent test of CPT symmetry in a lepton-baryon system by doing precision spectroscopy of antihydrogen. CTRAP, an improved Penning-Ioffe trap apparatus for creating, confining, and interacting with antihydrogen, has been constructed. CTRAP has a larger trapping volume than its predecessor to accommodate larger plasmas, and it includes both octupole and quadrupole coils to make it possible to use different optimized magnetic field geometries for antihydrogen creation and for laser cooling. Trapped antihydrogen atoms will be able to be detected by quickly turning off the magnetic trapping fields.

Unlike a previous apparatus in which the Ioffe magnets had to be quenched in order to achieve fast enough turnoff to detect antihydrogen above the cosmic-ray background, CTRAP has a quick-turnoff system for removing current from the Ioffe

coils on a timescale of tens of ms without quenching. Because the coil windings store enough energy to destroy themselves in the case of a quench, a quench detection system was also built; when a quench begins, this activates the quick turnoff system and safely dissipates the current in an external dump resistor before damage can occur. Observed voltage drops across magnet sections during a quench agree quite well with a simple analytical model of quench propagation. This model gives insight into how small changes to this magnet design affect quench propagation, which can provide a guide for future magnet designs. CTRAP is trapping antiprotons and positrons, and antihydrogen production and detection are expected soon.

Bibliography

[1] Dirac, P. A. M. The quantum theory of the electron. vol. 117, 610–624 (The Royal Society, 1927).

[2] Schwinger, J. On Quantum-Electrodynamics and the Magnetic Moment of the Electron. *Phys. Rev.* **73**, 416–417 (1948).

[3] Hanneke, D., Fogwell, S. & Gabrielse, G. New Measurement of the Electron Magnetic Moment and the Fine Structure Constant. *Phys. Rev. Lett.* **100**, 120801 (2008).

[4] Hanneke, D., Fogwell Hoogerheide, S. & Gabrielse, G. Cavity Control of a Single-Electron Quantum Cyclotron: Measuring the Electron Magnetic Moment. *Phys. Rev. A* **83**, 073002 (2011).

[5] R. S. Van Dyck, Jr., Schwinberg, P. B. & Dehmelt, H. G. New High-Precision Comparison of Electron and Positron g Factors. *Phys. Rev. Lett.* **59**, 26–29 (1987).

[6] Wu, C. S., Ambler, E., Hayward, R. W., Hoppes, D. D. & Hudson, R. P. Experimental Test of Parity Conservation in Beta Decay. *Phys. Rev.* **105**, 1413–1415 (1957).

[7] Lee, T. D. & Yang, C. N. Question of parity nonconservation in weak interactions. *Phys. Rev.* **104**, 254–258 (1956).

[8] Christenson, J. H., Cronin, J. W., Fitch, V. L. & Turlay, R. Evidence for the 2π decay of the K_2^0 meson. *Phys. Rev. Lett.* **13**, 138–141 (1964).

[9] Pauli, W. *Niels Bohr and the Development of Physics* (McGraw-Hill, New York, 1955).

[10] Lüders, G. Proof of the TCP theorem. *Ann. Phys.* **2**, 1 (1957).

[11] Jost, R. A remark on the CTP theorem. *Helv. Phys. Acta* **30**, 409–416 (1957).

[12] Sakharov, A. D. Violation of CP-invariance, C-asymmetry, and baryon asymmetry of the universe. *Uspekhi Fizicheskikh Nauk (Reprinted from Zhetf, Pisma v Redaktsiyu Vol. 5 p 32-35, 1967)* **161**, 61–64 (1991).

[13] Zwicky, F. The redshift of extragalactic nebulae. *Helv. Phys. Acta* **6**, 110 (1933).

[14] Schmidt, B. P., Suntzeff, N. B., Phillips, M. A. R. K. M., Schommer, R. A., Clocchiatti, A., Kirshner, R. P., Garnavich, P., Challis, P., Leibundgut, B. R. U. N. O. & Spyromilio, J. The high-z supernova search: measuring cosmic deceleration and global curvature of the universe using type ia supernovae. *The Astrophysical Journal* **507**, 46 (1998).

[15] Riess, A. G., Filippenko, A. V., Challis, P., Clocchiatti, A., Diercks, A., Garnavich, P. M., Gilliland, R. L., Hogan, C. J., Jha, S. & Kirshner, R. P. Observational evidence from supernovae for an accelerating universe and a cosmological constant. *The Astronomical Journal* **116**, 1009 (1998).

[16] Perlmutter, S., Aldering, G., Goldhaber, G., Knop, R. A., Nugent, P., Castro, P. G., Deustua, S., Fabbro, S., Goobar, A. & Groom, D. E. Measurements of ω and λ from 42 high-redshift supernovae. *The Astrophysical Journal* **517**, 565 (1999).

[17] Schwartz, M. D. *Quantum field theory and the standard model* (Cambridge University Press, 2014).

[18] Gell-Mann, M., Ramond, P. & Slansky, R. *Complex spinors and unified theories* (North Holland Publishing Co, 1979).

[19] Kostelecký, V. A. & Samuel, S. Spontaneous breaking of lorentz symmetry in string theory. *Physical Review D* **39**, 683 (1989).

[20] Kostelecký, V. A. & Potting, R. CPT and strings. *Nucl. Phys.* **B359**, 545–570 (1991).

[21] Kostelecký, V. A. & Potting, R. CPT, strings, and meson factories. *Phys. Rev. D* **51**, 3923–3935 (1995).

[22] Patrignani, C., Weinberg, D. H., Woody, C. L., Chivukula, R. S., Buchmueller, O., Kuyanov, Y. V., Blucher, E., Willocq, S., Höcker, A. & Lippmann, C. Review of particle physics. *Chin. Phys.* **40**, 100001 (2016).

[23] Ulmer, S., Smorra, C., Mooser, A., Franke, K., Nagahama, H., Schneider, G., Higuchi, T., Van Gorp, S., Blaum, K. & Matsuda, Y. High-precision comparison of the antiproton-to-proton charge-to-mass ratio. *Nature* **524**, 196–199 (2015).

[24] Smorra, C., Borchert, M. J., Ospelkaus, C., Mooser, A., Sellner, S., Matsuda, Y., Blaum, K., Walz, J., Quint, W. & Tanaka, T. A parts-per-billion measurement of the antiproton magnetic moment. *Nature* **550**, 371–374 (2017).

[25] Bluhm, R., Kostelecký, V. A. & Russell, N. Testing CPT with anomalous magnetic moments. *Phys. Rev. Lett.* **79**, 1432–1435 (1997).

[26] Ding, Y. & Kostelecký, V. A. Lorentz-violating spinor electrodynamics and penning traps. *Physical Review D* **94**, 056008 (2016).

[27] Hanneke, D. *Cavity Control in a Single-Electron Quantum Cyclotron: An Improved Measurement of the Electron Magnetic Moment*. Ph.D. thesis, Harvard University (2007). (thesis advisor: G. Gabriesle).

[28] Kostelecký, V. A. & Russell, N. Data tables for Lorentz and CPT violation. *Reviews of Modern Physics* **83**, 11 (2011, 2017 update arXiv:0801.0287v10).

[29] Petermann, A. Fourth Order Magnetic Moment of the Electron. *Helv. Phys. Acta* **30**, 407–408 (1957).

[30] Sommerfield, C. M. Magnetic Dipole Moment of the Electron. *Phys. Rev.* **107**, 328–329 (1957).

[31] Sommerfield, C. M. The Magnetic Moment of the Electron. *Ann. Phys. (N.Y.)* **5**, 26–57 (1958).

[32] Laporta, S. & Remiddi, E. Analytical Value of the Electron $(g-2)$ at Order a^3 in QED. *Phys. Lett. B* **379**, 283–291 (1996).

[33] Kinoshita, T. & Nio, M. Tenth-order qed contribution to the lepton $g-2$: Evaluation of dominant α^5 terms of muon $g-2$. *Phys. Rev. D* **73**, 053007 (2006).

[34] Aoyama, T., Hayakawa, M., Kinoshita, T. & Nio, M. Tenth-order electron anomalous magnetic moment: Contribution of diagrams without closed lepton loops. *Phys. Rev. D* **91**, 033006 (2015).

[35] Laporta, S. High-precision calculation of the 4-loop contribution to the electron g-2 in QED. *Physics Letters B* **772**, 232–238 (2017).

[36] Mohr, P. J., Newell, D. B. & Taylor, B. N. CODATA recommended values of the fundamental physical constants: 2014. *Journal of Physical and Chemical Reference Data* **45**, 043102 (2016).

[37] Nomura, D. & Teubner, T. Hadronic contributions to the anomalous magnetic moment of the electron and the hyperfine splitting of muonium. *Nucl. Phys. B* **867**, 236 (2013).

[38] Kurz, A., Liu, T., Marquard, P. & Steinhauser, M. Hadronic contribution to the muon anomalous magnetic moment to next-to-next-to-leading order. *Phys. Lett. B* **734**, 144 (2014).

[39] Prades, J., De Rafael, E. & Vainshtein, A. The hadronic light-by-light scattering contribution to the muon and electron anomalous magnetic moments. *Lepton Dipole Moments* **20**, 303 (2010).

[40] Olive, K. A. & Particle Data Group. Review of particle physics. *Chinese physics C* **38**, 090001 (2014).

[41] Parthey, C., Matveev, A., Alnis, J., Bernhardt, B., Beyer, A., Holzwarth, R., Maistrou, A., Pohl, R., Predehl, K., Udem, T., Wilken, T., Kolachevsky, N., Abgrall, M., Rovera, D., Salomon, C., Laurent, P. & Hänsch, T. W. Improved measurement of the hydrogen $1S - 2S$ transition frequency. *Phys. Rev. Lett.* **107**, 203001 (2011).

[42] Matveev, A., Parthey, C. G., Predehl, K., Alnis, J., Beyer, A., Holzwarth, R., Udem, T., Wilken, T., Kolachevsky, N. & Abgrall, M. Precision measurement of the hydrogen $1S - 2S$ frequency via a 920-km fiber link. *Physical Review Letters* **110**, 230801 (2013).

[43] Arnoult, O., Nez, F., Julien, L. & Biraben, F. Optical frequency measurement of the $1S-3S$ two-photon transition in hydrogen. *The European Physical Journal D-Atomic, Molecular, Optical and Plasma Physics* **60**, 243–256 (2010).

[44] De Beauvoir, B., Nez, F., Julien, L., Cagnac, B., Biraben, F., Touahri, D., Hilico, L., Acef, O., Clairon, A. & Zondy, J. J. Absolute frequency measurement of the $2S - 8S/D$ transitions in hydrogen and deuterium: New determination of the Rydberg constant. *Physical Review Letters* **78**, 440 (1997).

[45] Yerokhin, V. A., Berseneva, E., Harman, Z., Tupitsyn, I. I. & Keitel, C. H. g factor of light ions for an improved determination of the fine-structure constant. *Physical Review Letters* **116**, 100801 (2016).

[46] Sturm, S., Wagner, A., Kretzschmar, M., Quint, W., Werth, G. & Blaum, K. g-factor measurement of hydrogenlike $^{28}Si^{13+}$ as a challenge to QED calculations. *Physical Review A* **87**, 030501 (2013).

[47] Wang, M., Audi, G., Wapstra, A. H., Kondev, F. G., MacCormick, M., Xu, X. & Pfeiffer, B. The Ame2012 atomic mass evaluation. *Chinese Physics C* **36**, 1603 (2012).

[48] Bouchendira, R., Clade, P., da Guellati-Khet'lifa, S., Nez, F. & Biraben, F. New determination of the fine structure constant and test of the quantum electrodynamics. *Phys. Rev. Lett.* **106**, 080801 (2011).

[49] Lan, S.-Y., Kuan, P.-C., Estey, B., English, D., Brown, J. M., Hohensee, M. A. & Müller, H. A clock directly linking time to a particle's mass. *Science* **339**, 554–557 (2013).

[50] Müller, H. private communication (2017).

[51] Aoyama, T., Hayakawa, M., Kinoshita, T. & Nio, M. Complete tenth-order contribution to the muon $g-2$. *Phys. Rev. Lett* **109**, 111808 (2012).

[52] Prades, J., de Rafael, E. & Vainshtein, A. *Hadronic Light-by-Light Scattering Contribution to the Muon Anomalous Magnetic Moment*, chap. Hadronic Light-by-Light Scattering Contribution to the Muon Anomalous Magnetic Moment (World Scientific, Singapore, 2009).

[53] Burger, F., Feng, X., Hotzel, G., Jansen, K., Petschlies, M., Renner, D. B. & collaboration, E. T. M. Four-flavour leading-order hadronic contribution to the muon anomalous magnetic moment. *Journal of High Energy Physics* **2014**, 99 (2014).

[54] Jegerlehner, F. & Nyffeler, A. The muon g-2. *Physics Reports* **477**, 1–110 (2009).

[55] Bennett, G. W. and Bousquet, B. and Brown, H. N. and Bunce, G. and Carey, R. M. and Cushman, P. and Danby, G. T. and Debevec, P. T. and Deile, M. and Deng, H. and Deninger, W. and Dhawan, S. K. and Druzhinin, V. P. and Duong, L. and Efstathiadis, E. and Farley, F. J. M. and Fedotovich, G. V. and Giron, S. and Gray, F. E. and Grigoriev, D. and Grosse-Perdekamp, M. and Grossmann, A. and Hare, M. F. and Hertzog, D. W. and Huang, X. and Hughes, V. W. and Iwasaki, M. and Jungmann, K. and Kawall, D. and Kawamura, M. and Khazin, B. I. and Kindem, J. and Krienen, F. and Kronkvist, I. and Lam, A. and Larsen, R. and Lee, Y. Y. and Logashenko, I. and McNabb, R. and Meng, W. and Mi, J. and Miller, J. P. and Mizumachi, Y. and Morse, W. M. and Nikas, D. and Onderwater, C. J. G. and Orlov, Y. and Özben, C. S. and Paley, J. M. and Peng, Q. and Polly, C. C. and Pretz, J. and Prigl, R. and zu Putlitz, G. and Qian, T. and Redin, S. I. and Rind, O. and Roberts, B. L. and Ryskulov, N. and Sedykh, S. and Semertzidis, Y. K. and Shagin, P. and Shatunov, Yu. M. and Sichtermann, E. P. and Solodov, E. and Sossong, M. and Steinmetz, A. and Sulak, L. R. and Timmermans, C. and Trofimov, A. and Urner, D. and von Walter, P. and Warburton, D. and Winn, D. and Yamamoto, A. and Zimmerman, D. Final report of the E821 muon anomalous magnetic moment measurement at BNL. *Phys. Rev. D* **73**, 072003 (2006).

[56] Grange, J., Guarino, V., Winter, P., Wood, K., Zhao, H., Carey, R. M., Gastler, D., Hazen, E., Kinnaird, N. & Miller, J. P. Muon (g-2) technical design report. *arXiv preprint arXiv:1501.06858* (2015).

[57] Alexander, J., Battaglieri, M., Echenard, B., Essig, R., Graham, M., Izaguirre, E., Jaros, J., Krnjaic, G., Mardon, J. & Morrissey, D. Dark sectors 2016 workshop: community report. *arXiv preprint arXiv:1608.08632* (2016).

[58] Arkani-Hamed, N., Finkbeiner, D. P., Slatyer, T. R. & Weiner, N. A theory of dark matter. *Physical Review D* **79**, 015014 (2009).

[59] Holdom, B. Two U(1)'s and ε charge shifts. *Physics Letters B* **166**, 196–198 (1986).

[60] Jaeckel, J. & Roy, S. Spectroscopy as a test of Coulomb's law: A probe of the hidden sector. *Physical Review D* **82**, 125020 (2010).

[61] Davoudiasl, H., Lee, H.-S. & Marciano, W. J. Muon g-2, rare kaon decays, and parity violation from dark bosons. *Physical Review D* **89**, 095006 (2014).

[62] Banerjee, D., Burtsev, V., Cooke, D., Crivelli, P., Depero, E., Dermenev, A. V., Donskov, S. V., Dubinin, F., Dusaev, R. R. & Emmenegger, S. Search for invisible decays of sub-GeV dark photons in missing-energy events at the CERN SPS. *Physical Review Letters* **118**, 011802 (2017).

[63] Lees, J. P., Poireau, V., Tisserand, V., Grauges, E., Palano, A., Eigen, G., Brown, D. N., Derdzinski, M., Giuffrida, A. & Kolomensky, Y. G. Search for invisible decays of a dark photon produced in e^+e^- collisions at BaBar. *Physical Review Letters* **119**, 131804 (2017).

[64] Bœhm, C. & Silk, J. A new test for dark matter particles of low mass. *Physics Letters B* **661**, 287–289 (2008).

[65] Jean, P., Knödlseder, J., Lonjou, V., Allain, M., Roques, J.-P., Skinner, G. K., Teegarden, B. J., Vedrenne, G., von Ballmoos, P. & Cordier, B. Early SPI/INTEGRAL measurements of 511 kev line emission from the 4th quadrant of the galaxy. *Astronomy & Astrophysics* **407**, L55–L58 (2003).

[66] Bœhm, C., Hooper, D., Silk, J., Casse, M. & Paul, J. Mev dark matter: Has it been detected? *Physical Review Letters* **92**, 101301 (2004).

[67] Bœhm, C. & Ascasibar, Y. More evidence in favor of light dark matter particles? *Physical Review D* **70**, 115013 (2004).

[68] Berengut, J. C., Budker, D., Delaunay, C., Flambaum, V. V., Frugiuele, C., Fuchs, E., Grojean, C., Harnik, R., Ozeri, R. & Perez, G. Probing new light force-mediators by isotope shift spectroscopy. *arXiv preprint arXiv:1704.05068* (2017).

[69] Delaunay, C., Frugiuele, C., Fuchs, E. & Soreq, Y. Probing new spin-independent interactions through precision spectroscopy in atoms with few electrons. *arXiv preprint arXiv:1709.02817* (2017).

[70] Brodsky, S. J. & Drell, S. D. Anomalous Magnetic Moment and Limits on Fermion Substructure. *Phys. Rev. D* **22**, 2236 – 2243 (1980).

[71] Hoogerheide, S. F. *Trapped Positrons for High Precision Magnetic Moment Measurements*. Ph.D. thesis, Harvard University (2013). (thesis advisor: G. Gabrielse).

[72] Bourilkov, D. Hint for Axial-Vector Contact Interactions in the Data on $e^+e^- \to e^+e^-(\gamma)$ at Center-of-Mass Energies 192-208 GeV. *Phys. Rev. D* **64**, 071701R (2001).

[73] BIPM. Draft of the ninth SI brochure (2016).

[74] Newell, D. B., Cabiati, F., Fischer, J., Fujii, K., Karshenboim, S. G., Margolis, H. S., de Mirandes, E., Mohr, P. J., Nez, F. & Pachucki, K. The CODATA 2017 values of h, e, k, and N_A for the revision of the SI. *Metrologia* (2017).

[75] Rich, A. & Wesley, J. C. Current Status of the Lepton g Factors. *Rev. Mod. Phys.* **44**, 250–283 (1972).

[76] Compton, A. H. The magnetic electron. *Journal of the Franklin Institute* **192**, 145–155 (1921).

[77] Lamb, Jr., W. E. & Retherford, R. C. Fine structure of the hydrogen atom by a microwave method. *Physical Review* **72**, 241 (1947).

[78] Nafe, J. E., Nelson, E. B. & Rabi, I. I. The hyperfine structure of atomic hydrogen and deuterium. *Physical Review* **71**, 914 (1947).

[79] Breit, G. The effect of retardation on the interaction of two electrons. *Phys. Rev.* **34**, 553 (1929).

[80] Dyson, F. J. The s matrix in quantum electrodynamics. *Physical Review* **75**, 1736 (1949).

[81] Kusch, P. & Foley, H. M. The magnetic moment of the electron. *Physical Review* **74**, 250 (1948).

[82] Gardner, J. H. & Purcell, E. M. A precise determination of the proton magnetic moment in bohr magnetons. *Physical Review* **76**, 1262 (1949).

[83] Louisell, W. H. A experimental measurement of the gyromagnetic ratio of the free electron. (1953).

[84] Graff, G., Major, F. G., Roeder, R. W. H. & Werth, G. Method for measuring the cyclotron and spin resonance of free electrons. *Physical Review Letters* **21**, 340 (1968).

[85] Dehmelt, H. G. & Walls, F. L. "Bolometric" technique for the RF spectroscopy of stored ions. *Physical Review Letters* **21**, 127 (1968).

[86] Odom, B., Hanneke, D., D'Urso, B. & Gabrielse, G. New Measurement of the Electron Magnetic Moment Using a One-Electron Quantum Cyclotron. *Phys. Rev. Lett.* **97**, 030801 (2006).

[87] Gabrielse, G. & MacKintosh, F. C. Cylindrical Penning Traps with Orthogonalized Anharmonicity Compensation. *Intl. J. of Mass Spec. and Ion Proc.* **57**, 1–17 (1984).

[88] Tan, J. & Gabrielse, G. Synchronization of Parametrically Pumped Electron Oscillators with Phase Bistability. *Phys. Rev. Lett.* **67**, 3090–3093 (1991).

[89] Hoogerheide, S. F., Dorr, J. C., Novitski, E. & Gabrielse, G. High efficiency positron accumulation for high-precision magnetic moment experiments. *Review of Scientific Instruments* **86**, 053301 (2015).

[90] Dorr, J. *Quantum Jump Spectroscopy of a Single Electron in a New and Improved Apparatus.* Ph.D. thesis, Harvard University (2013). (thesis advisor: G. Gabrielse).

[91] Gabrielse, G. & Dehmelt, H. Observed relativistic mass increase for 0.3 eV electron. *Bull. Am. Phys. Soc.* **25**, 1149 (1980). Abstract.

[92] Penning, F. M. Die glimmentladung bei niedrigem druck zwischen koaxialen zylindern in einem axialen magnetfeld. *Physica (Utrecht)* **3**, 873 (1936).

[93] Goldman, J. D. *Planar Penning Traps with Anharmonicity Compensation for Single-Electron Qubits.* Ph.D. thesis, Harvard University (2011).

[94] Brown, L. S. & Gabrielse, G. Precision Spectroscopy of a Charged Particle in an Imperfect Penning Trap. *Phys. Rev. A* **25**, 2423–2425 (1982).

[95] Mount, B. & Myers, M. R. R. Atomic masses of ^{6}Li, ^{23}Na, $^{38,41}K$, $^{85,86}Rb$ and ^{133}Cs. *Phys. Rev. A* 042513 (2010).

[96] Gabrielse, G. Relaxation Calculation of the Electrostatic Properties of Compensated Penning Traps with Hyperbolic Electrodes. *Phys. Rev. A* **27**, 2277–2290 (1983).

[97] Gabrielse, G., Haarsma, L. & Rolston, S. L. Open-Endcap Penning Traps for High-Precision Experiments. *Intl. J. of Mass Spec. and Ion Proc.* **88**, 319–332 (1989). Ibid. 93:, 121 (1989).

[98] Gabrielse, G., Fei, X., Helmerson, K., Rolston, S. L., Tjoelker, R. L., Trainor, T. A., Kalinowsky, H., Haas, J. & Kells, W. First capture of antiprotons in a Penning trap: A keV source. *Phys. Rev. Lett.* **57**, 2504–2507 (1986).

[99] Gabrielse, G., Bowden, N. S., Oxley, P., Speck, A., Storry, C. H., Tan, J. N., Wessels, M., Grzonka, D., Oelert, W., Schepers, G., Sefzick, T., Walz, J., Pittner, H., Hänsch, T. W. & Hessels, E. A. Background-free observation of cold antihydrogen with field-ionization analysis of its states. *Phys. Rev. Lett.* **89**, 213401 (2002).

[100] Gabrielse, G., Larochelle, P., Le Sage, D., Levitt, B., Kolthammer, W. S., McConnell, R., Richerme, P., Wrubel, J., Speck, A., George, M. C., Grzonka, D., Oelert, W., Sefzick, T., Zhang, Z., Carew, A., Comeau, D., Hessels, E. A., Storry, C. H., Weel, M. & Walz, J. Antihydrogen production in a Penning-Ioffe trap. *Phys. Rev. Lett.* **100**, 113001 (2008).

[101] Gabrielse, G., Kalra, R., Kolthammer, W. S., McConnell, R., Richerme, P., Grzonka, D., Oelert, W., Sefzick, T., Zielinski, M., Fitzakerley, D., George, M. C., Hessels, E. A., Storry, C. H., Weel, M., Müllers, A. & Walz, J. Trapped antihydrogen in its ground state. *Phys. Rev. Lett.* **108**, 113002 (2012).

[102] DiSciacca, J. & Gabrielse, G. Direct measurement of the proton magnetic moment. *Phys. Rev. Lett.* **108**, 153001 (2012). (correction: an observed Δf_z of 20 rather than 50 Hz signaled a 0.3 μm cyclotron radius.).

[103] Goldman, J. & Gabrielse, G. Optimized Planar Penning Traps for Quantum-Information Studies. *Phys. Rev. A* **81**, 052335 (2010).

[104] Goldman, J. D. & Gabrielse, G. Optimized Planar Penning Traps for Quantum Information Studies. *Hyperfine Interact.* (2011).

[105] Brown, L. S. & Gabrielse, G. Geonium Theory: Physics of a Single Electron or Ion in a Penning Trap. *Rev. Mod. Phys.* **58**, 233–311 (1986).

[106] Dehmelt, H., Dyck, R. S. V., Schwinberg, P. B. & Gabrielse, G. Proposal to detect spin flips in geonium via linked axial excitation. *baps* **24**, 675 (1979). Abstract.

[107] Brown, L. S. Geonium lineshape. *Ann. Phys. (N.Y.)* **159**, 62–98 (1985).

[108] D'Urso, B. *Cooling and Self-Excitation of a One-Electron Oscillator*. Ph.D. thesis, Harvard University (2003). (thesis advisor: G. Gabrielse).

[109] Wineland, D., Ekstrom, P. & Dehmelt, H. Monoelectron oscillator. *Phys. Rev. Lett.* **31**, 1279 (1973).

[110] Odom, B. *Fully Quantum Measurement of the Electron Magnetic Moment.* Ph.D. thesis, Harvard University (2004). (thesis advisor: G. Gabrielse).

[111] Gabrielse, G., Fei, X., Orozco, L. A., Tjoelker, R. L., Haas, J., Kalinowsky, H., Trainor, T. A. & Kells, W. Thousand-fold improvement in the measured antiproton mass. *Phys. Rev. Lett.* **65**, 1317–1320 (1990).

[112] Phillips, D. F. *A Precision Comparison of the $\bar{p} - p$ Charge-to-Mass Ratios.* Ph.D. thesis, Harvard University (1996). (thesis advisor: G. Gabrielse).

[113] Brunner, S., Engel, T. & Werth, G. Field stabilization of a superconducting magnet by helium pressure control. *Measurement Science and Technology* **6**, 222 (1995).

[114] Van Dyck, J., Robert, S., Farnham, D. L., Zafonte, S. L. & Schwinberg, P. B. Ultrastable superconducting magnet system for a Penning trap mass spectrometer. *Review of Scientific Instruments* **70**, 1665–1671 (1999).

[115] Gabrielse, G. & Tan, J. Self-shielding superconducting solenoid systems. *J. Appl. Phys.* **63**, 5143–5148 (1988).

[116] Sari, S. O. & Carver, T. R. A simply constructed proton NMR probe for high field superconducting solenoid calibration. *Review of Scientific Instruments* **41**, 1324 – 1326 (1970).

[117] Schwinberg, P. B., Dyck, R. S. V. & Dehmelt, H. G. Trapping and Thermalization of Positrons for Geonium Spectroscopy'. *Phys. Lett. A* **81**, 119–120 (1981).

[118] Estrada, J., Roach, T., Tan, J. N., Yesley, P. & Gabrielse, G. Field Ionization of Strongly Magnetized Rydberg Positronium: A New Physical Mechanism for Positron Accumulation. *Phys. Rev. Lett.* **84**, 859–862 (2000).

[119] Marshall, M. Ph.D. thesis. Thesis work underway. (thesis advisor: G. Gabrielse).

[120] Hall, D. S. *Positrons, Antiprotons and Interactions for Cold Antihydrogen.* Ph.D. thesis, Harvard University (1997). (thesis advisor: G. Gabrielse).

[121] Van Dyck, Jr., R., Ekstrom, P. & Dehmelt, H. Axial, magnetron, cyclotron and spin-cyclotron-beat frequencies measured on single electron almost at rest in free space (geonium). *Nature* **262**, 776 (1976).

[122] Tan, J. N. & Gabrielse, G. One Electron in an Orthogonalized Cylindrical Penning Trap. *Appl. Phys. Lett.* **55**, 2144–2146 (1989).

[123] D'Urso, B., Van Handel, R., Odom, B., Hanneke, D. & Gabrielse, G. Single-Particle Self-Excited Oscillator. *Phys. Rev. Lett.* **94**, 113002 (2005).

[124] Gabrielse, G. & Dehmelt, H. Observation of inhibited spontaneous emission. *Phys. Rev. Lett.* **55**, 67–70 (1985).

[125] L. S. Brown, Gabrielse, G., J. N. Tan & Chan, K. C. D. Cyclotron Motion in a Penning Trap Microwave Cavity. *Phys. Rev. A* **37**, 4163–4171 (1988).

[126] Jackson, J. D. *Classical Electrodynamics, 2nd Edition* (John Wiley and Sons, Inc., New York, 1975).

[127] Gabrielse, G., Tan, J. N. & Brown, L. S. *Cavity Shifts of Measured Electron Magnetic Moments*, 389–418 (World Scientific, Singapore, 1990).

[128] Brown, L. S., Gabrielse, G., Helmerson, K. & Tan, J. Cyclotron Motion in a Microwave Cavity: Possible shifts of the Measured Electron g Factor. *Phys. Rev. Lett.* **55**, 44–47 (1985).

[129] Brown, L. S., Gabrielse, G., Helmerson, K. & Tan, J. N. Cyclotron motion in a microwave cavity: Lifetime and frequency shifts. *Phys. Rev. A* **32**, 3204–3218 (1985).

[130] D'Urso, B., Odom, B. & Gabrielse, G. Feedback Cooling of a One-Electron Oscillator. *Phys. Rev. Lett.* **90**, 043001 (2003).

[131] Wineland, D. & Dehmelt, H. Line shifts and widths of axial, cyclotron and g-2 resonances in tailored, stored electron (ion) cloud. *International Journal of Mass Spectrometry and Ion Physics* **19**, 251 (1976).

[132] Oreskovic, T. *Development of a cryogenic vacuum valve and an electromechanical switch for ALPHATRAP.* Master's thesis (2014).

[133] Tan, J. N. & Gabrielse, G. Parametrically-pumped electron oscillators. *Phys. Rev. A* **48**, 3105 (1993).

[134] Nayfeh, A. H. & Mook, D. T. *Nonlinear oscillations* (John Wiley & Sons, 2008).

[135] Lapidus, L. J. *Synchronization and Stochastic Behavior of Electrons in a Penning Trap.* Ph.D. thesis, Harvard University (1998). (thesis advisor: G. Gabrielse).

[136] Tan, J. N. *Cooperative Behavior in Cavity-Cooled, Parametrically- Pumped Electron Oscillators.* Ph.D. thesis, Harvard University (1992). (thesis advisor: G. Gabrielse).

[137] Van Dyck Jr, R. S., Moore, F. L., Farnham, D. L., Schwinberg, P. B. & Dehmelt, H. G. Microwave-cavity modes directly observed in a Penning trap. *Physical Review A* **36**, 3455 (1987).

[138] Bethe, H. A. Theory of diffraction by small holes. *Physical Review* **66**, 163 (1944).

[139] Bouwkamp, C. J. On the diffraction of electromagnetic waves by small circular disks and holes. *Philips Res. Rep.* **5**, 401–422 (1950).

[140] Cohn, S. B. Microwave coupling by large apertures. *Proceedings of the IRE* **40**, 696–699 (1952).

[141] Roberts, A. Electromagnetic theory of diffraction by a circular aperture in a thick, perfectly conducting screen. *JOSA A* **4**, 1970–1983 (1987).

[142] Nikitin, A. Y., Zueco, D., Garcia-Vidal, F. J. & Martín-Moreno, L. Electromagnetic wave transmission through a small hole in a perfect electric conductor of finite thickness. *Physical Review B* **78**, 165429 (2008).

[143] Dunseith, D. P., Truppe, S., Hendricks, R. J., Sauer, B. E., Hinds, E. A. & Tarbutt, M. R. A high quality, efficiently coupled microwave cavity for trapping cold molecules. *Journal of Physics B: Atomic, Molecular and Optical Physics* **48**, 045001 (2015).

[144] Oxley, P., Bowden, N. S., Parrott, R., Speck, A., Storry, C., Tan, J. N., Wessels, M., Gabrielse, G., Grzonka, D., Oelert, W., Schepers, G., Sefzick, T., Walz, J., Pittner, H., Hänsch, T. W. & Hessels, E. A. Aperture method to determine the density and geometry of anti-particle plasmas. *Phys. Lett. B* **595**, 60 – 67 (2004).

[145] Oxley, P. *Production of Slow Antihydrogen from Cold Antimatter Plasmas.* Ph.D. thesis (2003).

[146] Gabrielse, G., Fei, X., Orozco, L. A., Tjoelker, R. L., Haas, J., Kalinowsky, H., Trainor, T. A. & Kells, W. Cooling and slowing of trapped antiprotons below 100 meV. *Phys. Rev. Lett.* **63**, 1360–1363 (1989).

[147] Bowden, N. B. *Production of Cold Antihydrogen during the Positron Cooling of Antiprotons.* Ph.D. thesis, Harvard University (2003). (thesis advisor: G. Gabrielse).

[148] Speck, A. *Two Techniques to Produce Cold Antihydrogen.* Ph.D. thesis (2005).

[149] Brownnutt, M., Kumph, M., Rabl, P. & Blatt, R. Ion-trap measurements of electric-field noise near surfaces. *Reviews of Modern Physics* **87**, 1419 (2015).

[150] Dubin, D. H. E. & O'Neil, T. M. Trapped Nonneutral Plasmas, Liquids, and Crystals (the Thermal Equilibrium States). *Rev. Mod. Phys.* **71**, 87–172 (1999).

[151] Rolston, S. L. & Gabrielse, G. Cooling antiprotons in an ion trap. *Hyperfine Interact.* **44**, 233–245 (1988).

[152] Gabrielse, G. Penning traps, masses and antiprotons. In Bloch, P., Pavlopoulos, P. & Klapisch, R. (eds.) *Fundamental Symmetries*, 59–75 (Plenum, New York, 1987).

[153] DiSciacca, J. & et al. One-particle measurement of the antiproton magnetic moment. *Phys. Rev. Lett.* **110**, 130801 (2013).

[154] Ahmadi, M., Alves, B. X. R., Baker, C. J., Bertsche, W., Butler, E., Capra, A., Carruth, C., Cesar, C. L., Charlton, M., Cohen, S., Collister, R., Eriksson, S., Evans, A., Evetts, N., Fajans, J., Friesen, T., Fujiwara, M. C., Gill, D. R., Gutierrez, A., Hangst, J. S., Hardy, W. N., Hayden, M. E., Isaac, C. A., Ishida, A., Johnson, M. A., Jones, S. A., Jonsell, S., Kurchaninov, L., Madsen, N., Mathers, M., Maxwell, D., McKenna, J. T. K., Menary, S., Michan, J. M., Momose, T., Munich, J. J., Nolan, P., Olchanski, K., Olin, A., Pusa, P., Rasmussen, C. Ø., Robicheaux, F., Sacramento, R. L., Sameed, M., Sarid, E., Silveira, D. M., Stracka, S., Stutter, G., So, C., Tharp, T. D., Thompson, J. E., Thompson, R. I., van der Werf, D. P. & Wurtele, J. S. Observation of the hyperfine spectrum of antihydrogen. *Nature* **548**, 66–69 (2017).

[155] Enomoto, Y., Kuroda, N., Michishio, K., Kim, C. H., Higaki, H., Nagata, Y., Kanai, Y., Torii, H. A., Corradini, M. & Leali, M. Synthesis of cold antihydrogen in a cusp trap. *Physical review letters* **105**, 243401 (2010).

[156] Scampoli, P. & Storey, J. The AEgIS experiment at CERN for the measurement of antihydrogen gravity acceleration. *Modern Physics Letters A* **29**, 1430017 (2014).

[157] Smorra, C., Blaum, K., Bojtar, L., Borchert, M., Franke, K., Higuchi, T., Leefer, N., Nagahama, H., Matsuda, Y., Mooser, A., Niemann, M., Ospelkaus, C., Quint, W., Schneider, G., Sellner, S., Tanaka, T., Van Gorp, S., Walz, J., Yamazaki, Y. & Ulmer, S. BASE – the Baryon Antibaryon Symmetry Experiment. *The European Physical Journal Special Topics* **224**, 3055–3108 (2015).

[158] Zimmermann, C. & Hänsch, T. Laser spectroscopy of hydrogen and antihydrogen. *Hyperfine Interact.* **76**, 47–57 (1993).

[159] Maury, S. The Antiproton Decelerator: AD. *Hyperfine Int.* **109**, 43 – 52 (1997).

[160] Gott, Y. V., Ioffe, M. S. & Tel'kovskii, V. G. *Nuc. Fusion 1962 Suppl. Pt.* **3**, 1045 (1962).

[161] Pritchard, D. E. Cooling neutral atoms in a magnetic trap for precision spectroscopy. *Phys. Rev. Lett.* **51**, 1336 (1983).

[162] Mills, A. & Gullikson, E. Solid neon moderator for producing slow positrons. *Appl. Phys. Lett.* **49**, 1121–1123 (1986).

[163] Surko, C. M., Leventhal, M. & Passner, A. Positron plasma in the laboratory. *Phys. Rev. Lett.* **62**, 901–904 (1989).

[164] Fitzakerley, D. W., George, M. C., Hessels, E. A., Skinner, T. D. G., Storry, C. H., Weel, M., Gabrielse, G., Hamley, C. D., Jones, N. & Marable, K. Electron-cooled accumulation of 4×10^9 positrons for production and storage of antihydrogen atoms. *Journal of Physics B: Atomic, Molecular and Optical Physics* **49**, 064001 (2016).

[165] Gabrielse, G., Bowden, N. S., Oxley, P., Speck, A., Storry, C. H., Tan, J. N., Wessels, M., Grzonka, D., Oelert, W., Schepers, G., Sefzick, T., Walz, J., Pittner, H., Hänsch, T. W. & Hessels, E. A. Driven production of cold antihydrogen and the first measured distribution of antihydrogen states. *Phys. Rev. Lett.* **89**, 233401 (2002).

[166] M. Amoretti, et al. Production and detection of cold antihydrogen atoms. *Nature* **419**, 456–459 (2002).

[167] McConnell, R. P. *Laser-controlled charge-exchange production of antihydrogen.* Ph.D. thesis (2011).

[168] Müllers, A., Bottner, S., Kolbe, D., Diehl, T., Koglbauer, A., Sattler, M., Stappel, M., Steinborn, R., Walz, J., Gabrielse, G., Kalra, R., Kolthammer, W. S., McConnell, R. P., Richerme, P., Fitzakerley, D. W., George, M. C., Hessels, E. A., Storry, C. H., Weel, M., Grzonka, D. & Oelert, W. A semiconductor laser system for the production of antihydrogen. *New J. Physics* **14**, 055009 (2012).

[169] Gabrielse, G., Kolthammer, W. S., McConnell, R., Richerme, P., Wrubel, J., Kalra, R., Novitski, E., Grzonka, D., Oelert, W., Sefzick, T., Zielinski, M., Borbely, J. S., Fitzakerley, D., George, M. C., Hessels, E. A., Storry, C. H., Weel,

M., Müllers, A., Walz, J. & Speck, A. Centrifugal separation of antiprotons and electrons. *Phys. Rev. Lett.* **105**, 213002 (2010).

[170] Gabrielse, G., Kolthammer, W. S., McConnell, R., Richerme, P., Wrubel, J., Kalra, R., Novitski, E., Grzonka, D., Oelert, W., Sefzick, T., Fitzakerley, D. W., George, M. C., Hessels, E. A., Storry, C. H., Weel, M., Müllers, A. & Walz, J. Adiabatic cooling of antiprotons. *Phys. Rev. Lett.* **106**, 073002 (2011).

[171] McConnell, R., Gabrielse, G., Kolthammer, W. S., Richerme, P., Müllers, A., Walz, J., Grzonka, D., Zielinski, M., Fitzakerley, D. & George, M. C. Large numbers of cold positronium atoms created in laser-selected Rydberg states using resonant charge exchange. *Journal of Physics B: Atomic, Molecular and Optical Physics* **49**, 064002 (2016).

[172] Richerme, P., Gabrielse, G., Ettenauer, S., Kalra, R., Tardiff, E., Fitzakerley, D., George, M., Hessels, E., Storry, C., ahd A. Müllers, M. W. & Walz, J. Electric fields prevent mirror-trapped antiprotons in trapped antihydrogen studies **87**, 023422 (2013).

[173] E. Tardiff and the ATRAP collaboration (incl. E. Novitski). Two-Symmetry Penning-Ioffe Trap for Antihydrogen Cooling and Spectroscopy. *Manuscript in preparation* **79**, 031301 (2014).

[174] Blake, C. & Bull, C. IGBT or MOSFET: choose wisely. Tech. Rep., International Rectifier (2001).

[175] Chapman, D. & Norris, T. Copper for Busbars. Publication No. 22. Tech. Rep., Copper Development Association (2014).

[176] Felice, H. & Todesco, E. Quench protection analysis in accelerator magnets, a review of the tools. CERN Yellow Report CERN-2013-006 (2013). ArXiv:1401.3934.

[177] Wilson, M. N. *Superconducting Magnets* (Oxford University Press, 1983).

[178] Maddock, B. J. & James, G. B. Protection and stabilisation of large superconducting coils. vol. 115, 543–547 (IET, 1968).

[179] Yang, L., Brome, C. R., Butterworth, J. S., Dzhosyuk, S. N., Mattoni, C. E. H., McKinsey, D. N., Michniak, R. A., Doyle, J. M., Golub, R., Korobkina, E., OŠShaughnessy, C. M., Palmquist, G. R., Seo, P.-N., Huffman, P. R., Coakley, K. J., Mumm, H. P., Thompson, A. K., Yang, G. L. & Lamoreaux, S. K. Invited article: Development of high-field superconducting Ioffe magnetic traps. *Review of Scientific Instruments* **79**, 031301 (2008).

[180] Gerhold, J. Dielectric breakdown of helium at low temperatures. *Cryogenics* **12**, 370–376 (1972).

[181] ten Kate, H. Superconducting magnets: Quench propagation and protection (2013). URL `https://indico.cern.ch/event/194284/contributions/1472819/attachments/281522/393603/TenKate_-_CAS_-Handout-Quench-Erice-2103.pdf`.

[182] Manfreda, G. Review of ROXIE's material properties database for quench simulation. Tech. Rep. 24, TE Technology Dept. (2011).

[183] Marquardt, E. D., Le, J. P. & Radebaugh, R. Cryogenic material properties database (2002). URL `http://www.boulder.nist.gov/div838/cryogenics.html`. Updates online at http://cryogenics.nist.gov/MPropsMAY/materialproperties.htm.

[184] Verweij, A. CUDI: Users manual. *LHC-MMS, CERN* (2007).

[185] Drexler, E. S., Simon, N. J. & Reed, R. P. Properties of copper and copper alloys at cryogenic temperatures. NIST Monograph, NIST (1992).

[186] McAshan, M. S. MIITs integrals for copper and for Nb-46.5 wt Ti. *Preprint SSC* (1988).

[187] Jensen, J. E., Stewart, R. G., Tuttle, W. A. & Brechna, H. *Brookhaven National Laboratory Selected Cryogenic Data Notebook: Sections I-IX*, vol. 1 (Brookhaven National Laboratory, 1980).

[188] Kasen, M. B., MacDonald, G. R., Beekman Jr, D. H. & Schramm, R. E. Mechanical, electrical, and thermal characterization of G-10CR and G-11CR glass-cloth/epoxy laminates between room temperature and 4 K. *Adv. Cryog. Eng* **26**, 235–244 (1980).

[189] Hull, J. R., Wilson, M. N., Bottura, L., Rossi, L., Green, M. A., Iwasa, Y., Hahn, S., Duchateau, J. & Kalsi, S. S. Superconducting magnets. *Applied Superconductivity: Handbook on Devices and Applications* 423–425 (1965).

[190] Bottura, L. A practical fit for the critical surface of NbTi. *IEEE transactions on applied superconductivity* **10**, 1054–1057 (2000).

[191] Spencer, C., Sanger, P. & Young, M. The temperature and magnetic field dependence of superconducting critical current densities of multifilamentary Nb_3Sn and NbTi composite wires. *IEEE Transactions on Magnetics* **15**, 76–79 (1979).